AUTHOR: CRUICKSHANK, L.

TITLE: Development of novel lanthanide based particle tracers for rapid monitoring of soil erosion.

YEAR: 2016

OpenAIR citation:

CRUICKSHANK, L. 2016. Development of novel lanthanide based particle tracers for rapid monitoring of soil erosion. Robert Gordon University, PhD thesis. Held on OpenAIR [online]. Available from: https://openair.rgu.ac.uk

This work was submitted to- and approved by Robert Gordon University in partial fulfilment of the following degree:
Doctor of Philosophy, Faculty of Design and Technology, School of Engineering

Development of novel lanthanide based particle tracers for rapid monitoring of soil erosion

Laura Cruickshank

A thesis submitted in partial fulfilment of the
requirements of The Robert Gordon University,
Aberdeen for the degree of Doctor of Philosophy

January 2016

This research programme was carried out in
collaboration with The James Hutton Institute

Dedication

For my Mum and Dad, who taught me to always aim for the stars.

And for Chloe and Euan, I hope in some small way this helps teach you the same.

Declaration

I hereby declare that no portion of the work referred to in this thesis has been submitted in support for an application for another degree or qualification of this or another university or other institute of learning.

This is an original piece of work undertaken by myself. All results and work other than my own are clearly cited and acknowledged.

Acknowledgements

I wish to express my sincere thanks to the following:

Firstly I wish to express my immense gratitude to my supervisors, Simon Officer, Marc Stutter and Pat Pollard for all the support and advice given throughout the project.

A special thank you to all the staff and students in the centre for research, energy and the environment for many useful discussions and much encouragement. In particular to Morgan Adams who helped to remind me that research can be fun!

Thank you to the staff of the analytical chemistry labs, and engineering workshop, who were always there to give advice whenever needed.

Also, to everyone at the James Hutton Institute whose help was invaluable, particularly Samia Richards for guiding me patiently through a variety of new techniques, and Evelyne DelBois who helped obtain some of the SEM images included in this thesis.

Funded by the Institute for Innovation, Design and Sustainability (IDEAS) at the Robert Gordon University.

Finally I would like to thank my friends and family, particularly Neil, Chloe and Euan for providing endless encouragement, patience and support. You can finally get mummy back now!

Abstract

Soil erosion is a global problem, affecting much of the world's agricultural land. As the world's population increases, the pressures placed upon the land resource to provide space for food production, leisure, housing and industrial facilities also increases. Thus it is vital that the land resource is as productive as possible. As soil erosion is the major cause of soil degradation globally, it is vital that methods for accurately monitoring the degree of erosion from a site, and the effectiveness of any remediation attempts are available.

Reported here is the development of a novel soil erosion particle tracer, based upon a lanthanide chelate complex doped silica particle. The luminescent lanthanide chelate complexes were comprised of 2-thenoyltrifluoroacetone (TTA) and 2-pyridinol-1-oxide (2PO) coordinated with either trivalent europium or terbium ions. These complexes were then doped into silica sol-gel particles using a core shell technique.

This method resulted in the synthesis of two luminescent soil tracers, targeted to two of the key eroded soil fractions; fine silt (63-250 µm) and clay (< 1.2 µm). The behaviour of the tracers was analysed within three different soils obtained from the Glensaugh research station. They retained their luminescence when mixed with soil, and could be detected at concentrations of 10 mg tracer / kg soil using a standard benchtop fluorescence spectrometer (Perkin Elmer LS55B). Scanning electron micrographs indicated that the tracer particles interacted with the soil particles, whilst soil sedimentation experiments demonstrated that the tracer particles had a similar sedimentation pattern to natural soil particles. Soil microbial respiration studies were performed for the tracers and showed that the tracers did not significantly impact the soil microbial population. Studies of the luminescence stability of the tracer in soil over time showed that the tracer could be detected in the soil for one season (approximately 3 months).

A prototype rainfall simulator, designed to simulate the kinetic energy of raindrops on the surface of the soil, was developed, and used during a series of rainfall simulation experiments. These simulations were performed at two different rainfall intensities (30 and 90 $mm.h^{-1}$) and both of these conditions resulted in movement of the tracer particles within the plot. This movement was both horizontal, in overland flow over the plot surface, and vertical, through the plot. The pattern of tracer movement reflected that of the soil mass moved, and as such indicated that the tracers exhibited similar transport behaviour during the erosion simulations performed.

These initial simulations demonstrated that the tracers can be detected at low concentrations within the soil using standard laboratory equipment, and that they move with the eroded soil particles during simulated soil erosion experiments. As such, these tracers are excellent candidates for further study in larger scale erosion events.

Abbreviations

AGA – amino G acid monopotassium dye

ANOVA – analysis of variance

ATR - attenuated total reflection

BLD - below limit of detection

DMSO – dimethyl sulfoxide

D_2O – deuterium

DOE - design of experiments

DSC – differential scanning colorimetry

EDXA – energy dispersive x-ray analysis

FTIR – Fourier Transform Infrared

HMP – sodium hexametaphosphate solution

HOPO – hydroxy-pyridinones

HP-Ge – high purity – germanium

HTTA - free 2-thenoyltrifluoroacteone

ICP-OES – inductively coupled plasma – optical emission spectroscopy

ICP-MS – inductively coupled plasma – mass spectrometry

IR - Infra-red

LC-MS – liquid chromatography- mass spectrometry

Ln^{3+} - trivalent ion of the lanthanide series

LOD –	limit of detection
MRI –	magnetic resonance imaging
NMR –	nuclear magnetic resonance
PMT –	photomultiplier tube
REE -	rare earth element
REETM -	rare earth element tracer method
SAXS -	small angle x-ray scattering
SEM -	scanning electron microscope
SEPA –	Scottish Environmental Protection Agency
TEOS –	tetraethylorthosilicate
TGA –	thermogravimetric analysis
TMOS –	tetramethoxysilane
TTA –	coordinated 2-thenoyltrifluoroacetone
2PO –	2-pyridinol-1-oxide

Table of contents

List of figures

List of tables

Publications

Cruickshank, L., Officer, S., Pollard, P., Prabhu, R., Stutter, M., Fernandez, C. (2015). Rare Elements Electrochemistry: The Development of a Novel Electrochemical Sensor for the Rapid Detection of Europium in Environmental Samples Using Gold Electrode Modified with 2-pyridinol-1-oxide. Analytical Sciences, 31(7), pp.623–627.

Conference presentations

Cruickshank, L., Officer, S., Stutter, M., Pollard, P. (2015) Development of a lanthanide based particle tracer for soil erosion applications (Presentation) 7th Scottish Symposium on Environmental Analytical Chemistry, Robert Gordon University

Cruickshank, L., Officer, S., Stutter, M., Pollard, P. (2014) Development of a lanthanide based particle tracer for soil erosion applications (Poster). 9th International Soil Congress 2014, Side, Antalya.

Cruickshank, L., Officer, S., Stutter, M., Pollard, P. (2013) Development of a lanthanide based particle tracer for soil erosion applications (Presentation). 6th Scottish Symposium on Environmental Analytical Chemistry, University of Glasgow.

Cruickshank, L., Officer, S., Stutter, M., Pollard, P. (2014) Development of a novel fluorescent particle for soil tracing applications (Poster). 5th Scottish Postgraduate symposium for Environmental Analytical Chemistry, University of Aberdeen.

Chapter 1 - General introduction and literature review

1.1 Soils and soil structure

Land forms over twenty-nine per cent of the Earth's surface, the majority of which is covered with soil (Brady & Weil 2002). As the global population increases, the pressures placed upon this land to provide food, raw materials and leisure facilities will also increase. Therefore, in order to meet this growing demand it is vital that this precious resource is managed correctly. It has been estimated that approximately 95 % of food produced globally originates from land based sources, making management of the soil resource a vital concern as the global population continues to increase (Morgan 2009; Blanco & Lal 2010; Braimoh & Velk 2008).

Soils contain a mixture of organic and mineral components, the exact combination of which gives rise to many different soil types, each one with unique properties. Depending on the soil type, varying ratios of both the mineral and organic components form approximately 50 % of the total soil volume, and depending on the soil's moisture content, the remaining volume is then made up of varying amounts of air and water (Ashman & Puri 2002). Two separate processes are required for soil formation, the weathering of rocks to provide the mineral component, followed by the incorporation of this weathered material with organic matter, formed from the remains of plants and animals. Even once formed, soils are constantly changing as material is moved both within the landscape and the soil itself (Ashman & Puri 2002). Mineral particles, at or near the soil surface, can be moved by wind or water and deposited in new locations, sometimes great distances from their original location. Within the soil, mineral and organic matter can also be moved horizontally, along the soil surface, or vertically, down through the soil, depending on its ability to move with water (Ashman & Puri 2002). This results in layers within the soil that are rich in some materials and depleted in others. These layers are known as horizons (See figure 1-1), with the upper horizons normally containing the greatest concentrations of nutrients essential for plant growth as well as plant available soil moisture (Ashman & Puri 2002).

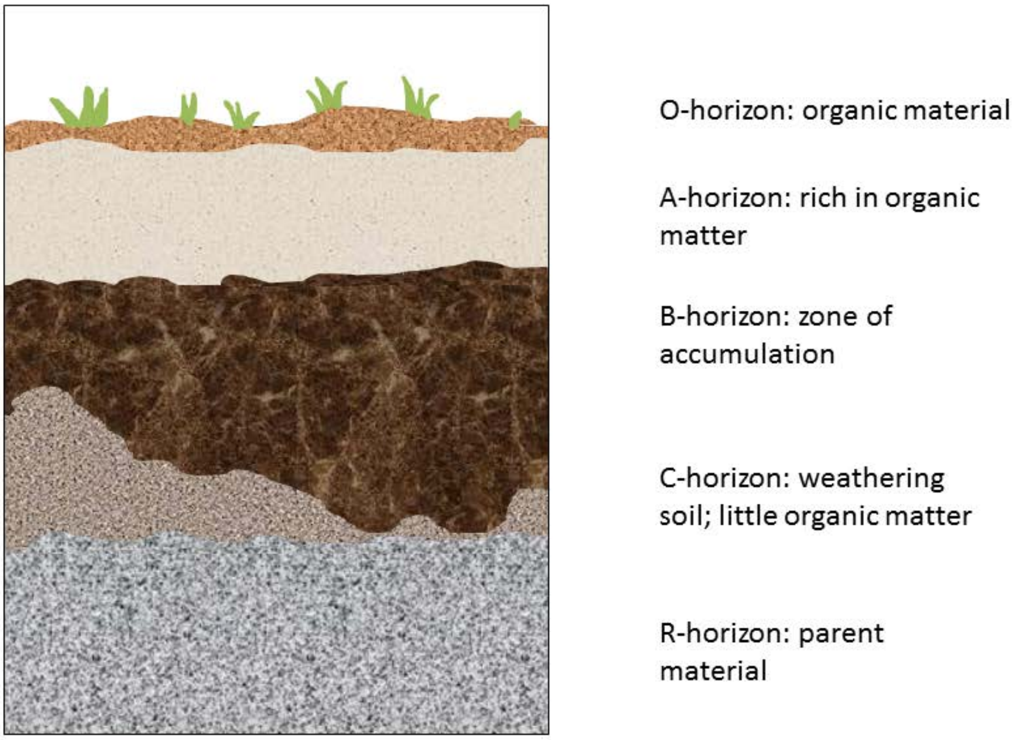

Figure 1-1 Diagram of soil section showing soil horizons (adapted from Anthoni 2000).

Soil is essential for our continued way of life on earth, but the slow rates of soil formation mean it must be considered as a finite resource that needs to be preserved (Brady & Weil 2002). Soil erosion, particularly erosion due to water, is one of the largest contributors to the soil degradation which threatens the soil resource (Morgan 2009; Verheijen et al. 2009).

1.2 Soil Erosion

Soil erosion is a natural process by which soil particles are moved from one area and deposited in another (Ashman & Puri 2002). In undisturbed landscapes, erosion is a gradual two stage process that occurs when the impact of water causes detachment of soil particles followed by their subsequent transport away from the site, by a variety of mechanisms including movement due to wind and water (Morgan 2009; Nearing 2012). In undisturbed landscapes this process occurs at approximately the same rate as soil formation, resulting in little or no change in the total volume of soil (Ashman & Puri 2002).

Archaeological evidence indicates that since the beginning of early agriculture, the rate of soil erosion has been accelerated in cultivated areas, resulting in the overall loss of soil (Dotterweich 2013). Accelerated soil erosion appears to always be the result of mankind's actions, and history shows that many of those early civilisations, dependent on agriculture, declined, at least in part, due to the mismanagement of their natural resources (Ashman & Puri 2002; Dotterweich 2013). The most common processes known to result in soil degradation are deforestation, for land or fuel wood, overgrazing and agriculture, all of which continue to be prevalent in today's societies (Everett et al. 2008; Osman 2014).

Soil erosion can have widespread effects, both at the site of erosion itself, and in the wider environment surrounding the site. On site effects generally result from a reduction in soil quality, primarily due to nutrient loss as topsoil is transported away from the site, and a decrease in the rooting depth. Additionally, the water holding capacity of the soil is dependent on soil structure, and is often reduced as the structure alters (Stevens & Quinton 2008; Nearing 2012). This effect is often masked in the developed world where the addition of artificial fertilizers can be used to compensate for nutrient loss, but is generally considered to be one of the main impacts in the developing world (Blanco & Lal 2010). Long term, this reduction in soil quality represents a serious threat to the sustainability of productivity within these areas, despite the addition of artificial fertilizers (Virto et al. 2014). Eventually their suitability for certain types of agriculture is threatened, as crops in particular are heavily dependent upon the upper soil horizons (Morgan 2009).

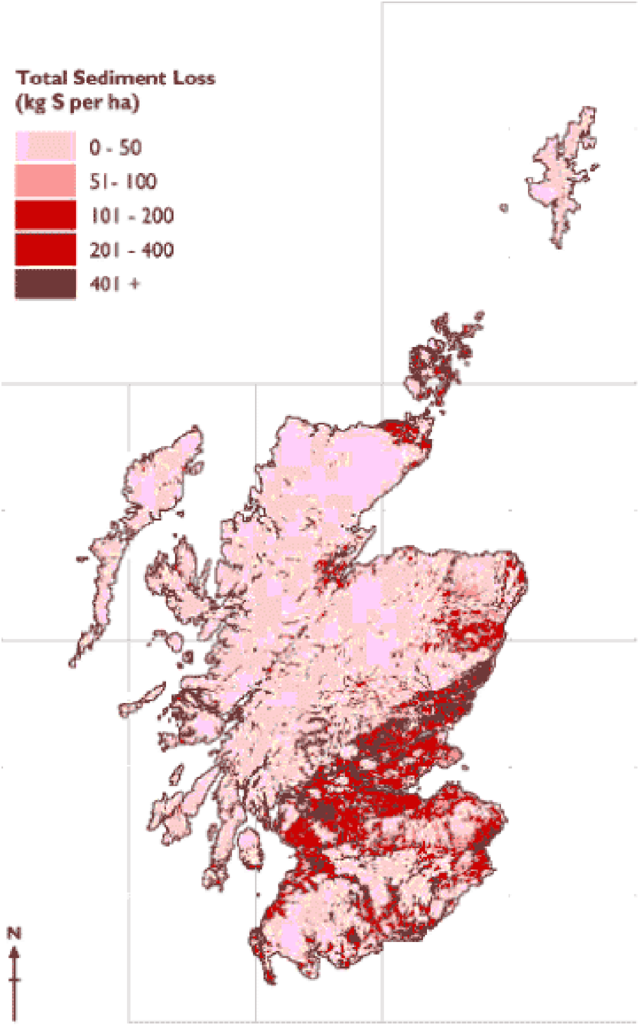

Figure 1-2 Spatial distribution of the total modeled annual sediment loss from point and diffuse sources to ground and surface waters in Scotland (Towers et al. 2006).

The soil transported away from the erosion site can be deposited in many places, including neighbouring fields and within the field itself. The main offsite effect resulting from soil erosion is the deposition of soil within watercourses and it is possible for this to involve large quantities of soil (see figure 1-2) (Dotterweich 2013; Towers et al. 2006; Virto et al. 2014). This disrupts the ecosystems of the watercourses, contaminates drinking water, silts up dams and may increase the severity of downstream flooding. Within developed countries, offsite effects are often the most noticeable and damaging (Morgan 2009). Flooding can result in the loss or damage to structures such as roads and houses, loss of crops, either washed away or covered in mud, and the death of animals (Brady & Weil 2002). An increase of soil particles present as sediment in rivers can cause damage to aquatic life, covering bottom dwellers in a layer of silt, silting up fish gills and suffocating filter feeders (Pimentel & Kounang 1998). The eroded soil is often rich in agricultural pollutants, which are generally concentrated within the upper soil horizons and even small quantities of these can pollute watercourses (Stevens & Quinton 2008; Ashman & Puri 2002). Eutrophication of watercourses can also occur, due to the sudden increase in nutrients from the soil, especially phosphate, which is believed to be a limiting factor in algae growth within watercourses (Chapman et al. 2001; Gyssels et al. 2002). Rapid and larger than normal algal blooms can be poisonous to fish and reduce the amount of light available for aquatic flora (Clark 1985; Pimentel & Kounang 1998), therefore, the marine aquaculture sector in particular can experience significant losses and disruption as a result.

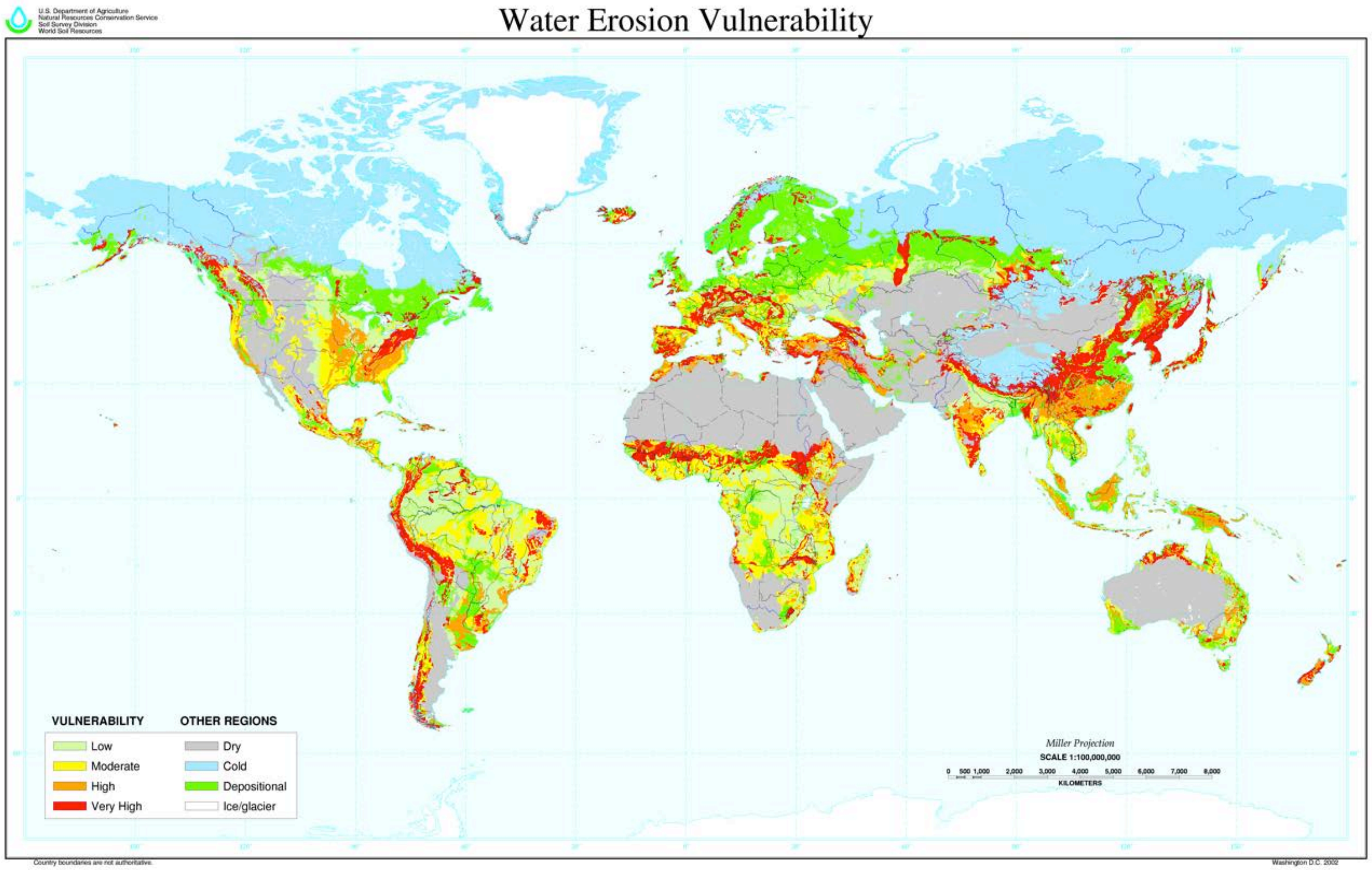

Figure 1-3 Map showing vulnerability of soils to water erosion (adapted from USDA-NRCS 1998).

It is estimated that 38 % of agricultural land (749 M ha) can be classified as degraded (Osman 2014), with erosion by water the cause of approximately 56 % of soil degradation, affecting around 11 million square kilometres (see figure 1-3) (Scherr 1999). A further 26 % of soil degradation is believed to be the result of wind erosion, affecting an estimated area of 5.5 million square kilometres (Verheijen et al. 2009) however it has not yet been determined to what extent tillage erosion contributes to soil degradation worldwide. At present erosion rates, it is calculated that as much as 30 tonnes of soil per hectare are lost in Africa, South Asia and South America and 17 tonnes per hectare in Europe and the USA (Ashman & Puri 2002). One example of this can be seen within the USA, where the effect of the 200-year history of intensive agriculture has been well studied and indicates that a significant amount of the country has lost more than 75 % of the topsoil through erosion, and the majority of the country has lost between 25 and 75 % (Anthoni 2000). Analysis of three sites in the Lunan catchment in Scotland found that at two of the sites, soil was lost at twice the rate of soil deposition (Dobbie et al. 2011). The rate of soil erosion also at the third site was also significantly higher than the rate of deposition (Dobbie et al. 2011). All of these values were above the proposed tolerable soil erosion rate for Europe (Verheijen et al. 2009). Areas that remain as a natural ecosystem experience little or no soil loss by erosion, whilst those areas that have been subjected to intensive farming are the most affected (see figure 1-4) (García-Ruiz 2010). Many areas in Africa and South America show the greatest rates of soil erosion globally, due to enforced, unsuitable agricultural practices (Dotterweich 2013). As soil erosion is a gradual process, the effects of soil erosion have only become evident relatively recently, with scientific studies only commencing in the early 20th century.

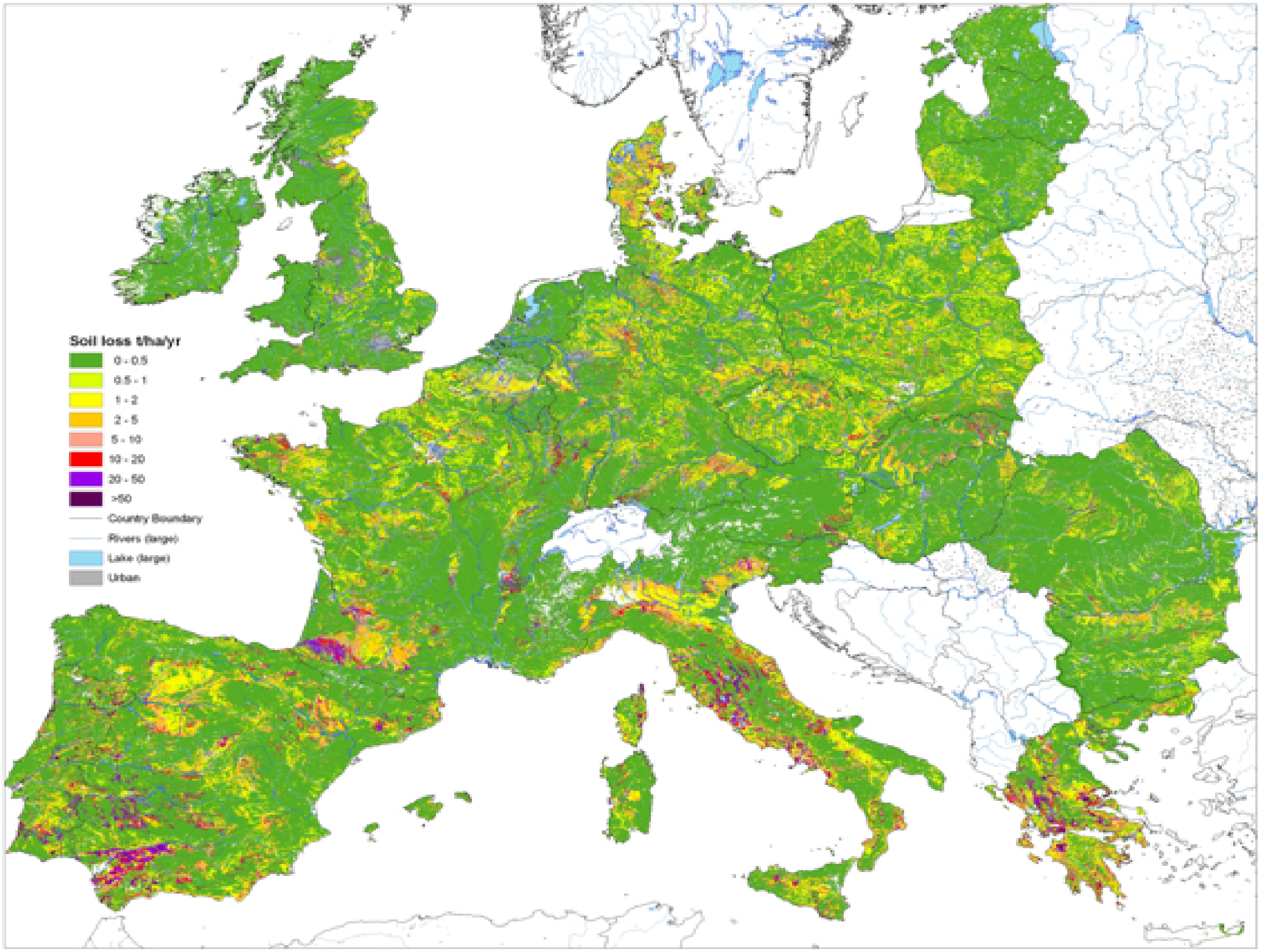

Figure 1-4 Map showing estimated annual soil loss in Europe (Kirby et al. 2004).

Soil is created at a rate as low as 1 tonne/hectare, and as such needs to be treated as a finite resource, with measures taken to reduce the rates of soil erosion (Ashman & Puri 2002). Such measures have been put in place in the UK, and as a result, the level of soil erosion has remained constant, but these measures have yet to further reduce the rate at which it occurs (Stevens & Quinton 2008). However, little is still known about the mechanisms of soil erosion, in particular how erosion rates vary with the spatial variations found naturally within the landscape. As such, current methods to reduce soil erosion are primarily based on the overall characteristics of the site including the gradient and topography of the land, the type of soil and the size of any given field (García-Ruiz 2010). In order for individual systems to be considered, information about the source and deposition sites is vital.

The upper soil horizons are those most susceptible to wind and water erosion and are also the richest in the nutrients required for plant growth. Any process which causes the soil to be left bare for any period of time, but in particular over periods of heavy rain and storm activity, can increase the rate at which soil erosion occurs (Stevens & Quinton 2008). Factors such as intense rainfall, loss of vegetation, sudden changes in climate, for example a change in rainfall patterns or wind conditions, steep slopes and changes in land use by humans, ranging from deforestation to housing development, can all have an affect on soil erosion (Morgan 2009). Thus soil erosion is a global problem, and the precise mechanisms require further investigation both to identify new methods to reduce erosion rates, and to allow monitoring of any such attempts (Zhang et al. 2008).

Erosion is a two-stage process, involving the initial detachment of soil particles followed by their subsequent transport away from the site (Ashman & Puri 2002). There are several mechanisms by which soil erosion can occur, the most common of which are erosion by water or wind and as the result of tillage.

1.2.1 Water erosion

Water erosion is the most common form of erosion, and results from rain directly or indirectly detaching soil particles, followed by their subsequent transport (Stevens & Quinton 2008; Kinnell 2005). Raindrops can cause the direct detachment of soil particles, resulting in a mechanism of water erosion known as rainsplash redistribution (Kinnell 2005). During a rainstorm, the flow of water away from an erosion site can detach and transport soil from rills and gullies, giving rise to rill erosion (Dotterweich 2013; Pimentel & Kounang 1998). Rills are small channels, resulting from concentrated overland flow, that are not considered to be permanent landscape features as they can be ploughed out. Continued transport of soil from rills results in the deeper, permanent features, known as gullies, which cannot be removed by ploughing (Clark 1985).

Rainsplash redistribution occurs when raindrops hit the soil surface with sufficient energy to detach soil particles (see figure 1-5) (Kinnell 2005). Soil particles are carried upwards with the raindrop as it rebounds from the soil surface after impact and then redistributed on the soil surface, at most a few centimetres away from their initial starting point (Brady & Weil 2002; Kinnell 2005). This process can result in the movement of significant quantities of soil, followed by redistribution over the soil surface, with only a slight downhill movement on steep slopes (Virto et al. 2014). Due to the high energy needed for raindrops to detach the soil particles, this form of erosion is most common in equatorial regions where intense storms are common (Pimentel & Kounang 1998). Soil particles that have been detached and redistributed can be carried away from the site if sufficient volumes of overland flow (or sheet wash) are also present, or by the wind if a period of drought follows, drying the soil surface (Li et al. 2006; Brady & Weil 2002).

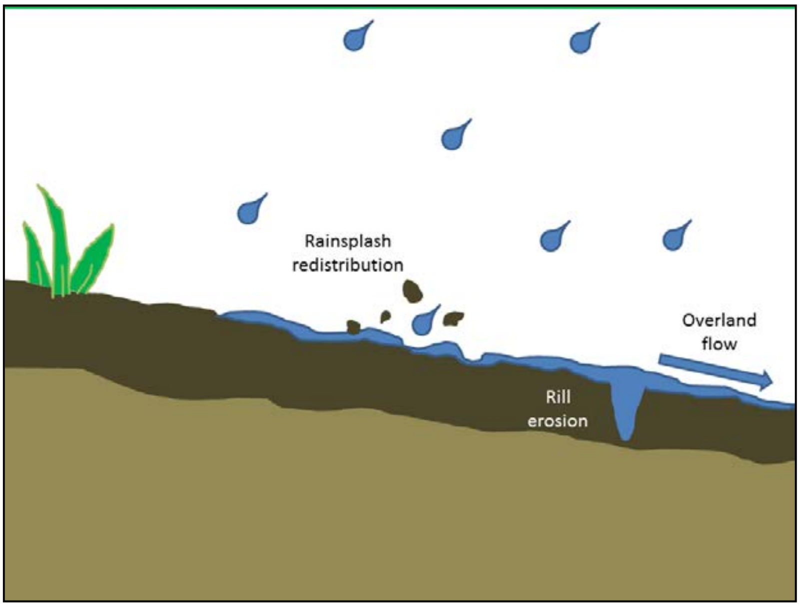

Figure 1-5 Diagram showing mechanism of rainsplash redistribution and overland flow (adapted from Anthoni 2000).

Overland flow is also the cause of a second type of water erosion, rill erosion (see figure 1-5). Overland flow occurs when water cannot infiltrate the soil, either because the soil is fully saturated or the rate of rainfall is too intense to allow infiltration of water (Dotterweich 2013; Ashman & Puri 2002). The resulting overland flow moves under the influence of gravity in a thin sheet across the soil surface, however, having lost the majority of the kinetic energy it possessed as rain, it is generally unable to detach or transport soil particles. As the soil surface is not uniform, overland flow will eventually begin to collect in small surface depressions. If rainfall continues and the depressions begin to overflow, water with a higher kinetic energy is released; this water continues to flow downhill at greater speeds and in larger quantities. As the kinetic energy of the overland flow increases, further detachment of soil particles again occurs. These detached particles are then transported away within the overland flow, leaving a small depression behind in the soil surface. This depression forms a preferential pathway for any further overland flow, resulting in further erosion of the area. Eventually a small linear feature known as a micro rill develops (Ashman & Puri 2002). Most of the micro rills are filled with sediment, and no further erosion occurs, however a subset become the larger rills, which allow greater volumes of overland flow to move within them (Ashman & Puri 2002; Morgan 2009).

Subsequent erosion of these rills can lead to the formation of gullies, which become large landscape features, in which all the soil contained within can be completely eroded away to expose the bed rock (Ashman & Puri 2002). The overland flow is then transported away from the site, along with any eroded soil particles, which are eventually deposited further down the rill or gully, in watercourses or along coastal regions (Brady & Weil 2002; Dotterweich 2013). In order to improve erosion prediction models and to further develop conservation methods, it is important to obtain a greater understanding of the precise mechanisms involved in both rainsplash redistribution and rill erosion (Zhang et al. 2008).

In addition to rainwater, it is known that both melt water and frost can cause soil erosion (Dotterweich 2013). The mechanisms of both forms of erosion are poorly understood, however it is believed that melt water erosion occurs in a similar manner to rill erosion. One possible mechanism for frost erosion is that damage can be caused to the soil structure by the sudden and forceful expansion of water during freezing (Morgan 2009).

1.2.2 Wind erosion

The movement of air over the soil surface can also provide sufficient energy to cause the detachment and subsequent transport of soil particles, especially of fine, dry particles (Ashman & Puri 2002). The mechanisms by which the detached particles move depends upon their size (see figure 1-6). Small particles, such as clay, which form fine soil, can become airborne, and once they have done so, do not readily settle out again (Lal 1994). Heavier particles, such as sand particles, move by saltating (or jumping) over the ground in a sheet, whilst particles that are heavier still roll across the surface. As the concentrations of soil particles contained within the air increase, the erosive potential of the air moving over the soil surfaces also increases (Morgan 2009). Wind erosion is capable of moving soil particles 1,000’s of kilometres, and is not reliant on gravity to provide kinetic energy so, unlike water erosion, wind can move soil uphill (Morgan 2009).

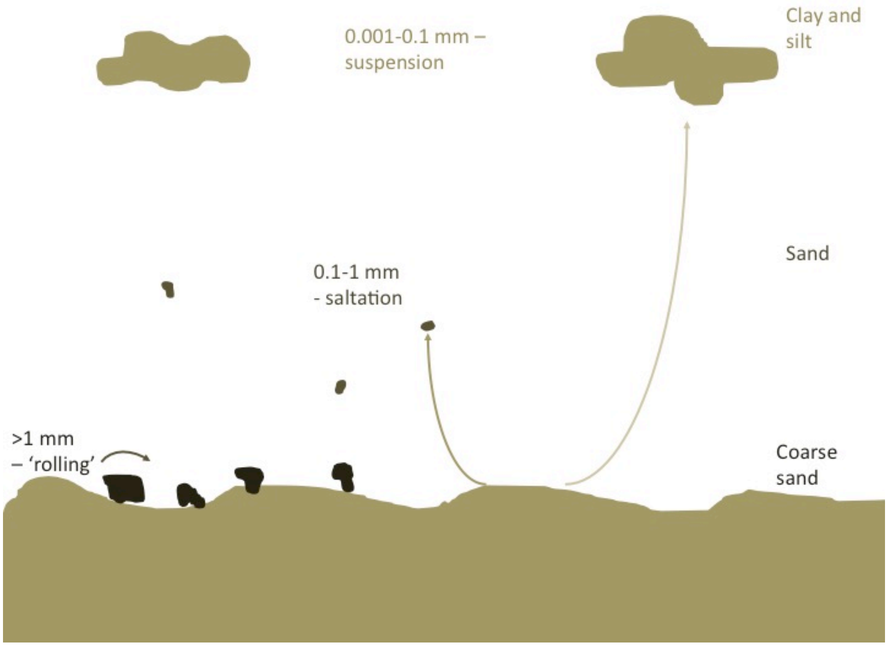

Figure 1-6 Diagram showing different mechanisms of wind erosion (adapted from Anthoni 2000).

1.2.3 Tillage erosion

Tillage erosion can result in significant soil erosion within areas reserved for agriculture, and it has been suggested that in some agricultural landscapes, in temperate climates, tillage erosion may have a greater impact than erosion by water (Quine et al. 1999). As such it is becoming recognised as an important soil erosion process. Tillage erosion caused by ploughing results in significant changes in the physical, chemical and biological characteristics of the soil, as well as a reduction in top soil depth and exposure of the sub soil (Thapa et al. 1999). Soil redistribution can cause significant variations in the productivity of the field, and the movement of topsoil down slopes. However, as yet, little study has been undertaken of the relationship between tillage detachment and tillage displacement (Quine et al. 1999; Zhang et al. 2001).

1.3 Suspended particulate matter

Particulate matter present naturally within a freshwater system can result from two major sources, allochthonous and autochthonous (Ashman & Puri 2002). Autochthonous matter is formed within the river water column, normally from microorganisms such as algae and a small quantity of precipitated minerals. Allochthonous matter is matter transported in from outwith the system and includes eroded soil (Thomas & Meybeck 1992). Human activity can affect the levels of both autochthonous and allochthonous matter, either by increasing the amount of plant and algal life within the system, therefore increasing the amount of autochthonous matter or by altering the erodability of the soils surrounding the system, thus altering the levels of allochthonous matter (Brady & Weil 2002; Thomas & Meybeck 1992).

Transport within streams, rivers and lakes results in a separation of the transported matter based upon size and density. Thus two fractions are normally present within the system, a suspended and geochemically active fraction, and a relatively inactive coarse material found within the river bed (Thomas & Meybeck 1992; Bonte et al. 2000). The chemical composition of particulate matter varies depending on the origin, but the major elements found consist of silicon, aluminium, iron, manganese, magnesium, calcium, sodium, potassium, titanium, phosphorous, carbon and nitrogen along with a variety of trace elements (Braimoh & Velk 2008; Bonte et al. 2000; de Carlo et al. 2004; Koiter et al. 2013; Russell et al. 1998). The presence of suspended particulate matter within freshwater can have a large impact upon the water quality. In particular, soluble compounds, such as phosphates and nitrates can leach from the particles, increasing the concentration in the surrounding system and promoting plant growth and algal blooms (Thomas & Meybeck 1992). Additionally, large quantities of particulate matter can smother bottom dwellers, and limit light penetration within the system (Ashman & Puri 2002).

A number of methods are currently used to monitor the amount of soil lost during erosion events, and determine the origin of suspended particulate matter.

1.4 Methods of monitoring soil erosion

A wide variety of methods are available to monitor soil erosion. These include traditional methods such as erosion plots that have been used for many years to provide data on the rates of soil erosion within field systems (Boix-Fayos et al. 2006; Blanco & Lal 2010). These erosion plots can take a wide variety of forms including closed, bounded and open erosion plots, which collect overland flow to allow levels of suspended soil particles to be analysed (Boix-Fayos et al. 2006; Blanco & Lal 2010). They can cover areas of 1 m^2 to tens of square metres, and be subjected to natural or simulated conditions, such as rainfall (Boix-Fayos et al. 2006). The soil morphological method for erosion losses compares the thickness and composition of horizons in cultivated and undisturbed sites to obtain a value for soil loss during the entire period of cultivation (Belyaev et al. 2009). Whilst all these methods can provide valuable information as to the average rates of erosion within the plot studied and allow direct measurement of real world conditions, they are generally considered time consuming and expensive, and provide little information on spatial variations in soil erosion and redeposition of soil particles within the field itself (Belyaev et al. 2009; Yang et al. 2008; Morgan 2009).

A range of monitoring techniques relating to the chemical properties of soils and sediments, such as elemental composition, radioisotopes, fluorescence spectra and magnetic responses, have been developed.

1.4.1 Sediment fingerprinting

Ratios of the elements found within the soil are generally unique to the region from which it originated (Walling 2005). Analysis of the different quantities of the elements within particulate and dissolved matter has been extensively used to identify the most likely origination of deposited soil within a river catchment (Walling 2005; Russell et al. 1998; Stutter et al. 2007). Sediment fingerprinting can be applied to a range of study areas, varying from field plots to river basins and look at single events, to long term sediment deposition (>10,000 years).

Sediment fingerprinting has been used to trace the source of suspended sediment within catchments and river basins, using a variety of trace, heavy and base metals, reviewed by Walling (2005). Sediment fingerprints are multielemental in nature, and the precise choice of elements varies between studies, however phosphorus, carbon and nitrogen are common to most fingerprints. In addition to these, most studies analysed a variety of differing trace metals including calcium, manganese, magnesium, copper, aluminium, cobalt and nickel using inductively coupled plasma – mass spectrometry (ICP-MS) (Poleto et al. 2009; Carter et al. 2003). Research has also been undertaken to identify the relationship between land use within a catchment and suspended sediment within rivers (Stutter et al. 2007; Stutter & Lumsden 2008). Studies have used sediment fingerprinting to estimate changes of suspended sediment quantities over a nine year period, and to determine the differing effects of storm events and moderate flow conditions (Coynel et al. 2004; Stutter et al. 2009; Stutter et al. 2008). One problem which has needed to be addressed in respect of sediment fingerprinting is the development of a model to allow comparison of data across a range of soil types and particle sizes (Koptsik et al. 2003; Walling et al. 1993). Consideration must also be given to the choice of elements to be included in the fingerprint (Collins & Walling 2002; Walling 2005).

Sediment fingerprinting can be used to identify the most likely source of any suspended sediment contained within a system, but cannot provide a direct link between the suspended sediment and this source. This is a problem common to all tracer methods relying on naturally occurring markers. However, a major limitation of sediment fingerprinting is its inability to link sediments to source conclusively (Koiter et al. 2013; Smith & Blake 2014).

1.4.2 Radioisotopes as erosion tracers

Much of the literature is concerned with the use of the fallout radioisotope ceasium-137, a gamma emitter and fission product deposited as the result of nuclear weapons testing, such deposition appears to be relatively uniform within field systems (Ventura et al. 2001; Parsons & Foster 2011). Since the ban on atmospheric testing of nuclear weapons in the 1970’s, the rate of deposition of ceasium-137 has been very low, except in areas affected by the Chernobyl disaster in 1986 (Everett et al. 2008; Sac et al. 2008). Ceasium-137 can be used to quantify soil erosion, and also provides spatial resolution as ceasium-137 adsorbs tightly to soil particles (Everett et al. 2008). Gamma spectrometry of dried, 2 mm sieved soils is used to detect the level of gamma radiation in soil samples from a site of interest and this can be compared to that of a reference site, unaffected by erosion, from which the average losses of the previous 35-40 years can be calculated (Sac et al. 2008). This provides data which is unaffected by extreme weather events which can make analysis of data from traditional methods, taken over a period of a few years, difficult (Parsons & Foster 2011). In addition, only a single sampling trip is required, and results are obtained quickly. The largest drawback of using ceasium-137 as a soil tracer lies in the choice of reference site. Such a site must have the same geomorphic parameters as the study site, as well as the same rainfall, but must not be subject to any form of accelerated erosion (Sac et al. 2008). In addition, in many areas of Europe the deposition of ceasium-137 as the result of the Chernobyl disaster is often not uniform, making the correct selection of the reference site even more important (Poreba 2006). The short half-life of ceasium-137 (30.2 years) means that in many areas the sensitivity of this method is beginning to reduce (Everett et al. 2008; Parsons & Foster 2011). Whilst caesium-137 can be used to identify sites of soil deposition, it is not able to prove a link to a specific erosion site (Stevens & Quinton 2008). In many cases a link between sites of soil erosion and soil accumulation is necessary to both understand the soil erosion process, and to allow validation of soil erosion models (Parsons & Foster 2011; Stevens & Quinton 2008). Limitations to the caesium-137 method can be overcome in part by combining data with that obtained from other radionucleotides such as beryllium-10 (Willenbring & Blanckenburg 2010). Caesium-137 has also been used to study soil translocation during tillage erosion events (Lobb et al. 1995). Caesium-137 was mixed with soil from the site of interest, and movement of this labelled soil was monitored using a gamma ray spectrometer.

Other radioelements have been used as soil erosion tracers, either applied or naturally present tracers, alone or as part of a set of elements analysed (Zapata

2003). Applied caesium-134 has a shorter half-life than caesium-137 of two years and is not naturally present in soils at a detectable level, and has also been used as a tracer of soil erosion (Quine et al. 1999). Application of caesium-134 to target soils allowed soil redistribution by tillage to be monitored using gamma spectrometry, which provided some direct evidence for the magnitude of soil erosion (Quine et al. 1999). The shorter half life of caesium-134 makes it preferable to caesium-137, however, even the small number of samples obtained during the study required a significant amount of both fieldwork and analysis time (Quine et al. 1999). Perrin et al. (2006) reported the use of four naturally present radioelements to determine rates of general soil erosion – potassium, uranium, thorium and caesium using portable high purity – germanium (HP-Ge) gamma spectrometers. This gamma spectrometer allowed for *in situ* measurements to be obtained, and reduced the sampling time to a minimum. However, comparison with laboratory results indicated large differences in the values obtained as soil depth increased, indicating that these results lacked sensitivity. Other groups have used beryllium-7 (Blake et al. 1999; Taylor et al. 2012) to monitor levels of water erosion using a radiometer, whilst (Xu et al. 2013) used plutonium isotopes. Again these were the result of nuclear fallout, and the movement of soil by erosion or human activity have changed the concentrations of these elements within the soil. Plutonium-239 and -240 have longer lifetimes than caesium-137 and as such are being investigated as alternatives to caesium isotopes. Xu *et al*. (2013) demonstrated that the erosion patterns as determined by both caesium-137 and the two plutonium isotopes were similar. However, this method also requires the careful choice of a suitable reference site, and is similarly able to only provide information on long term erosion rates, not on single or seasonal events.

1.4.3 Rare earth elements

The rare earth element tracer method (REETM) has also been used to study the origins of sediments within a catchment. The rare earth element (REE) is deployed at a site of interest, and the concentration of these elements in deposited sediment determined to link the site of deposition with the site of erosion. One of the great advantages of this method is the ability of the REE to bind strongly to soil, whilst not altering the natural movement of the eroded soils (Zhu et al. 2010). In addition, they display little vertical movement, incorporate evenly within aggregates and are present at low background levels within most soils. The majority of research using REETM has focused on sediment delivery into surrounding catchments, but other groups have used this method for quantitative analysis of erosion rates within simulated erosion experiments (Liu et al. 2004) and the measurement of rill erosion (Li et al. 2006). Detection of the lanthanides can be through ICP-MS or neutron activation analysis, which whilst capable of detecting low concentrations of these elements, required extensive sample preparation, were expensive and required skilled operators.

1.4.4 Applied ions

The use of applied ions, such as chloride and bromide, have been used to study the movement of soil moisture and runoff (McGuire et al. 2007; Newman et al. 1997), and also in the study of tillage erosion (Lobb et al. 1999). These studies involved either the application of potassium chloride to the soil surface (Lobb et al. 1999), a solution of bromide and chloride ions (Buchter et al. 1997), mixing of the soil with lithium bromide solution prior to repacking (McGuire et al. 2007) or analysis of naturally occurring chloride ions (Newman et al. 1997). The modelling of runoff allowed the movement of water within a complex landscape to be determined, and as transport of eroded soil particles mediated by water erosion events is linked to runoff, allows the estimation of erodibility of different areas of a catchment (Lobb et al. 1999). This in turn allows remediation efforts to be concentrated within areas of a catchment with the greatest effect upon the sediment load within that catchment (McGuire et al. 2007). One advantage of this method is that it allows for both spatial and temporal analysis. However, as the ions are water soluble, this approach can only determine the movement of water through the soil, not the movement of soil particles associated with erosion. In addition, the sample preparation and analysis methods, which include ion chromatography (Newman et al. 1997; Buchter et al. 1997), automated colorimetry (Lobb et al. 1999) and ion selective electrodes (McGuire et al. 2007) were complex.

1.4.5 Dyes

Dye tracers have been used to trace soil water movement within field systems through to associated watercourses (Tauro et al. 2012). Soil water is often associated with sediment movement, and as such can be a contributing factor to soil erosion, carrying away any detached soil particles and depositing them into water courses (McGuire et al. 2007). Detection for these dyes is normally fluorometric. Amino G acid monopotassium salt (AGA) (McGuire et al. 2007) and potassium permanganate (Zhang et al. 2010) have both been used to trace the movement of overland flow from sites of erosion to the point of entry into the surrounding catchment. AGA dye was detected using a fluorometer, whilst potassium permanganate was monitored visually. In other studies, a fluorescent dye was used to determine the leading edge of water flowing during rainfall simulations into the factors affecting rill and interrill erosion processes (Nearing et al. 1999). The advantage of many dye studies is that the dyes are often inexpensive, easy to detect *in situ* or with minimal sample preparation, and simple to deploy. The major disadvantage is that they generally only provide information of the movement of water during erosion events, not of the soil and sediment particles. They are also normally short lived in the environment (hours or days) and as such can only provide a snap shot of water movement, are easily diluted and need to be used in high concentrations in order to be effectively detected against the soil background.

None of these methods provide a direct link between the deposited sediments or soils, and the site of erosion. As such, attention has turned to alternative, particle based methods, which in general require fewer samplings and are capable of providing spatial data on the variation of erosion and deposition rates within the study area. Particle tracers vary from the detection of radioisotopes such as caesium-137 to the incorporation of aluminium cubes and painted rock fragments into the topsoil (Thapa et al. 1999; Ventura et al. 2001; Zhang et al. 2001).

1.4.6 Physical tracers

Physical tracers, such as painted rock fragments and aluminium cubes, have been particularly used in the study of tillage erosion. Tiessen et al. (2007) also reported the use of brightly coloured aquarium gravels. These tracers are mixed in with the topsoil of a designated area, and the soil repacked to its original state (Quine et al. 1999; Zhang et al. 2004). The area is then ploughed, and the fragments and cubes recovered (Quine et al. 1999). A study performed with these tracers did demonstrate soil movement as the result of tillage, with the majority of the tracers being recovered (Quine et al. 1999). Analysis of the tillage erosion was based on recovery of the tracers from the soil followed by either analysis of dry weight or manual counting. However, collection of data was time consuming, as the tracers have to be separated from the soil prior to analysis (Zhang et al. 2004).

1.4.7 Applied particle tracers

One alternative to these tracer methods is the use of magnetic particles or coated beads. These can be applied to the soil and measured before and after any erosion events in a non-destructive manner, *in situ,* using a magnetometer (Zhang et al. 2004). Magnetic beads can be produced which are the same approximate size and density of natural soil aggregates, suggesting they act in a similar manner, however the manufacture of these beads with similar morphology has proven complicated (Ventura et al. 2001). In addition, although analysis is quick and inexpensive once the equipment has been obtained, the initial set up costs are high (Zhang et al. 2004). Ventura et al. (2001) used polystyrene beads embedded with magnetite to study the movement of soil by overland flow and rill erosion. Measurements were made using a magnetic susceptibility meter *in situ*, and samples of run off and sediment were taken for extraction of the tracer within the laboratory for quantification of the tracer concentration. Zhang et al. (2001) identified some of the key properties an effective soil tracer should possess, including a high affinity to adsorb to soil particles, low solubility and the ability to be used in low background concentrations. Tracers should also not interfere with the mechanisms of soil transport, be easily and inexpensively measured as well as being non-toxic to the environment and should not be taken up by plants.

The behaviour of applied particle tracers is often monitored by the use of soil erosion simulators. This allows the behaviour of the tracer under controlled conditions, either on a small scale within the laboratory, or on a larger scale in the field (Blanco & Lal 2010). These erosion simulators include a section of characterised soil (the erosion plot), and a rainfall simulator that sits a set distance above the plot. The rainfall simulator can be adjusted to provide different rainfall intensities directly onto the plot. Generally, overland flow is collected at the base of the plot to determine movement of the tracer. Ventura *et al* (2001) used a laboratory study to monitor the movement of magnetite embedded in polystyrene beads by overland flow, whilst another group (Liu et al. 2004) looked at the movement of REE down the plot, analysing the RRE concentration at a number of different points along the soil surface. This allowed redistribution of the soil within the site to be analysed. A number of problems arise when designing and using an erosion simulator, including determining the physical size of the plot, droplet size from the rainfall simulator, and the ability for the soil to drain naturally. Performing the erosion simulation within a field allows a large plot to be chosen, and as the soil is usually undisturbed the plot has natural drainage. However, control of the environment surrounding the plot is limited, and rainfall is normally produced by the means of a sprinkler system that produces a fine mist (Kinnell 2005). This mist lacks the kinetic energy on impact with the soil, and reduces the effect of soil dissociation by rains drops, potentially altering the erosion mechanism. This can be countered in the laboratory by producing a smaller rainfall simulator which produces discrete droplets with similar kinetic energy to raindrops, but with a limited plot size (Lilly et al. 2009; Kinnell 2005). As the soil structure has to be disturbed to move the soil into the laboratory, the drainage of rainwater from the plot is altered, and thus the behaviour of the soil during the erosion event might also be altered. As such, whilst a valuable tool in determining the behaviour of tracers during erosion events, the design and use of an erosion simulator must be carefully designed.

A Scottish government report on soil erosion in Scotland recognised the threat soil erosion posed to Scotland's soil resource, in particular to peat land, which is eroding at an accelerated rate to that of other soil types. Two of the recommendations to come from this report were the need to monitor soil erosion rates in relation to any agricultural management strategies put into place, and the necessity to calibrate soil erosion models using quantitative measurement of actual soil erosion rates (Towers et al. 2006) Many soil erosion field assessments are qualitative, judged visually, and determined to be none, slight, moderate or severe (Blanco & Lal 2010). As such, visual assessment depends greatly upon personal judgement and comparison of different sites classified in this manner can lead to inaccurate conclusions. The use of soil erosion tracers provides a method to avoid this source of systematic error, by providing a measurement method which can be standardised across laboratories. None of the above tracers fulfil all the prerequisites identified by Zhang et al. (2001) so there is a need for the development of a tracer which can be identified within soil, but is easy and inexpensive to detect, and which can adsorb effectively onto soil particles. Such a tracer would also provide data as to the spatial movement of soil within the field, as well as link the erosion site to downstream sites of deposition. One potential method of monitoring soil erosion is by the use of luminescent lanthanide chelate based silica particles.

1.5 Lanthanides and lanthanide chelate complexes

The lanthanides are a group of elements comprising of the 14 elements that follow lanthanum in the periodic table (atomic numbers 57-71) (Binnemans 2009). Along with the actinides they form the f-block elements, with the 4f orbital being progressively filled as you move across the period. The lanthanides share a variety of similarities across the group, one of which is the photoluminescent properties of their trivalent ions.

1.5.1 Lanthanide photochemistry

Upon irradiation with ultraviolet radiation, the lanthanides normally emit photons within the visible or near-infrared areas of the electromagnetic spectrum, with each ion having a number of different emissive states (Dieke 1968; Hemmila & Laitala 2005). Figure 1-7 contains a representation of the many electronic transitions possible for each of the lanthanides, and also indicates which result in the emission of photons within the visible range (Dieke 1968). As the 4f transitions involved in luminescence are shielded by the filled 5s and 5p orbitals, many of these emissive states are unaffected by the surrounding environment and are free from crystal field splitting. Crystal field splitting occurs when an electric field causes degenerate electron orbital states (normally d or f orbitals) to split into a further series of higher and lower energy levels (see figure 1-8)(Werts 2005). This shielding results in the differences between orbital states being lower than spin coupling, so all states are equally populated, and no splitting of emission peaks are observed (Aspinall 2001). Common exceptions to this are cerium and europium, both of which have been shown to display crystal field splitting, and wavelength shifts for hypersensitive transitions dependent upon the chemical environment of the trivalent ion (Dorenbos 2002; Aspinall 2001), and are affected by small changes within the first coordination sphere of these ions (Peacock 1975). The trivalent lanthanide ions possess a number of characteristics that make them valuable as luminescent probes. Principal of these are the long Stokes shift, sharp emission bands and long luminescent lifetimes (usually in the µs range instead of the ns range for molecular fluorophores). These properties allow lanthanide luminescence to be easily discerned from background radiation and have meant that probes based on the lanthanides have been used extensively in environmental samples.

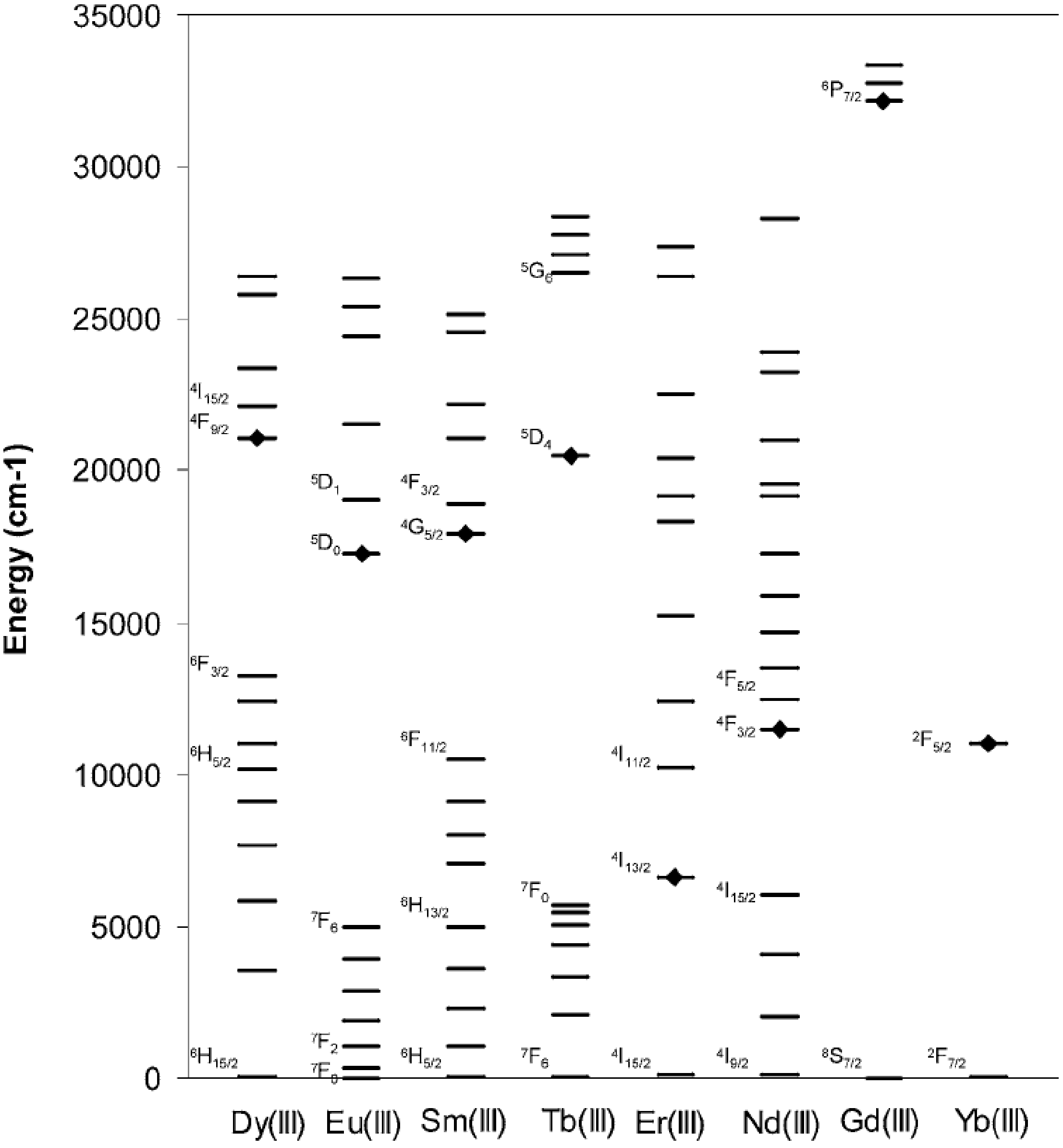

Figure 1-7 Energetic levels of various luminescent lanthanides. Black dots relate to the emittive energy level (Hemmila & Laitala 2005).

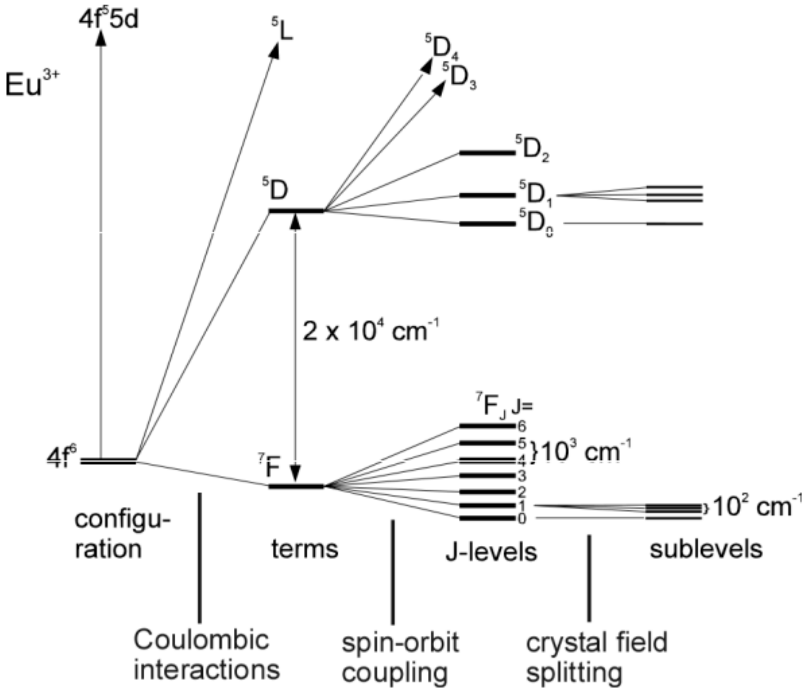

Figure 1-8 The interactions leading to the different electronic energy levels for the [Xe] $4f^6\ 5d^0$ configuration of Eu^{3+} (six electrons in the 4f orbitals) (taken from Werts 2005).

The sharp peaks, with narrow bandwidths of the lanthanide ions are not only distinctive against the broad peaks generally present within biological backgrounds, but also provide a high level of colour purity (Armelao et al. 2010; Binnemans 2009). This feature makes the lanthanides ideal for use in complex systems where the analysis of multiple targets is desirable, as the signals from a number of probes, each labelled with a different lanthanide can be easily resolved (Armelao et al. 2010; Hemmila & Laitala 2005; Yuan & Wang 2006).

The transitions involved in luminescence are Laporte-forbidden, and as such occur at low rates, making lanthanide luminescence intensities low (Atkins & de Paula 2005). These transitions are easily quenched by molecular oxygen, water or surrounding inorganic or organic matrices, where combinations of vibrational states allow excited electrons to return to a ground state via a non-radiative pathway and so the luminescence intensity of lanthanide luminescence is weak (Werts 2005).

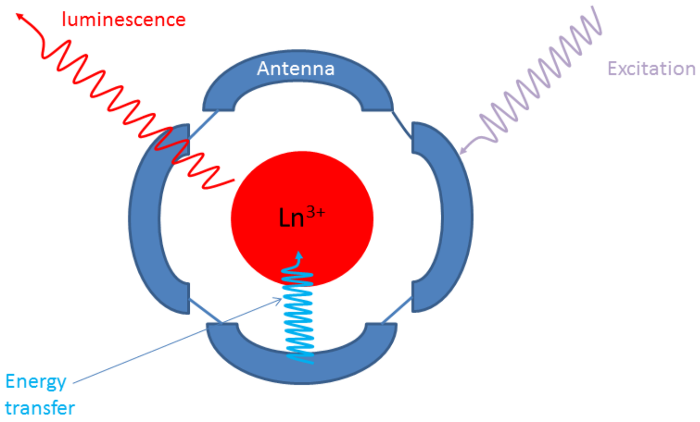

Figure 1-9 Diagram illustrating the antenna effect for sensitization of trivalent lanthanide ions (adapted from Moore et al. 2009)

1.5.2 Luminescent lanthanide complexes

Lanthanide luminescence can be dramatically enhanced by the association of an appropriate organic chromophore with the trivalent lanthanide ions (Kaltsoyannis & Scott 1999; Armelao et al. 2010). Such chromophores have wide absorption spectra, and transfer this excitation energy to the lanthanide ion via intramolecular transfer, often termed the antenna effect (see figure 1-9) (Moore et al. 2009; Parker & Williams 1996). The mechanism by which lanthanide complexes emit lanthanide specific luminescence is summarized in figure 1-10. An electron within the ligand is promoted to an excited singlet state via the absorption of a quantum of energy, generally within the UV region (Armelao et al. 2010; Binnemans 2009; Moore et al. 2009). This excited electron then either returns to its ground state via the emission of a photon of light (fluorescence) or it can undergo a non-radiative, Laporte forbidden process to a longer lived excited triplet state (Binnemans 2009; Moore et al. 2009; Bünzli & Piguet 2005). The excited triplet state electron can return to a ground state via the emission of a photon of light (phosphorescence) or via intersystem crossing in which the energy is transferred non-radiatively to the excited state of the coordinated lanthanide ion. This now excited lanthanide ion can then return to its ground state via the emission of lanthanide specific luminescence. Thus, lanthanide complexes can emit intense luminescence despite low molar absorptivities (Georges 1993; Parker & Williams 1996; Werts 2005). The ideal chelate will saturate the coordination shell of the lanthanide ion, preventing molecules such as water or molecular oxygen binding, which deactivate the lanthanide ion, and therefore enable an efficient transfer of energy from the organic compound to the ion (Armelao et al. 2010; Moore et al. 2009). Of all the trivalent lanthanide ions, terbium and europium are most commonly used in practical applications, as they have high luminescence intensities, long decay times and are not quenched by the many organic molecules used within fluid solutions (Bünzli & Piguet 2005; Armelao et al. 2010). The lanthanides act as hard Lewis bases during coordination, so many of the chelates used within lanthanide complexes contain donor N, O or F groups (Kaltsoyannis & Scott 1999). Of these, groups such as the β-diketonates are some of the most common and well characterized ligands (see figure 1-11) (Binnemans 2009; Parker & Williams 1996). These ligands are generally multidentate, with two donor oxygen groups present within the diketone region, and a high level of conjugation, allowing them to efficiently absorb quanta of electromagnetic radiation within the ultra violet and visible regions (Binnemans 2009).

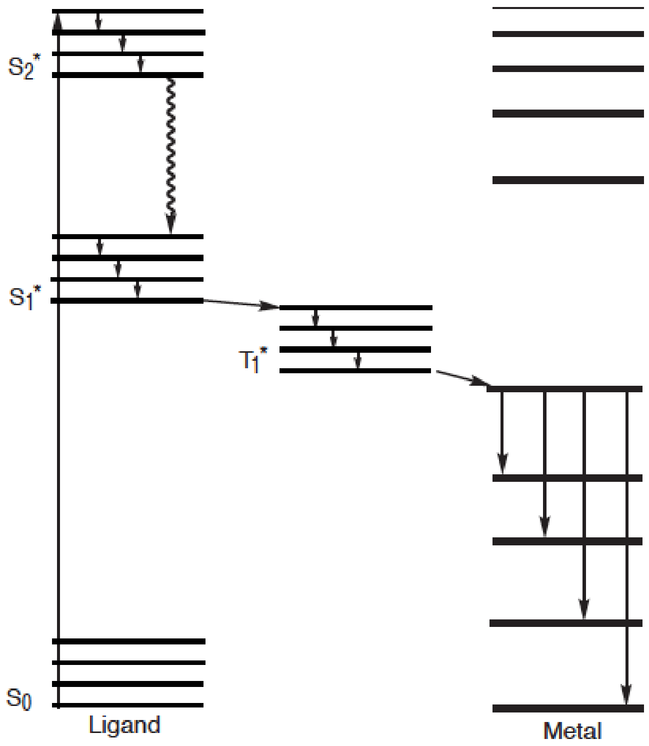

Figure 1-10 Schematic diagram of ligand to lanthanide energy transfer mechanism (Jenkins & Murray 1998).

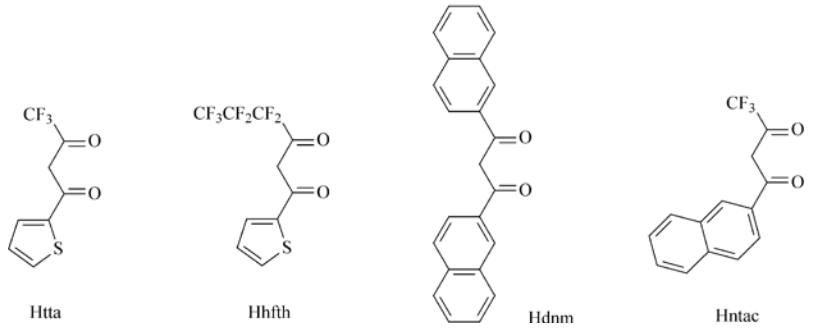

Figure 1-11 Examples of structures of β-diketones with aromatic and heterocyclic substituents in keto form. Htta – 2-thenoyltrifluoroacetone, Hhfth - 4,4,5,5,6,6,6-heptafluoro-1-(2-thienyl)-1,3-hexanedione, Hdnm - dinaphthoylmethane ,Hntac – 2-naphthoyltrifluoroacetone (adapted from Binnemans 2005)

One method by which quenching of the trivalent lanthanide ion by molecules such as water and molecular oxygen can be prevented, is through the incorporation of the lanthanide chelate into silica particles, so increasing its stability.

1.6 Silica sol-gel particles

The sol-gel method allows the formation of solid materials from liquid precursors via the formation of a suspension of colloids (sol). Stöber *et al* (1968) reported a method for the production of silica based particles of controlled size and morphology using a sol-gel method. The sol-gel particles are produced as a result of a hydrolysis reaction allowing the formation of a colloidal suspension from a metal alkoxide precursor, which subsequently polymerizes to form a metal oxide network with the liquid phase (Binnemans 2009; Stöber et al. 1968). In the case of silica sol-gel particles this precursor is a silica alkoxide, the most common being tetramethoxysilane (TMOS) and tetraethylorthosilicate (TEOS) and a series of hydrolysis and condensation steps take place in a mutual solvent.

Hydrolysis:

$Si(OR)_4 + nH_2O \rightarrow Si(OR)_{4-n}(OH)_n + nROH$ Equation 1.1

Condensation of this intermediate reaction product eventually results in silica formation:

$(RO)_3Si\text{-}OR + HO\text{-}Si(OR)_3 \rightarrow (RO)_3Si\text{-}O\text{-}Si(OR)_3 + ROH$ Equation 1.2

or

$(RO)_3Si\text{-}OH + HO\text{-}Si(OR)_3 \rightarrow (RO)_3Si\text{-}O\text{-}Si(OR)_3 + H_2O$ Equation 1.3

A scheme of the silica sol-gel process can be seen in figure 1-12, with the TEOS precursor undergoing (a) hydrolysis and (b) condensation, leading to large particulate networks of silica (Brinker & Scherer 1990; Wright & Sommerdijk 2000). These networks then condense and harden to form discrete particles (Wright & Sommerdijk 2000). It has been shown within the literature that the first stage of particle formation is the formation of silica fractals in the nm size range (Gutsche et al. 2015; Green, Lin, et al. 2003). Once the number of these fractals reaches a critical limit, a process of nucleation occurs during which the fractals first combine to form nuclei, followed by addition of further silica monomers to the surface of the particles, eventually forming a smooth, spherical monodisperse particle. Evidence supporting this mechanism has been obtained using small angle x-ray scattering (SAXS), a method by which the size and morphology of nanoparticles can be determined, for particles synthesized at low temperatures (Green, Jayasundara, et al. 2003).

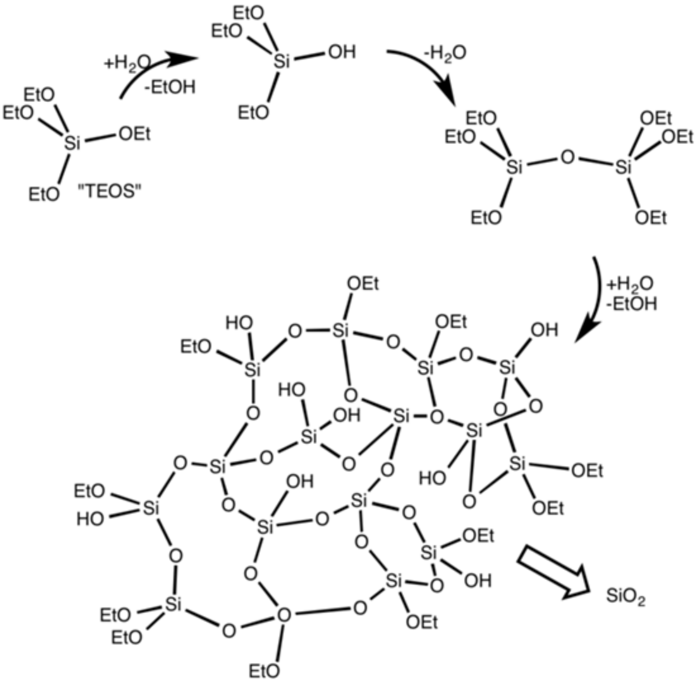

Figure 1-12 Schematic outlining the silica sol-gel process (Brinker & Scherer 1990).

These reactions occur slowly, and a catalyst (generally an acid or base) is incorporated into the system to increase the reaction rate. Whilst the end products are the same for both types of catalyst, the reactions occur via different mechanisms (see figures 1-13 and 1-14), which result in the resultant particles possessing different properties. Acid catalysed hydrolysis results in dense particles, with few cross links and small pores, whilst base hydrolysed particles have more cross-links and larger pores.

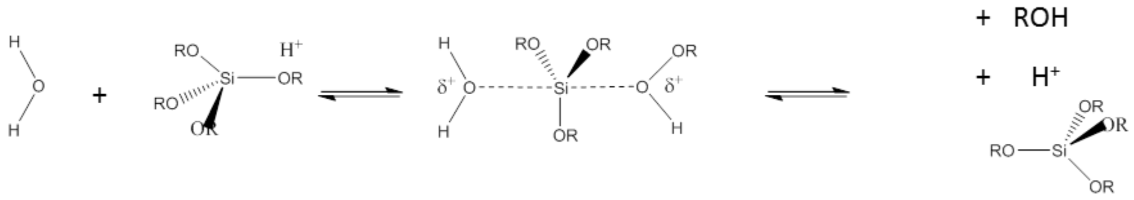

Hydrolysis

Condensation

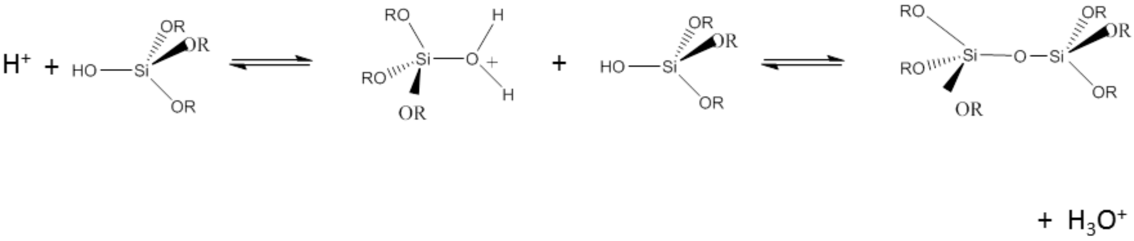

Figure 1-13 Acid catalysed silica sol-gel reaction mechanisms (adapted from Wright & Sommerdijk 2000).

Hydrolysis

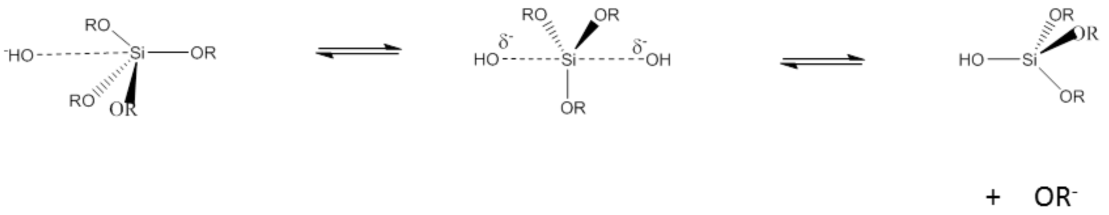

Condensation

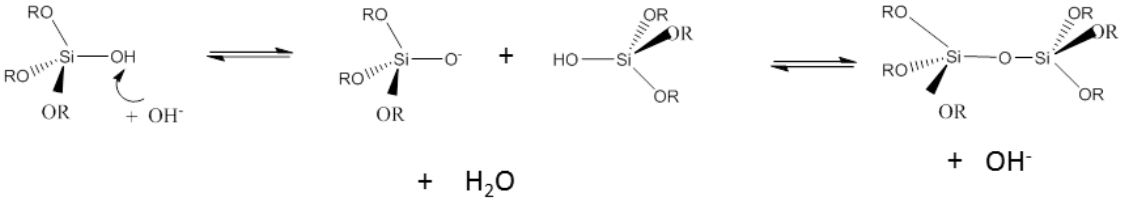

Figure 1-14 Base catalysed silica sol-gel reaction mechanisms (adapted from Wright & Sommerdijk 2000).

There are a number of advantages to this method, including the low temperatures (often close to room temperature) at which the reactions occur and the chemically mild conditions used. This means that temperature or chemically sensitive organic molecules, such as dyes (Al Dwayyan et al. 2012; Rossi et al. 2005) and proteins (Zhao et al. 2004; Santra et al. 2001), can be incorporated into the resulting particles. In addition, due to the high purity of the precursors used, the resultant products also have a high purity, ideal for applications in environmental and biological systems, where the presence of even a low amount of impurity could have an adverse effect. The resultant silica particles are optically transparent within the visible and near ultraviolet regions of the electromagnetic spectrum, and thus find many applications within the optical imaging sectors (Wang et al. 1998; Patra et al. 1999). The size of the particles can be varied by changing the concentrations of the reactants, as well as the temperature, with particle sizes between 40 nm and 60 µm reported (Rossi et al.

2006; Shimura & Ogawa 2007).

There is a wide range of techniques other than the silica sol-gel process which results in the formation of monodisperse particles within the size ranges desirable for a soil particle tracer. These include the use of polymers (such as poly(methyl methacrylate)) (Dowding & Vincent 2000) or zeolites (Cundy & Cox 2003; Tao et al. 2006). However, whilst both of these processes would result in suitable sized particles, the chemical and thermal processes used within their synthesis are harsher than those used during the Stöber sol-gel process (Lev et al. 1995; Binnemans 2009). This would limit the incorporation of organometallic complexes such as lanthanide chelate complexes into the matrix, and could also potentially result in the leeching of chemicals used during synthesis reactions into the environment (Lev et al. 1995).

1.6.1 Lanthanide complex doped sol-gels

Recently, much research has been devoted to the incorporation of lanthanide complexes into silica sol-gels, and evidence suggests that this incorporation can increase the stability of both lanthanide ions and lanthanide complexes (Binnemans 2009; Feng & Zhang 2013; Lechevallier et al. 2013). Modification of the Stöber method results in a sol-gel process by which lanthanide chelates can be easily incorporated into the silica matrix (Binnemans 2009). The resultant particles are uniform, thermally stable and the luminescent lanthanide chelate is distributed evenly throughout the silica matrix (Binnemans 2009). The particles act to shield and stabilize the lanthanide chelate complex, and as such reduce the effects of quenching and bleaching, producing an amplified, reproducible signal (Binnemans 2009). However, it has also been observed that the addition of a lanthanide ion into the reaction mixture can affect the morphology of the resulting silica particles (Lu & Yan 2008). This can vary from a change in size, loss of the smooth spherical appearance to the formation of amorphous masses of silica, with little or no evidence of the monodisperse spheres normally characteristic of this process. Little work has yet to be done on identifying the exact mechanism by which this phenomenon occurs, but it is most likely due to either the incorporation of the lanthanides within the silica matrix, or a steric effect due to the large ionic radii of the ions. This effect often appears to be concentration dependent, with a critical concentration, above which the spherical structure is completely lost.

Much of the recent literature is concerned with the use of lanthanide based silica particles in bioassays, as they are non-toxic to biological systems. Rossi *et al* (2006) reported the use of luminescent silica particles as probes for the cancer marker protein HER2/neu by the attachment of an appropriate antibody to the particle surface, thus allowing cancer cells to be identified. Another group used luminescent silica particles to identify the pathogen *Escherichia coli* O157:H7 *in situ* (Zhao et al. 2004).

1.7 Research aims and thesis overview

The primary aim of this research was therefore to develop a stable luminescent soil tracer that preferentially bound and behaved as natural soil particles, and could be quickly and easily detected within soil and sediment samples.

This was achieved through a series of objectives:

- The development of a lanthanide chelate complex suitable for use within the environment.
- Preparation of suitable sized silica sol-gel particles, of similar size to commonly eroded soil fractions.
- Synthesis of lanthanide doped silica particles of a narrow size range for use as a soil particle tracer.
- Analysis of soil tracer interactions.
- Behaviour of the tracers during simulated erosion events.

A review of the literature within chapter one has demonstrated the need for an effective tracer for use in the monitoring of both soil erosion events and subsequent remediation efforts. Such a tracer would allow for a more efficient and sustainable use of both agricultural land and the surrounding catchments. The unique luminescent properties of lanthanide chelates, and the stability of silica sol gel particles provides an ideal means by which such a tracer could be developed. Such particles would be easy to identify even against the background fluorescence levels present in biological systems, and should remain stable within the environment.

The synthesis and characterization of the novel lanthanide complexes developed during this study are detailed in chapter two. The objective for this chapter was to develop a lanthanide chelate complex of which the luminescent properties would remain stable within environmental samples (such as soils, river water and sediments). Additionally, the choice of chelates used was designed to reduce the toxicity of the complex in soils, rivers, plants and animals.

Chapter three details the production of silica particles of suitable size for use in soil erosion tracer studies. Two different particle sizes, covering the fine silt and colloidal clay size range, were synthesized using a variation on the Stöber sol-gel method. A Taguchi factorial design was employed during the development of the colloidal clay particles to identify the key factors affecting particle size. The incorporation of the lanthanide chelate complex into the silica particles to produce the final soil erosion tracers is also discussed.

The behaviour of the tracer within soil and sediment samples is detailed in chapter four. This chapter also includes details of the characterization of three different soils taken from the Glensaugh research station. Sedimentation patterns of the tracers within these soils are also discussed, along with SEM studies of the interaction between the tracers and natural soil particles. Microbial respiration studies were used to estimate the toxicity of the lanthanide complexes and tracers within the soil environment, and the luminescent stability of the tracer over time is detailed.

Chapter five reports the development of a laboratory based soil erosion simulator which included a rainfall simulator capable of producing rainfall of constant intensity. This simulator was then used to determine the behaviour of the synthesised tracer within a characterised soil during erosion events under different rainfall intensities.

Chapter six contains an overall summary of the work presented, along with general conclusions and suggestions for future work.

Chapter 2 – Synthesis and characterisation of lanthanide chelate complexes.

2.1 Introduction

Lanthanide chelate complexes have been widely used for detection in systems with complex fluorescence backgrounds, such as bioassays. The long luminescent lifetimes and high quantum efficiencies aid in this detection. However, as one of the key traits of a soil tracer is low or no toxicity to the environment, it was important that the toxicity of the ligands used within these complexes were also considered.

2.1.1 The hydroxy-pyridinones

The hydroxy-pyridinones (HOPO) are a group of chemicals based upon a pyridinone ring substituted with a hydroxyl group (see figure 2-1). These compounds have been researched as magnetic resonance imaging (MRI) contrast agents (Moore et al. 2007), immobilised chelators in heavy metal contaminated water clean up (Yantasee et al. 2009) and for use in biological assays (Moore et al. 2010). As such, lanthanide based complexes derived from these molecules have the potential to provide a highly luminescent but environmentally non-toxic luminophore for tracing applications.

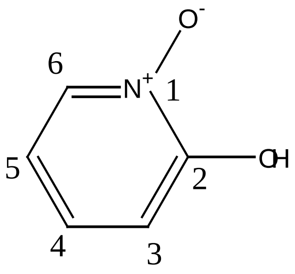

Figure 2-1 Structure of 2-pyridinol-1-oxide.

2.1.2 Quantum yield

The quantum yield of a fluorophore can be thought of as the amount of absorbed light that is subsequently emitted as luminescence (Crosby & Demas 1971), and is often displayed as:

$$\Phi = \frac{k_r}{k_r - k_{nr}} = k_r \tau_s$$

Equation 2-1

Where Φ = quantum yield, k_r is the rate constant for radiative deactivation from $S_1 \rightarrow S_0$ an excited to a ground state with emission of luminescence, k_{nr} is the rate constant for non-radiative deactivation from an excited to a ground state and τ_S is the lifetime of the excited state.

The quantum yield of a luminescent analyte is normally determined by comparison of the analyte to a standard of known quantum efficiency (Lunstroot 2008). In the case of lanthanide chelate complexes, the overall quantum yield is measured, which is dependent upon both the efficiency of the energy transfer to the lanthanide ion, and the lanthanide luminescence efficiency (Binnemans 2009). Using the comparative method, the absorption and emission at a point can be compared to that of the standard, or the gradients of absorption against luminescence of the analyte and standard can be used to determine the quantum efficiency (Lunstroot 2008). For many applications this comparative value is sufficient, and determination of the absolute quantum yield is not necessary (Lunstroot 2008).

2.1.3 Fluorescence lifetimes

Once the molecules contained within a luminescent sample are excited by a light source, they return to a ground state by the emission of a photon. The time taken for this to occur is random, and as such the decay of such a sample follows an exponential curve, with the number of photons emitted reducing over time (as shown in figure 2-2). The stability of the excited state varies between fluorophores, and as such the luminescent lifetime of a fluorophore is an important luminescent property. Fluorophores with a long lifetime, such as the lanthanides and lanthanide complexes, are of particular use in systems where large background signals may be present (such as biological systems and soil), as the measurement of luminescent emission can be delayed to a point at which the, usually short lived, background luminescence has decayed, thus allowing detection of lower levels of luminescence from the fluorophore of interest. The lifetime of an excited state molecule is simply the average amount of time a molecule remains in the excited state prior to return to the ground state, and is often represented by the equation:

$$\tau = \frac{1}{\Gamma + k_{nr}} \qquad \text{Equation 2-2}$$

Where τ = luminescent lifetime, Γ = emissive rate of the fluorophore and k_{nr} = rate of non-radiative decay to the ground state.

Luminescent lifetimes can be measured in the time or frequency domains, known as pulse and phase fluorimetry, respectively. The most commonly employed methods for determining luminescent lifetimes are normally performed via pulse fluorimetry, using specifically designed spectrophotometers. Temperature has an effect on luminescent lifetime, and measurements are normally performed on solutions of fluorophores maintained at 77 K to minimise the rate of non-radiative decay via molecular collisions. Alternatively, measurement at room temperature of samples in a solid state can be performed, know as room temperature phosphorescence.

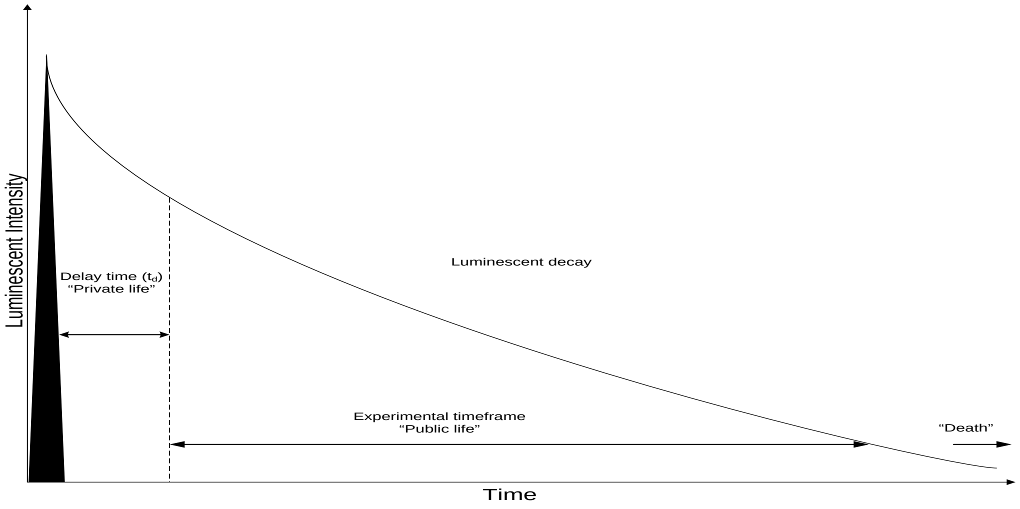

Figure 2-2 Diagram showing stages of luminescent decay, including some of the important stages in lifetime determination (Rendell & Mowthorpe 1987).

2.1.4 Aim and objectives

The aim of this chapter was to synthesise and analyse luminescent lanthanide complexes based upon one of the HOPOs, 2-pyridinol-1-oxide (2PO). This was achieved through a series of specific objectives:

- Determination of ligand triplet state to identify appropriate lanthanides to give luminescent complexes.
- Analysis of the resultant complexes using infrared (IR) (Fourier transform infra-red (FTIR) and Raman spectroscopy), liquid chromatography-mass spectrometry (LC-MS), nuclear magnetic resonance (NMR) and thermogravimetic analysis to determine the coordination structure of the synthesised complexes.

- Determination of the luminescent properties of the complexes using UV-visible absorbance and fluorescence spectroscopies, to allow the characterisation and identification of the most suitable complexes for use within the soil tracer particles.

2.2 Materials and methods

2.2.1 Chemicals and reagents

Lanthanides were obtained as lanthanide chloride hexahydrates, 99.9% purity. 2-Thenoyltrifluoroacetone (HTTA) and 2 pyrdinol-1-oxide (2PO) were 99% purity, whilst ethanol used for synthesis, ethylene glycol, sulphuric acid and acetone were analytical grade and obtained from Sigma-Aldrich. HYDRANAL composite 5, and HYDRANAL methanol dry solutions for Karl Fisher titrations were also obtained from Sigma-Aldrich. Quinine sulphate bisphosphate, dimethylsulfoxide, cresyl violet and methanol used for quantum yield determination were spectroscopy grade and obtained from Sigma-Aldrich. Triethylamine was reagent grade and obtained from Fisher Scientific, d_6-DMSO and D_2O were obtained from Cambridge isotopes laboratories.

2.2.2 Synthesis of lanthanide chelate complexes

Lanthanide 2-pyridinol-1-oxide ($Ln(2PO)_3$) complexes were synthesized using the method described by Tedeschi et al. (2003). An example of a typical synthesis using europium was as follows: europium chloride hexahydrate (0.3664g, 1 mmol) was dissolved in 100 ml distilled water, whilst 2PO (0.367g ,3.3 mmol) dissolved in 20 mL distilled water. The 2PO solution was then added dropwise whilst stirring to the europium solution. The resulting solution was then allowed to evaporate to leave yellow crystals, which were soluble in ethanol, methanol, ethylene glycol and DMSO, sparingly soluble in water and insoluble in acetone.

Lanthanide thenoyltrifluoroacetone-2PO ($Ln(TTA)_3 2PO$) complexes were synthesized using a method adapted from (Gai et al. 2010). An example of a typical synthesis using Eu^{3+} was as follows: europium chloride (0.3664g, 1 mmol) and TTA (0.6665g, 3 mmol) was dissolved in 50 mL ethanol, and the pH adjusted to 6-7 using triethylamine. 2PO (0.1112g, 1 mmol) was then dissolved in 20 mL distilled water, and then added dropwise under stirring to the europium TTA mixture. The resulting solution was then allowed to evaporate to leave yellow crystals, which were soluble in ethanol, methanol, ethylene glycol and DMSO and insoluble in water and acetone.

All lanthanide chelate complexes were purified via recrystallization using an ethanol/acetone precipitation method, and then air-dried at 70 °C to constant weight.

2.2.3 Determination of lowest triplet state

The lowest triplet state was determined using time-delayed phosphorescence measurements, which allowed the emissive energy level of the ligand to be determined. As, in order for intramolecular transfer from the ligand to the lanthanide to occur the lanthanide must possess an emissive energy level slightly lower in energy to the lowest triplet state of the ligand, this allowed specific lanthanides to be targeted. Phosphorescence excitation and emission spectra were obtained using an Edinburgh Instruments FLS920 spectrometer with a microsecond Flash lamp source (µF900) and a Hamamatsu blue PMT. $Gd(2PO)_3$ and $Gd(TTA)_3 2PO$ were dissolved in ethanol at a concentration of 1 $mg.mL^{-1}$ then spotted onto Whatman number 1 filter paper and allowed to dry in air prior to analysis. Excitation spectra were obtained between 300 and 400 nm, and emission spectra between 400 and 500 nm with excitation and emission silt widths of 10 nm and a 395 nm excitation filter in place. The microsecond flash lamp was set to a frequency of 100 Hz, with the detector time gating set to a 2 ms delay and a 98 ms gate width.

2.2.3 Infra-red analysis of chelate complexes

Fourier Transform – infra red (FTIR) and Raman spectroscopy were performed for all lanthanide complexes synthesised, in order to identify the functional groups present within the ligands, and identify any changes due to coordination with the lanthanides ions. All Raman spectra were obtained using an Avalon Instruments RamanStation R3, the settings for which can be found in table 2-1 below. FTIR spectra were obtained on either a Perkin-Elmer spectrum BX with a Pike MIRacle ATR cell, or a Thermo-scientific Nicolet iS10 equipped with a smart iTR cell. The settings used for FTIR analysis can be found in table 2-2 below. All samples were analysed in powder form, with no further preparation.

Table 2-1 Settings for Raman spectroscopy.

Start	3,600 cm^{-1}
Stop	20 cm^{-1}
Spacing	2 cm^{-1}
Measurement time	180 s
Scans	4
Exposure time	45 s

Table 2-2 Settings for FTIR spectroscopy.

Start	4,000 cm^{-1}
Stop	600 cm^{-1}
Scans	200
Interval	2 cm^{-1}
Resolution	4 cm^{-1}

2.2.4 Nuclear magnetic resonance spectroscopy and Flow injection analysis.

NMR analysis was performed to identify any changes in the structure of the ligands once coordinated with the lanthanide ions. As NMR analysis provides information as to the chemical environment of the nuclei this technique was used to identify any changes in the structure of the ligands following coordination with the lanthanide ion, NMR analysis was performed using a Brucker ultrashield 400. Proton NMR spectra were obtained in d_6DMSO between 0 and 15 ppm relative to TMS, at 400 mHz.

Flow injection analysis was performed on an Agilent 1200 series LC/MS equipped with a 6130-quadrapole mass spectrometer. Methanol was used as the mobile phase, with the column bypassed. The accelerating voltage was varied from 20-260 V; samples were prepared in methanol at a concentration of 1 $mg.mL^{-1}$ with 5 µL injection volume.

2.2.5 Thermogravimetric analysis and Karl Fisher titrations

Thermogravimetric analysis (TGA), DSC and Karl Fisher Titrations were performed to determine the presence of any water present within the lanthanide complexes, which would indicate the inner coordination sphere was not completely filled. The presence of this water could affect the efficiency of the lanthanide complex. Additionally, TGA and DSC provided information on the thermal stability of the complexes relative to the free ligand. TGA was performed on a TA instruments Q500 in platinum sample holders. Samples were directly weighed into the holder and heated at a rate of 20 $°C.min^{-1}$ to 1,000 °C. The same heating rate was used for Differential scanning colorimetry (DSC), performed on a TA instruments Q100 using aluminium sample holders. Samples were heated to a final temperature of 500 °C.

Karl Fisher titrations were performed using a Meterohm KF titrino 870 plus, with HYDRANAL composite 5, and HYDRANAL methanol dry solutions.

2.2.6 Fluorescence emission and excitation

Fluorescence emission and excitation spectra were obtained to determine if the complexes displayed lanthanide specific emission due to excitation of the ligands. Fluorescence emission and excitation spectra were obtained using crystallised chelate complexes at room temperature. Spectra were obtained on an Edinburgh Instruments FLS920 spectrometer using a Xe900 light source and a Hamamatsu blue PMT. Samples were mounted using a quartz glass powder cell, mounted at 45° to the excitation and emission spectra. Unless otherwise stated excitation spectra were obtained between 200 and 500 nm whilst emission spectra were obtained between 480 and 650 nm, using a 395 nm excitation filter.

2.2.7 Quantum yield and fluorescence lifetime measurement

Quantum yield determinations were performed to determine the efficiency of the fluorescence process relative to quinine sulphate bisphosphate in 0.1 M sulphuric acid, with the lanthanide chelate complexes dissolved in ethanol to a final concentration of 1ppm (Jobin Yvon Horiba 2012). UV-visible absorbance spectra were obtained using a Perkin-Elmer Lambda900 spectrometer in a 10 mm path length quartz cuvette, ensuring the absorbance did not exceed 0.05 at a slit width of 3 nm. Fluorescence emission spectra were obtained using a Perkin-Elmer LS-50B fluorescence spectrometer using a 10 mm path length quartz cuvette with an excitation and emission slit width of 3 nm. The excitation wavelength was set to that of the lanthanide complex of interest for both the complex and reference samples and a 395 nm excitation filter was used for all fluorescence measurements. Quantum yields were calculated from the uv-visible and fluorescence spectra obtained using Spekwin32 (Menges 2013) in standard quantum yield determination mode.

Fluorescence lifetime determinations were performed using an Edinburgh Instruments FLS920 spectrometer using a µFlash light source and a Hamamatsu blue PMT. Samples were analysed in the solid state, using a quartz powder holder at room temperature in conjunction with a 395 nm excitation filter. Excitation and emission wavelengths were set based on the emission and excitation maxima for the individual complex used with excitation and emission silt widths set at 10 nm. The microsecond flash lamp was set to a frequency of 10Hz; with the detector time gated using a 5 ms delay and 20 ms gate width. Lifetimes were obtained over 4000 channels, using a 5 ms delay with an 8 ms acquisition time. Lifetime decay curve fits were determined using a tail fit using the Edinburgh Instruments F900 software provided.

2.3 Results and discussion

2.3.1 Triplet state determination

The lowest triplet state of each ligand was determined to identify the energy of phosphorescence photons emitted by the ligands (Gutierrez et al. 2004; Rendell & Mowthorpe 1987). These photons are available for intramolecular transfer to the lanthanide ions, and the energy of the emitted photons can be matched to the emission excited states of the lanthanides that result in an emissive state (Gutierrez et al. 2004). This allows the most suitable lanthanide ions to be identified, i.e. those most likely to be sensitized by the ligand. As the emission bands of gadolinium are in the UV, phosphoresce analysis in the visible region of the Gd^{3+} ion incorporated into the complex allows emission from the lowest triplet state to be determined (Gutierrez et al. 2004). The complex was analysed as a solid at room temperature to reduce the effects of deactivation and multiple vibrational levels of the excited and ground state complexes seen at room temperature.

Analysis of the $Gd(2PO)_3$ complex can be seen in figure 2-3 (a), and indicates that the lowest triplet state for this ligand was 454 nm. From the Deike diagram, the lanthanides with emissive energy levels close to, but lower than, this energy by approximately 2000 cm^{-1} were found to be Pr, Tb, Eu, Dy, Ho and Er (Dieke 1968; Li et al. 2001). Whilst the effect of scattering means that other peaks were present within the spectrum, the identity of this peak as the triplet state was confirmed by analysis of the excitation spectra of each peak, to determine if it was dependent upon the excitation wavelength used to excite the sample. A peak at 208 nm was only seen for the triplet state peak. An identical analysis was performed for the Gd(TTA)$_3$2PO complex (figure 2-3 (b)), which identified the lowest triplet state of this ligand was at 466 nm. The wavenumber of this peak was found to be 21.4 x 10^3 cm^{-1}. From the Deike diagram, the lanthanides with emissive energy levels close to, but lower than, this energy were found to be Pr, Eu, Tb, Dy, Ho and Er (Gutierrez et al. 2004). The long lifetime of Eu and Tb luminescence is known to be of particular advantage for use within probes, especially use within environmental samples, where background fluorescence can lower sensitivity. As such, the complexes used for the synthesis of the erosion tracers focused upon Eu^{3+} or Tb^{3+}.

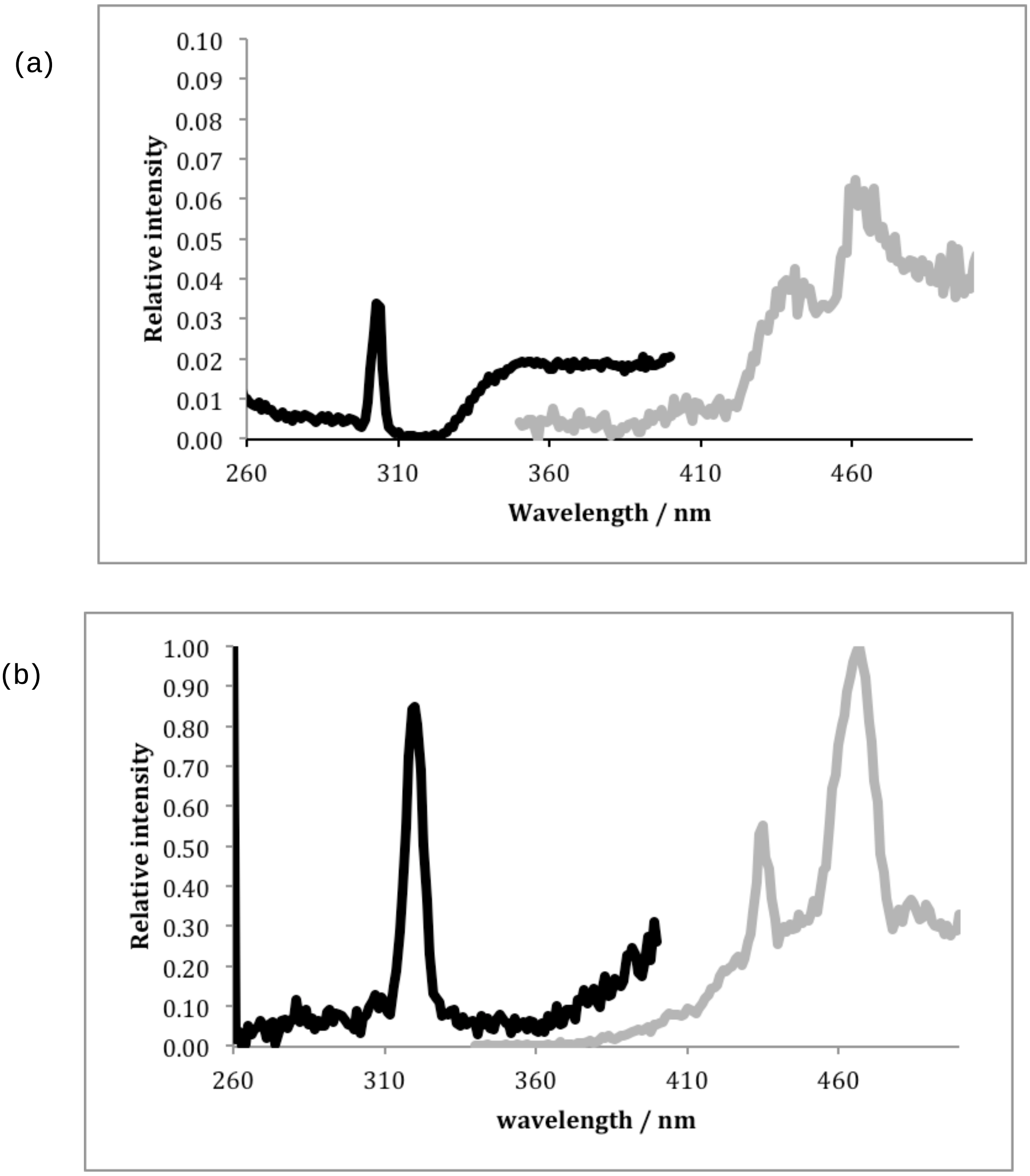

Figure 2-3 Time resolved spectra obtained for (a) $Gd(2PO)_3$ and (b) $Gd(TTA)_32PO$ (obtained on a Edinburgh Instruments FLS920 in time delay mode, excitation at 208 nm, excitation and emission slit width: 10 nm, 2 ms delay, 98 ms gate width).

2.3.2 Infra-red analysis

All complexes synthesised were analysed using FTIR and Raman to determine the functional groups present within the complexes. An example of spectra obtained during FTIR analysis of 2PO, $Eu(2PO)_3$ and $Tb(2PO)_3$ can be seen in figure 2-4. Raman spectra for these compounds can be seen in figure 2-5 and appendix I. Spectra for Eu(TTA)$_3$2PO and Tb(TTA)$_3$2PO can be found in figures 2-6 (FTIR) and 2-7 (Raman) and appendix I figure A-1.

FTIR analysis of all of the complexes indicated the presence of a metal band around 1200 cm^{-1} not seen within the free ligands. There was also a shift within the C-N-O group of 2PO, characteristic of a bonded oxygen group, indicating that the 2PO ligand coordinates with the lanthanide through this group, as has been found in other studies (Tedeschi et al. 2003). This band shift was also identified within the Raman spectra, however, the metal band was not present within these spectra. Within Eu(TTA)$_3$2PO and Tb(TTA)$_3$2PO the carbonyl band present within TTA was shifted to an ester band within the complex, indicating coordination with the metal via the oxygen present within the acetone chain. This was in agreement with reported findings from other TTA containing lanthanide complexes (Lv et al. 2007). Additionally the band associated with the CF$_3$ group at (1440-100 cm^{-1}) was no longer present within the lanthanide complex, probably due to the binding of the ligand reducing the movement of the CF$_3$ bond (Gai et al. 2010; Lv et al. 2007). Again, these bands, and their relative shifts were also present within the Raman spectra, and in particular for the carbonyl to ester shift, were easier to discern.

This shift in band pattern was diagnostic of the lanthanide coordinating with the ligands to form a complex, and provided information about the coordination sites. In addition, knowledge of the IR band patterns for the free complex could be used to determine whether the complex remained stable once doped within the tracer, and also to identify any possible changes to the structure of the complex once incorporated into the tracer.

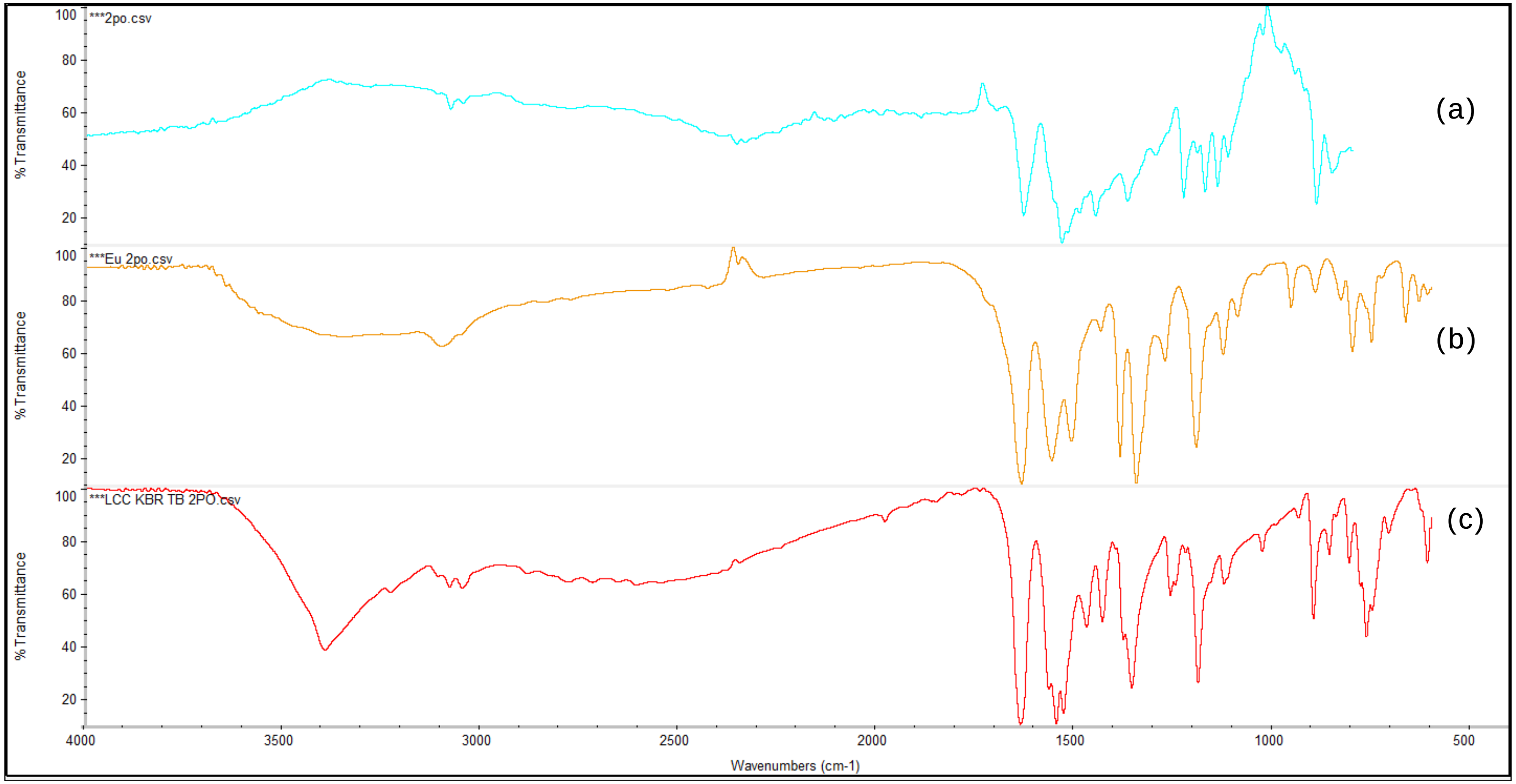

Figure 2-4 FTIR spectra for (a) 2PO, (b) $Eu(2PO)_3$ and (c) $Tb(2PO)_3$

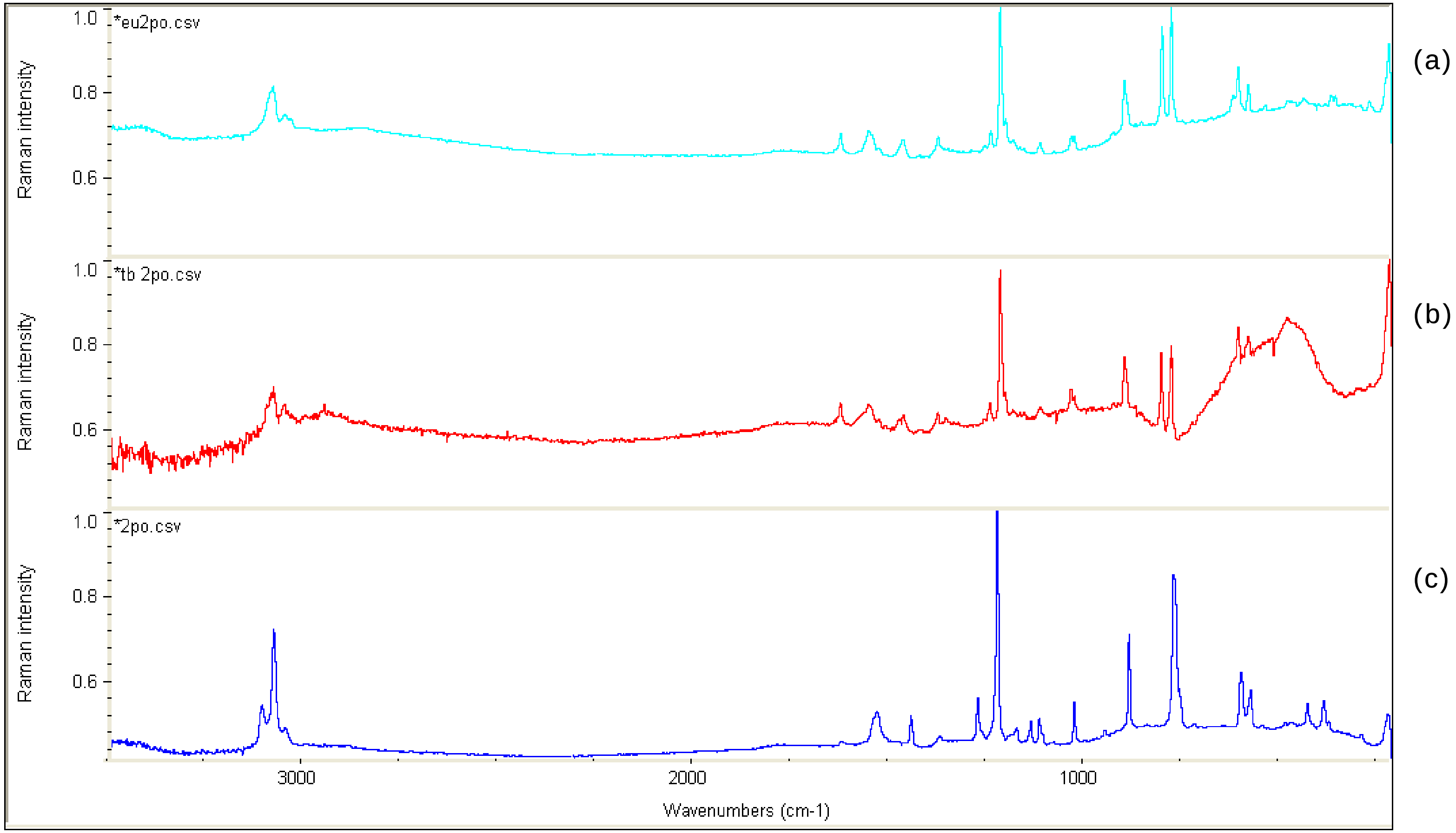

Figure 2-5 Raman spectra for (a) Eu(2PO)$_3$, (b) Tb(2PO)$_3$ and (c) 2PO

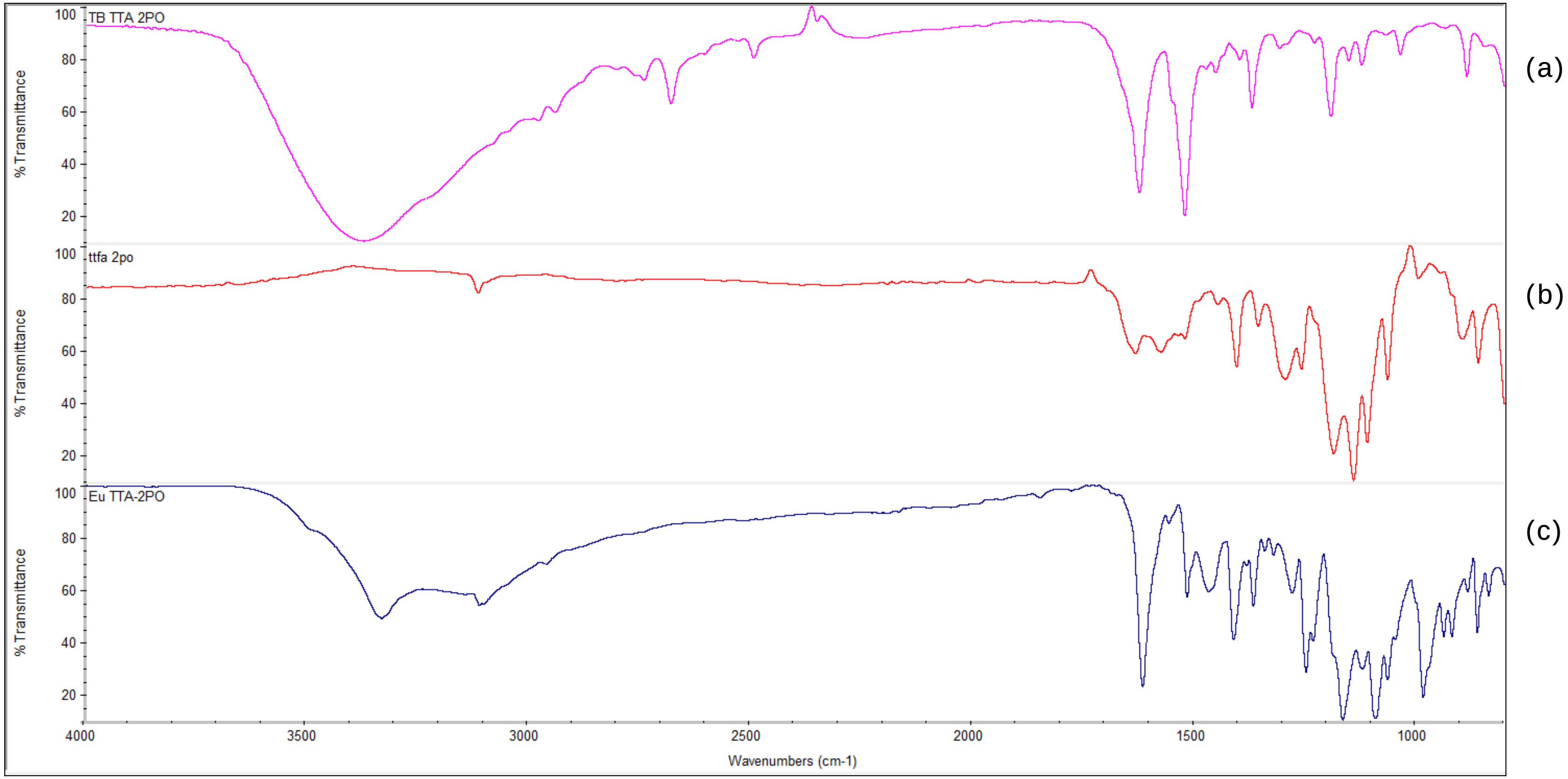

Figure 2-6 FTIR spectra for (a) $Tb(TTA)_3 2PO$, (b) 3:1 mixture HTTA:2PO and (c) $Eu(TTA)_3 2PO$

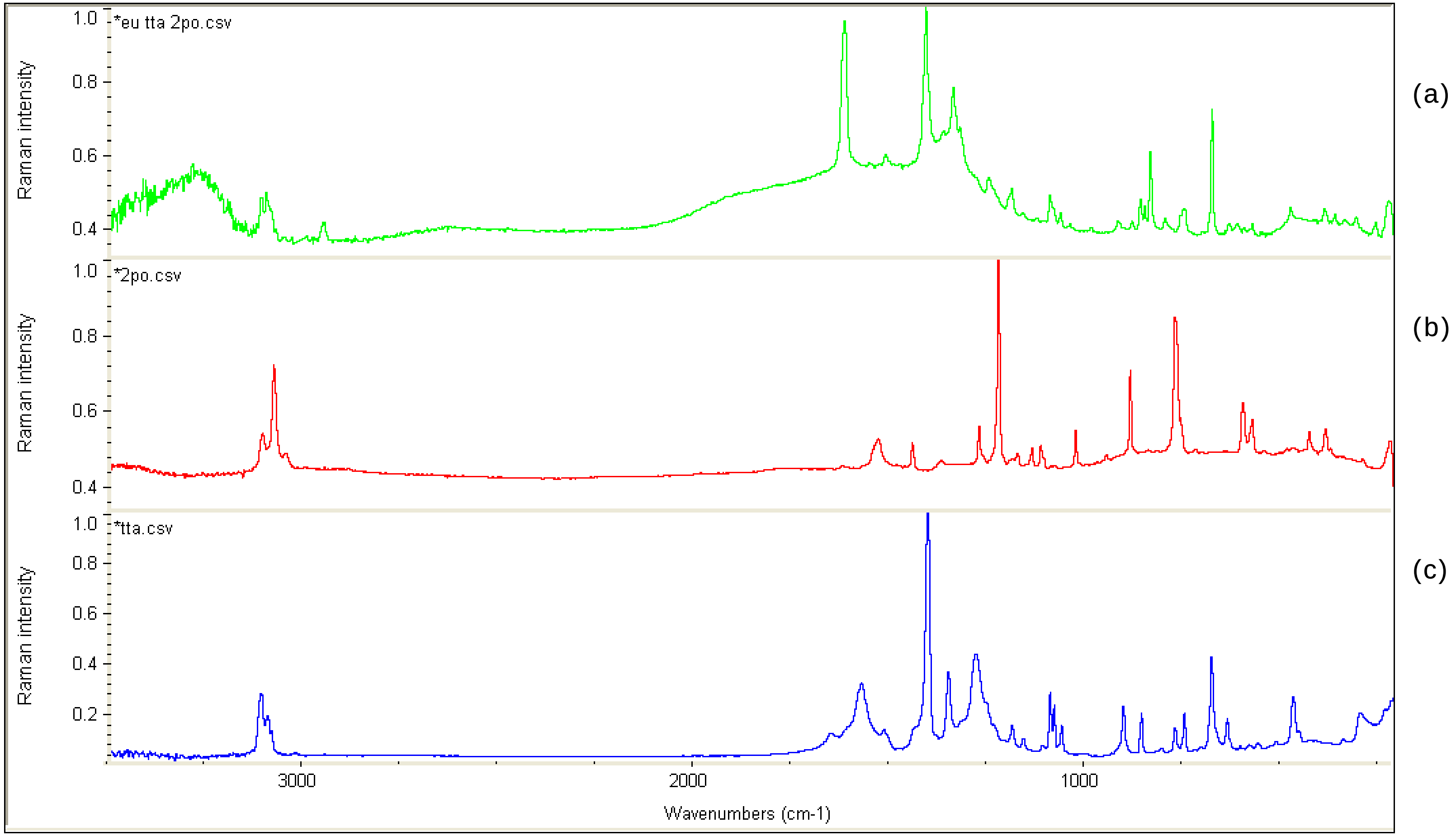

Figure 2-7 Raman spectra for (a) Eu(TTA)$_3$2PO, (b) HTTA and (c) 2PO

2.3.3 Nuclear magnetic resonance

Nuclear magnetic resonance spectroscopy was performed using complexes containing the non-paramagnetic trivalent lanthanide ion, lanthanum. The presence of a paramagnetic ion (including europium and terbium) within a sample causes a reduction in the ^{1}H peak heights closest to the ion due to magnetic relaxation, thus preventing alterations to the molecules structure being determined (Bakhmutov 2011; Skoog et al. 2007). Selected NMR peaks obtained for these complexes, and the precursors can be found in table 2-3. Predicted structures for the complexes and proton assignments for the precursors can be found in figure 2-8 (NMR spectra can be found in appendix I).

Table 2-3 Chemical shifts from NMR spectra obtained for TTA and 2PO either free (uncoordinated) or coordinated to La^{3+}.

		Chemical shift / PPM		
Ligand	Proton	Uncoordinated	Coordinated	Difference / PPM
TTA	H2	7.33 (t, *J*= 4 Hz, 1H)	7.24 (t, *J* = 9.2 Hz, 1H)	-0.09
	H3	8.35 (d, *J*= 2 Hz, 1H)	8.02 (d, *J* = 5.6 Hz, 1H)	-0.33
	H1	8.19 (d, *J*= 2.8 Hz, 1H)	7.97 (d, *J*= 16 Hz, 1H)	-0.22
	H1'	6.97 (s, 2H)	7.18 (s, 2H)	0.21
2PO	H4	7.89 (dd, *J*= 8.8, 2.4 Hz, 1H)	7.90 (dd, *J* = 6.8, 2.4 Hz, 1H)	0.01
	H2	7.36 (m, *J*= 17.6, 2 Hz, 1H)	7.35 (m, *J* = 15.2, 2 Hz, 1H)	-0.01
	H1	6.49 (dd, *J*= 9.2, 1.6 Hz, 1H)	6.50 (dd, *J* = 10.8, 1.6 Hz, 1H)	0.01
	H3	6.18 (td, *J*= 15.2, 1,6 Hz, 1H)	6.22 (td, *J* = 15.6, 1.6 Hz, 1H)	0.04

The most pronounced changes in chemical shift appeared in protons associated with the TTA ligand when complexed with La. The increased chemical shift of the H2’ proton indicates a decrease in electron density surrounding the proton. This would be expected during coordination, as La would draw electrons towards itself, so decreasing the electron density near the C=O coordination site (between C1’ and C3’). This would be associated with a decrease in shielding of protons within the thenoyl ring closest to the site of coordination, as delocalised electrons within the ring move towards the La^{3+} ion to stabilise the complex, as seen in the increase in chemical shift for protons at H2 and H1. The smallest effect was seen at H2, furthest from the La^{3+} ion and the site of coordination. A smaller change in chemical shift is seen for the protons of 2PO, most likely due to the stabilising effect of the pyridine ring, and the availability of lone pairs of electrons from the nitrogen atom to stabilise the C-O and N-O bonds involved in coordination. Additionally, due to the steric structure of the 2PO, the pyridine ring would remain further from the La^{3+} ion and the acetone chain of TTA.

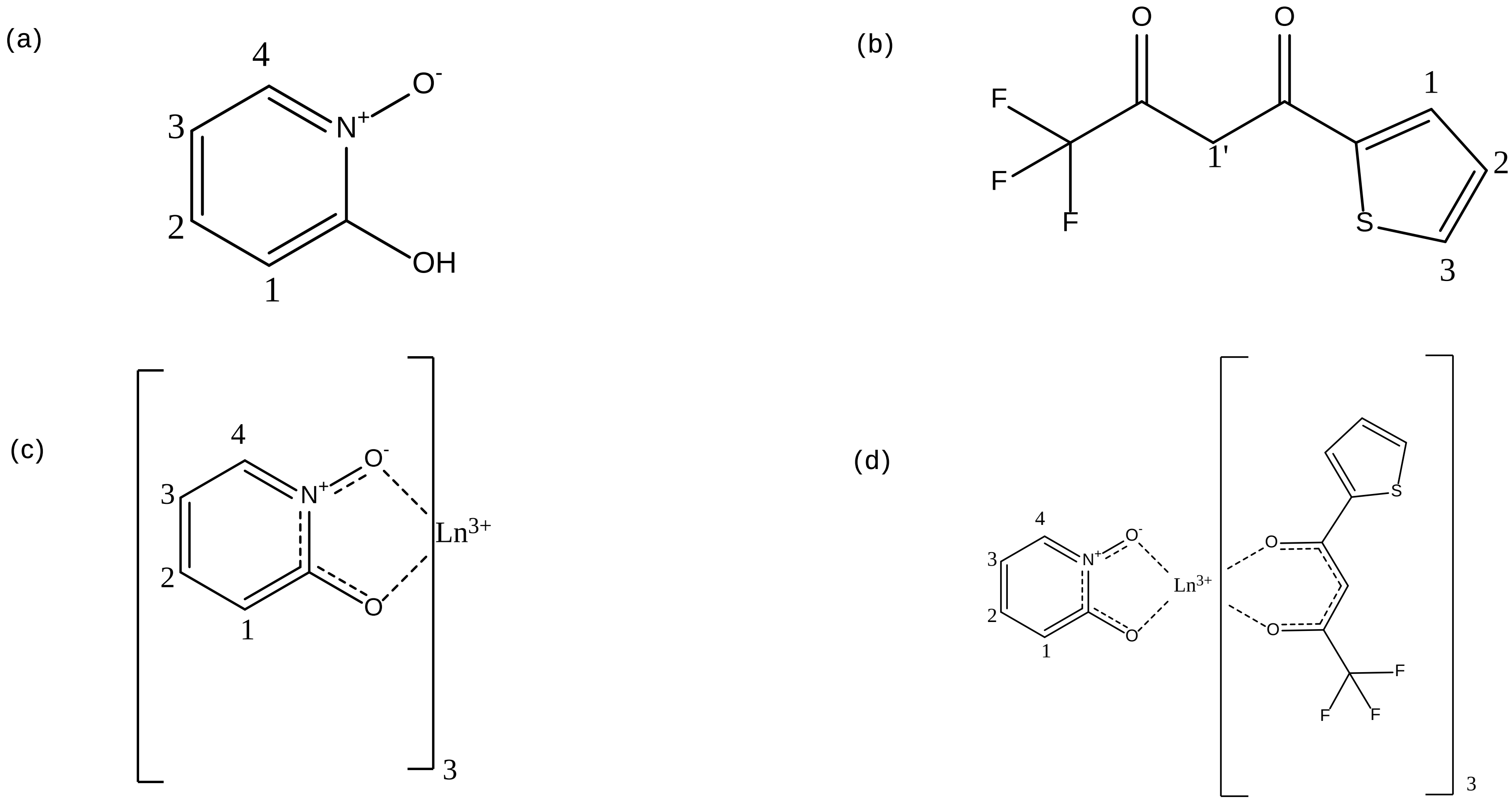

Figure 2-8 Structure of ligands, including proton assignments, used during NMR analysis (a) 2PO and (b) TTA and predicted structure of (c) Ln(2PO)$_3$ and (d) Ln(TTA)$_3$2PO.

2.3.4 Flow injection analysis – mass spectrometry

Flow injection analysis- mass spectrometry was used to identify the molecular mass of the complexes in methanol solution, to allow prediction of the complex structure. Samples containing gadolinium and dysprosium were particularly informative, as these lanthanides have distinct mass spectrometry profiles due to the abundance of naturally occurring stable isotopes (Henderson & McIndoe 2005). For both these metals, mass spectra with the expected profiles indicated a molecular ion with the formula $Ln(2PO)_3$ and $Ln(TTA)_3 2PO$ for each of the synthesised complexes (as shown in figure 2-9 and tables 2-4 and 2-5). Within the mass spectra it was also possible to identify the formation of various expected adducts, and also the presence of lower molecular mass peaks, where some of the individual ligand molecules have been lost.

Table 2-4 Observed and predicted mass of molecular ion for 2PO containing complexes.

Lanthanide	Predicted mass of molecular ion (m/z)	Observed mass of molecular ion (m/z)
Gd	490.6	490.7
Dy	495.8	495.8
Tb	492.2	492.0
Eu	485.3	485.0

Table 2-5 Observed and predicted mass of molecular ion for TTA-2PO containing complexes.

Lanthanide	Predicted mass of molecular ion	Observed mass of molecular ion
Gd	934.9	934.8
Dy	940.1	939.7
Tb	936.6	935.6
Eu	929.6	928.8

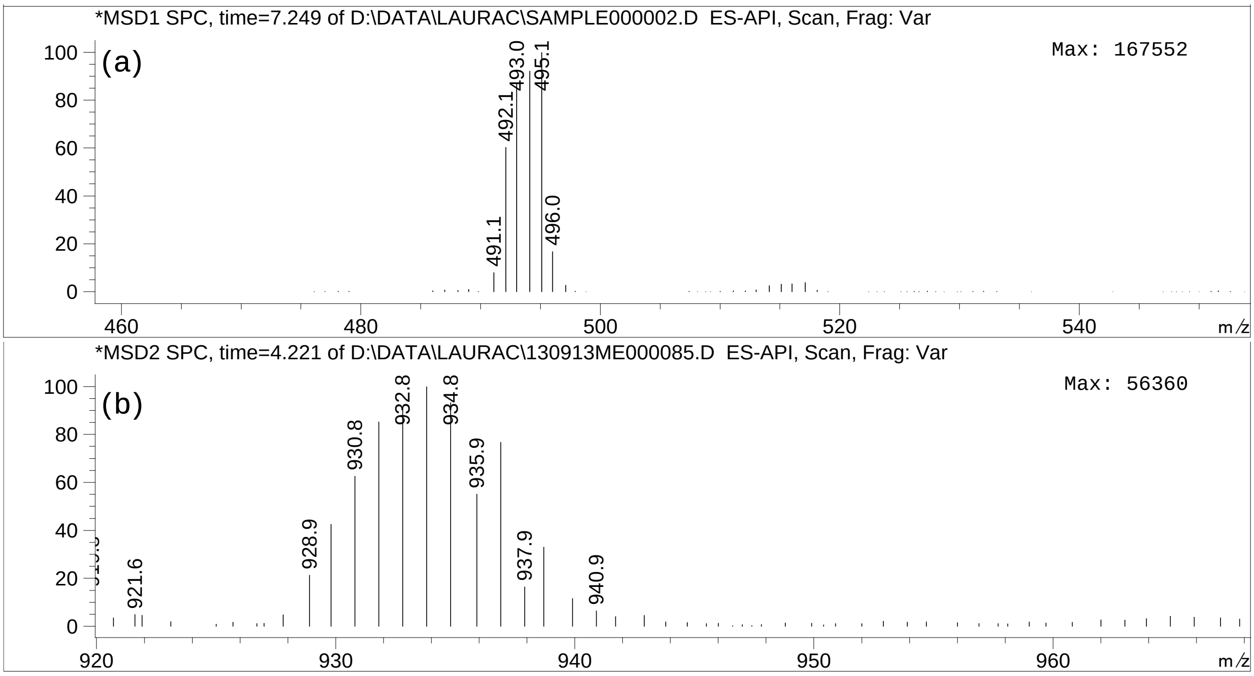

Figure 2-9 Mass spectra obtained for (a) $Dy(2PO)_3$ and (b) $Gd(TTA)_3 2PO$.

Taken in association with the other data obtained for the complexes, this indicated that predicted structures detailed in figure 2-8 were accurate for these complexes with all the lanthanides studied.

2.3.5 Determination of coordinated water

The presence of water within the coordination shell of a lanthanide complex can reduce the luminescent quantum efficiency of the complex. In order to ascertain if the complexes contained coordinated water, Thermogravimetric analysis (TGA) and differential scanning colorimetry were performed on complexes of $(2PO)_3$ and $(TTA)_3 2PO$ with Eu^{3+} and Tb^{3+}. TGA thermograms can be seen in figure 2-10 and DSC curves in figure 2-11. Within the TGA thermograms, no peak was present at 100 °C in any sample, indicating that no water was present within the complexes.

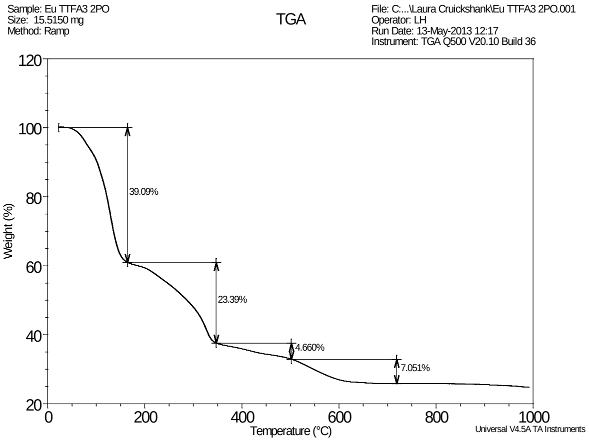

Figure 2-10 TGA curve for $Eu(TTA)_3$ 2PO

Furthermore DSC analysis indicated that no coordinated water was present, with endothermic melt peaks being the first peaks seen in the spectra. For each compound there was a discrete melt and crystallisation event, as indicated by the presence of endo- and exothermic peaks. In the 2PO complexes, the melting point increased from 147-152 °C to 168 °C for the $Eu(2PO)_3$ complex, and 175 °C for the $Tb(2PO)_3$. For the $(TTA)_3 2PO$ a similar increase in melting point was seen, with the melting point from 40-44 °C for TTA, to 69 °C in $Eu(TTA)_3 2PO$ and multiple peaks at 88, 118 and 160 °C for $Tb(TTA)_3 2PO$. Within the Eu

$(TTA)_3 2PO$, a peak at 43 °C, which likely relates to the melting point of uncoordinated TTA was also present. These multiple peaks were most likely due to formation of the complex from multiple ligands, with each component bound more or less strongly to the lanthanide ion, and therefore its own melting point. The melt and crystallisation peaks for the $(2PO)_3$ for both the terbium and europium complexes occur at higher temperature than the $(TTA)_3 2PO$ complexes, showing that the $(2PO)_3$ complexes were more thermally stable (Yu et al. 2005). Additionally, the $Tb(TTA)_3 2PO$ has a far higher crystallisation and melt temperature than $Eu(TTA)_3 2PO$, again indicating that the Tb^{3+} complexes were more thermally stable than the Eu^{3+} (Kang et al. 2005). This was mirrored for the $(2PO)_3$ complexes, although the difference was not so acute. It is interesting to note that the $Tb(TTA)_3 2PO$ spectrum appears to show thermal degradation of the complex at a similar point to the crystallisation peaks, and particularly around 350 °C (Yu et al. 2005). It is possible that these peaks, in particular the second peak, not seen in other spectra; are associated with the thermal breakdown of the complex itself.

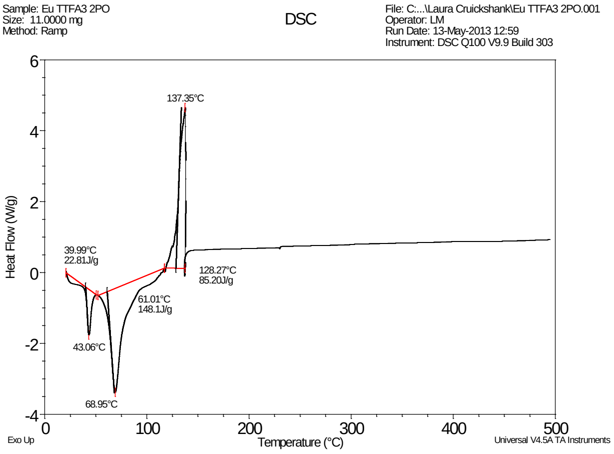

Figure 2-11 Differential Scanning Colorimetry curve for $Eu(TTA)_3 2PO$

Karl Fischer titrations were used to further determine if any coordinated water was present within the $(2PO)_3$ and $(TTA)_3 2PO$ complexes of Eu^{3+} and Tb^{3+}. No coordinated water was present within any of the samples tested, in agreement with the data obtained from TGA and DSC, further indicating that the ligands completely fill the inner coordination shell of the lanthanide ions used. Details of the titrations can be found in appendix I table A-1. The analysis of the coordinated water within the complexes indicated that the coordination sphere of the trivalent lanthanide ions was filled, and that the complexes existed in a single form. As the complexes excluded common deactivators of lanthanide luminescence, such as water, the luminescence characteristics of the complexes were analysed to determine suitability for use as an environmental tracer.

2.3.6 Fluorescence spectroscopy

The emission and excitation spectra of all complexes were determined to identify the emission and excitation maxima. These allowed any sensitization of the lanthanides used by the ligands to be identified, and demonstrated if the emission spectra was characteristic of the specific lanthanide. It also resulted in spectra that could allow detection and comparison of the complexes within the different chemical environments of the silica sol-gel beads and environmental samples. All fluorescence spectra were obtained in the solid state, to reduce the level of quenching due to molecular oxygen and water.

Examples of the spectra obtained can be seen in figure 2-12 with each spectrum showing the fluorescence emission characteristic of the lanthanide used. This indicates, that as predicted from the triplet state analysis (section 2.3.7), both Eu^{3+} and Tb^{3+} were sensitized by these ligands. As all of these complexes show lanthanide specific luminescence, all complexes were then assessed to identify which complex would be most effective as a soil erosion tracer.

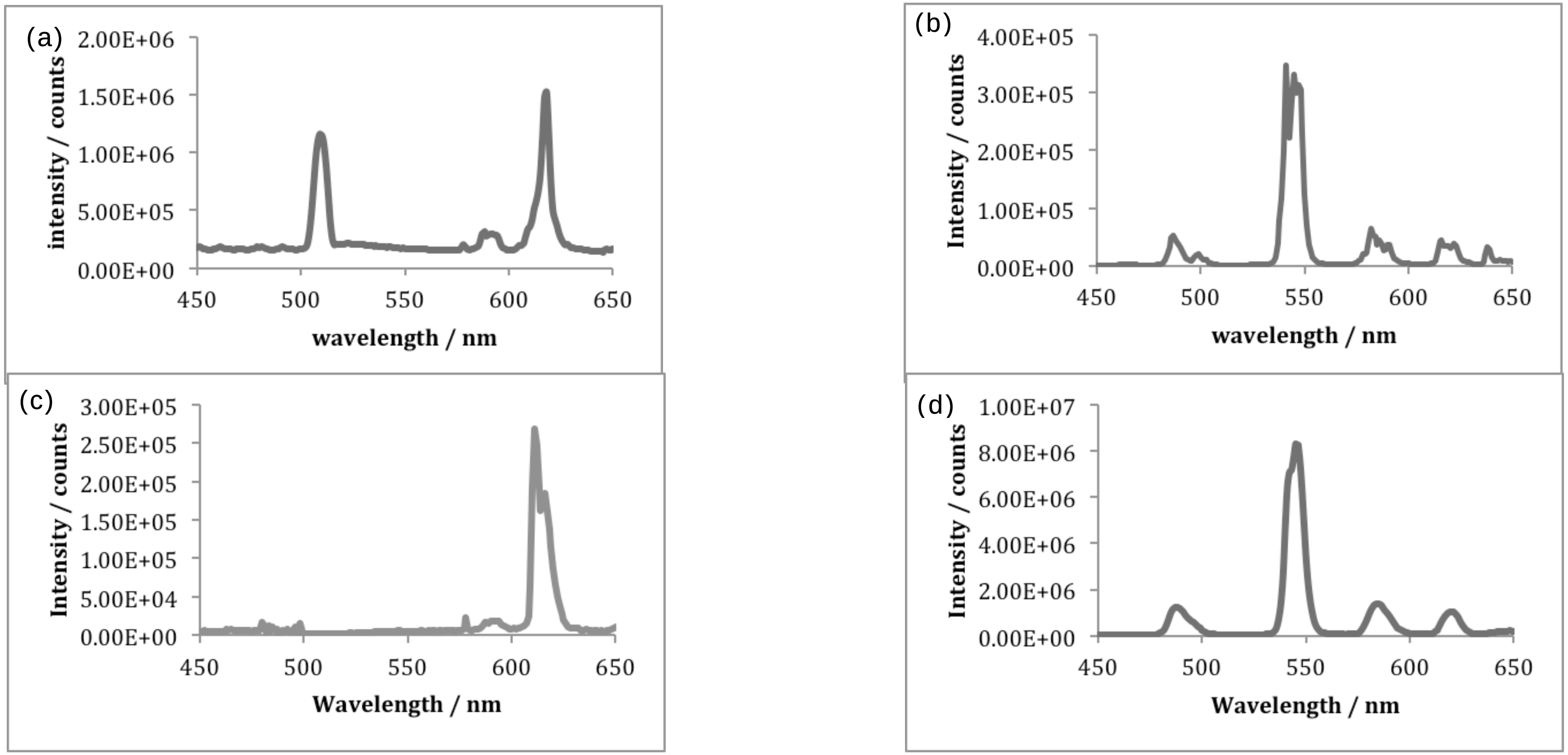

Figure 2-12 Fluorescence emission spectra for (a) Eu(2PO)$_3$ (b) Tb(2PO)$_3$ (c) Eu(TTA)$_3$2PO and (d) Tb(TTA)$_3$2PO obtained on a Edinburgh Instruments FLS920, excitation at 320 nm (Tb^{3+} complexes) or 350 nm (Eu^{3+} complexes), excitation slit width: 2 nm and emission slit width: 4 nm.

2.3.7 Lifetime determination

Due to the complex organic matter contained within soils, a large amount of background fluorescence, not specific to the analyte of interest, may be present. If this overlaps the region in which the analyte emits, then it may severely increase the limit of detection of the tracer. However, such background fluorescence is normally short-lived (within the ns range). Time resolved fluorescence (TRF) can allow the spectrometer to limit the effect of this background fluorescence by delaying measurement for a period of µs, allowing longer lived lanthanide luminescence to be the only signal detected (see section 2.1.3). The longer the luminescent lifetime, the longer the measurement can be delayed, reducing the amount of background fluorescence, and maximising the signal to noise. In order to identify the ideal amount of time such a delay should be, it is essential to determine the lifetime of the complex of interest, allowing a delay time which reduces the background fluorescence to a minimum, whilst not allowing too much of the signal from the complex to be lost. By balancing these two, a high level of sensitivity can be obtained using this technique.

Luminescent lifetimes of the complexes were determined at room temperature, in the solid state. This reduces the amount of quenching resulting from molecular oxygen, water and molecular collisions with solvent molecules. The lifetimes determined for each complex can be seen in table 2-6, with a reduced Chi-squared (χ^2) value of below 1.2 considered to indicate an acceptable fit (Boens et al. 2007). An example decay curve for $Eu(TTA)_3 2PO$ can be found in figure 2-13. All the complexes can be analysed using a single curve fit, indicating that all of the lanthanide ions are in the same environment, and therefore that only one form of the complex was present. Tail-fit was used to determine the lifetime, as this was the technique which best describes the curve for fluorophores with lifetimes of greater than µs periods (Boens et al. 2007; Rendell & Mowthorpe 1987). As the values for these lifetimes were longer than that of normal background fluorescence signals, which are usually ns in length, they were suitable for use within an environmental tracer. In order to determine if these complexes would be detectable at low levels, the quantum efficiency of each complex was then determined.

Table 2-6 Luminescent lifetimes of the complexes synthesised during the study, using a tail fit method.

Complex	Lifetime (µs)	χ^2
$Eu(2PO)_3$	472.69	0.997
$Tb(2PO)_3$	41.72	0.991
$Eu(TTA)_32PO$	482.54	0.967
$Tb(TTA)_32PO$	58.29	1.035

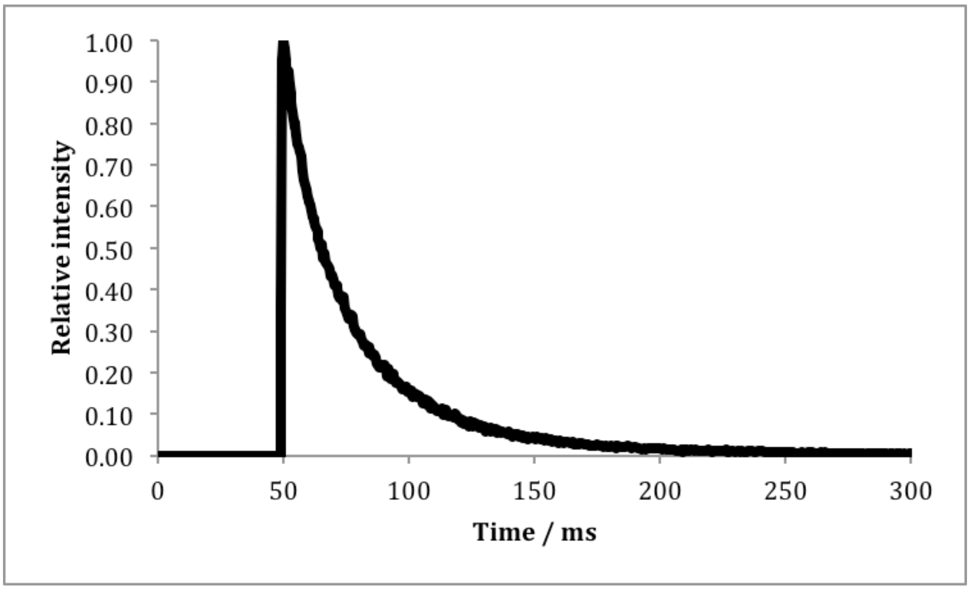

Figure 2-13 Decay curve obtained for $Eu(TTA)_32PO$ (obtained on a Edinburgh Instruments FLS920 in time delay mode, excitation at 350 nm, excitation and emission slit width: 10 nm, obtained over 4000 channels, with 0.1 ms delay, 8 ms acquisition time).

For each of the complexes analysed, the luminescent lifetime was reproducible within both different samples of a synthesis, and between different synthesis reactions. For example, for three measurements of the Eu(TTA)$_3$.2PO complex, lifetimes of 482.54, 477.32 and 488.04 µs were obtained. Analysis of the luminescent lifetime of another synthesis reaction for this complex resulted in a luminescent lifetime of 475.64 µs. This indicated that the coordination chemistry of the lanthanides was similar between individual reactions, and across a batch of complex. As such, any lanthanide complex used to dope the silica particles should have similar characteristics to those studied during luminescent lifetime measurements.

2.3.8 Quantum yield

An effective particle tracer should be detectable at very low concentrations, and the use of a lanthanide chelate complex with a high quantum efficiency would allow measurement at lower concentrations. It is therefore important to determine the quantum efficiency of the lanthanide chelate complexes used in order to optimise the level of detection of the luminescent particles synthesised.

All quantum yields were determined relative to quinine hemisulphate dihydrate in 0.1 M sulphuric acid (Jobin Yvon Horiba 2012). The quantum yield of this fluorophore has been determined empirically to be 54 %, and has an excitation wavelength within the range used for the lanthanide complexes (Jobin Yvon Horiba 2012). The quantum yields determined for all complexes are detailed in table 2-7

Table 2-7 Luminescent quantum yields calculated for the complexes synthesised within the study (quantum yields calculated by specwin32, in basic quantum yield mode (Menges 2013))

Complex	Quantum yield (%)
Eu(2PO)$_3$	0.8
Tb(2PO)$_3$	2.2
Eu(TTA)$_3$2PO	9.9
Tb(TTA)$_3$2PO	8.8

The quantum yields of the 2PO$_3$ complexes were similar to that reported in the literature (Moore et al. 2010; Jocher et al. 2008; Tedeschi et al. 2003). The low quantum yield of Eu^{3+} has been previously reported, and is believed to be due to the closeness of the energy level of the triplet state and emissive state of the trivalent ion, allowing deactivation of the complex via a back transfer mechanism (Moore et al. 2008). For both the Eu(TTA)$_3$2PO and Tb(TTA)$_3$2PO complexes the quantum yields were considered high enough to be suitable for use in an environmental tracer.

2.4 Conclusions

The lanthanide complexes formed with both 2PO and TTA$_3$2PO resulted in a yellow powder that dissolved in two of the solvents commonly used during the sol-gel process, ethanol and methanol. This is the first time the TTA$_3$.2PO complexes have been reported. IR analysis indicated that the 2PO ligand coordinated with the lanthanide ion via the oxygen and N-O group and the TTA ligand via the C=O groups. NMR analysis of the lanthanum complex also indicated that coordination was via these groups. Thermogravimetric analysis and Karl Fisher titration suggest that no coordinated water was present within the complexes, and mass spectrometry data provided a molecular ion consistent with complexes containing $(2PO)_3$ or $(TTA)_3 2PO$ respectively. Thus the complexes can be represented by $Ln(2PO)_3$ and $Ln(TTA)_3 2PO$. In combination with Tb^{3+} and Eu^{3+} the complexes exhibited luminescence characteristic of the specific lanthanide, however the quantum yields and luminescent lifetimes of the $(TTA)_3 2PO$ complexes were higher and longer respectively. As such the $(TTA)_3 2PO$ based complexes were determined to be the most suitable for use within an environmental tracer, and as such were used in all further investigations.

Chapter 3 – Synthesis and characterization of silica sol-gel particles

3.1 Introduction

In order to develop a particle tracer which would remain stable within the environment from the lanthanide complexes developed within chapter 2, it was necessary to develop a method of incorporating them into a non-toxic matrix. This matrix could both protect the complex from environmental factors, such as moisture, and also provide a particle which could be altered to move in a similar manner to the target soil particles. Therefore the complexes were incorporated into silica particles created using a sol-gel method.

3.1.1 Sol-gel synthesis

The sol-gel method provides a simple, low temperature method for obtaining silica glasses and particles with high purity. In 1968, Stöber *et al* reported a method for the production of silica based particles of controlled size and morphology using a sol-gel method. The sol-gel particles are produced as a result of a hydrolysis reaction allowing the formation of a colloidal suspension from a metal alkoxide precursor, which subsequently polymerizes to form a metal oxide network with the liquid phase. In the case of silica sol-gel particles this precursor is a silica alkoxide, the most common being tetramethoxysilane (TMOS) and tetraethylorthosilicate (TEOS). The resultant silica particles are optically transparent within the visible and near ultraviolet regions of the electromagnetic spectrum, and thus find many applications within the optical imaging sectors (Jin et al. 2012; Shen et al. 2013; Cooper et al. 2013). As the sol-gel process occurs at low temperatures, often around room temperature, and under chemically mild conditions, there is the possibility of incorporating temperature or chemically sensitive species into the sol-gel matrix, such as proteins and organic molecules. Recently much research has been devoted to the incorporation of lanthanide chelates into silica sol-gels, and evidence suggests that this incorporation can increase the stability of both lanthanide ions and lanthanide chelate complexes (Jin et al. 1997; Feng & Zhang 2013; Nakahara et al. 2015; Zaitoun et al. 2008; Zaitoun et al. 2013).

3.1.2 Lanthanides doped sol-gels

Incorporation of lanthanide chelate complexes into sol-gel derived silica particles has resulted in particles suitable for applications varying from bio imaging and bioassays (Rossi et al. 2005; Santra et al. 2001; Insin et al. 2008; Bae et al. 2012) to environmental (Yin et al. 2012) and engineering applications (Cingarapu et al. 2014). However, the addition of both lanthanide ions and associated complexes to sol-gel particles has been shown to affect the morphology of the particles synthesised, disrupting the formation of monodisperse spheres, most likely due to the formation of insoluble lanthanide hydroxides (Lu & Yan 2008). The addition of the lanthanide complex to a ‘shell’ of silica surrounding a core particle of desired size and morphology is one possible method of forming particles which retain the desirable characteristics of sol-gel particles, whilst incorporating the highly luminescent lanthanide complexes.

3.1.3 Aim and objectives

The aim of this chapter was to synthesise particles of suitable size for use as soil erosion tracers, and to incorporate luminescent lanthanide complexes into these particles to give a luminescent soil particle tracer. This was achieved through a series of specific objectives:

- Determination of the conditions required to synthesise tracers within the two key eroded soil size ranges; fine silt and colloidal clay.
- Incorporation of the lanthanide chelate complexes synthesised in chapter 2 to give luminescent particles.
- Analysis of the surface groups present on the particles to identify potential interactions with natural soil particles, and to confirm successful doping of the complex.
- Analysis of the luminescent spectra of the synthesised particles, and determination of the luminescent lifetime to allow appropriate detection settings to be identified.
- Determination of doping efficiency and luminescence intensity of the synthesised particles over a range of dopant concentrations, to identify conditions that provided good levels of luminescent intensity with low concentrations of dopant to reduce the cost of tracer synthesis.

3.2 Sol-gel synthesis

3.2.1 Chemicals and reagents

Ammonium hydroxide (28-30 %), tetraethylorthosilicate, hydrochloric acid, nitric acid and ethanol were all obtained from Fisher Scientific and used without modification. Potassium bromide anhydride, terbium and europium chloride hexahydrates were 99.9 % purity whilst thenoyltrifluoroacetone (HTTA) and 2-pyridinol-1-oxide (2PO) were 99 % purity and were all obtained from Sigma Aldrich.

3.2.2 Methods for particle synthesis

Three synthesis methods were chosen to synthesise particles within the size range for the two key eroded soil particle fractions, fine silt and colloidal clay. This allowed particles of appropriate size, with the desired spherical monodisperse morphology to be produced.

3.2.2.a Ammonium hydroxide hydrolysed particle synthesis

Ammonium hydroxide hydrolysed particles were synthesized according to the method described by Rossi et al (2006) with the following modifications; 1.3 mL TEOS in 3.7 mL ethanol was added drop wise whilst stirring to 3 mL ammonium hydroxide in 22 mL ethanol. These volumes were altered in subsequent experiments based on a Taguchi orthogonal design, as detailed in Table 3 - 1. Experiments were performed at room temperature using stirrer plates, or at reduced temperature (5, 10 or 15 °C) on a Thermo Scientific MaxQ4000 refrigerated shaking incubator shaking at 250 rpm. The resulting particles were collected by centrifugation at 4000 rpm, washed three times in ethanol then dried at 70 °C to constant weight in an air oven. All synthesis was carried out in triplicate, with the resulting replicates combined prior to further analysis.

Table 3 - 1 Conditions used for synthesis of ammonium hydroxide particles (A-D indicates experiment set used during initial experiments, 1-12 were obtained during a Taguchi design of experiments, and DOE1-4 were developed to further refine average particle sizes following the results of the Taguchi design of experiments).

Experimental set	Ammonium hydroxide / mL	Temperature / °C	Time / hours
A	3	20	1
B	7	20	1
C	10	20	1
D	7	5	1
1	12	20	1
2	10	20	2
3	8	20	1
4	4	20	2
5	12	15	1
6	10	15	2
7	8	15	1
8	4	15	2
9	12	5	1
10	10	5	2
11	8	5	1
12	4	5	2
DOE 1	8	5	0.5
DOE 2	7	5	1
DOE 3	9	5	1
DOE 4	8	10	1

3.2.2.b Acid hydrolysed particle synthesis

Acid hydrolysed particles were synthesized according to the method described by Karmaker et al (2000). Distilled water (50 mL) was adjusted to a pH of 1.35 with 4 M hydrochloric acid and 5 mL of this acid-water mixture was added drop wise to 41.36 mL of TEOS under stirring. This solution was then covered and stirred at 250, 550 or 660 rpm for 30 minutes after the formation of a cloudy solution. The resulting solution was then filtered through a Whatman 0.45 µm cellulose nitrate filter and then washed three times with ethanol and twice with acetone then dried at 70 °C to constant weight in an air oven.

3.2.2.c Core shell particle synthesis

Core-shell particles were produced using a method adapted from Gai et al (2010). Core particles (0.1g) were placed in 60 mL of ethanol and stirred for 30 minutes, after which 1.2 mL of ammonium hydroxide in 80 mL of distilled water was added. The resulting solution was then stirred for a further 30 minutes. TEOS (1.3 mL) was then added drop wise, then left overnight under stirring. The resulting solution was then filtered through a Whatman 0.45 µm cellulose nitrate filter and washed three times with ethanol and three times with water then dried at 70 °C to constant weight in an air oven.

3.2.2.d Lanthanide doped particles

Particles doped with lanthanide complexes were synthesized in the same manner as undoped particles (see section 3.2.2.*a* and 3.2.2.*b*), with the addition of the lanthanide chloride and chelates prior to the addition of TEOS. For example, terbium doped particles at a molar ratio of 0.5% Tb:Si were synthesised by the addition of $TbCl_3.6H_2O$ (0.0113 g, 1 mmol), TTA (0.0199 g, 3 mmol) and 2PO (0.0032 g, 1 mmol) directly to the reaction mixtures prior to the addition of TEOS, and mixed until completely dissolved. Experiments were performed at 5 °C on a Thermo Scientific MaxQ4000 refrigerated shaking incubator shaking at 250 rpm. The resulting particles were collected by centrifugation at 4000 rpm, washed three times in ethanol then dried at 70 °C to constant weight in an air oven. All synthesis was carried out in triplicate, with the resulting replicates combined prior to further analysis.

3.2.3 Methods for analysis of synthesised particles

A number of spectroscopic and microscopic methods were used to analyse the synthesised particles. This allowed particle size, shape, luminescence properties and surface groups to be analysed.

3.2.3.a Analysis of particle size and morphology

Particle size and morphology for the ammonium hydroxide particles (and core-shell particles synthesized with ammonium hydroxide cores) were determined using an SEM microscope. Images were obtained with either a Carl Zeiss Sigma VP or a Carl Zeiss EVO-LS10 using the secondary electron detector. The beam current was set to 1 kV for the Sigma VP with a working distance of 2.9 mm, at a magnification of 100 thousand times using extended pressure. For the EVO-LS10 the beam current was set to 5 kV, with the working distance and magnification varied as appropriate to the sample. Samples were prepared in acetone prior to spotting onto carbon discs, then air dried prior to analysis. Particle diameter measurements were obtained from the acquired electron micrographs using ImageJ, for at least 100 discrete particles from each sample.

Particle size analysis of particles based on acid hydrolysed synthesis was performed on a Malvern Instruments MastersizerE using a microcell and 300 mm lens. Particle morphology was analysed using light and SEM microscopy. Light microscopy images were obtained using a Meji inverted microscope, using either bright field illumination or a mercury lamp and 350 nm excitation and 590 nm emission filters for fluorescence images of doped particles. SEM microscopy was performed on a Carl Zeiss EVO-LS10 using extended pressure and the secondary electron detector. The accelerating voltage was set to 20 kV, and the working distance at 8 mm.

3.2.3.b Analysis of surface groups and elements

In order to identify the elements present on the surface of the particles, EDXA was performed using a Carl Zeiss EVO-LS10 coupled with an Oxford Instruments INCA at a working distance of 8 mm and an accelerating voltage of 20 kV.

Surface groups were determined by FTIR and Raman spectroscopy were performed for all particles synthesised using the methods found in section 2.2.6 and tables 2-1 and 2-2.

3.2.3.c Fluorescence spectroscopy

Fluorescence spectroscopy was performed on an Edinburgh Instruments FLS920 spectrometer using a Xe900 light source. Samples were mounted in a quartz glass powder sample holder at 45° to the excitation source. Unless otherwise stated excitation spectra were obtained between 250 and 450 nm whilst emission spectra were obtained from 480 to 650 nm for terbium containing samples, and 450 to 700 nm for europium containing samples, using a 395 nm emission filter, over 5 scans, with a dwell time of 0.5 s.

In order to determine the relationship between fluorescence intensity and the concentration of lanthanide complex added, samples were prepared in KBr discs to maintain a constant concentration of particles between analyses. Particles (0.0004 g) were mixed with 0.1 g of KBr and pressed into a disc using a Specac KBr press. Samples were mounted at 45° in a quartz glass powder cell within the spectrometer and spectra obtained between settings for fluorescence intensity measurements

Fluorescence lifetime determinations were performed as detailed in section 2.2.5.

3.2.3.d Determination of doping efficiency

The doping efficiency for the particles was determined using ICP-OES following a lithium metaborate flux procedure to mobilise the lanthanide ions. Particles (0.0125 g) were mixed with 2.5 g of a lithium metaborate flux in a platinum crucible. This crucible was then heated to 1,200 °C in a Carbolite RHF 1600 furnace, for 20 minutes. The crucibles were then removed from the furnace, swirled gently to mix and returned to the furnace for a further 5 minutes. After which, samples were removed and quenched over ice until cool. The flux mixture was then dissolved in 2 % nitric acid and accurately made up to 100 mL with deionised water, prior to storage at 4 °C until analysis could be completed.

The concentration of lanthanide in the sample was determined using a PerkinElmer Optima 3600 ICP-OES. Europium emission was measured at 381.967 nm, and terbium at 350.917 nm, in a 2 % nitric acid matrix. The concentration of the lanthanide in the sample was then converted to the amount of lanthanide present in the initial 0.1 g of core particles used during the synthesis to allow calculation of per cent doping efficiency for each particle, using equation 3.1.

$$Doping\ efficiency\ (\%) = \frac{Concentration\ of\ lanthanide\ in\ particles}{Concentration\ of\ lanthanide\ in\ reaction\ mixture}\ x\ 100$$

Equation 3.1

3.3 Results and discussion

Three different approaches were used to produce silica particles doped with the lanthanide complexes within the desired soil fraction size ranges of fine silt (63 – 250 µm) and colloidal clay (< 1.2 µm).

3.3.1 Synthesis of silica sol-gel particles in the colloidal clay size range (<1.2 µm)

A series of experiments were performed in order to obtain a particle of appropriately 1 µm to simulate the soil colloidal clay fraction. Initial experiments were based upon a series of experiments that analysed the effect of ammonium hydroxide concentration of particle size reported by Rossi et al (2006), and indicated that particle size increased with increased ammonium hydroxide concentration and reduced temperature (Table 3-1 experiments A-D, figures 3-1 and 3-2). (Tables containing particle size data for all particles synthesised can be found in appendix I.) This is in agreement with the data reported by Rossi et al (2006), in which similar particle sizes were obtained at room temperature. The only exception to this was synthesis conditions B, which resulted in the formation of irregular shaped particles. These particles were small in size (between 88 and 150 nm), formed aggregates and resembled fractal particles isolated during the initial stages of particle formation, and could indicate that the sol-gel reaction occurred slowly, or was incomplete under these conditions. In order to determine if the particles were incompletely formed due to a slow reaction speed it would be necessary to repeat the synthesis over longer time periods.

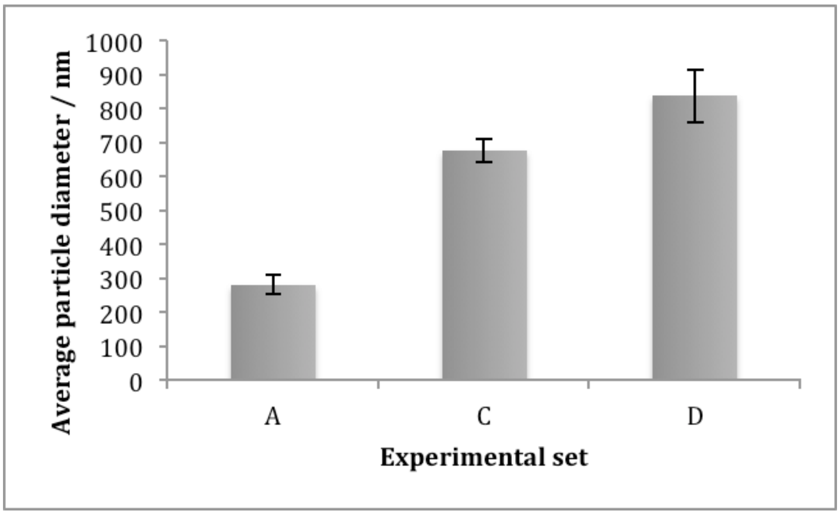

Figure 3-1 Particle sizes obtained during initial experiments into factors affecting ammonium hydroxide catalysed silica sol-gel particle synthesis (error bars indicate standard deviation of average particle sizes measured).

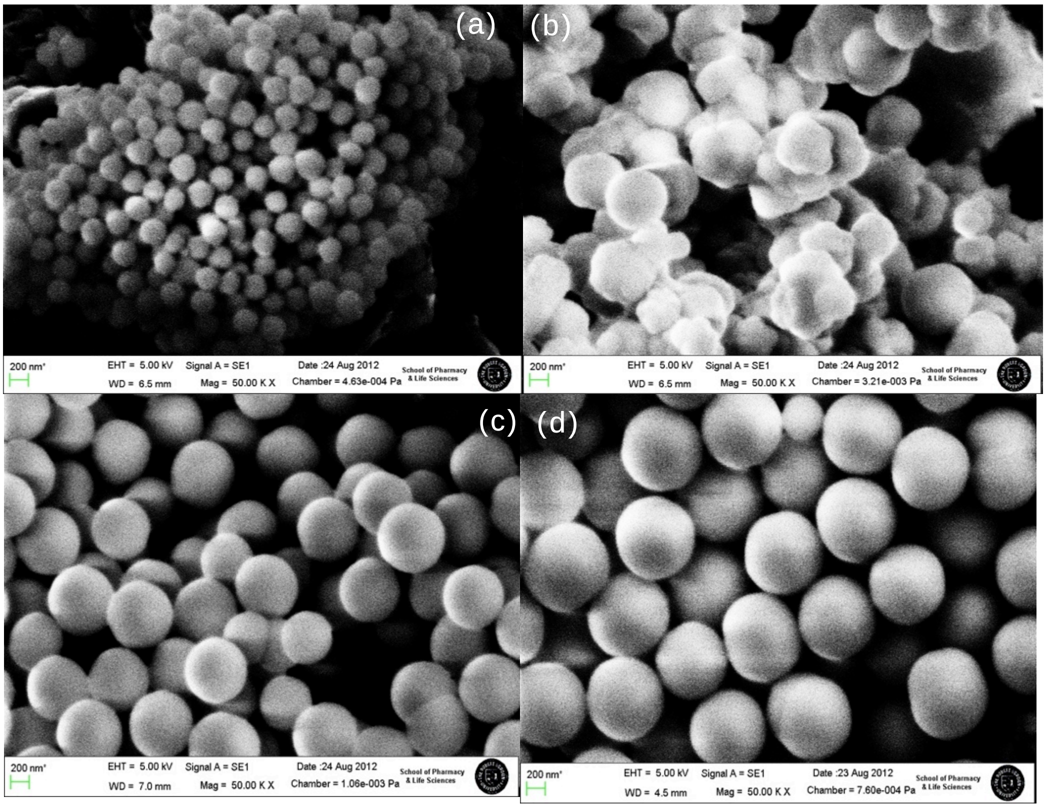

Figure 3-2 SEM images of particles (a) experimental set A (3 mL ammonium hydroxide, 20 °C), (b) experimental set B (7 mL ammonium hydroxide, 20 °C) (c) experimental set C (10 mL ammonium hydroxide, 20 °C) and (d) experimental set D (7 mL ammonium hydroxide, 5 °C). All reactions were run for 1 hour.

Based on the data obtained during the initial experiments a Taguchi factorial design of experiments was performed to further explore the effect of temperature and ammonium hydroxide volume. This allowed the conditions resulting in synthesis of particles close to the 1 μm to be identified. Length of synthesis was also included as an additional factor, to allow the optimum synthesis time to be determined. The factorial design generated 12 different experimental sets, numbered 1-12 in table 3-1, covering a range of ammonium hydroxide volumes (4, 8, 10 and 12 mL), temperatures (5, 15 and 20 °C) and durations (1 and 2 hours). The particles obtained were all spherical and monodisperse, with the average particle diameter varying from 358 to 837 nm as can be seen in figures 3-3 and 3-4. Analysis of variance (ANOVA) analysis (one-way, without replication) indicated that the difference in particle size between these experiments was highly significant ($p < 0.001$). In order to determine which factor had the greatest impact on particle size; principal component analysis of the factorial design was undertaken and found ammonium hydroxide was the most important factor controlling particle size, as can been seen in the mean effects plot (see figure 3-5) with temperature contributing to almost as great a degree. It was also clear that a volume of ammonium hydroxide between 7 and 9 mL increased particle size under these conditions, with the particle size decreasing rapidly at lower volumes and more steadily at higher volumes. This was likely due to the speed at which the reaction takes place. In the presence of little catalyst the reaction occurs slowly, and is more likely to form many small nuclei than add to already formed ones (Brinker & Scherer 1990; Gutsche et al. 2015; Costa et al. 2003). Whilst at high concentrations the rate of reaction will be high, with nucleus addition occurring before the fractals coalesce (Green, Jayasundara, et al. 2003; Green, Lin, et al. 2003). Whilst the data obtained from this series of experiments confirmed the importance of ammonium hydroxide in particle formation, it is important to note that the concentration of ethanol did not remain constant throughout these experiments, demonstrating that under these synthesis conditions the ratio of ethanol:ammonium hydroxide was the critical relationship governing particle size. Thus when the volume of ammonium hydroxide used was increased, for example from 3 to 7 mL, the volume of ethanol decreased from 25.7 to 21.7 mL and the particle size increased. This demonstrates what has been hypothesized previously in the literature about the link between ammonium hydroxide and ethanol connections (Rossi et al. 2005; Stöber et al. 1968; Hench & West 1990; Shimura & Ogawa 2007; Lindberg et al. 1997). The temperature of the synthesis mixture will affect the rate at which the hydrolysis and condensation reactions occur, as well as the likelihood of nuclei coalescing. When these reactions occur rapidly, smaller particles are formed as the addition of silica onto the initial fractal particles occurs quickly, before the fractals can combine (Hench & West 1990). From the mean effects plot for temperature (as shown in figure 3-5), it was apparent that a lower synthesis temperature increased the particle size. The reaction time affects the particle size and morphology due to the rate at which particle formation occurs. If the reaction rate is very slow, then long periods of time are needed for the formation of particles to reach completion (Brinker & Scherer 1990). As such, the time required for the particles to reach the desired size must be considered. Data obtained from the different experimental sets indicated that synthesis of particles of an appropriate size could be achieved within a 1-hour time frame (figures 3-4 and 3-5).

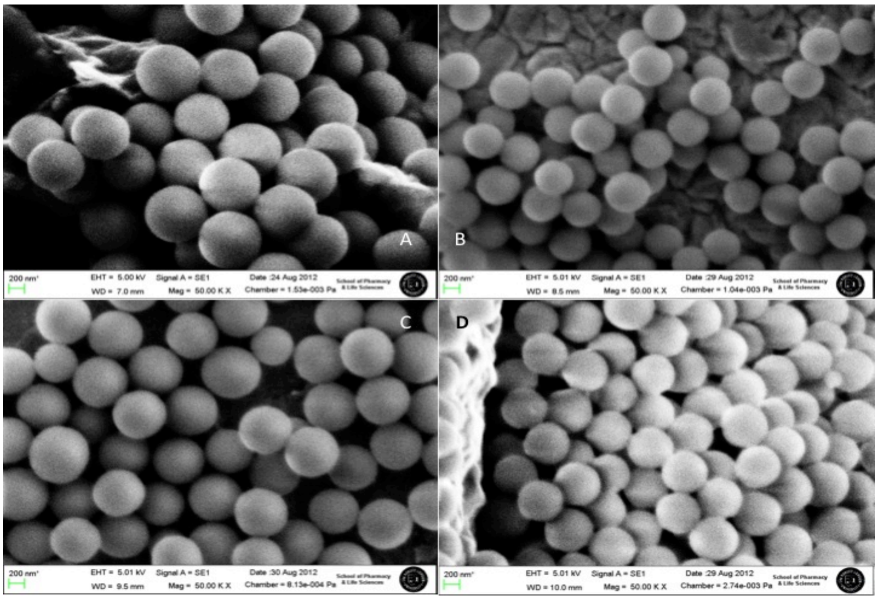

Figure 3-3 Example SEM images of particles obtained during Taguchi design of experiments (a) experimental set 2 (10 mL ammonium hydroxide, 20 °C, 1 hour), (b) experimental set 5 (12 mL ammonium hydroxide, 5 °C, 1 hour), (c) experimental set 9 (12 mL ammonium hydroxide, 20°C, 1 hour), (d) experimental set 12 (4 mL ammonium

hydroxide, 5°C , 2 hours).

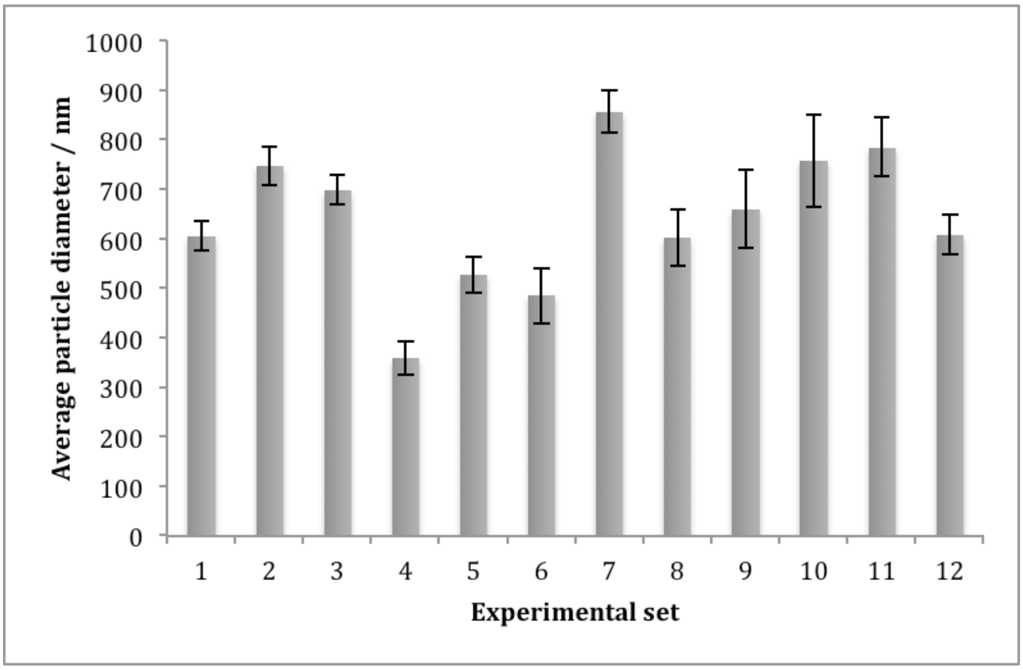

Figure 3-4 Average diameter of particles obtained during Taguchi factorial design (error bars indicate standard deviation of average particle sizes measured).

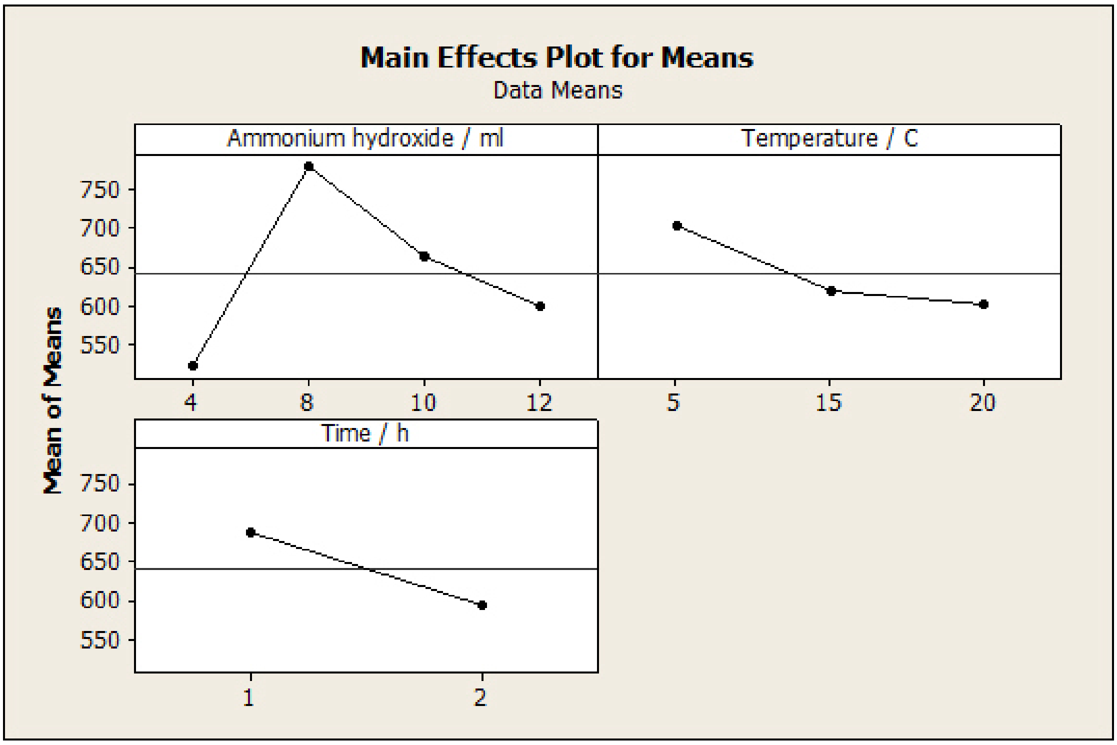

Figure 3-5 Main effect plot for means generated during Taguchi design of experiments and test of the design (Samples 1-12 and DOE 1-4).

Having identified the levels of each factor that increased the average particle size (volume of ammonium hydroxide and temperature), a final set of experiments was performed (Table 3-1 DOE 1-4) to increase the particle size closer to 1 µm and test the Taguchi design. This resulted in the formation of a 950 nm particle; ideal for use as a soil colloidal clay tracer as its size closely approximates the size of the particles in the colloidal clay fraction (see figures 3-6 and 3-7). These particles were referred to as the colloidal clay sized particles in all further experiments.

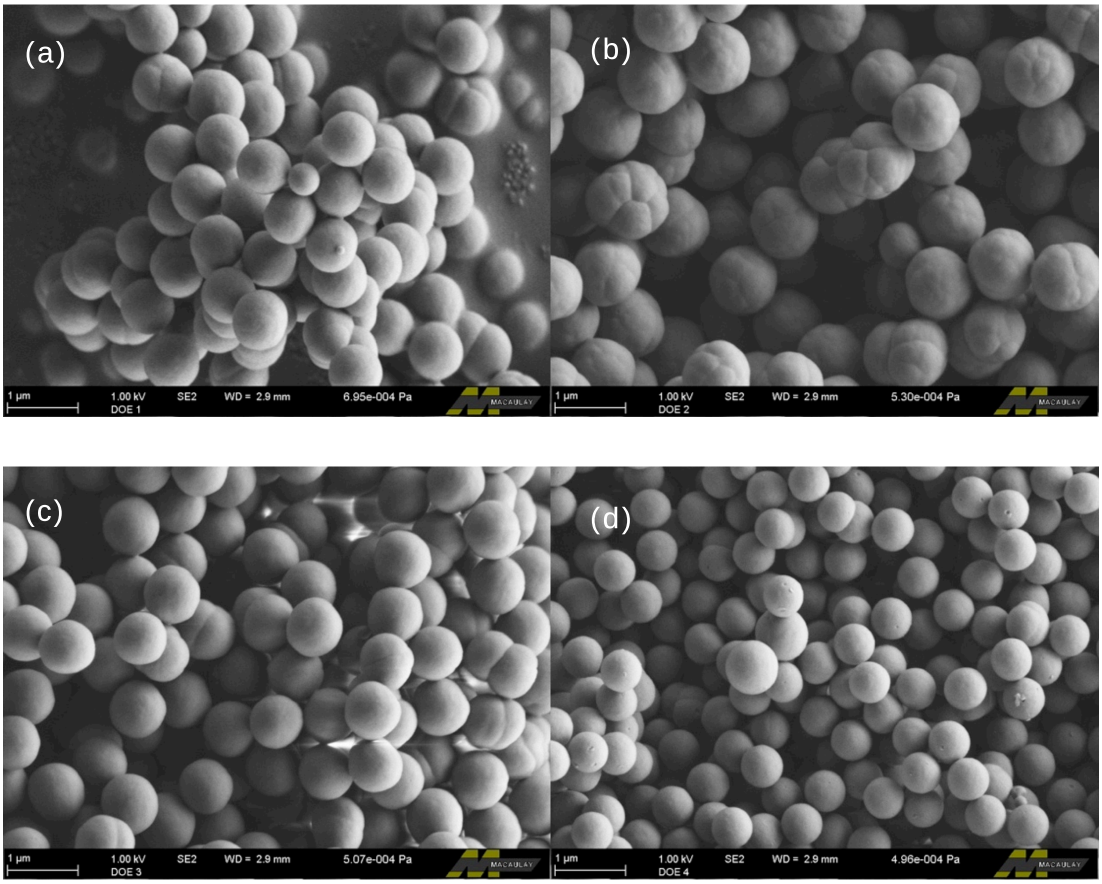

Figure 3-6 SEM images of particles obtained during test of Taguchi design (a) DOE1, (b) DOE2, (c) DOE3, (d) DOE4.

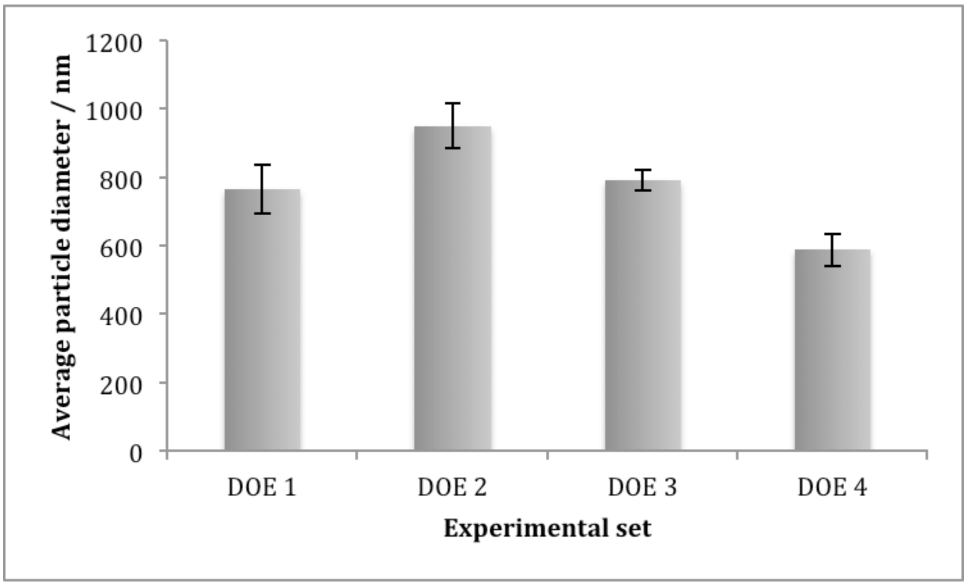

Figure 3-7 Average diameters of particles obtained during test of Taguchi design (error bars indicate standard deviation of average particle sizes measured).

3.3.2 Synthesis of particles within the fine silt size range (63-250 µm)

Particles within the fine silt range were synthesized using hydrochloric acid as a catalyst. Karmaker *et al* (2000) reported a method for the synthesis of particles up to 60 µm in diameter when synthesised at stirring speeds of 250 rpm. Repetition of this method stirred at 250 rpm on a magnetic stirrer yielded particles with an average diameter of 166 µm across three replicates (see figures 3-8 and 3-9). This allowed the affect of stirring speed on average particle diameter to be analysed at 250, 550 and 660 rpm, and the synthesis conditions that resulted in particles of approximately 150 µm to be identified. Such particles would be roughly equivalent to the median soil particle size within the fine silt range and as such would be appropriate to use as a soil tracer.

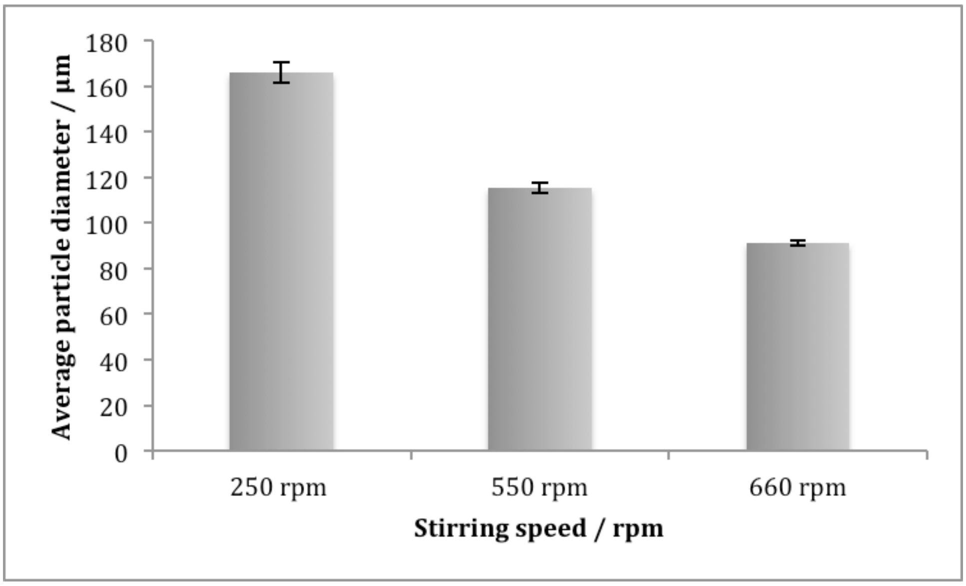

Figure 3-8 Average diameter of particles synthesised at different striring speeds using a hydrochloric acid hyrdolysed method (error bars indicate standard deviation of average particle sizes measured).

Upon examination of the reaction mixture it became apparent that two layers were formed, an acidified lower layer with a pH of approximately 4, and an upper layer with a pH of 6, closer to that of TEOS. Karmaker *et al* (2000) hypothesised that the acidified layer contained a partially hydrolysed hydrated TEOS layer from which the silica sol-gel particles formed. This was supported by observations made during this study, where the particles were all found within this layer. It was also hypothesised that the synthesised particles ripen and condense within the upper layer of the reaction mixture (Karmakar et al. 2000). This hypothesis would explain the difference in particle sizes between the two studies, as the previous study used a shaking platform to agitate the reactions, whilst a magnetic stirrer was used during this study. The centrifugal force of the magnetic stirrer would most likely cause droplets at the top of the sol to detach and enter the upper layer to ripen and form particles. Shaking is more likely to mix the upper and lower layers together at their boundary, resulting in small sections of the lower sol entering the upper layer to ripen. If this was indeed the case, then altering the speed at which the mixture was stirred should alter the particle size. In order to test this hypothesis the stirrer was set to two additional stirring speeds (550 rpm and 660 rpm) on a six point magnetic stirrer controlled from a single controller to ensure each stirrer was set to the same rotational speed. As predicted, increased speed reduced the particle size, as smaller but more numerous droplets of the hydrolysed sol entered the upper layer to ripen (see figures 3-8 and 3-9). At 550 rpm a particle with low standard deviation and more consistent particle size (115.25 ± 2.11μm) within the fine silt range was produced. This stirring speed was therefore used during all other acid hydrolysed synthesis reactions. The 115 μm particles synthesised (550 rpm) were referred to as the fine silt sized particles in all further experiments.

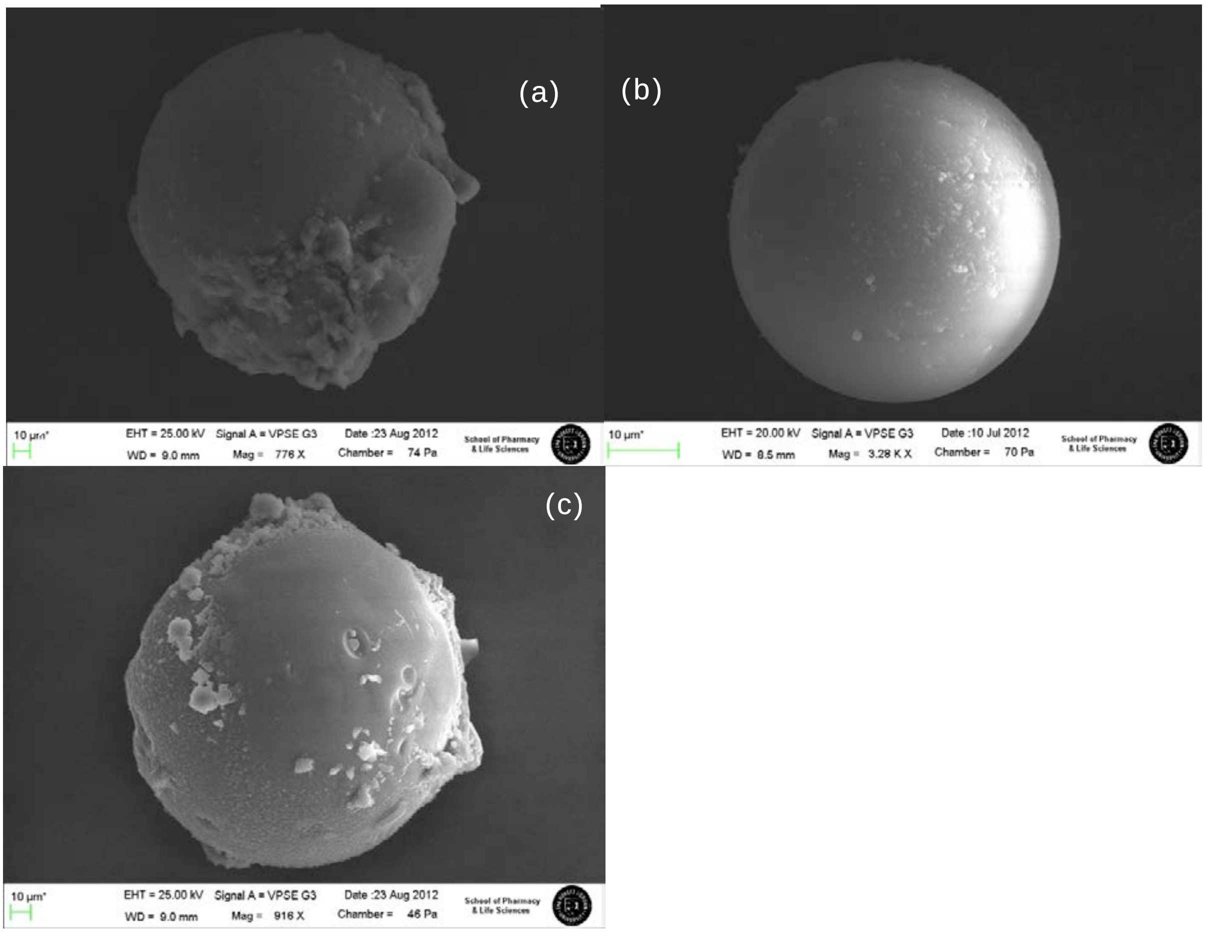

Figure 3-9 Scanning electron micrographs of acid hydrolysed particles synthesised at (a) 250 rpm, (b) 550 rpm and (c) 660 rpm.

3.4 Synthesis of lanthanide doped particles

In order to incorporate the lanthanide complexes synthesised in chapter 2 into these silica particles, two different approaches were used.

3.4.1 Direct doping of lanthanide complex into particles

Initial lanthanide doped particles were synthesized by doping the lanthanide complexes directly into the reaction mixture of the particles, at a concentration ratio of 0.06% Ln^3:Si (as detailed in section 3.2.2.*d*). It was found for both the ammonium hydroxide and acid hydrolysed particles that the addition of lanthanide complexes during synthesis resulted in the loss of the spherical, monodisperse morphology characteristic of particles synthesized by the method. Round particles could be seen embedded in an amorphous mass of silica, for clay sized particles, reflecting more the fractal particles found during the early stages of particle formation. For the fine silt particles, monodiperse particles were obtained, but the morphology became irregular upon the addition of even low concentrations of the lanthanide complexes (0.06% Ln:Si). This phenomenon has been noted before in previous studies, and appears to be the result of the interaction of the lanthanide with the silica matrix (Moran et al. 2001; Lu & Yan 2008; Attia et al. 2012). Energy dispersive x-ray analysis indicates that the concentration of lanthanide was higher within the amorphous region, reinforcing the likelihood that it was the interaction between the metal ion and the silica matrix that disrupts particle formation. Due to the wide variety of particle sizes, and morphology it was decided that a more uniform particle, which could be simply modelled, and all of which would interact and move at similar rates and ways, would be more effective as a soil erosion tracer. Therefore an alternative method based on the principle of core-shell particles was adopted.

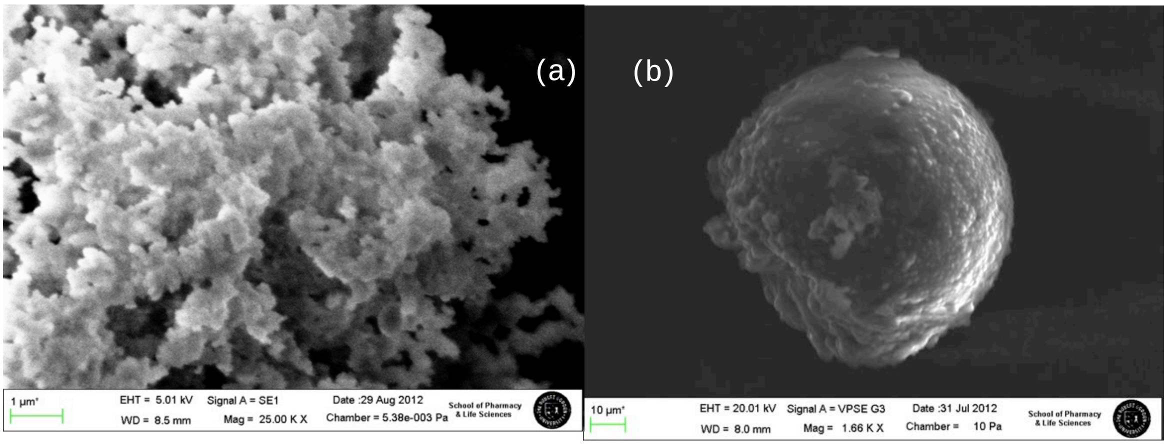

Figure 3-10 Scanning electron micrographs of (a) ammonium hydroxide catalysed particles doped with 0.06 % Tb(TTA)$_3$2PO:Si and (b) acid hydrolysed particles doped with 0.6 % Eu(TTA)$_3$2PO:Si

3.4.2 Formation of lanthanide doped core-shell particles

Core-shell particles are formed when an initial particle with desirable properties is coated with a shell, which can be used to add additional properties onto the surface of the particle. Core-shell particles were synthesized for two reasons. Firstly, it was hoped that the incorporation of the lanthanide complex into a silica shell surrounding a core of desired morphology would allow spherical monodisperse particles to be synthesized in the presence of the lanthanide at higher concentrations and without the changes in morphology seen when doped directly into the particles. Secondly, the localisation of the lanthanide complex within a shell on the surface of the particles had the potential to reduce the length of time the tracer luminesce can be detected as mechanical, microbial and chemical degradation of the organic ligands should happen quicker at the surface of the particles. This would allow analysis of the same sites in subsequent years without interference from previously deployed tracers.

Core-shell particles were made using both the acid hydrolysed fine silt and ammonium hydroxide hydrolysed colloidal clay sized particles. The method for the addition of the silica shell was identical for both particle sizes, and involved a second sol-gel reaction using the previously synthesised core particles as precursors. SEM images indicated that the shell was successfully incorporated onto both particle size ranges, however, although the shell appeared complete on the colloidal clay sized particles, it appeared to form patches on the fine silt sized ones. As such, it was possible to estimate the thickness of the shell, which appeared to be less than 5 nm. Thus the addition of the shell did not significantly affect the overall particle size when compared to that of the core particles (0.5 % increase in particle size for colloidal clay tracer and 0.004 % for fine silt particles).

In addition to the acid hydrolysed fine silt particles, core-shell particles using a commercially available precursor (obtained from British Optical Limited) within a similar size range (100 µm) were synthesised. This precursor is inexpensive with a relatively narrow particle size and is borosilicate based. Core-shell particles synthesised using this precursor had a similar morphology to those based on acid hydrolysed particles, although the shell appeared to be slightly more complete (see figure 3-12).

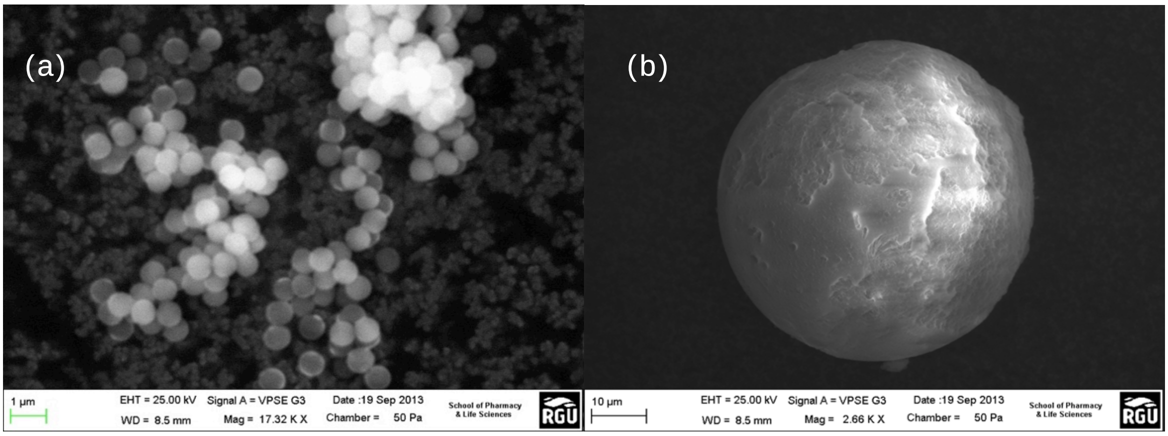

Figure 3-11 Scanning electron micrographs of core-shell particles synthesised using (a) ammonium hydroxide hydrolysed core particles, shell doped with 1.5% Tb^{3+} $TTFA_3.2PO:Si$ and (b) acid hydrolysed core particles, shell doped with 1.5% Eu^{3+} $TTFA_3.2PO:Si$

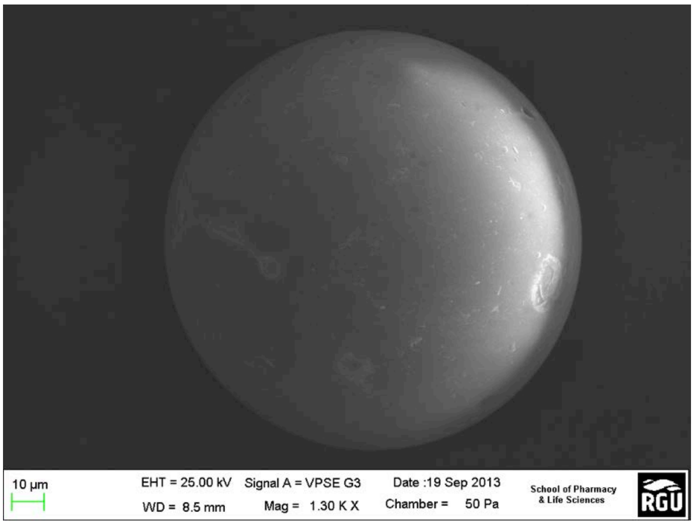

Figure 3-12 Scanning electron micrographs of core-shell particles synthesised using commercially available silica beads, with a shell doped with 1.5% Eu^{3+} $TTFA_3$.2PO:Si

3.5 Particle characterisation

To allow the successful incorporation of the lanthanide complex to be ascertained, and to determine their luminescent properties of the complexes were retained, a series of particle characterisations were performed.

3.5.1 IR and X-ray analysis of particles

IR analysis of the synthesised particles was performed in order to determine the functional groups present upon the surface of the particles. In addition, as silica is not Raman active (as the vibrations do not involve a change in polarisability), the dopant present within the silica particles could also be analysed using Raman spectroscopy. FTIR analysis of all particles identified the presence of O-Si-O (1100 cm^{-1}) and Si-OH (850 cm^{-1}) groups on the surface of the particles, indicating that the particles were indeed composed of silica (Wang et al. 2010; Karmakar et al. 2000) (see figure 3-13). Additionally, on some of the acid hydrolysed particles it was possible to identify some CH_2H_5 groups (1250 cm^{-1}) (Karmakar et al. 2000) which indicated that under these reaction conditions at least, not all of the TEOS precursor was completely hydrolysed, and so ethyl groups remained on the surface of the particles.

Particles doped with the TTA_3.2PO complexes displayed many of the functional groups present within the complex. FTIR analysis identified the presence of C=O groups from TTA on the particle surface. Raman spectroscopy identified the presence of CF_3 (1110 cm^{-1}) from TTA in addition to the substituted pyridine ring and CH_2-N (1454 cm^{-1}) bonds present within the 2PO complex (see figure 3-14).

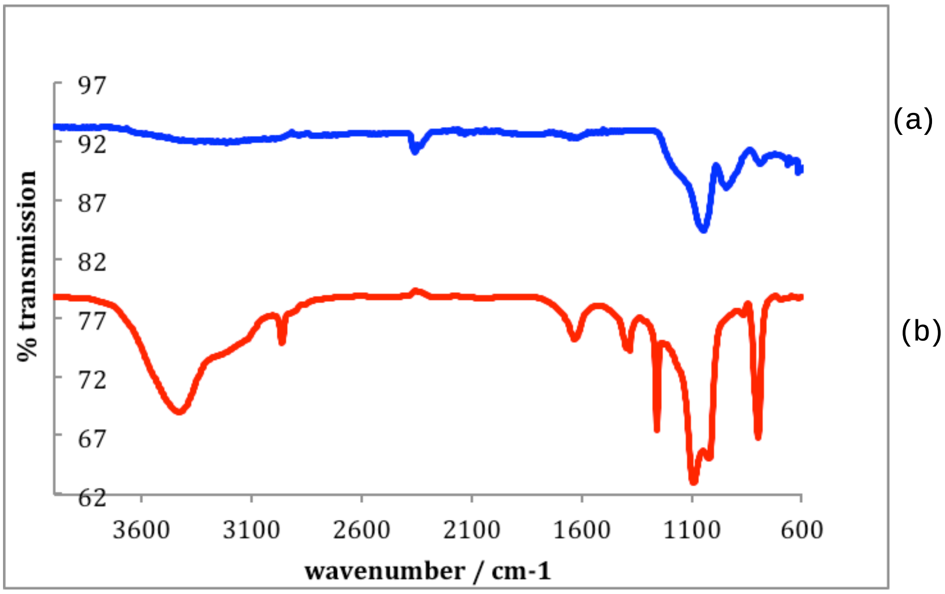

Figure 3-13 FTIR spectra of synthesised particles (a) blank particle synthesised using ammonium hydroxide (experimental set 9) (b) core-shell acid hydrolysed particle doped with $Eu(TTA)_3$2PO.

This confirms the presence of the complex within the doped particles, and indicates that it was present on the surface of the particles. This potentially has implications for the binding of the tracer to soil, as the functional groups present on the complex could interact with the functional groups present within the soil, in addition to the interaction of the silica which forms the particles. Raman spectra of the blank particles show weak peaks around 918, 795 and 460 nm, which are indicative of Si-O-Si transitions and identify the presence of silica. As the functional groups contained within the lanthanide complexes were not present within the precursors these peaks confirm the presence of the lanthanide complex on the surface of the particles.

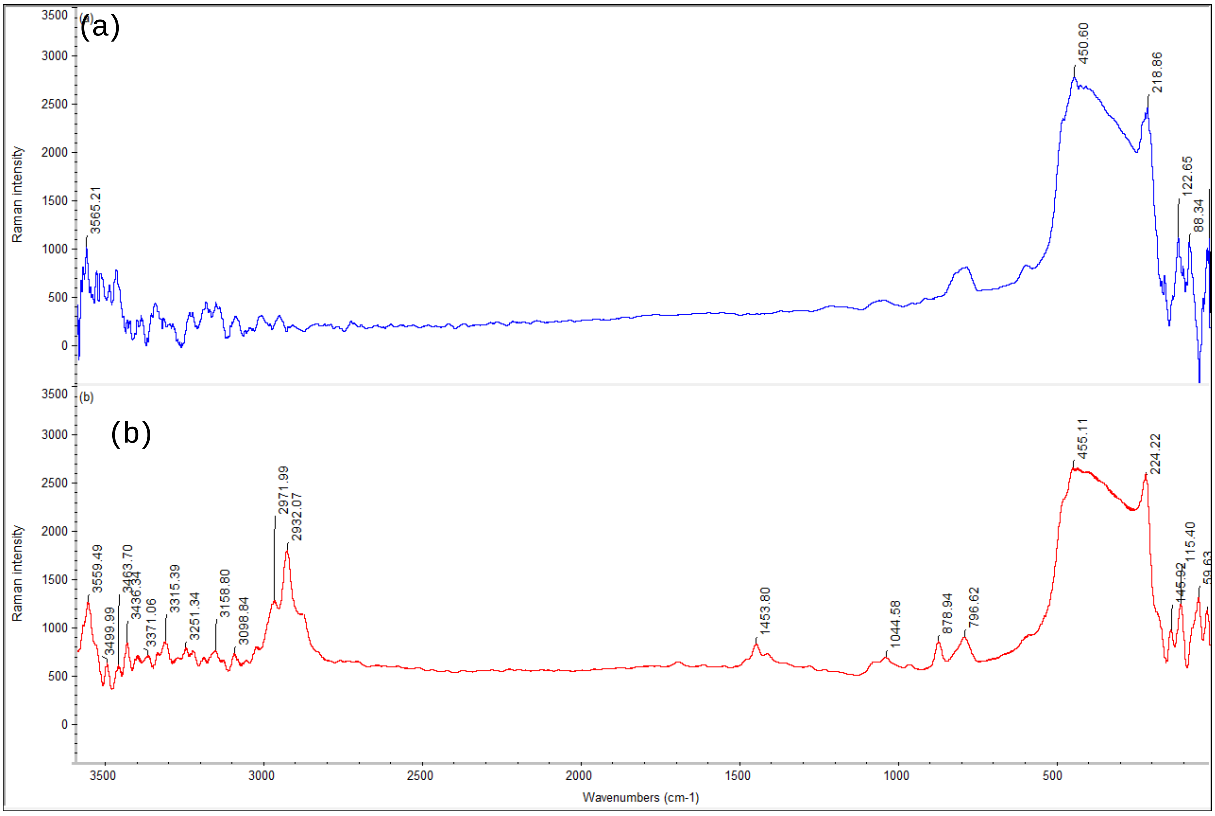

Figure 3-14 Raman spectra of synthesised particles (a) blank particle synthesised using ammonium hydroxide (experimental set 9) (b) core-shell acid hydrolysed particle doped with Eu(TTA)$_3$2PO.

EDXA allows the identification of elements present on the surface of an object, generally in association with SEM. EDXA was performed for both core-shell particles to determine if the lanthanides were present on the surface of the particles. Terbium could be seen on the surface of the clay tracer particles (see figure 3-15) and europium in the shell of the fine silt particles. For the fine silt sized particles, no metal was detected when the exposed core was analysed, indicating that the complex is confined to the shell of the particle as predicted. EDXA also identified the presence of fluorine and sulphur within the shell, which would indicate the presence of the ligands within the shell. EDXA spectra for the commercial core based particle can be found in appendix I, and also identify the presence of europium on the particle surface.

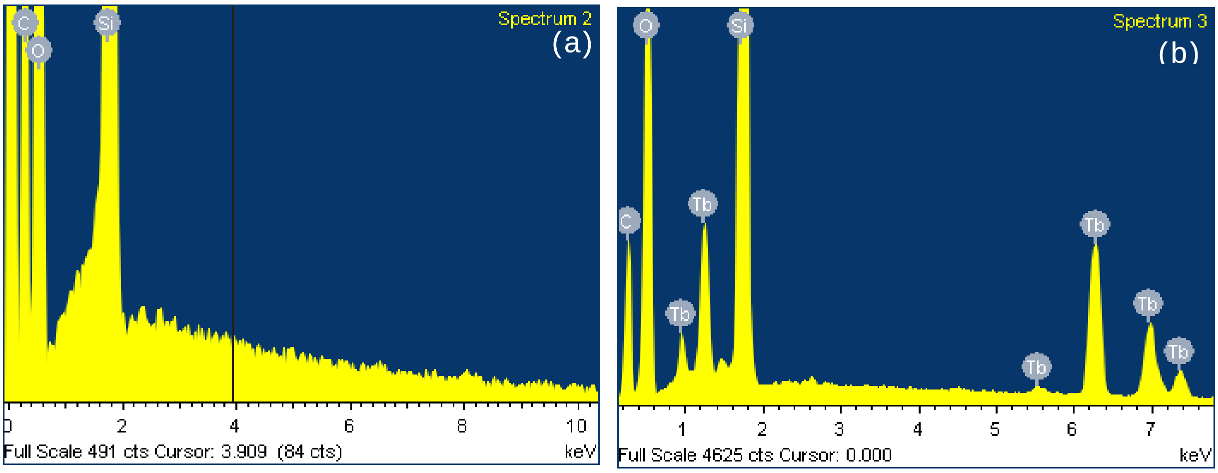

Figure 3-15 EDXA spectra for core-shell particles (a) ammonium hydroxide hydrolysed core particles and (b) ammonium hydroxide hydrolysed core particles, shell doped with 1.5 % $Tb(TTA)_3 2PO$:Si

The above chemical characterisations of the particles identified the successful incorporation of the lanthanide chelate into the shell with all central core particles whilst maintaining monodisperse particles in a narrow size range. As such the luminescence characteristics of the particles were then analysed to determine if they were suitable for use as a soil based tracer.

3.5.2 Fluorescence microscopy

Fluorescence microscopy of the larger, fine silt particles produced using both the synthesised core (detailed in 3.3.2), and the commercially available core (section 3.4.2), was also performed. It was not possible to adequately resolve the smaller clay tracer particles. Under UV illumination, the core-shell particles can clearly be seen to luminesce red, characteristic of the Eu^{3+} containing complex incorporated into these particles (see figure 3-16). When water was used to mount the tracers this luminescence remained stable, indicating that the complex, normally deactivated by water, was shielded from the environment by the silica shell. This was in agreement with other examples of silica particles found within the literature, which also show a stabilisation of luminescence in the presence of water, generally attributed to stabilisation of the complex, and eradication of coordinated water (Binnemans 2009; Binnemans et al. 2004; Lu & Yan 2008). In order to quantify the luminescence intensity of the two fine silt tracers, along with the clay tracer, which could not be imaged using fluorescence microscopy, the luminescent spectra of the particles were then analysed.

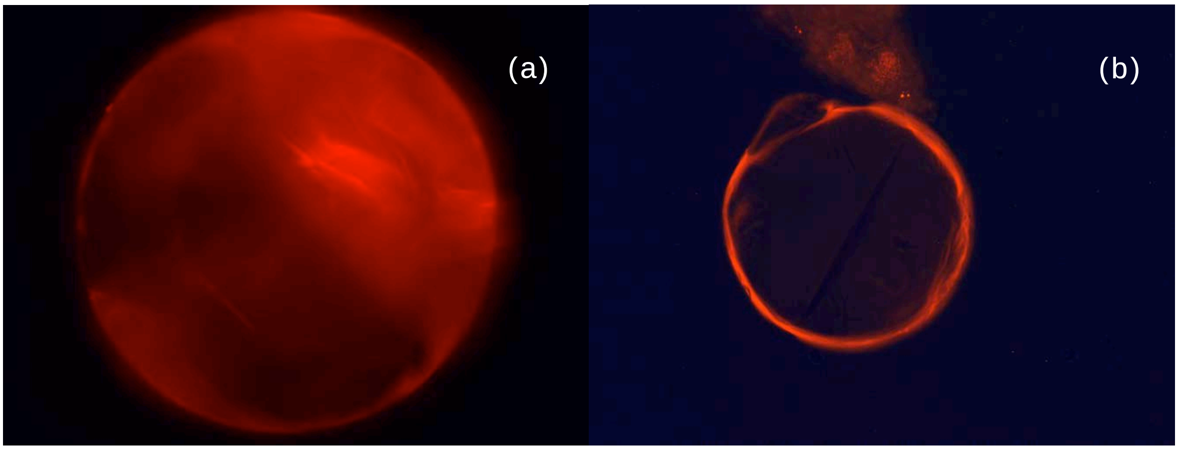

Figure 3-16 Fluorescence micrographs for core-shell particles synthesised using two different silica core particles, with a shell doped with 1.5 % Eu(TTA)$_3$2PO:Si and (a) acid hydrolysed core particles (magnification 100x); or (b) commercially available silica core particles (magnification 40x)

3.5.3 Fluorescence intensity of lanthanide doped particles

Addition of the Eu(TTA)$_3$2PO complex into the silica matrix resulted in a shift of the $^5D_0 \rightarrow {}^7F_2$ emission from 612 to 618 nm (see figure 3-17). This transition is known to be affected by both the coordination sphere of the trivalent europium, and the chemical environment surrounding it (Görller-Walrand & Binnemans 1998; Lechevallier et al. 2013). This was likely due to the interaction of the lanthanide ion with the silica matrix, slightly altering the energy levels of the lanthanide ion and is a phenomenon that has been observed previously (Zhang et al. 1999; Binnemans 2009; Enrichi et al. 2008). The luminescence spectrum obtained for the terbium doped clay tracer remained unchanged from that of the free complex, as the major transition within the spectrum were largely unaffected by the environment of the ion (Görller-Walrand & Binnemans 1998; Aspinall 2001) (see figure 3-17).

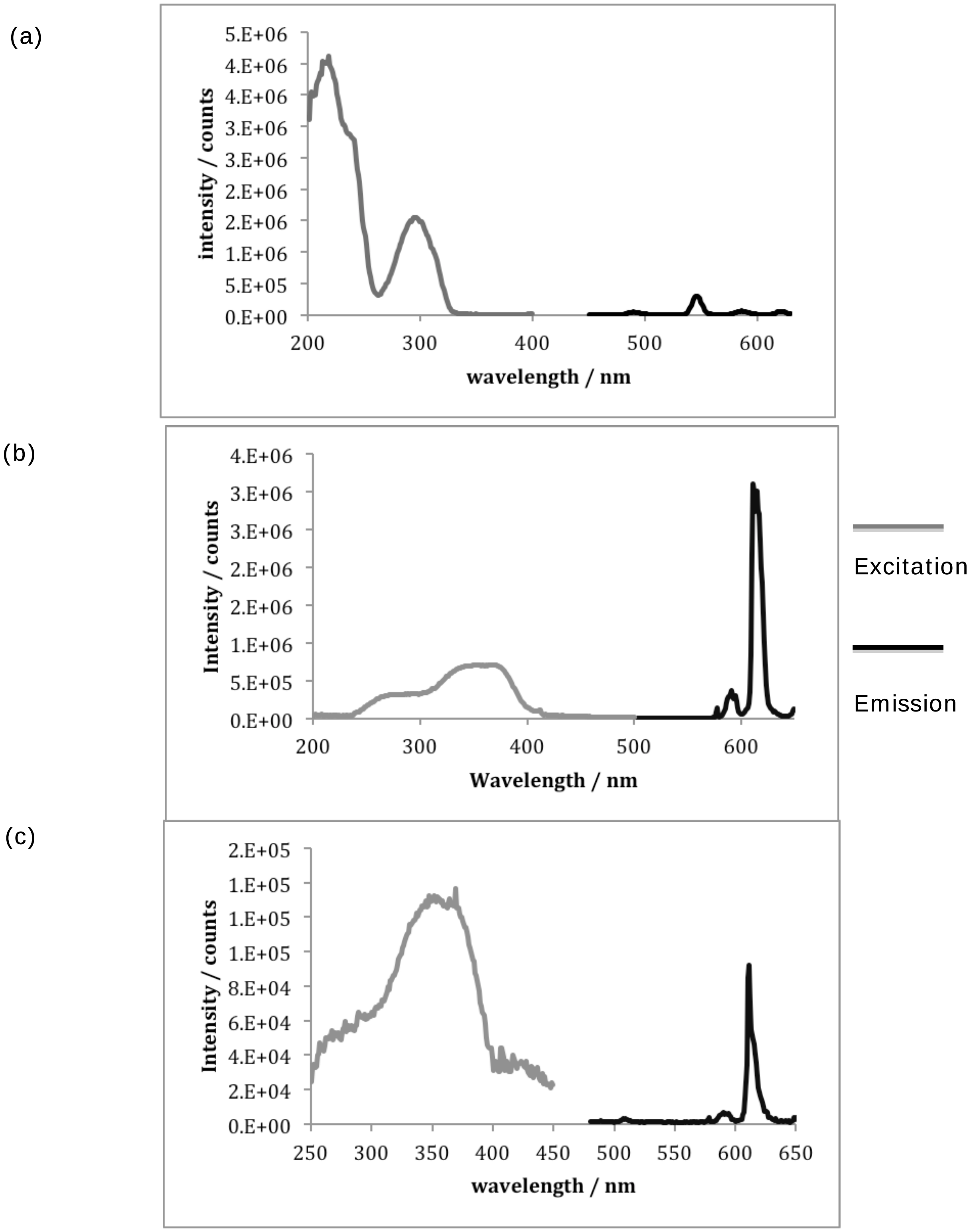

Figure 3-17 Fluorescence excitation and emission spectra for (a) core-shell ammonium hydroxide particles doped with 1.5% Tb(TTA)$_3$2PO:Si, (b) core-shell acid hydrolysed particles doped with 1.5% Eu(TTA)$_3$2PO:Si and (c) core-shell commercially available silica particles doped with 1.5% Eu(TTA)$_3$2PO:Si.

The lifetimes of all synthesised core-shell particles were also determined using surface reflectance spectroscopy (Rendell & Mowthorpe 1987) with the lifetime of the core-shell Eu(TTA)$_3$2PO fine silt particles found to be 732.93 μs (χ^2 = 1.109) using a tail fit analysis. For the same complex using the commercially available core particles the lifetime was found to be 679.91 μs (χ^2 = 1.107), compared with 482.54 (χ^2 = 0.967) for the free complex. The lifetime of lanthanide complexes doped into a silica shell often increases due to the stabilising effect of the matrix, which increases the stability of the excited state, reducing the likelihood of electronic transition to a lower energy state, therefore increasing the luminescent lifetime of the complex. The lifetime of the lanthanide complex within the acid hydrolysed core-shell particles was greater than that for the commercially available silica particles, but for the purposes of a tracer this must be weighed up against the financial and time costs of synthesizing the acid hydrolysed particles. For the core-shell Tb(TTA)$_3$2PO ammonium hydroxide doped particles the luminescent lifetime was 58.97 μs (χ^2 = 1.099) compared with 58.29 (χ^2 = 1.035) for the free complex. The lifetime of the terbium complex was again lower than that of the europium complex, as was seen in the free complex, but also showed a slight increase above that of the complex alone. Again, this is most likely due to the stabilizing effect of the silica matrix, and is expected, as terbium complexes tend to have lower lifetimes than europium containing ones due to the many rapid, non-radiative transitions available (Armelao et al. 2010; Moore et al. 2009).

3.5.4 Lanthanide complex doping efficiency.

The effect of increasing concentration of the lanthanide complex during synthesis was investigated to identify the most appropriate concentration to use for tracer production. The morphology, doping efficiency and luminescent intensity of core-shell particles synthesized at six different concentrations were analysed.

SEM analysis of the morphology of the particles showed that the spherical morphology was maintained until the concentration of Eu^{3+}: Si exceeded 3 %. For the terbium doped particles this occurred at concentration above 2 % Tb^{3+}:Si. Above this, the shell that was added became rough and misshapen (as shown in figures 3-18 and 3-19).

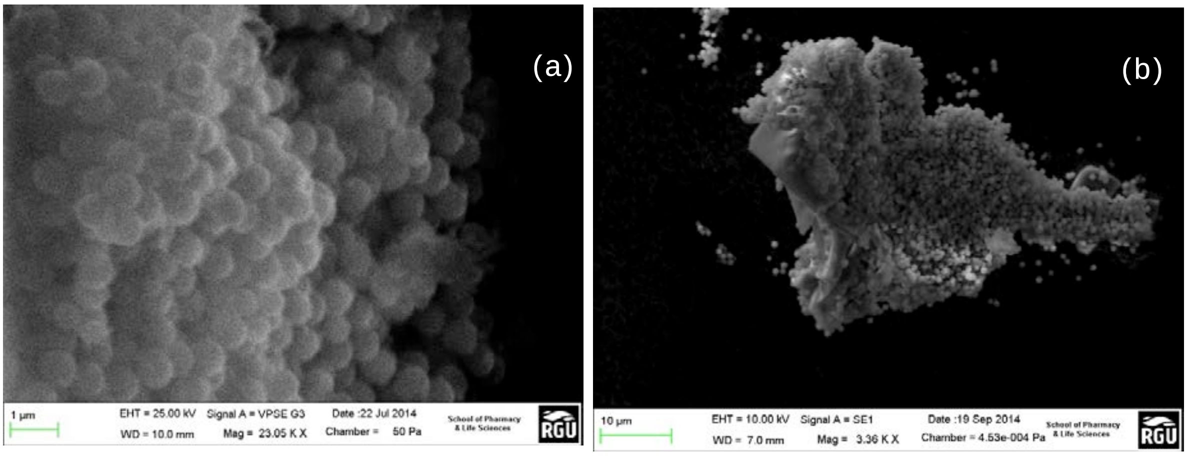

Figure 3-18 Scanning electron micrographs of core-shell particles synthesised using ammonium hydroxide hydrolysed core particles, with shell doped with (a) 0.5 % Tb(TTA)$_3$2PO:Si and (b) 5 % Tb(TTA)$_3$2PO:Si.

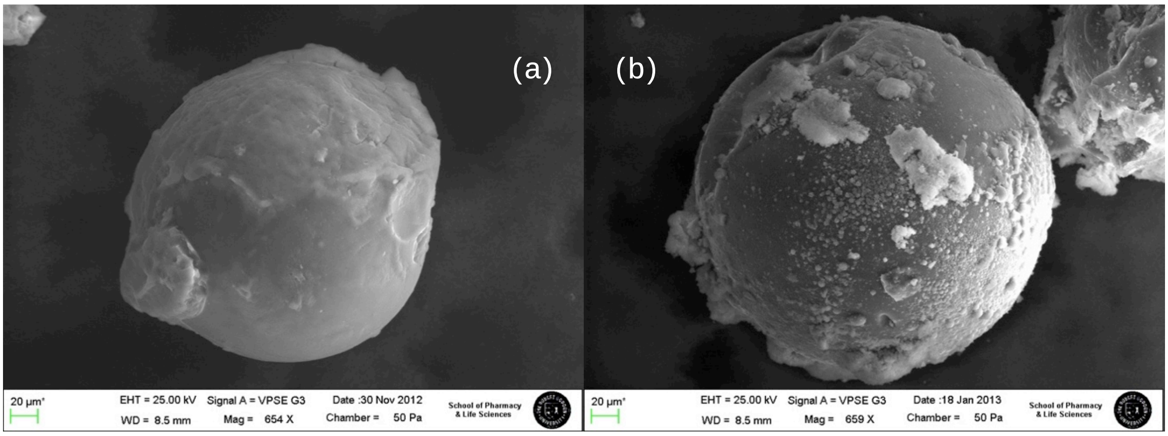

Figure 3-19 Scanning electron micrographs of core-shell particles synthesised using acid hydrolysed core particles, with shell doped with (a) 0.5 % Eu(TTA)$_3$2PO:Si and (b) 5 % Eu(TTA)$_3$2PO:Si.

In order to determine the doping efficiency at each concentration, a lithium metaborate flux was performed to mobilise the metal present within the particles. This analysis was performed in triplicate for each sample, and three samples for each concentration were synthesized, as detailed in section 3.2.3.e. A graph of the doping efficiency can be seen in table 3-2, and demonstrated that doping efficiency showed a gradual increase with europium concentration except at 1.5 % Eu:Si. At this point, a large increase in the doping efficiency was observed. It had been hypothesized in the literature (Jin et al. 2012; Enrichi et al. 2008; Attia et al. 2012), that the formation of insoluble lanthanide hydroxides both limits the doping efficiency and affects the morphology of the particles produced. In order to determine if this was the case for this series of results, the amount of europium hydroxide formed within the reaction mixture was determined. This was performed by creating a reaction mixture for each concentration containing all components except for TEOS, to prevent the formation of new silica, which would sequester the lanthanide from the reaction mixture. After shaking overnight, the resulting mixture was filtered to remove the insoluble hydroxide and a sample taken. The hydroxide was then acidified with hydrochloric acid to mobilise the lanthanide ions trapped within the filter. A further sample was then taken, and all samples were analysed for europium content using ICP-OES. In the acidified samples, all the europium initially added was present, however in the samples taken from the reaction mixture, a significant amount of the metal was removed (as shown in table 3-5). This indicated that the formation of insoluble lanthanide hydroxides reduced the amount of europium available for incorporation into the silica shell. The percentage of the original amount of lanthanide added followed the same pattern as the doping efficiency of the particles. This confirms that the formation of lanthanide hydroxides in base catalysed sol-gel reactions does indeed significantly reduce the amount of available lanthanide, thus reducing the doping efficiency.

The doping variation with each initial lanthanide concentration can be seen in Figure 3-20. There was generally a linear increase in amount of dopant present within the beads with increased concentration of lanthanide added to the reaction mixture. These values were subject to a degree of uncertainty as shown by the relatively large error bars in figure 3-20. This is most likely to due to the nature of the sample preparation process, which has multiple stages, and relied on the subsample being representative of the bulk and then on the complete mobilisation of europium. Due to this complex procedure, it is likely that the percentage recovery of the europium from the particles would vary between individual reactions. This was also the case for luminescent intensity when measured using surface reflectance spectroscopy and diluted in KBr. However, at 1.5 % there was a sharp increase in doping efficiency and luminescent intensity, and was consistent for all three replicates analysed. This trend was also observed in the study of the insoluble hydroxide formation, indicating that at this concentration the formation of lanthanide hydroxides was less favourable than at 1 or 2 %. As using this concentration provided particles with similar levels of luminescence to that of far higher concentrations (e.g. 3 %), it was determined that this concentration would be the most effective for use within the tracers, as it did not affect the morphology of the particles, and gave a high level of luminescence for a limited amount of lanthanide, reducing the cost of tracer production. A similar increase in europium specific luminescence with increased Eu:Si concentration up to 3.5 % in thin films has previously been reported (Lu et al. 2010) A similar, but less defined trend was seen for the $Tb(TTA)_3 2PO$ doped particles (see Figure 3-21). This could be due to the differing pH level for formation of the lanthanide hydroxides, or could be an artefact of the study, as only one set of samples were analysed. It has been shown that the basicity of the lanthanide hydroxides decreases with increasing atomic number, and therefore the terbium ion would form a less basic hydroxide (Aspinall 2001). Additionally thermogravametric data (see section 2.3.5) indicated that the terbium complex was more stable than the europium complex, so it is possible that a greater amount of the terbium is present as a complex than as free terbium, again reducing the effect of the loss of terbium in the reaction mixture as terbium hydroxide. However, a slight, off trend, increase in the fluorescence level at 1.5% Tb:Si concentrations indicates that this concentration ratio is also appropriate for use in the terbium doped colloidal clay tracer particles. There is also a marked increase in the doping efficiency of the particles at 1.5% (see figure 3-6), again indicating that this was the most appropriate concentration to use during tracer particles synthesis.

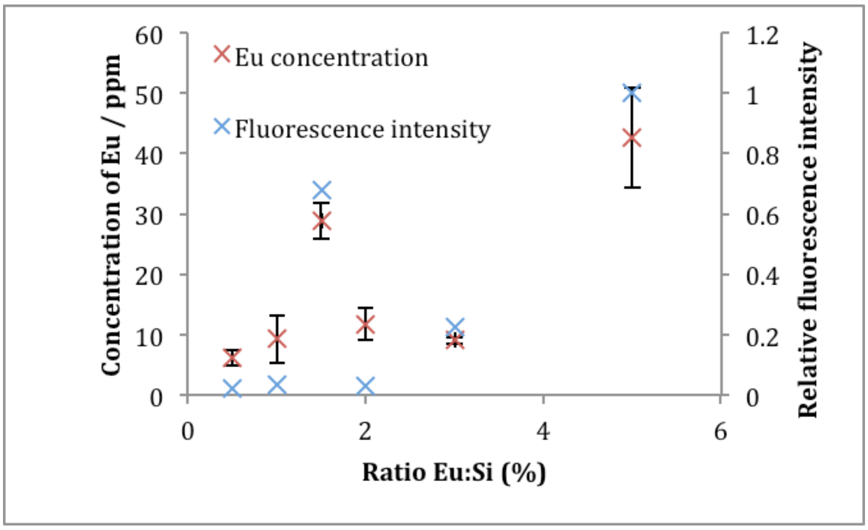

Figure 3-20 Graph showing the effect of increased Eu(TTA)$_3$2PO concentration in core-shell acid hydrolysed particles on fluorescence intensity and the concentration of Eu present within the particles. (Error bars indicate standard deviation between all samples analysed using this process).

Table 3-2 Doping efficiency for Eu(TTA)$_3$2PO in core-shell acid hydrolysed particles

Ratio of Eu:Si / %	Doping efficiency / %
0.5	56.7
1.0	43.6
1.5	89.8
2.0	27.3
3.0	14.0
5.0	39.7

Table 3-3 Concentration of Eu in the ammonium hydroxide reaction mixture used for the synthesis of luminescent shells on tracer particles, and also the total Eu recovered once these samples were acidified to mobilise europium hydroxide.

Ratio of Eu:Si / %	Concentration Eu in reaction mixture (ppm)	Concentration Eu in acidified mixture (ppm)
0.5	0.063	0.001
1.0	0.333	0.003
1.5	1.256	0.014
2.0	0.666	0.005
3.0	0.853	0.017
5.0	1.669	0.037

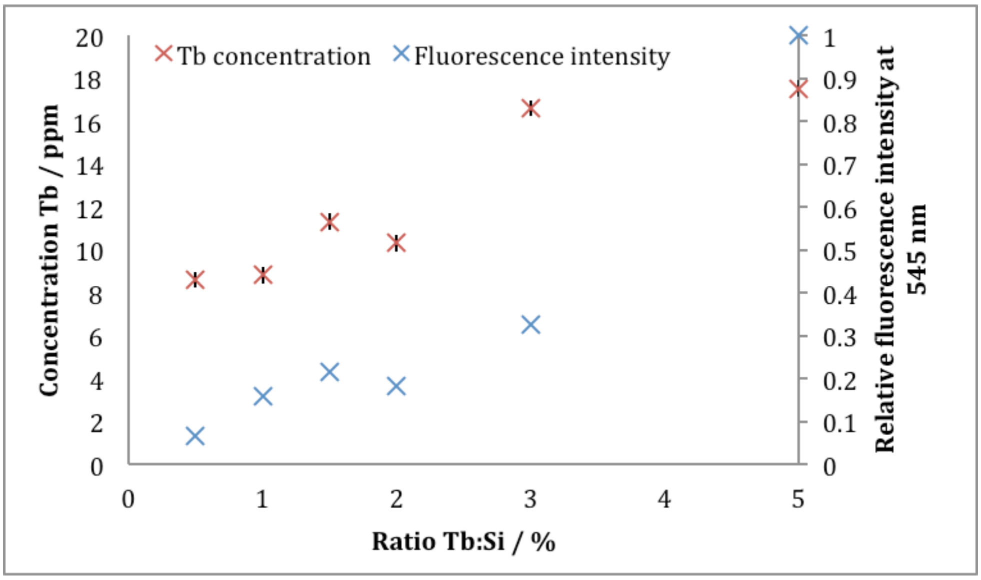

Figure 3-21 Graph showing the effect of increased Tb(TTA)$_3$2PO concentration in core-shell ammonium hydroxide hydrolysed particles on fluorescence intensity and the concentration of Tb^{3+} present within the particles (Error bars show standard deviation for triplicate ICP-OES measurements on each sample).

Table 3-4 Doping efficiency for Tb(TTA)$_3$2PO in core-shell ammonium hydroxide hydrolysed particles

Ratio of Tb:Si / %	Doping efficiency / %
0.5	13.1
1.0	59.9
1.5	51.3
2.0	38.8
3.0	51.3
5.0	26.3

Previous studies have found that the addition of lanthanide ions to the particles results in the loss of the spherical, monodisperse morphology characteristic of sol-gel particles synthesized in this manner (Enrichi 2008; Feng & Zhang 2013; Binnemans 2009; Attia et al. 2012). It has been hypothesized that this effect is dependent upon the ratio of the lanthanide ions to silica present within the precursors. One group performed a series of studies at different lanthanide to silica concentration ratios, and identified concentrations at which, under those particular conditions, did not affect the morphology of the particles, whilst resulting in luminescent particles (Enrichi et al. 2008). This group used europium oxide as a dopant, and found no disruption to the morphology of the particles produced until a value of 1.5 % Eu:Si was added. Within this study, the use of europium ratios up to 2 % Eu:Si still resulted in spherical monodisperse particles (Enrichi et al. 2008). The most likely reason for the change in effective dopant concentration is the stabilising nature of the ligands, which would protect the formation of both lanthanide hydroxide and Ln-Si coordinate bonds within the particles, so reducing the disrupting effect of the trivalent europium ion during particle synthesis (Enrichi et al. 2008; Attia et al. 2012).

3.6 Conclusions

Two methods have been used to produce particles within two key size ranges of eroded soil (fine silt and colloidal clay). Through the use of a factorial design of experiments, the effect of three key conditions in the sol-gel process (volume of ammonium hydroxide, temperature and time) were analysed. This resulted in the formation of a particle within the colloidal clay size range of 950 nm in diameter. An acid based hydrolysis method was used to synthesise a particle 115 µm in diameter, with a size distribution which remained within the size limits for the fine silt fraction. When the lanthanide complexes were incorporated directly into the silica particles, a loss of the spherical, monodisperse characteristics was observed, which was hypothesized to be due to the formation of insoluble lanthanide hydroxides. However, incorporation of the complexes into a secondary silica shell on the surface of the particles did not alter the morphology of the final doped particles at concentrations of up to 2 % Ln:Si. This is the first reported use of a blank silica core coated with a lanthanide complex doped shell. At 1.5 % Ln:Si, the doping efficiency of the complex was at its highest, and the luminescent intensity of the particles also showed an off trend increase in intensity relative to other concentrations analysed. This was most marked in the europium doped particles, where analysis of the amount of europium hydroxide formed showed a similar trend to both doping efficiency and luminescent intensity. From this study it was therefore apparent that the formation of lanthanide hydroxide was directly linked to both the doping efficiency and the luminescent intensity of the resultant particles. As yet, no similar studies as to the effect of lanthanide concentration on doping efficiency and lanthanide hydroxide formation have been reported. EDXA and IR analysis confirmed that the complex was present on the surface of the particles. The presence of the complex on the surface of the particles could also have an implication for the lifetime of the tracer within the soil, as it is more accessible to microbial and chemical attack potentially reducing its persistence within the soil. The incorporation of the lanthanide complex into the silica particles increased the luminescent lifetime of both complexes, in a previously reported stabilization process resulting from the interaction of the silica matrix and lanthanide ions. These lifetimes were extended to 732.93 μs and 58.97 μs for the europium and terbium complexes respectively. Most bench top fluorescence spectrometers are capable of obtaining time delayed spectra with a 0.01 ms delay, therefore all of the tracers synthesized during this study should be able to be detected using a standard fluorescence spectrometer operating in phosphorescence mode. Based on the successful production of the correct size of beads, and the optimisation of the doping concentrations, the behaviour of these beads can therefore be determined in a variety of soil samples.

Chapter 4 – Soil characterisation and initial tracer studies

4.1 Introduction

An effective soil particle tracer should mimic transport of the indigenous soil or sediment, be non-toxic and have a high detection sensitivity. As yet, no tracer that fulfils all of these requirements has been developed. Within the UK, the most prevalent form of erosion is water erosion, and so there remains a need to develop a particle tracer better suited for use in these conditions. In order to effectively test the particle tracers developed during this study, it was necessary to investigate the behaviour of the particle within a range of typical soils. Three soil samples, with varying pH, organic matter content and reactive mineral phases were obtained from the James Hutton Institute research station at Glensaugh.

4.1.1 Chapter aims and objectives

The aim of the work detailed within this chapter was to characterise the behaviour of the developed tracers within real soil samples. This was achieved through a series of specific objectives:

- Collection and characterisation of a variety of soils
- Imaging of tracer binding within soils
- Analysis of fluorescence emission and stability of tracers within soils
- Microbial respiration studies of tracers in soil to determine tracer soil toxicity
- Determination of soil sedimentation behaviour of the synthesised tracers in the presence of soil.

4.2 Materials and methods

4.2.1 Chemicals and reagents

All reagents were used as supplied and reagent grade quality. Sodium hexametaphosphate (HMP) was obtained from Sigma-Aldrich, whereas cresol red, potassium chloride, sodium bicarbonate, purified agar and glucose were obtained from Fisher Scientific.

4.2.2 Soil collection and characterisation

4.2.2.a Soil collection site: Glensaugh research station

The Glensaugh research station is situated within the Grampian region, and comprises a mixture of permanent pasture, rotational pasture and semi-natural grassland, extending to 1,000 hectares (The James Hutton Institute 2013) (see figure 4-1). The estate has an annual rainfall of 1040 mm, and lies between 120 and 450 meters above sea level and is divided into two geological zones by the Highland boundary fault (The James Hutton Institute 2013). The soils to the North of the fault belong to the Strichen Association, varying from brown forest soils to peaty podzols on higher ground, whilst to the South of the fault, soils are derived from Old Red Sandstone, comprising of peaty podzols and humus-iron podzols (The James Hutton Institute 2013).

Figure 4-1 Glensaugh research station with improved pasture in grey, permanent pasture in yellow and woodland in green (The James Hutton Intitute 2013)

The soil used for soil and tracer interaction experiments was obtained from the James Hutton Research Station at Glensaugh, Scotland (56°53'55.91"N, 2°33'0.28"W) (see Figure 4-2). Topsoil (0-7 cm) was sampled using a spade (see figure 4.2). Two of the soils were Cambisols (soils 1 and 2) and the third was a Peaty Podzol (soil 3).

All soils were part of the Corby Association, Kinord Series, with soil 1 classified as a brown forest soil, soil 2 classified locally as a cultivated brown forest soil and soil 3 classified as a Humus iron podzol (Glentworth & Hart 1943). Soils 1 and 3 were collected close to clear erosion scars within the landscape, and therefore were likely to be erodible soils (see Figure 4-3). After collection the soils were sieved through a 2 mm mesh, sealed and then stored at 4 °C until needed.

Figure 4-2 Soil collection sites for (a) soil one, (b) soil two and (c) soil three.

Figure 4-3 Erosion scar present within field near to collection site for soil one

4.2.2.b Soil density and particle size determination

Soil dry bulk density was determined by use of a soil core sample taken of undisturbed top soil from each site immediately prior to collection. The dry mass of the soil was recorded following drying at 105 °C in a drying oven (Gallenkamp). The soil density was calculated as follows:

Soil bulk density (g/cm^3) = Dry soil weight (g) / Soil volume (cm^3) **Equation 4. 1**

Particle size determination was performed on a MastersizerE (Malvern instruments) using a stirred sample cell and a 300 mm lens. Samples were dispersed in 5% HMP solution by shaking overnight at room temperature on a shaking incubator (Thermo Scientific MaxQ4000) at 200 rpm. Results for each sample were averaged over three replicate measurements.

4.2.2.c Soil moisture, loss on ignition and C:N ratio determination

Soil moisture and loss on ignition determinations were performed on triplicate samples of the collected soils. After being accurately weighed into porcelain crucibles, the samples were heated to 105 °C for four hours, then allowed to cool in a desiccator. The dried samples were then reweighed to determine the percentage moisture content, prior to being heated to 450 °C for a further four hours. Samples were again cooled in a desiccator, prior to being accurately weighed once more to determine the mass of the ignited soil. Soil percentage moisture was calculated as below:

$$\text{Soil moisture (\%)} = \frac{(W_2 - W_3)}{(W_2 - W_1)} \text{ X } 100 \qquad \text{Equation 4. 2}$$

Where weight of empty crucible is W_1, weight of crucible and sample is W_2 and W_3 is the weight of the crucible and oven dried at 105 °C sample.

The following equation was used to calculated the percentage loss on ignition:

$$\text{Loss on ignition (LOI) \%} = \frac{(W_2 - W_3)}{(W_2 - W_1)} \text{ X } 100 \qquad \text{Equation 4. 3}$$

Where weight of empty crucible is W_1, weight of crucible and oven dried at 105 °C soil is W_2 and W_3 is the weight of the crucible and ignited soil.

C:N ratio determination was used to characterise the carbon and nitrogen content and ratios for each soil using a Thermo FlashEA 1112 Elemental Analyser. Samples were prepared in two different manners. A 2 mm sieved sample of each soil was air dried at 30 °C prior to milling, and provided the C:N ratio of the bulk soil sample. Each soil, at field moisture, was also minimally dispersed by gentle shaking in deionised water then immediately wet sieved through 150, 75 and 25 µm sieves and the fractions between 150-75 and <25 µm collected and air dried at 30 °C prior to milling.

4.2.2.d Oxalate extractable ions

In order to determine the concentrations of exchangeable ions within the three different soil types, an acid-ammonium oxalate extraction was performed. The acid ammonium oxalate reagent was prepared immediately prior to the extraction to a concentration of 0.4 M in deionised water, in a volumetric flask. This solution was then diluted to a working concentration of 0.2 M, again in deionised water and the pH adjusted to 3.02. A 30 mL aliquot was added to 50 mL centrifuge tubes containing 0.0600g sample of each soil. Samples were then shaken in the dark for 4 hours at 200 rpm on a gyratory shaker (Model G2, New Brunswick Scientific), before being separated by centrifugation at 4,000 rpm. The supernatant was then filtered through a 0.45 µm syringe filter (Nalgene) and stored at 4 °C until elemental analysis. Samples were analysed using a Agilent 7700 Inductively Coupled Plasma – Mass Spectrometer (ICP-MS).

4.2.2.e IR analysis

FTIR analysis was performed on all milled samples to provide an indication of the composition of the organic matter within each soil (Artz et al. 2008). In addition, the milled 150-75 and <25 µm fraction were also analysed to determine the organic groups contained within the two fractions targeted by the tracers. Analysis was performed as detailed in section 2.2.6.

4.2.3 Behaviour of synthesised tracers in soil

4.2.3.a Scanning electron microscopy

SEM was performed in order to determine if the tracer associated with the natural soil particles present within the characterised soils. Soil and tracer mixtures (10 mg tracer in 10 g soil one) were imaged using a Sigma EVO-LS10 scanning electron microscope operating in extended pressure mode, using the secondary electron detector. Samples containing the colloidal clay tracer were analysed using a standard stage, whilst samples containing the fine silt tracer were analysed using a Peltier stage, allowing analysis of the interaction between the tracer and soil at field moisture. Samples were mounted on aluminium stubs using adhesive carbon tabs (Agar Scientific). For wet mount samples the accelerating voltage was 20 kV, with a beam current of 300 µA and an I probe value of 120 pA. The extended pressure target was set to 590 Pa and the humidity at 89.9 %. Settings for the colloidal clay tracer were as stated in 3.2.3.b.

4.2.3.b Fluorescence analysis

Initial stability studies of the tracer's fluorescence signal in soil samples were performed in 2 mm sieved soil. Samples were analysed directly using surface reflectance fluorescence spectrometry in a custom made sample holder (as shown in figure 4.4). Analysis was performed in soils at both field moisture and air dried overnight at room temperature following addition of the tracers.

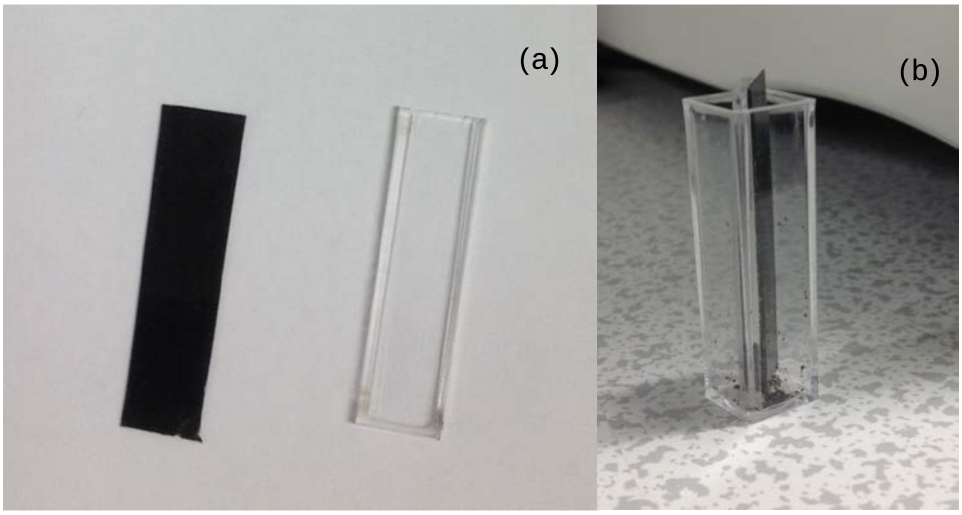

Figure 4-4 Sample holder developed for the analysis of surface reflectance fluorescence (a) sample holder and (b) sample holder mounted in a cuvette.

Fluorescence emission and excitation analysis was performed in the solid state on an Edinburgh Instruments FLS900 spectrometer using an Xe900 light source and a Hamamatsu blue PMT. Excitation spectra were obtained between 220 and 400 nm, with an excitation wavelength of 320 nm, an emission wavelength of 545 nm and excitation and emission slit widths of 5 nm. Emission spectra were obtained between 350 and 650 nm, with an excitation and emission slit width of 1 nm. Both excitation and emission spectra were corrected using correction factors incorporated into the F900 software (Edinburgh Instruments). Soil and tracer fluorescence emission analysis was performed using a Perkin Elmer LS50 B in phosphorescence mode. Spectra were obtained between 450 and 640 nm, at an excitation wavelength of 320 nm, with an excitation slit width of 8 nm and an emission slit width of 6 nm. A delay of 0.03 ms was used, with a cycle time of 200 ms, a gate time of 1 ms and 1 count per cycle.

4.2.3.c Stability study

In order to determine the lifetime during which the tracer can be detected in the soil, a stability study was performed at a series of concentrations using soil 1 and the fine silt tracer. Mixtures of soil at field moisture and tracer were made at tracer concentrations of 100, 50, 10, 5, 1, 0.5, 0.1 and 0.01 $mg.g^{-1}$ of tracer to soil. An initial sample was taken of the thoroughly mixed samples, which were then stored in the dark at 9 °C to replicate typical field conditions in Scotland. After thorough mixing a sample was removed and air-dried overnight prior to analysis in a PE LS50B fluorescence spectrometer. Samples were taken after 0, 34, 70, 105 and 133 days, and the percentage loss of luminescent intensity determined. Luminescence intensity was measured using a single scan mode, with an excitation wavelength of 350 nm, an emission wavelength of 618 nm and excitation and emission slit widths of 10 and 5 nm respectively. Three measurements were taken at each concentration for each time point, and the standard deviation of these measurements was determined to provide the error of each reported value.

4.2.3.d Soil microbial respiration rates

In order to assess the toxicity of the tracer to the soil microbial population, a series of soil respiration experiments were carried out using a microbiological plate-based respiration detection system (MicroResp) (Campbell et al. 2003); with respiration measurements for both basal (i.e. the *in*-situ respiration) and glucose induced respiration rates (i.e. potential respiration as a measure of community size using glucose as a carbon source). Each treatment (0.0100 g) to be studied (see table 4-1) was added to 8.00 g of test soil (fresh mass) and mixed thoroughly. The soil and tracer mixes were then added to individual columns of 96 well plates (Nalgene) and soil respiration rates measured according to the MicroResp protocol (Campbell et al. 2003). This resulted in eight repetitions of the respiration values for each of the treatments. In addition, two soil only blanks, at the ends of the plates, and a previously studied orange particle tracer (Pollard et al. 2007) were incorporated to allow any potential contamination between treatments to be identified. Following conversion via a pre-determined calibration curve between CO_2 production and colour change in the indicator gel, plus scaling with appropriate constants (temperature and headspace volumes), oxygen standard respiration rate was determined as mg O_2. soil dm^{-1}. $hour^{-1}$. Statistical analysis was performed using Minitab 16 (Minitab Inc.). One-way ANOVA without replication was used to determine the significance of any differences in data obtained for the factorial design, whilst one-way ANOVA with replication was used for analysis of soil microbial respiration activity. Significance was determined at the 95 % confidence level.

Table 4-1 MicroResp treatments

Column	Additive
1	None (soil control)
2	Fine silt tracer (synthesised core)
3	Fine silt tracer (commercial core)
4	Colloidal clay tracer
5	$Eu(TTA)_3 2PO$
6	$Tb(TTA)_3 2PO$
7	Orange tracer
8	Core particle (clay)
9	Core particle (fine silt)
10	Core particle (commercial)
11	None (soil blank)

4.2.3.e Soil sedimentation experiments

Sedimentation studies were performed using the pipette method with 5% HMP as the dispersant (Van Reeuwijk 2002) at room temperature (20 °C). Sieved soil (5.00 g, 2 mm) at field moisture was mixed with 0.0500g of the tracer prior to the addition of 40 mL of HMP. These samples were shaken overnight, then enough deionised water added to make the samples up to 100 mL. Samples were then decanted into a settling jar and mixed thoroughly for 1 minute. A 10 mL sample was taken after 40 s containing the fine silt and colloidal clay fractions (as classified using the International System) and again after 6 hours (colloidal clay fraction). Samples were collected using Whatman number 1 filter paper, and allowed to dry prior to analysis. Fluorescence analysis was performed directly on the filter paper, using an Edinburgh instruments FLS920 spectrometer equipped with a μs flash lamp, 395 nm emission filter and a Hamamatsu blue PMT. Spectra were obtained between 450 and 700 nm, using a 395 nm emission filter, over 5 scans, with a dwell time of 0.5 s and an excitation wavelength of 350 nm for the fine silt tracer, and 320 nm for the clay tracer.

4.3 Results and discussion: Soil characterisation

In order to analyse the behaviour of the synthesised tracers within a variety of soil types, the three soils detailed in section 4.2.2.a were characterised.

4.3.1 Soil density, moisture content and particle size

The soil density and moisture content of each soil type can be found in table 4-2, and were similar to soil bulk densities previously recorded in this region (1.16 ± 0.02 g/cm^3 for soils around the sites of soils one and two and 0.94 ± 0.01 g/cm^3 for area around soil three) (as shown in figure 4-5) (Norton et al. 2009). Typical soil bulk densities for fine silt, sandy and clay soils range from 1.1-1.7 g/cm^3, with soils containing high organic contents (such as peats) having bulk densities of less than 0.5 g/cm^3 (Cresswell & Hamilton 2002). The two improved soils (soils one and two) fall within this range, whilst soil three (humus podzol), which had a more peaty organic A horizon had a lower soil bulk density than these soils, but greater than that of a true organic rich peat soil. The pH of the three soils was low (see table 4-2), but representative of the soils within the selected sampling site. Whilst it would have been advantageous to have analysed the tracers in a wider range of soil pH the isolation of the lanthanide complexes from the aqueous environment by the silica matrix would most likely prevent all but the most extreme pH ranges from affecting the luminescence of the tracer. It is possible that the interaction of the tracers with the soils could be altered with pH, as interactions between the soil and tracer could change depending on the ionisation state of the surface groups present. In order to determine if this was the case, the behaviour of the tracer in a wider range of both soil types and pH would need to be analysed.

Table 4-2 Summary of soil characterisation data for the three soils and fractions.

Soil	Soil type (as determined by (Glentworth and Hart, 1943)	Fraction	pH	Soil bulk density (g/cm^3)	C:N	Moisture content	Loss on ignition (%)
1	Brown forest soil	2 mm	4.97	1.08	10.74	29.71 ± 0.41	10.05 ± 0.56
		fine silt			11.32		
		colloidal clay			9.80		
2	Cultivated brown forest soil	2 mm	5.03	1.21	10.36	21.93 ± 0.42	7.02 ± 0.52
		fine silt			10.56		
		colloidal clay			9.35		
3	Humus iron podzol	2 mm	4.41	0.90	14.92	35.33 ± 0.27	24.95 ± 0.83
		fine silt			15.24		
		colloidal clay			15.16		

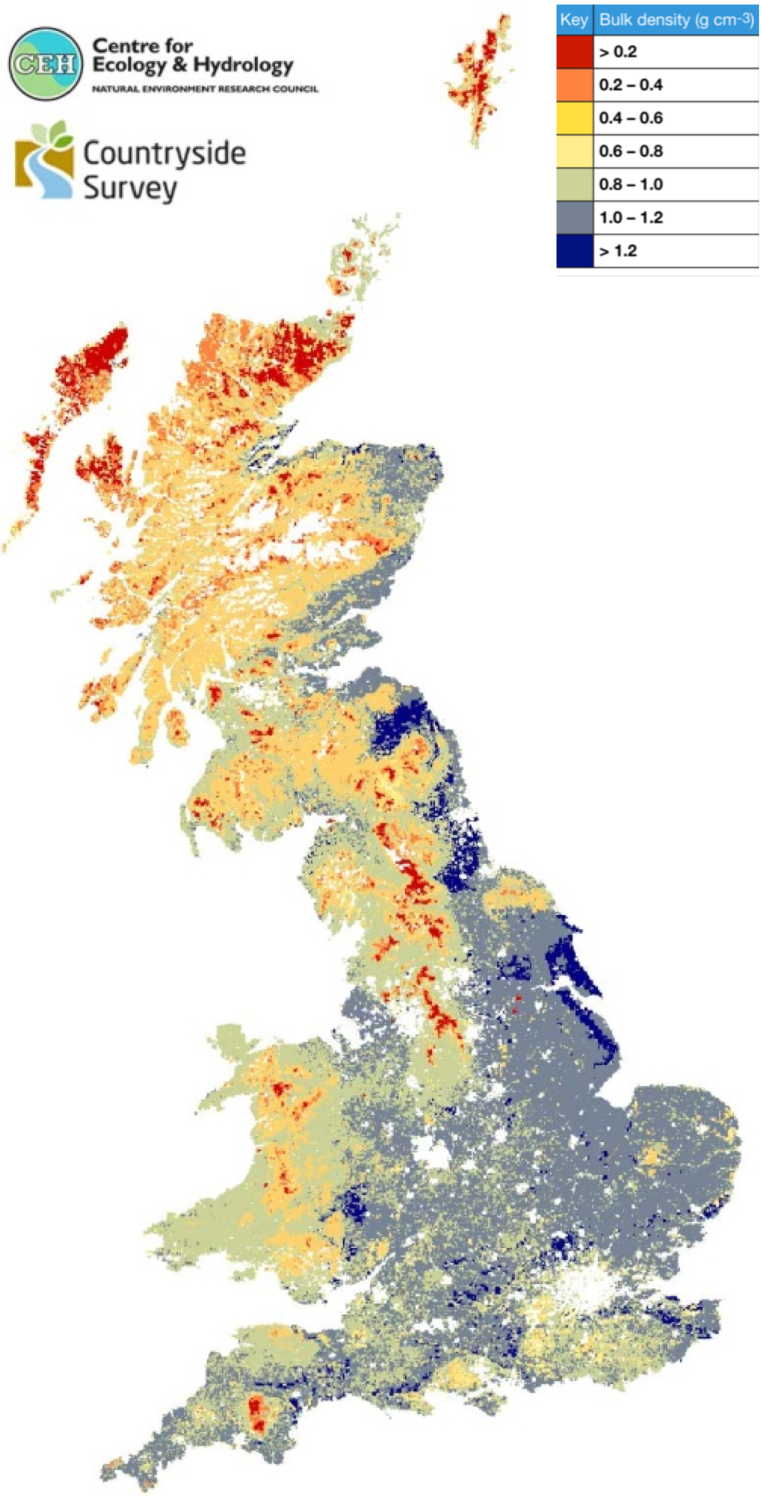

Figure 4-5 Topsoil bulk density in the UK in 2007 (Taken from (Norton et al. 2009))

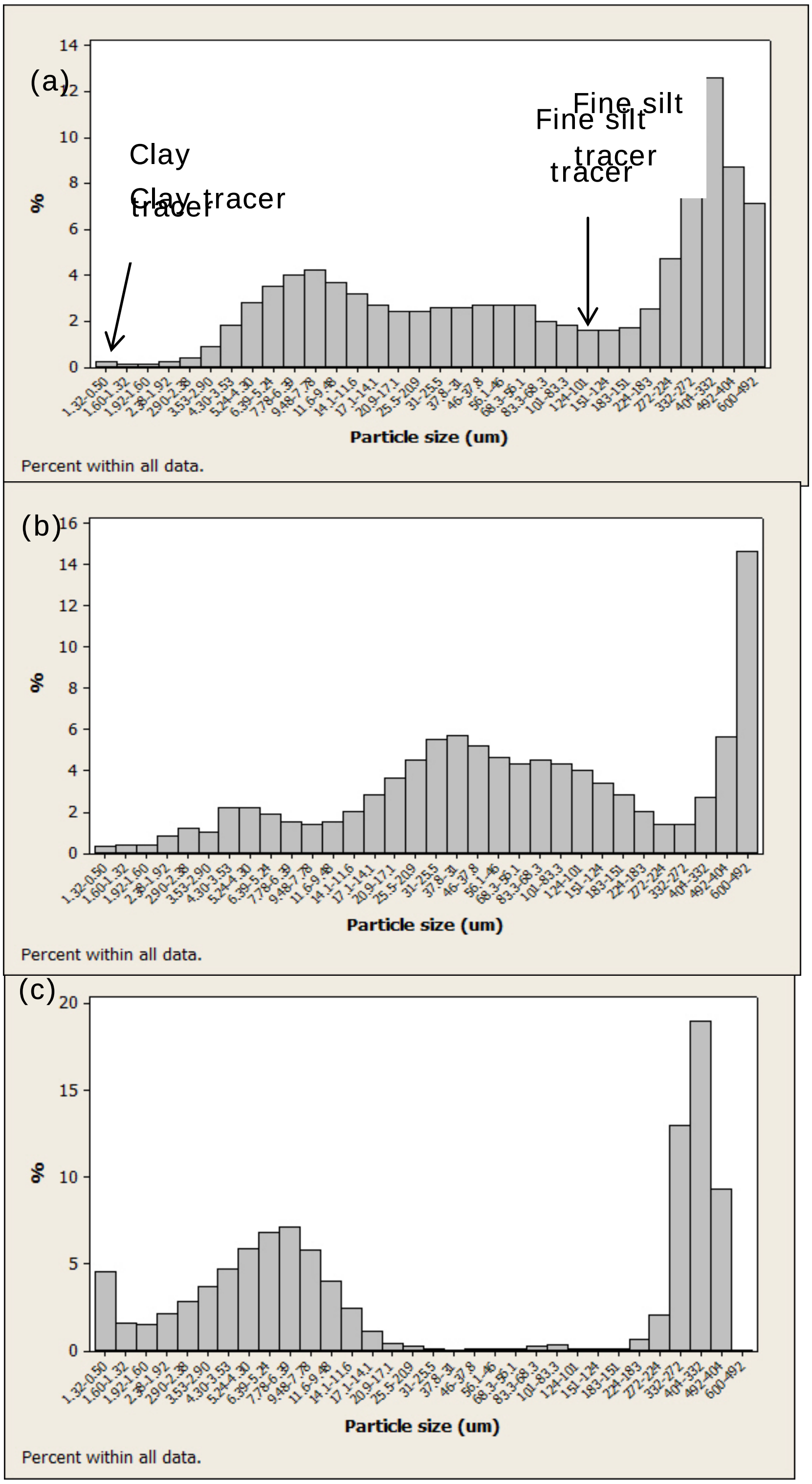

Figure 4-6 Histograms showing distribution of particle sizes within the three soils collected from Glensaugh research station, after dispersal in hexametaphosphate, determined using a MastersizerE particle sizer (a) soil 1, (b) soil 2 and (c) soil 3

The particle sizes for each soil was also determined using a particle sizer, in order to identify the distribution of particle sizes within each soil in relation to the synthesised tracers (as shown in figure 4-6). Soil one contained a large proportion of soil particles within the fine silt range (63 to 250 μm), and soil three within both the colloidal clay (< 1.2 μm) and fine silt range. Within soil two, the majority of the particles sit outwith these fractions, although they are still represented. This indicates that for these three soil types the tracers synthesised were appropriate.

4.3.2 Loss on ignition, C:N ratio determination

The total carbon for soils one and two was between 3-5%, with C:N ratios similar between soils one and two at the lower end of the range typical for cultivated soils (8-17:1) (Brady & Weil 2002) (as shown in figure 4-7 and appendix I table A-5). The C:N ratio was higher for soil three, associated with a larger total carbon content (15%), as expected for a more organic soil (Brady & Weil 2002). For soils one and two there was a higher ratio of carbon to nitrogen in the fine silt samples than the clay fraction. This was as expected as the majority of the organic matter will be present in the larger soil aggregates where it acts to stabilise the particles, whilst the nitrogen present would be associated with the mineral fraction of which the clay fraction would contain a higher proportion (Brady & Weil 2002). Within soil three there was only a small difference in the C:N ratio of the two fractions, probably indicating the presence of more humic substances and complex long chain organics associated with this soil type. It is possible that the amount of organic matter, in particular organic acids and carbohydrates could affect the binding of the particle to the soils, as the silica groups and functional groups of the complexes present on the surface of the particles are most likely to interact with these groups. This will affect the strength of the binding and incorporation of the tracers into the soil particles, potentially affecting the way in which the tracers are transported. The presence of high levels of organic molecules have the potential to interfere with the luminescent detection of the tracer by increasing the background fluorescence levels, unless time resolved luminescence spectroscopy is used (Tauro et al.

2012).

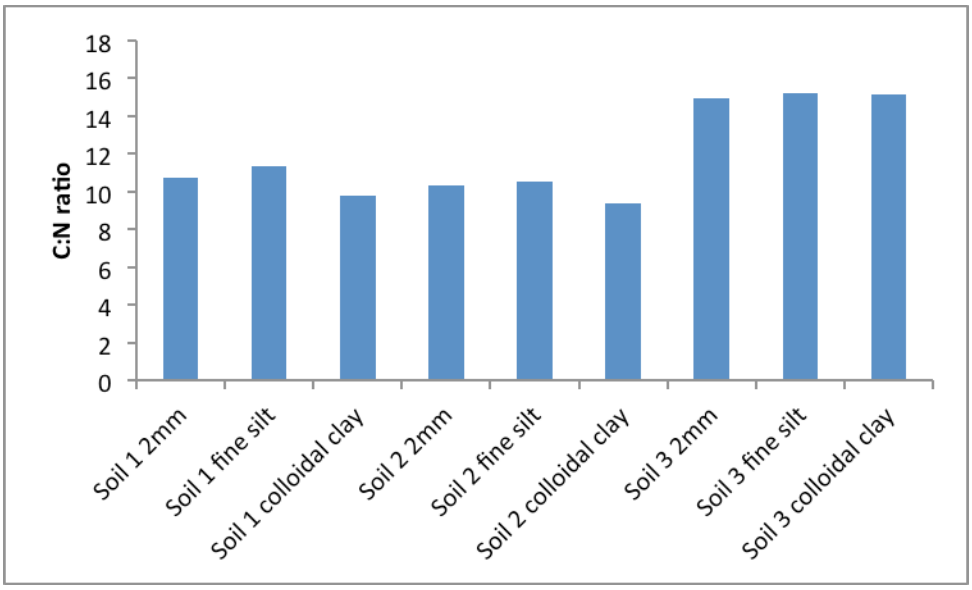

Figure 4-7 Carbon:nitrogen data for the three soils, and three soil fractions (2 mm, fine silt (750-150 µm) and clay (< 25 µm).

The loss on ignition values were also typical for these types of soils (as shown in table 4-3). The carbon contents measured within the C:N determination represents the total carbon present within the soils, whilst the loss on ignition values represent the total amount of combustible organic matter. Therefore the loss of mass seen within these samples represents the loss of the total organic component, not just the carbon, and is therefore (approximately two-fold) greater. The relationship between the two will depend on the precise chemical composition of the organic components present, and as such varies from soil to soil.

Table 4-3 Loss on ignition (LOI) values obtained for the three soils collected from the Glensaugh Research Station

	Average LOI (%)	Standard deviation (%)
Soil 1	10.05	0.56
Soil 2	7.02	0.52
Soil 3	24.95	0.83

4.3.3 Oxalate extractable ions

Acid ammonium oxalate extraction specifically removes aluminium, iron, manganese and alluminosilicates, as well as active, short range order, amorphous oxides and organic complexes from soils (Carter 1993; Michéli et al. 2006). The presence of silica, iron and aluminium promote the formation of soil aggregates due to the precipitation of hydroxides, phosphates, carbonates and oxides (Bronick & Lal 2005). The levels of all elements were highest in soil one, and lowest in soil three (see figure 4-8 and appendix I table A-6). This was expected, as soils one and two are improved soils, whilst soil three is an unimproved soil. Silicon was present at low concentrations in the 2 mm fraction of soil three, and could not be detected in the other two fractions. Again, this was expected as soils with a more organic origin often have lower silica levels than other soils. It was also interesting to note, that the elements were generally present in lower concentrations in the fine silt fraction than the other two fractions. As the wet sieving process by which the fractions were collected separated out the clay fraction from the fine silt fraction, this was likely due to a lower concentration of small clay particles, with high surface areas available for the extraction of the elements. As these elements (in the form of ions) are generally associated with the clay structures, this depletion in the fine silt fraction would account for the lower concentrations found within this fraction (Brady & Weil 2002). This argument is strengthened by the concentrations being generally higher in the 2 mm fraction, which was not wet sieved, and therefore contained both the fine silt and clay fractions.

It is anticipated that an interaction between these ions and the silica and organic groups present on the surface of the synthesised tracers will affect the incorporation of the tracer particles into the natural soil particles. As the three different soils have different oxalate extractable ion profiles, these three soils should provide information on the ability of the tracer to interact with a variety of soils.

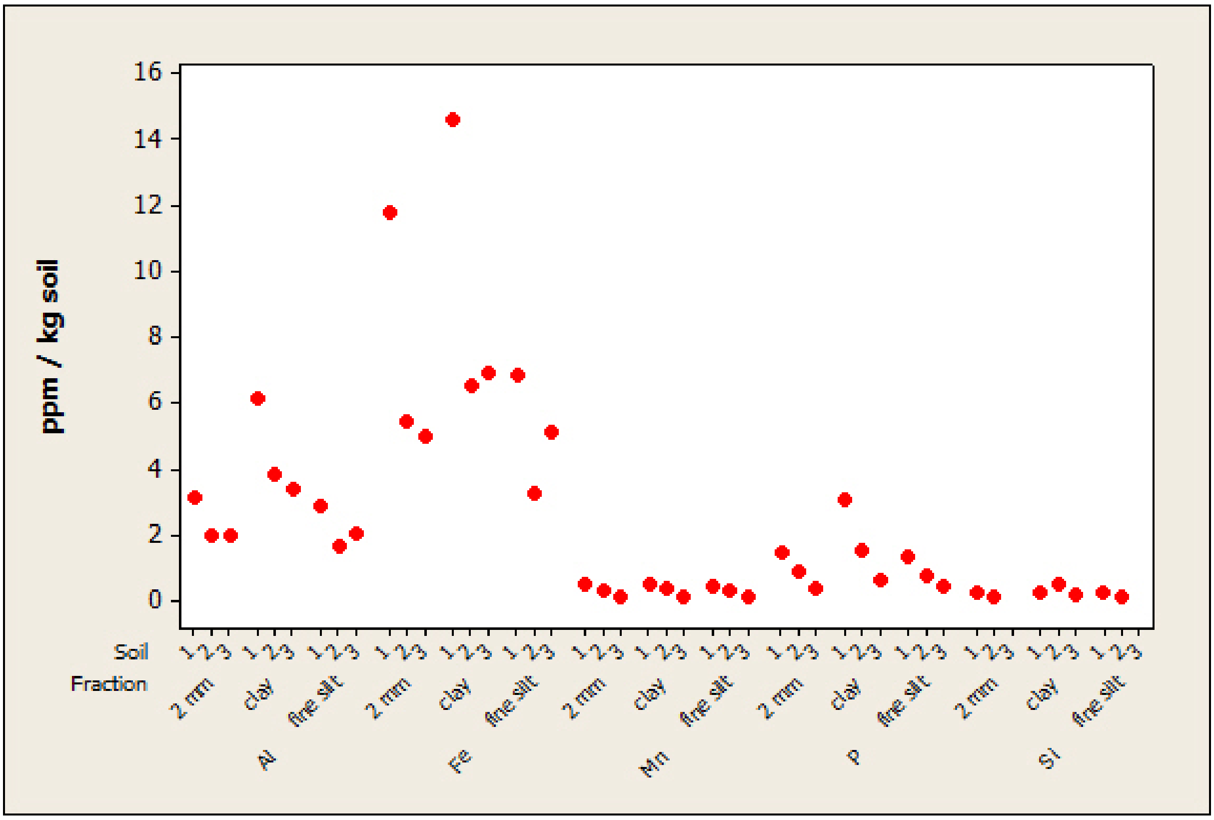

Figure 4-8 Concentrations of oxalate extractable ions present within whole soil, fine silt (750 – 150 µm) and clay (<25 µm) containing fractions of the three soils collected from the Glensaugh research station

4.3.4 Analysis of functional groups by infra-red

As organic groups present on the surface of the soil particles could influence the binding of the tracer, and also interfere with tracer detection, FTIR analysis of the three soils was performed (as shown in figure 4-9). Analysis of milled 2 mm sieved and dried soil showed the presence of hydroxyl (3,650-3,600 (bonded) and 3,500-3,200 cm^{-1} (free)), waxes (in the form of aliphatic CH_2 and CH_3 stretch (3,000-2,800 cm^{-1}), carboxylate ($R\text{-}COO^-$ stretch) (1,660-1,517 cm^{-1}), unsubstituted aromatics (C=C stretch) (1,510 cm^{-1}), carbohydrate (C-O stretch) (1,061 cm^{-1}), silica (1,100 and 790 cm^{-1}) and aromatic (C-H out of plane bend) groups (777 cm^{-1})(Artz et al. 2008). Whilst these three groups were present within each soil type, the relative proportions changed. Of these three groups, those most likely to interact with the tracer particles were the hydroxyl, carboxylate and aromatic groups, as they could potentially interact with the lanthanide ion and chelate functional groups present on the tracer particle surface (Armelao et al. 2010; Parker & Williams 1996). Within the 2 mm sieved samples, the proportion of bonded hydroxyl groups in each soil type remained constant, but there was a significant increase in the proportion of free hydroxyl groups within soil 1. As the free –OH groups are more likely to interact with the tracer particles than the bonded groups, this suggests that interactions via this mechanism would be more favourable in soil one than the other soil types. A similar increase in the proportion of aromatic groups within soil one was also seen, again indicating the potential for increased interaction between the soil and tracer. The proportion of the wax groups present within soils one and two were similar, however there was an increase within soil three. As soil three is a peaty podzol, the rate at which organic matter is broken down would be far slower than that of the cultivated soils one and two and persistent organic groups such as the waxes would be expected to be found at greater proportions within soil three. A similar pattern was found for the carboxylate and unsubstituted aromatic groups. The presence of the increased carboxylate groups within soil three could increase the binding affinity of the synthesised tracers. However, many of these groups are present within fluorophores, and as such indicate that the background fluorescence levels within this soil could be higher than the other two samples, with the potential to interfere with detection of the tracer.

Analysis was also performed on three different soil fractions (2 mm - whole soil; 75-150 µm – fine silt and <2 µm – clay). In soils one and two there appeared to be little difference in the functional groups present within the soil organic matter of the 2 mm and fine silt fractions. However there was a significant difference between these fractions and the clay fraction, with an increase in all the functional groups. This could be the result of the greatly increased surface area of the clay fraction, resulting in more of the soil organic matter contained in this fraction being presented on the particle surface and thus interacting with the IR radiation. Alternatively, it could be that this fraction is associated with more degraded soil organic matter, rich in the functional groups analysed (Artz et al. 2008; Brady & Weil 2002). Within soil three, a difference was present between all three fractions. As peaty podzols are known to have deep, complex organic layers with a wide variety of humic and organic substances (Artz et al. 2008), it is likely that these also have a wide variety of sizes and interaction mechanisms, causing the spectral profile of each fraction to vary.

FTIR spectra for each 2 mm sieved soil following ignition at 450 °C, to remove the organic components were obtained to determine the contribution of the mineral components of the soil to the spectra (as shown in figure 4-10). Analysis of these spectra identified the presence of silica within the peaks around 1,100 cm^{-1}, as expected, but the peak shifted from 999 cm^{-1} and the shape changed following ignition. This suggests that both the silica mineral and carbohydrate organic groups contribute to the 999 cm^{-1} peak seen in the whole soil samples. The peaks identified at approximately 1,640 cm^{-1} and 3,350 cm^{-1} were no longer present within the ignited samples, further confirming the classification of these peaks as organic aromatics and waxes.

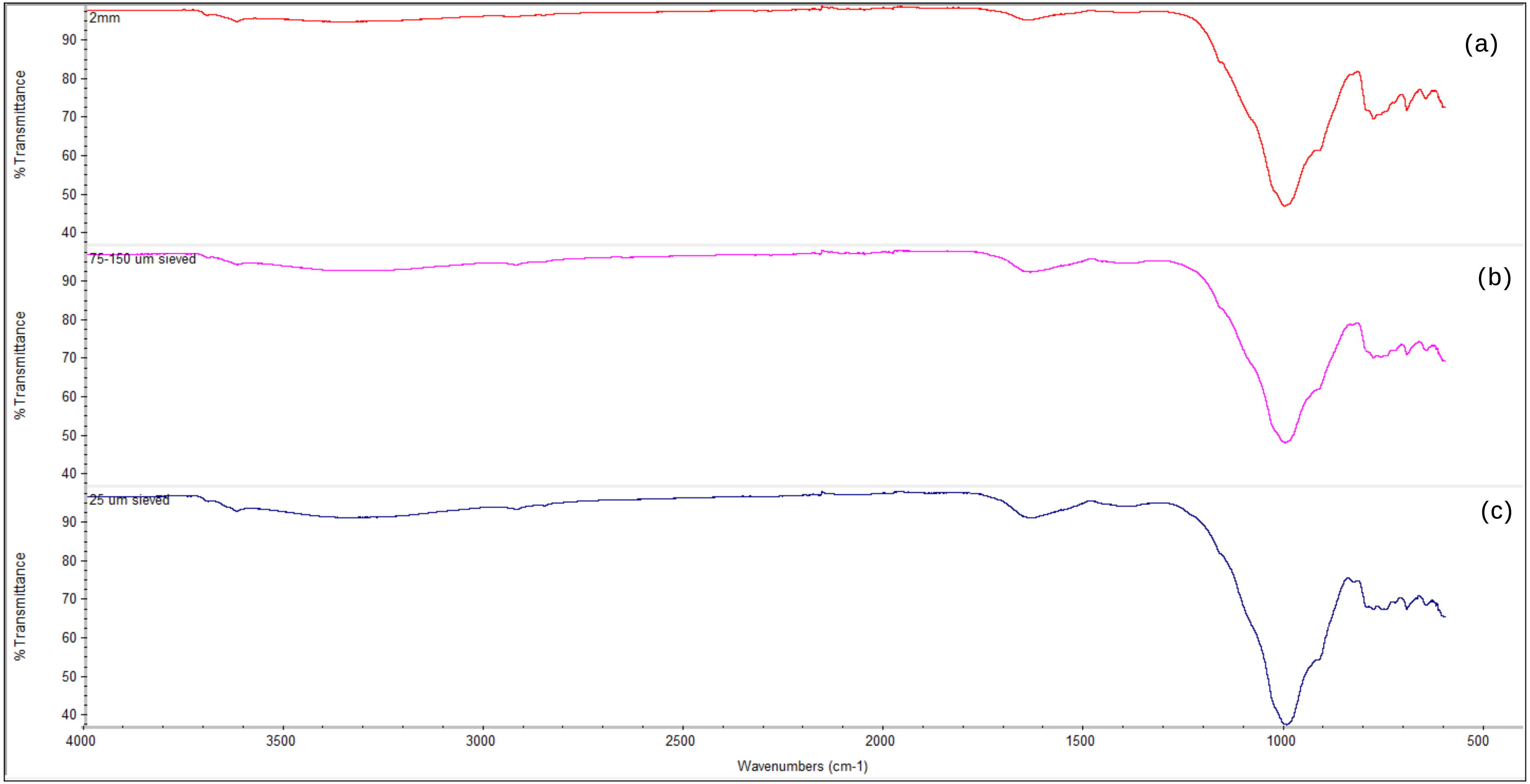

Figure 4-9 FTIR spectra obtained using an ATR attachment for dried milled and sieved samples obtained from soil one collected from the Glensaugh research station (a) 2 mm (b) 75-150 µm and (c) <25 µm

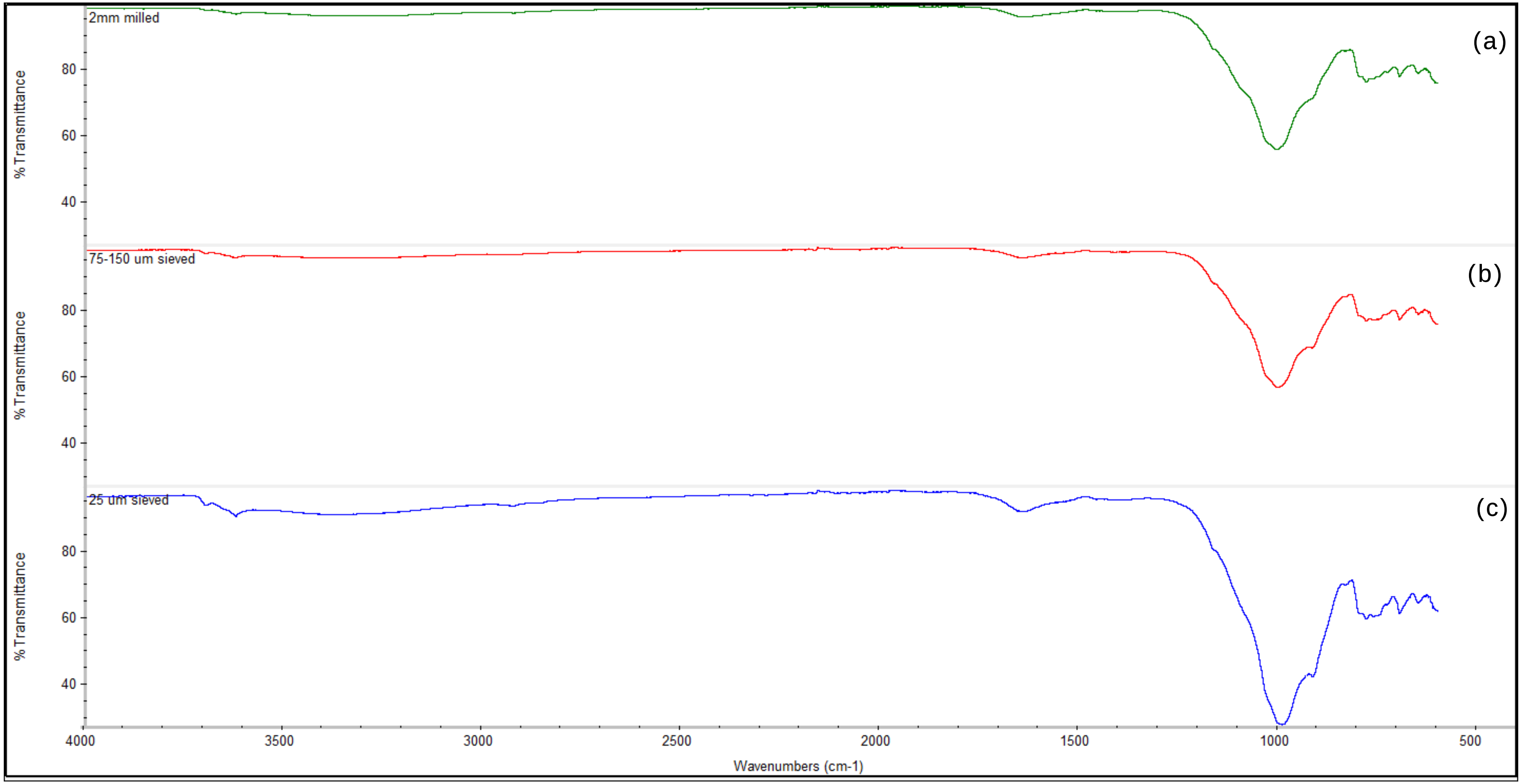

Figure 4-10 FTIR spectra obtained using an ATR attachment for dried milled and sieved samples obtained from soil two collected from the Glensaugh research station (a) 2 mm (b) 75-150 µm and (c) <25 µm

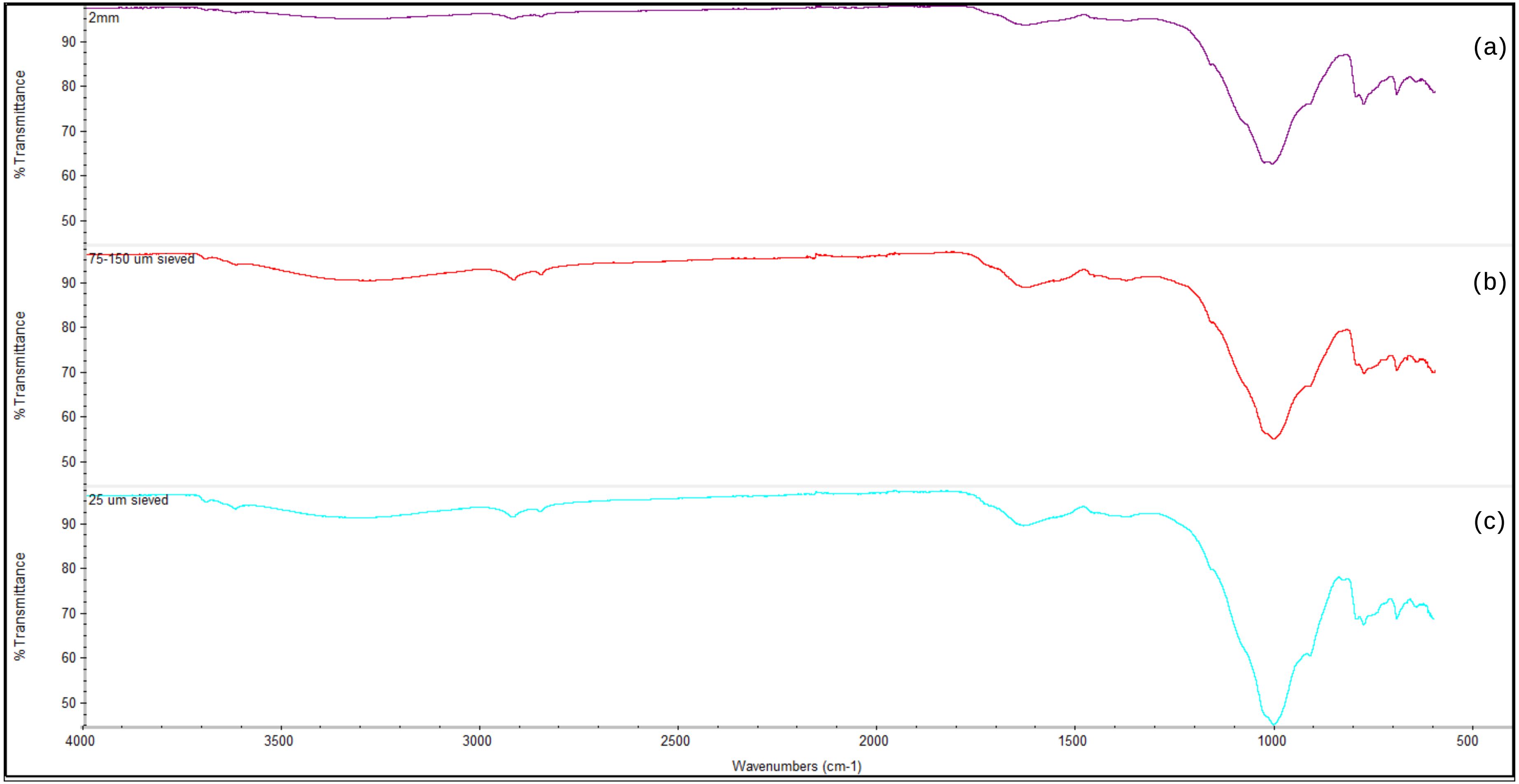

Figure 4-11 FTIR spectra obtained using an ATR attachment for dried milled and sieved samples obtained from soil three collected from the Glensaugh research station (a) 2 mm (b) 75-150 µm and (c) <25 µm

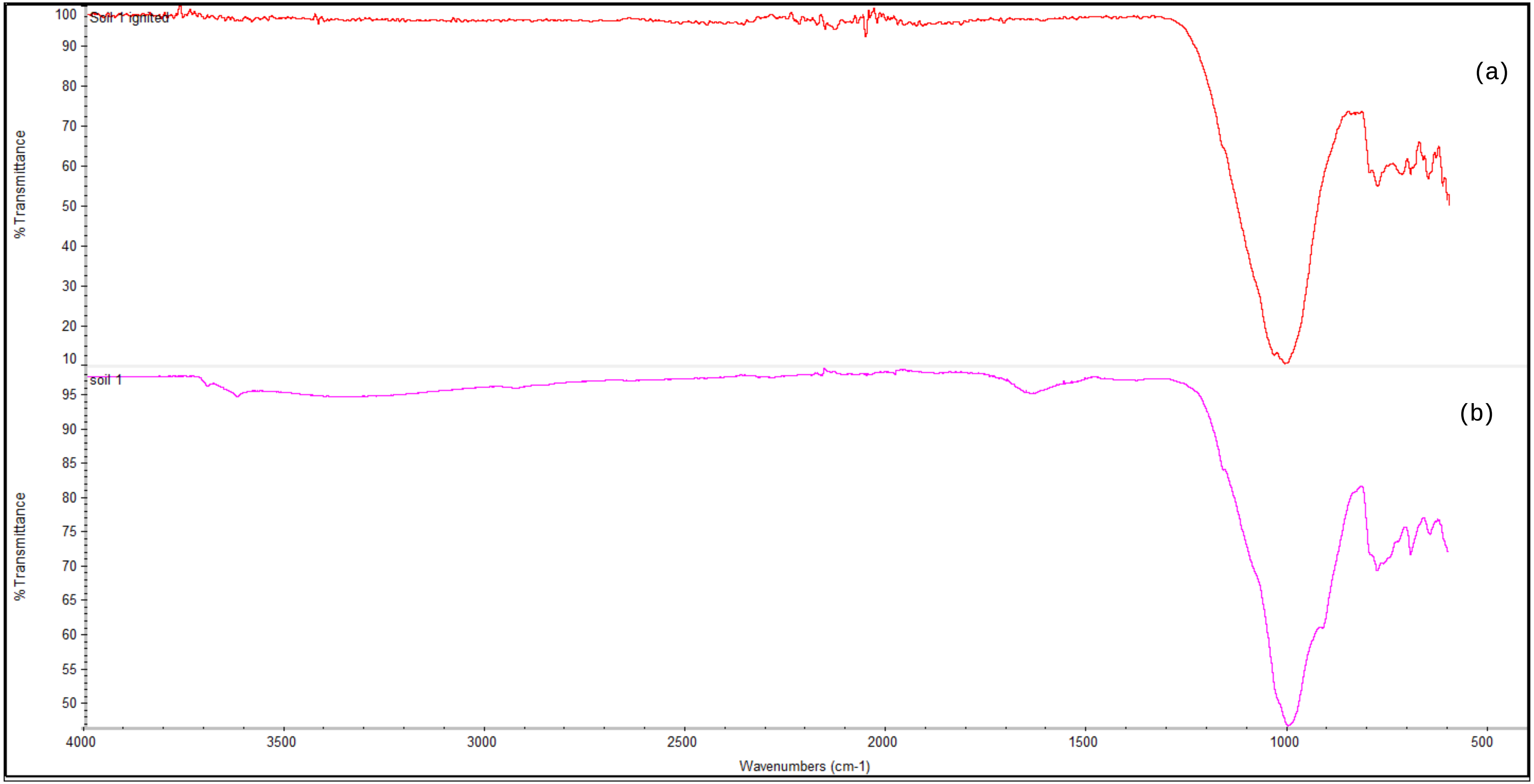

Figure 4-11 FTIR spectra of 2 mm sieved and dried soil samples (a) prior to and (b) following ignition at 450 °C for soil one collected from the Glensaugh research station

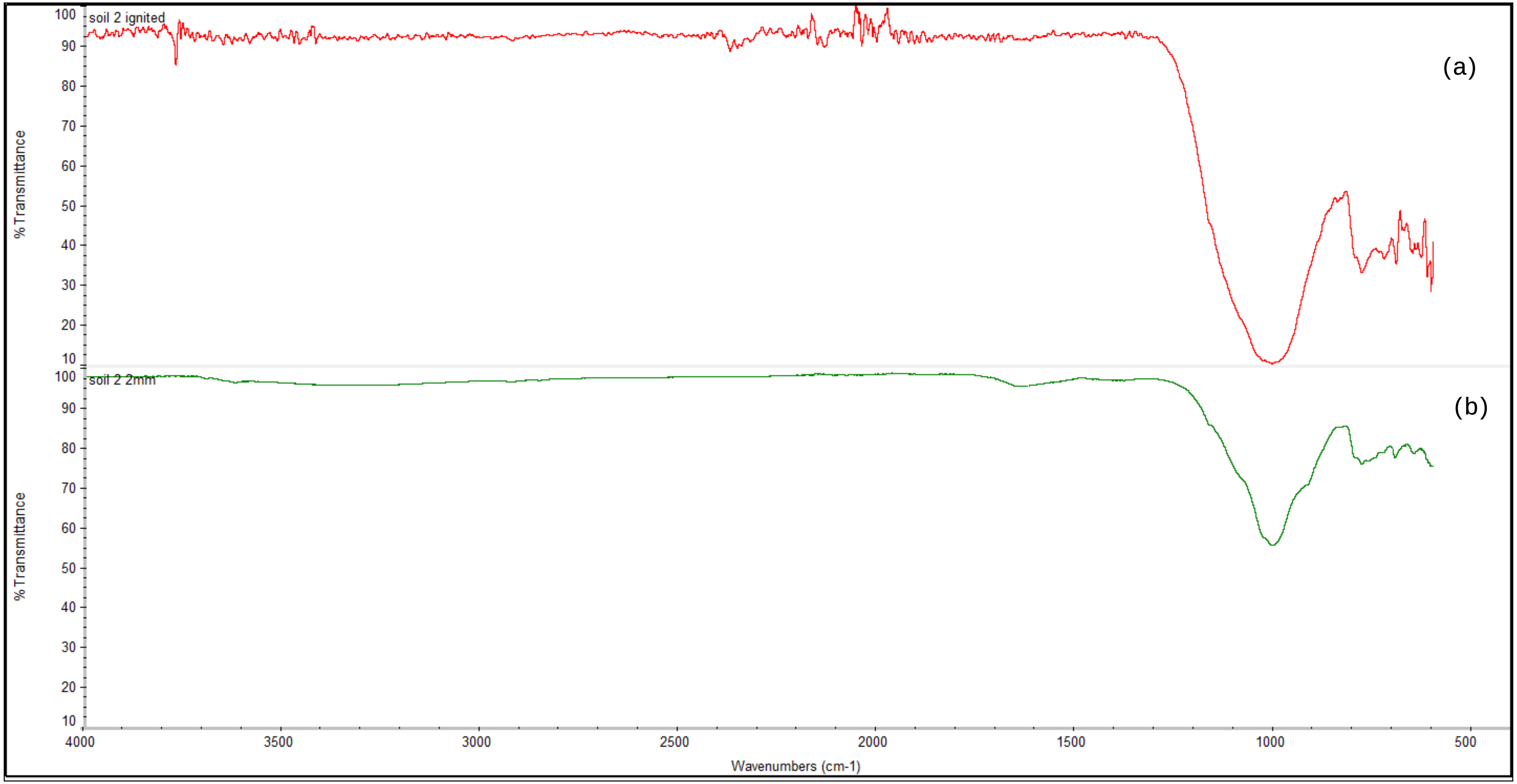

Figure 4-12 FTIR spectra of 2 mm sieved and dried soil samples (a) prior to and (b) following ignition at 450 °C for soil two collected from the Glensaugh research station

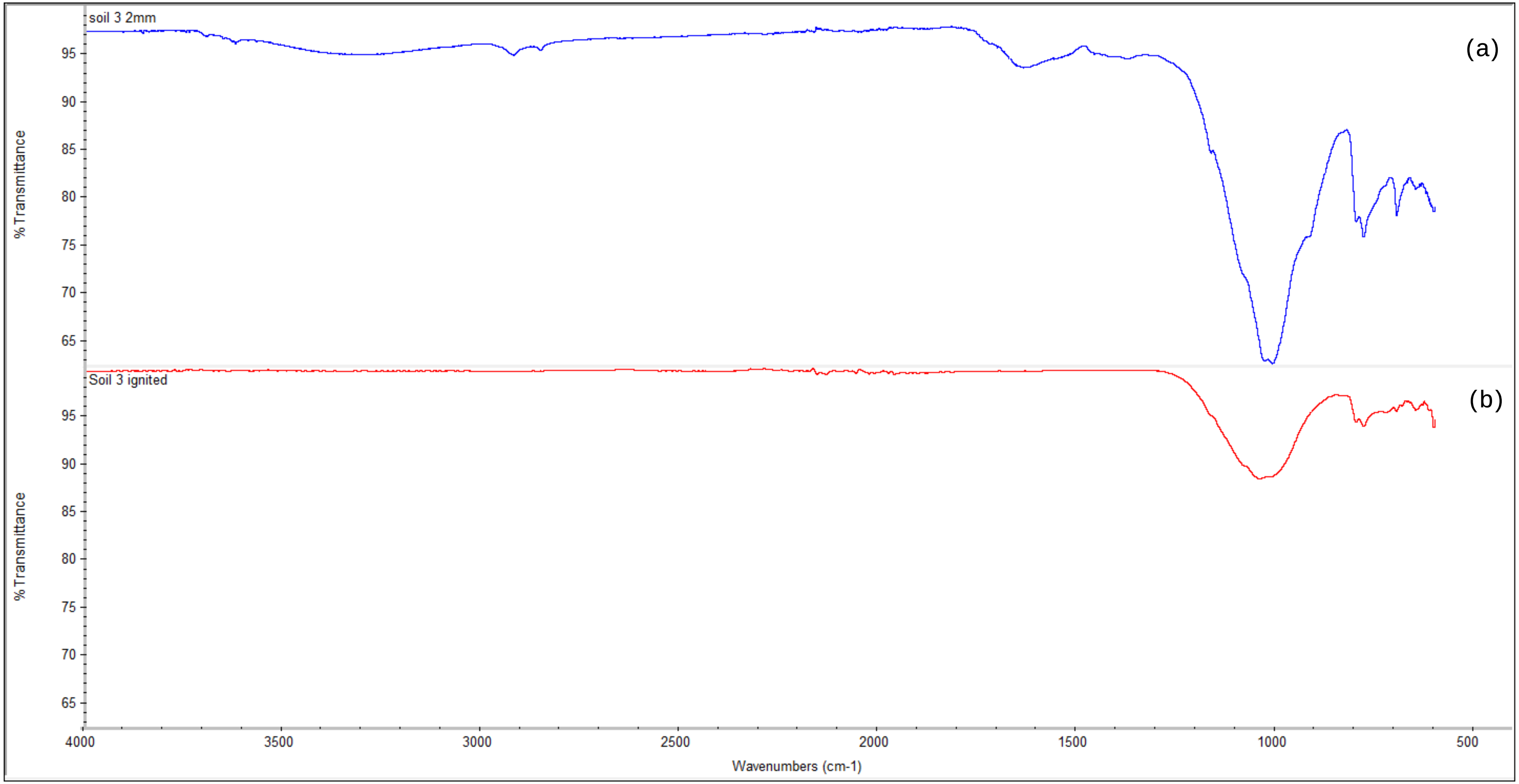

Figure 4-13 FTIR spectra of 2 mm sieved and dried soil samples (a) prior to and (b) following ignition at 450 °C for soil three collected from the Glensaugh research station

4.4 Results and discussion: analysis of behaviour of synthesised tracers in soil

4.4.1 Scanning electron microscopy

Having obtained luminescent tracers of appropriate size in section 3.4.2, a series of experiments to analyse their behaviour with the soil were performed. Initially the tracer was mixed with soil at field moisture to determine whether the lanthanide specific luminescence of these particles was retained, and if the particles remained stable in the soil environment. Scanning electron micrographs verified the presence of the tracers on the surface of natural soil particles (as shown in figure 4-11). Analysis of the fine silt tracer particles in soil on a wet stage at field moisture showed that the particles bound to the surface of the soil particles in a natural state. This could be determined by the presence of the tracers on all surfaces of the soil particles, not just on the top surface. However, it was not possible to resolve the clay tracer using this technique as they exceeded the limit of resolution for this instrument under these conditions. As the silica and organic complexes present on the tracer particle surfaces should be able to interact with the hydrated clay and organic components, this provides evidence that the tracer particles can incorporate into natural soil aggregates.

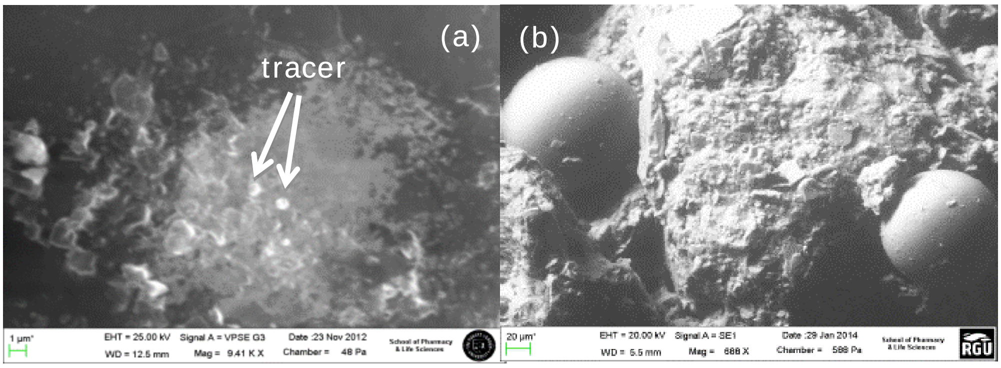

Figure 4-14 Scanning electron micrographs obtained of the synthesised tracers mixed with soil one collected from the Glensaugh research station (a) colloidal clay tracer (b) fine silt tracer

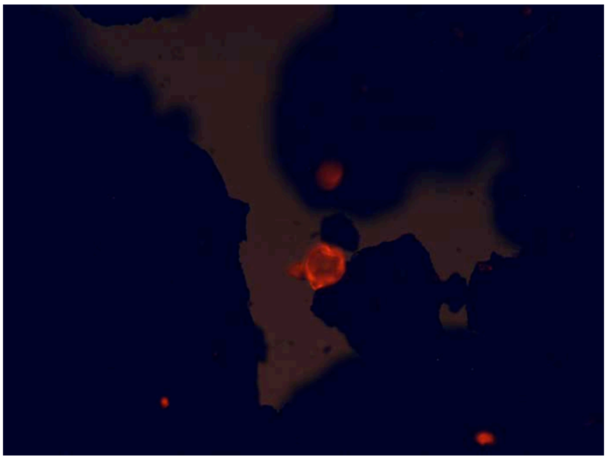

Figure 4-15 Fluorescence microscope image of the europium doped fine silt tracer mixed with soil one at field moisture collected from the Glensaugh research station (300 X magnification, 340 nm excitation filter, 600 nm emission filter).

Fluorescence microscopy of the fine silt tracer within soil at field moisture showed the presence of europium specific luminescence when excited at the excitation maxima for the lanthanide complex (as shown in figure 4-12). This shows that the luminescence of the fine silt tracer remained stable within the soil environment, and as such it should be possible to detect the tracer following collection with minimal sample treatment or directly in situ.

4.4.2 Fluorescence analysis

The luminescent spectra of the tracers in both wet and dry soil were obtained to determine which would be the best method of detecting the tracer within soil and sediment samples. The tracers were mixed with 2 mm sieved soil and analysed first at field moisture, and then again after air-drying at room temperature overnight. For all tracers and soil types the lowest limit of detection was seen when the air dried 2 mm samples were analysed, as was expected as the background fluorescence due to the organic components of the soil was lower (Tauro et al. 2012). The presence of the fine silt tracers could be detected in all three soil types using a benchtop spectrometer in both wet and dry samples as shown in figure 4-13), however the colloidal clay tracer could not be identified in any wet soil sample (as shown in figure 4-14). This was most likely due to the short luminescent lifetime of this tracer (58.97 μs), meaning the luminescent signal from the lanthanide was lost within the background fluorescence. The colloidal clay tracer could be detected in the dried samples for soils one (as shown in figure 4-14) and two, but not soil three. This was likely to be due to the background luminescent levels present, as this soil was more organic in nature than the other two cultivated soils. An alternative more sensitive Edinburgh instruments research level modular spectrometer, which requires higher operational cost and required a greater level of user training was also used to analyse the samples. This spectrometer uses a more powerful light source, with higher quality optics and a more sensitive PMT detector than the benchtop spectrometer, and as such should be able to discriminate lower intensity luminescent signals. Using this spectrometer the tracer could be detected in all samples (as shown in figure 4-15). This instrument was therefore used for sedimentation studies to allow the detection of the tracer in all soil types, and at lower luminescence intensities, and all analysis was performed on dried samples to reduce the effect of the background fluorescence.

Due to the long luminescence lifetime of the tracer, soil and tracer samples could be analysed with the instrument set in phosphorescence mode allowing for clear identification of the tracer against the soil background. The fluorescence signal of the tracers remained stable in the soil, meaning the tracer would be detectable during deployment. Fluorescence detection of the tracer was performed directly from a sample of filter paper used to filter out the suspended sediment, using a bench top spectrometer.

Analysis of the tracer within soil showed that the tracer interacted with the soil, and that the fluorescence was detectable against the soil background. In order to effectively monitor the level of tracer within the soil over time, it was important to determine the stability of tracer fluorescence over time.

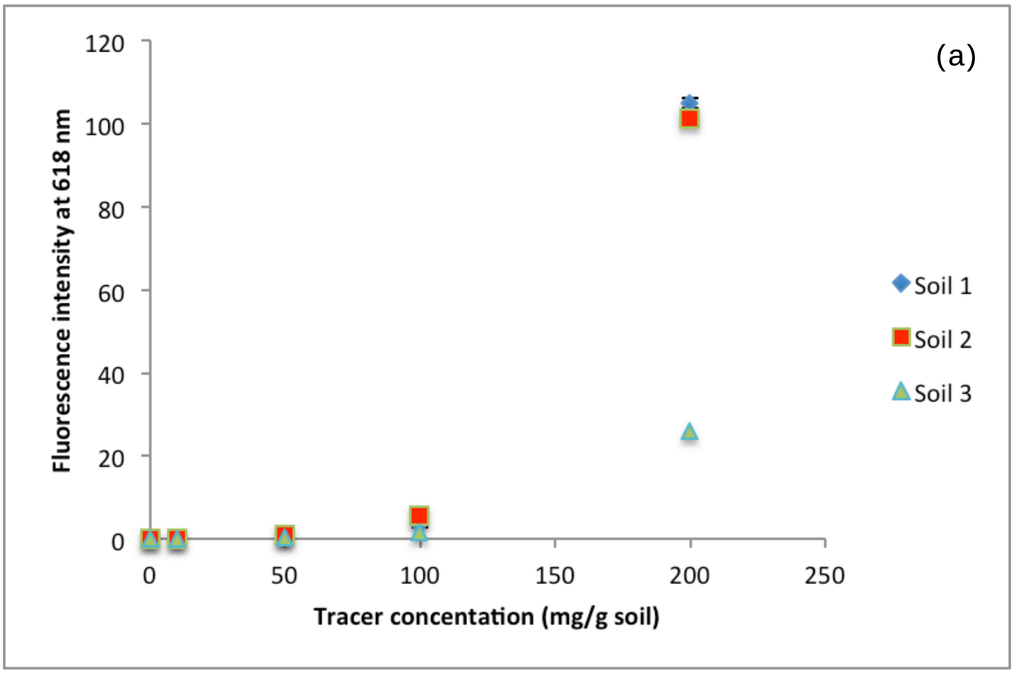

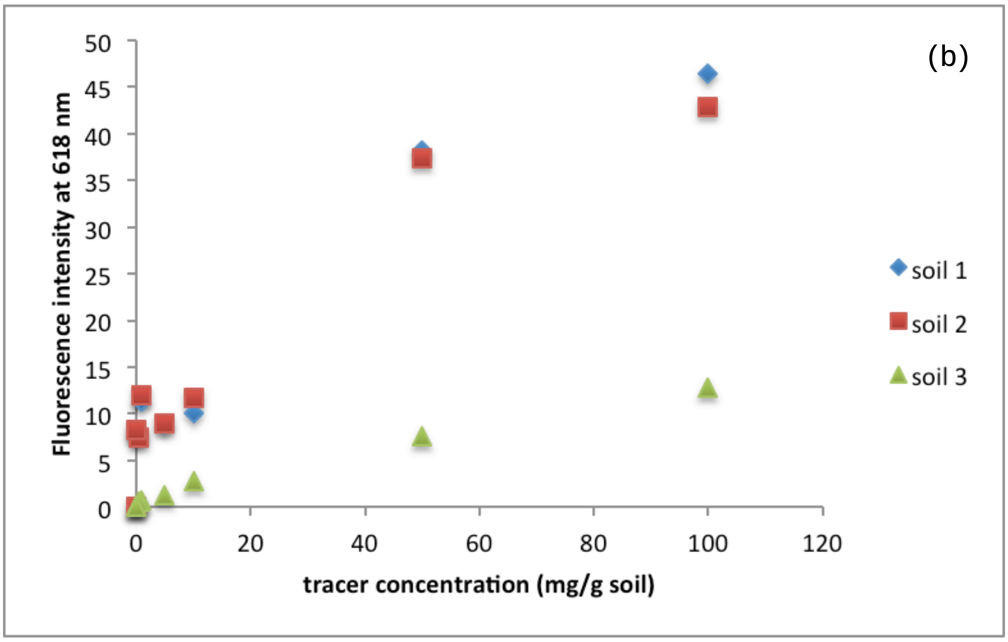

Figure 4-16 Graphs of fluorescence intensity showing luminescence of the fine silt tracer in (a) wet and (b) dry 2 mm sieved soils with a Perkin Elmer LS50B benchtop spectrometer in phosphorescence scan mode, excitation at 350 nm, excitation and emission slit width: 10 nm, 395 nm emission filter, 0.1 ms delay. Dried soil samples contained the same equivalent mass of tracer to soil. Error bars show standard deviation for triplicate measurements on each sample.

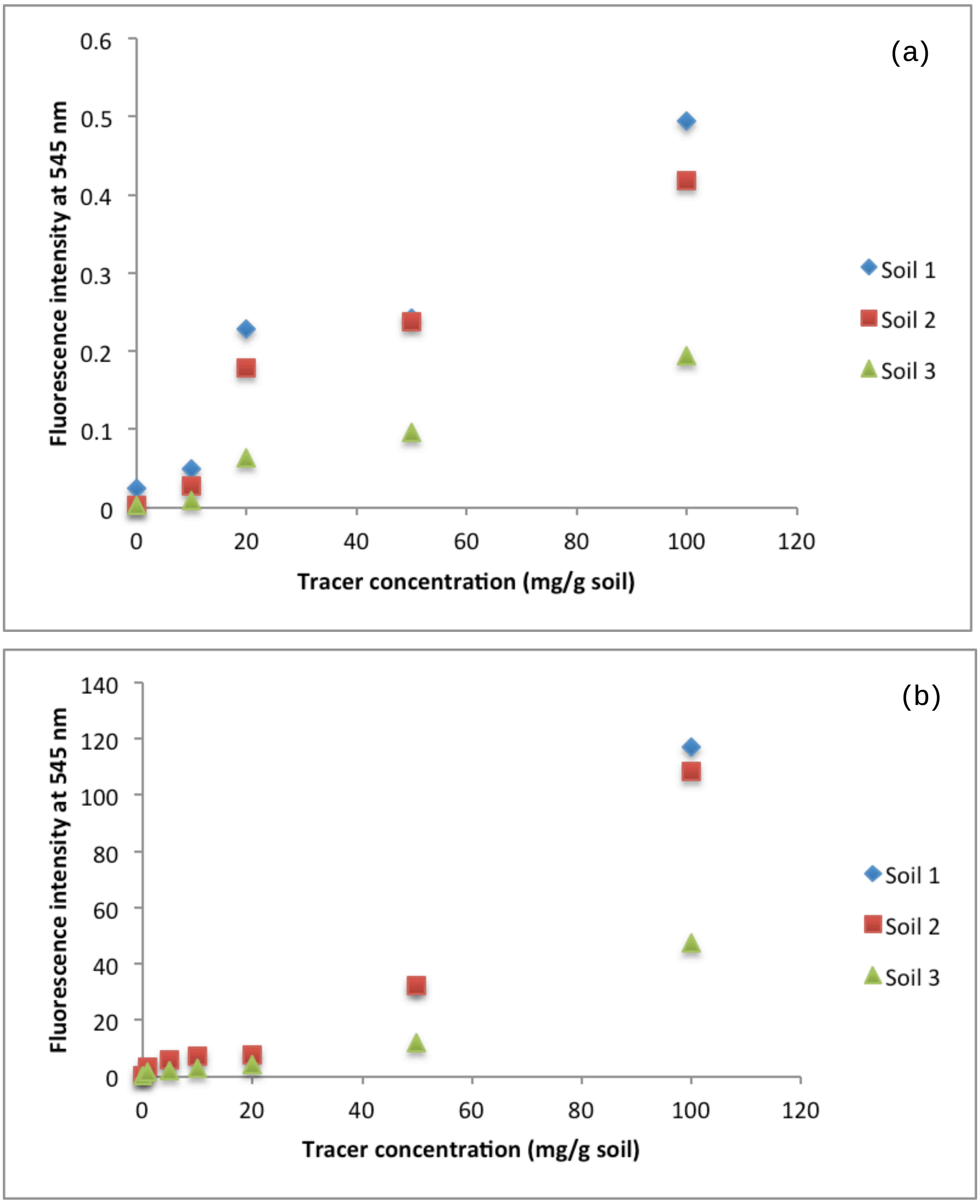

Figure 4-17 Graphs of fluorescence intensity showing luminescence of the clay tracer in (a) wet and (b) dry 2 mm sieved soils with a Perkin Elmer LS50B benchtop spectrometer in phosphorescence scan mode, excitation at 320 nm, excitation and emission slit width: 10 nm, 395 nm emission filter, 0.03 ms delay. Error bars show standard deviation for triplicate measurements on each sample.

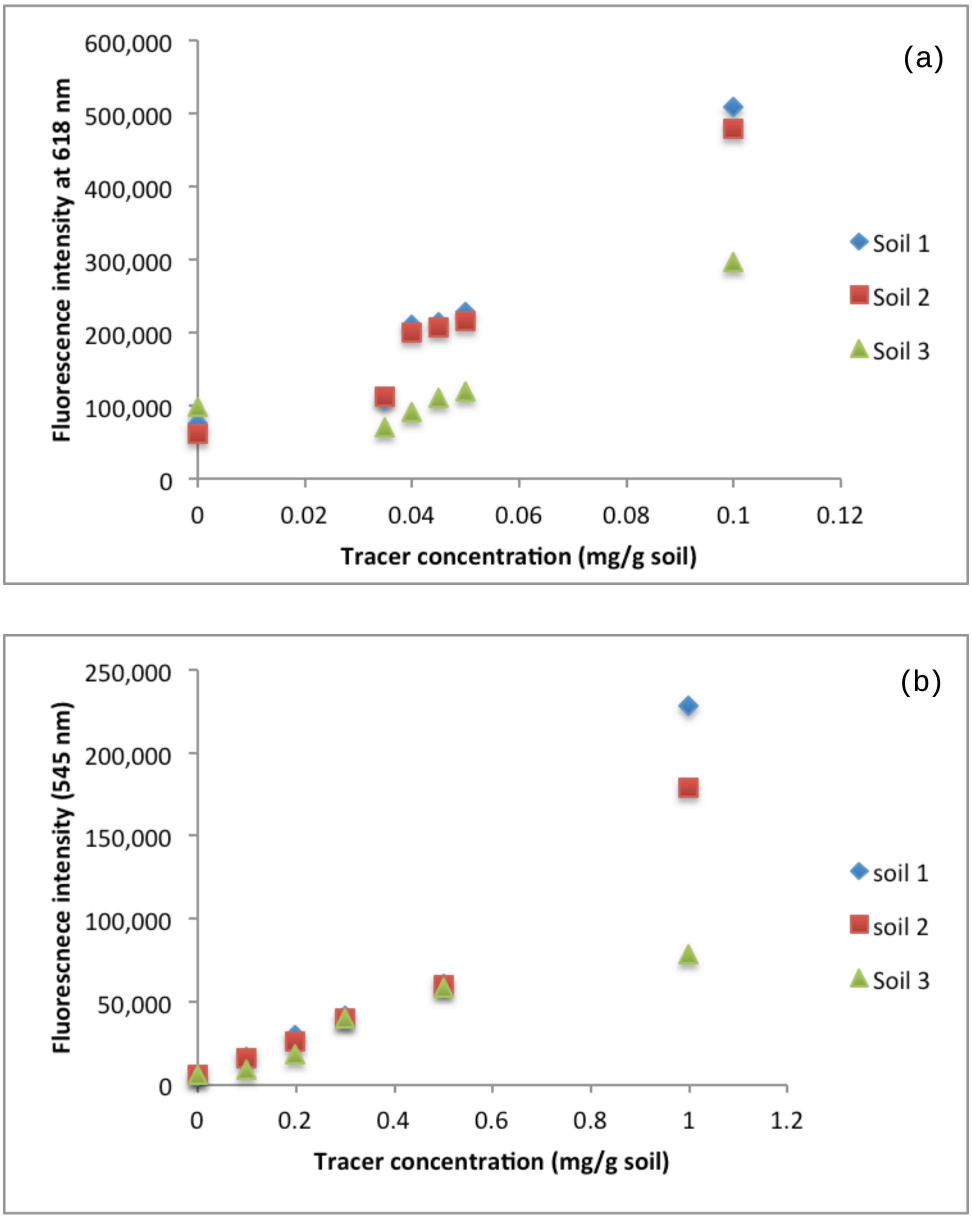

Figure 4-18 Graphs of fluorescence intensity showing luminescence of the (a) fine silt and (b) clay tracer in dry 2 mm sieved soils with an Edinburgh Instruments FLS920 spectrometer in time delay mode, excitation at 320 (clay) or 350 nm(fine silt), excitation and emission slit widths: 4 nm, 395 nm emission filter, 0.2 ms delay). Error bars represent standard deviation of fluorescence intensity between the three simulations performed.

4.4.3 Stability study

In order to determine the length of time during which the tracer could be detected within the soil, the fine silt tracer was mixed at various concentrations with soil 1 and stored at 9 °C, typical of average soil temperatures in Scotland (Stutter et al. 2007). Samples were taken at different time points, and the luminescent intensity of the samples compared to identify any changes over time. Throughout the course of the study, there was a decrease in the intensity of the tracers (as shown in figure 4-16). Over the course of the study there was a high degree of variation in the percentage of the remaining luminescence intensity between the starting tracer concentrations analysed. This was particularly notable after 30 days. This is likely to be partially due to the natural variation of subsampling from a bulk mixture, and therefore some sub-samples may not have been truly representative of the bulk samples. Additionally, as the starting luminescence intensity for the lower concentration mixtures were closer to the soil background levels, these values would have been more greatly affected by variations in luminescent background. This level of variation drops over time, as the level of luminescence intensity drops towards the limit of detection. At this point, it is likely that any variation in the luminescence intensity is due to variation in the soil background. After approximately three months, the luminescence was not discernible from background levels on the Perkin Elmer benchtop instrument. This reduction was likely due to a variety of mechanisms, including leeching and chemical and microbial degradation. Therefore, the useable detection lifetime of the tracer within this soil is three months (one season). This would allow the movement of the tracer to be analysed for about one season after application, with the tracer then dropping below the limit of detection, allowing reapplication later in, or the following, year. The production of calibration curves similar to those in figures 4-13 to 4-15 would allow the actual concentration of the tracer throughout the useable lifetime to be calculated from the measured intensity, taking into account any reduction over time. Thus the tracer could be used to follow seasonal changes, and also provide information on the effectiveness of remediation efforts deployed during the same period in following years, without interference from any previously applied tracer. This would be of benefit in comparison to other applied particle tracers, such as magnetic tracers, for which no reduction in detectable intensity has been reported (Guo-Qing et al. 2011). In addition, the fairly rapid breakdown of the lanthanide complexes within the tracer will lessen any potential toxic effects, as the concentrations of lanthanides contained within the tracer are far lower than those naturally occurring within the environment. Whilst the ligands were chosen because of their reported use in medical (Moore et al. 2010; Moore et al. 2007; Selvan et al. 2010; Xu et al. 2004) and environmental applications (Yantasee et al. 2009), and therefore low levels of toxicity, the breakdown of the organic ligands by chemical and microbial means, will also prevent any potential effects of these molecules within the environment. In order to determine if the tracer was toxic to the soil microbial population, the soil microbial respiration rate was analysed.

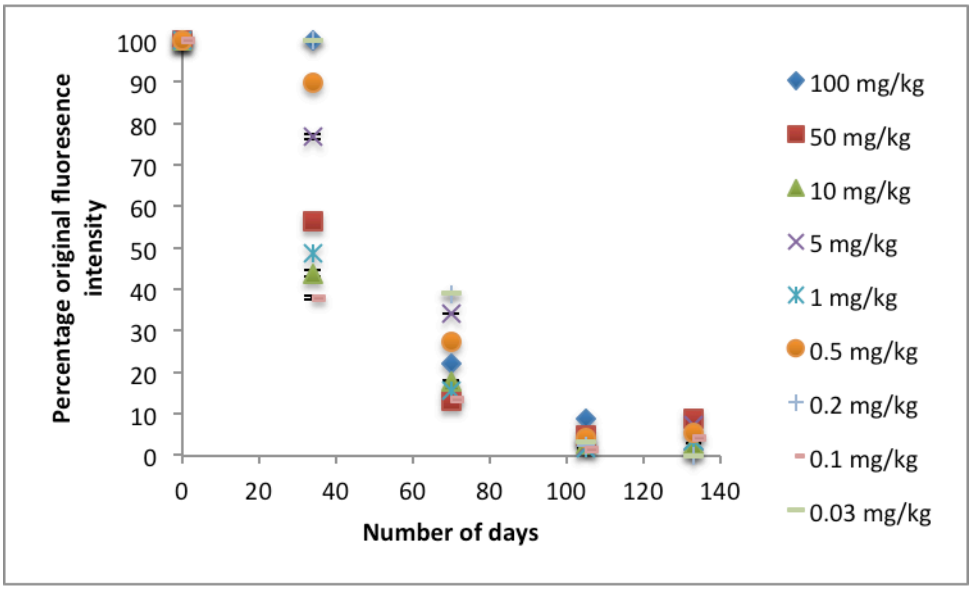

Figure 4-19 Luminescence intensity of the fine silt tracer mixed with soil one and stored at 9 °C in the dark to determine the stability of tracer fluorescence over time.

4.4.4 Soil microbial respiration rates

Soil respiration studies are a commonly used method for assessing the impact of a set of conditions on soil health. Such studies provide an indication for the general effects of treatments on the soil ecosystem as a whole, although tests on individual populations (such as plants and soil invertebrates) are needed to specifically assess any effect on these populations. As such they were used to assess whether the presence of the tracer had any ecological toxicity impacts on the activity of the indigenous soil microbial community (Campbell et al. 2003). The microbial respiration rate was determined in the presence of the lanthanide complexes, doped and undoped silica particles and an alternative particle tracer (Pollard et al. 2007) and using one way ANOVA to identify if any constituent of the tracer was toxic in the soil environment, and also in comparison to commercially-available tracers (as shown in figure 4-17).

The presence of the silica particles themselves, and the alternative particle tracers used (labelled in Table 4-1 as orange tracer), did not affect the respiration rates significantly. One-way ANOVA confirms that no significant difference was present between these three treatments at the 95 % confidence level (p value = 0.987). Grouping information obtained using the Tukey method (Minitab 17, number of families = 5), also identified no significant difference between the treatments at a confidence level of 99.84%. Within soils one and two, a decrease in the glucose induced microbial respiration rate could be seen in the presence of the free complexes. This was most likely due to the effect of the TTA ligand, which is known to be an inhibitor of cellular respiration acting on the respiratory chain at complex II (Ingledew & Ohnishi 1977; Yan & Cohen 2007). However, as the mass of the complex was the same as the mass of the doped tracer, the relative concentrations were far higher than that added within the tracer. This decrease was only seen in samples supplemented with glucose, and the difference was significant for both tracers in both soils under these conditions. In soil three, no significant difference in respiration rate was observed, although the variation in rate for all samples was greater than in the other soils.

For the $Eu(TTA)_3 2PO$ complex, the difference between respiration rates of the soil only and the soil with free complex did show statistical significance at the 95 % confidence level (p value = 0.032). One possibility for this is that the higher organic content of this soil provided a buffer against the effects of the complex, or that the higher and more varied microbial population often associated with more organic soils were less affected by the tracer (Kumpiene et al. 2007; White et al. 1999). Upon incorporation of the complex into the silica matrix to form the tracer, no significant difference in microbial respiration rate was seen between the soil with and without tracer added. This demonstrated that incorporation of the complex within the silica particles reduced its effect upon microbial populations, in addition to the far lower relative concentrations used than with the complex alone. This is believed to be the first study of applied soil particle tracers, and has shown that whilst the complex itself does decrease the microbial respiration rates by up to 33 %, incorporation of the complex into a silica matrix mitigated that effect, and the resulting tracers showed no significant reduction in respiration rate within the soils studied. Comparison between the synthesised tracers and the orange tracer (Pollard et al. 2007), showed that there was no difference in the toxicity of the two tracers synthesised during this study and those previously deployed. As the luminescent intensity of the tracer decreased over time, most likely due to loss of the complex from the tracer particle, it is likely that any toxicity would also decrease over time.

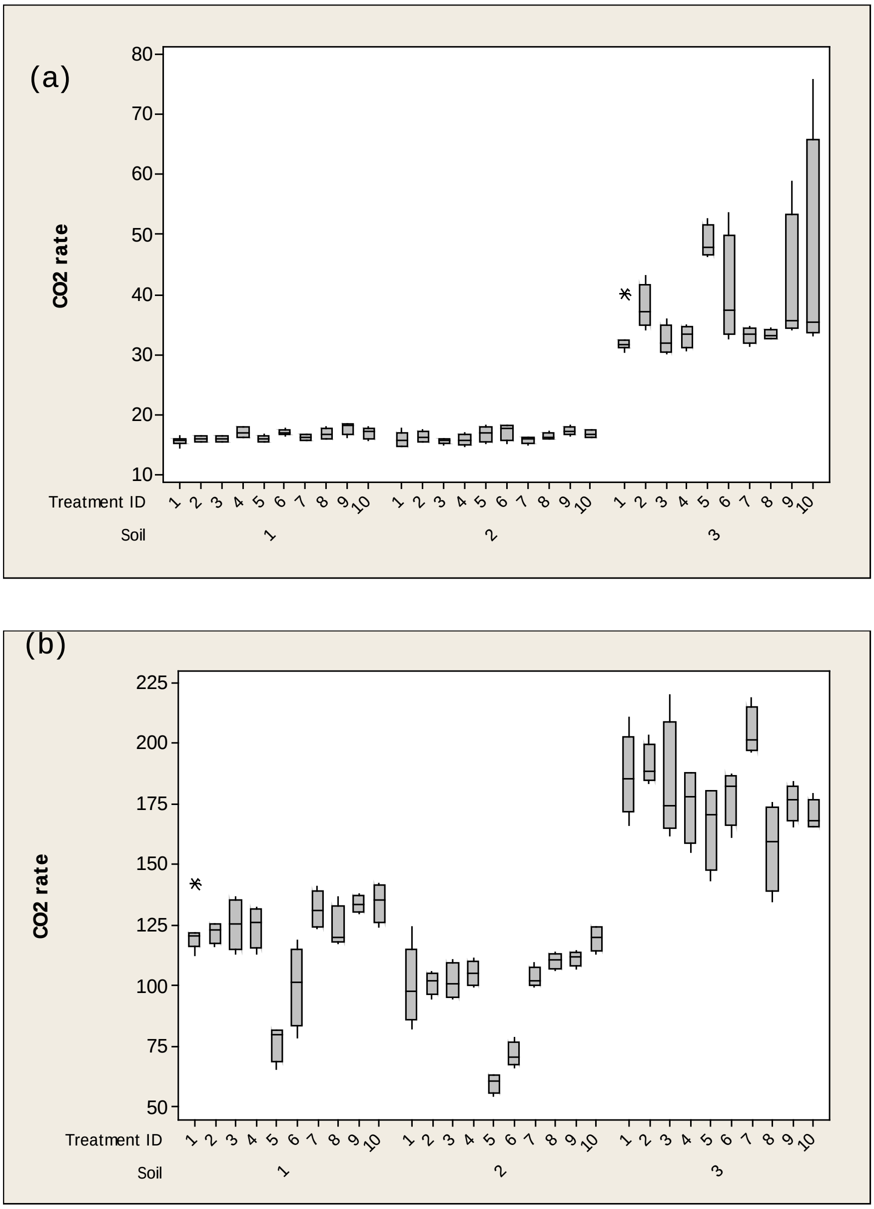

Treatment key:

1 – Soil control

2 – Fine silt tracer (synthesised core)

3 - Fine silt tracer (commercial core)

4 – Clay tracer

5 – Eu(TTA)$_3$2PO

6 - Tb(TTA)$_3$2PO

7 – orange tracer

8 – Clay tracer core

9 – Fine silt tracer core (synthesised)

10 –Fine silt tracer core (commercial)

Figure 4-20 Boxplots showing the CO$_2$ production rate during soil microbial respiration experiments performed using the MicroResp system (a) Basal respiration rate and (b) glucose induced respiration rate.

4.4.5 Soil sedimentation experiments

Soil sedimentation experiments were performed to identify the sedimentation patterns of the synthesised tracer. Each tracer was designed to mimic the processes of erosion, namely suspension versus sedimentation in soil runoff and ultimately a river, of the equivalent size fraction of soils to which they could be applied in erosion studies. Hence, sedimentation experiments were performed within the three different soil types collected to analyse sedimentation behaviour of the tracers with the sampled soils. Samples were analysed initially with an Edinburgh Instruments FLS320 fluorescence spectrometer, which allowed a more accurate analysis of the sedimentation patterns to be obtained, particularly in soil three, where it was not possible to detect the clay tracer using the bench top spectrometer, and was able to detect the fine silt tracer at lower concentrations than in the other, less organic soils.

Analysis of the blank soils (without tracer) did not detect the presence of any terbium or europium specific luminescence, and as such any lanthanide specific luminescence detected in the samples containing tracer demonstrated the presence of the tracers within the sample (as shown in figure 4-18). In soils mixed with the tracers, both the clay and fine silt tracers could be detected in the combined fine silt/clay sample (taken after 40s) (see section 4.2.3.*e*) in all three soils. Within the clay sample (taken after 6 hours of settling time) only the terbium based clay tracer could be detected, with no presence of the europium based fine silt tracer within these samples (as shown in figure 4-18). This was the case for all three soils, and demonstrated that the tracers exhibit similar sedimentation patterns to the natural soil particles under these conditions. As such, the tracers synthesised should behave in a similar manner to natural soil particles during erosion events, and provide an accurate record of soil and sediment movement.

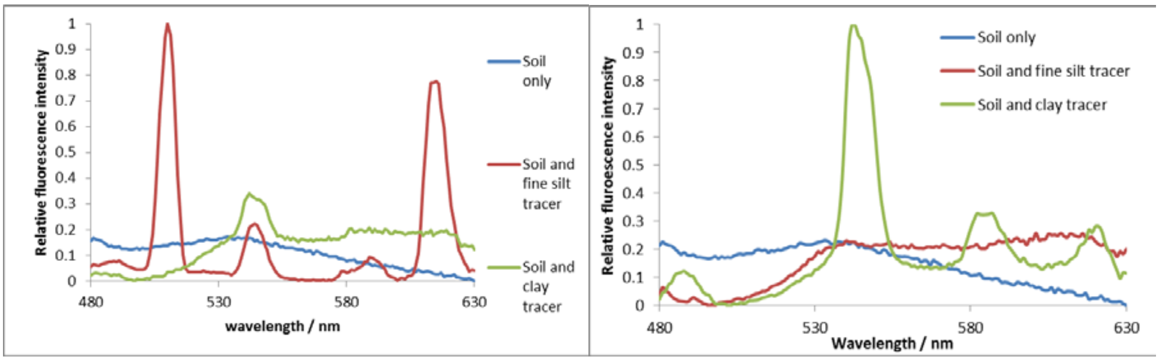

Figure 4-21 soil sedimentation spectra obtained for the fine silt and clay tracers mixed with soil one, (a) after 40 s and (b) after 6 hours (obtained on a Edinburgh Instruments FLS920 in time delay mode, excitation at (a) 350 nm (fine silt tracer) or (b) 320 nm (clay tracer), excitation and emission slit width: 4 nm, 395 nm emission filter, 0.2 ms delay).

4.5 Conclusions

This chapter characterised soils from three different sites within the Glensaugh research station and their interaction with the synthesised tracers. As shown in table 4-3, the bulk densities, C:N ratios and loss on ignition values were typical for soil types within this region, whilst analysis of their particle size distribution indicated that the two tracer sizes synthesised (950 nm and 115 µm), were appropriate for tracing applications involving these soils. SEM and fluorescence microscopy images obtained for the tracers mixed with soils showed that the tracers incorporated into the natural soil particles. For the fine silt tracer, it was possible to visualise the luminescent particles within the soil at field moisture, showing that the europium specific luminescence remained stable in the soil environment. This was further confirmed and characterised using surface reflectance fluorescence spectroscopy of the soil and tracer mixtures. Using this technique it was possible to detect all of the synthesised tracers within the three soils. Over time, a gradual decrease in the luminescent intensity of the fine silt tracer was observed, with the intensity dropping below detectable levels after 105 days. Thus the tracer had a detection lifetime of approximately 3 months, or one season. This would allow the use of the tracers at the same site each year without interference from previously deployed tracers.

Analysis of the tracers potential toxicity within the environment was also investigated via a soil microbial respiration rate assay. This was conducted using both basal respiration rates, and glucose induced respiration rates. Under both conditions, no significant effect on the amount of carbon dioxide produced was identified for any of the synthesised tracers. This indicated that the tracers do not have a toxic effect on soil microbial populations, although further study on the effects on plant and aquatic life would be necessary prior to deployment within environmental sites. Finally, in order to determine the movement of the tracer during erosion events, and within watercourses, a series of sedimentation experiments using the soil and tracer mixtures were performed. These experiments demonstrated that the tracers settled out with their targeted soil fractions (fine silt and clay), and as such should display similar sedimentation behaviours during soil erosion events. Based on this, the tracers were deemed to have appropriate behaviours and characteristics for deployment within laboratory based, small-scale soil erosion simulations prior to application within field systems.

Chapter 5 – Soil erosion simulations

5.1 Introduction

The synthesis of two erosion tracers (chapter 3) and further characterisation of their behaviours within three different soil types (chapter 4), has been performed to determine their suitability for use within a soil environment. Following this, a series of preliminary soil erosion simulations were performed to determine the potential of these tracers to monitor soil movement during erosion events. These simulations were performed within the laboratory at two different rainfall intensities using a prototype rainfall simulator.

5.2 Aim and objectives

The aim of this chapter was to observe the behaviour of the two synthesised tracers during simulated soil erosion events. This was achieved through a series of specific objectives:

- The design and production of a soil erosion simulator for use within laboratory space.
- Calibration of a rainfall simulator to provide constant rainfall intensities.
- Quantification of soil sediment movement within overland flow and water travelling vertically through the erosion plot.
- Determination of fluorescence spectra of collected sediments to identify the presence of the applied tracers.
- Analysis of fluorescence intensity at wavelengths specific to those of the applied tracers to allow estimation of tracer concentrations.
- Analysis of tracer movement in relation to time of rainfall and intensity.

5.3 Development of soil erosion simulator

In order to assess the transport behaviour of the developed tracers within the soil, a series of preliminary laboratory based erosion simulations were performed. The prototype simulator designed for this consisted of two main sections, an erosion plot containing the soil and tracer, and a rainfall simulator designed to produce rainfall of a constant controllable intensity (as shown in figure 5-1).

5.3.1 Rainfall simulator

The rainfall simulator was produced using a plastic enclosure, into which 4 mm holes were drilled every 40 mm (as shown in figure 5-2). Pipette tips (200 µl) were then inserted into these holes, and the gap between the tip and the enclosure sealed with silicone. An additional 8 mm hole was drilled in the side of the box, just above the level of the pipette tips and a section of flexible hose was fixed with silicone to connect the rainfall simulator to the reservoir. The water reservoir consisted of a Marriote bottle with a capacity of 10 L (as shown in figure 5-1). The size of the pipette tips was chosen to create droplets of water, similar to natural raindrops, which would cause disruption and redistribution of the soil by rain splash erosion prior to the movement of the disturbed soil in over land flow (Kinnell 2005).

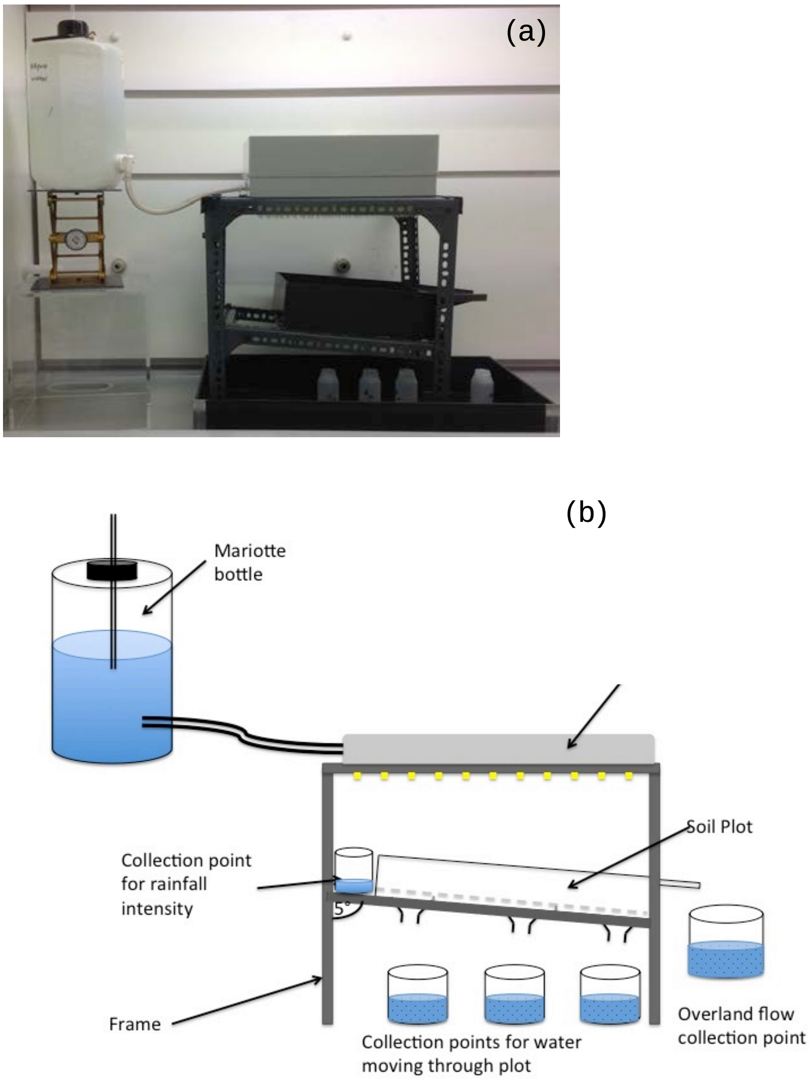

Figure 5 -1 Soil erosion simulator developed for analysis of soil and tracer movement (a) photo (b) schematic.

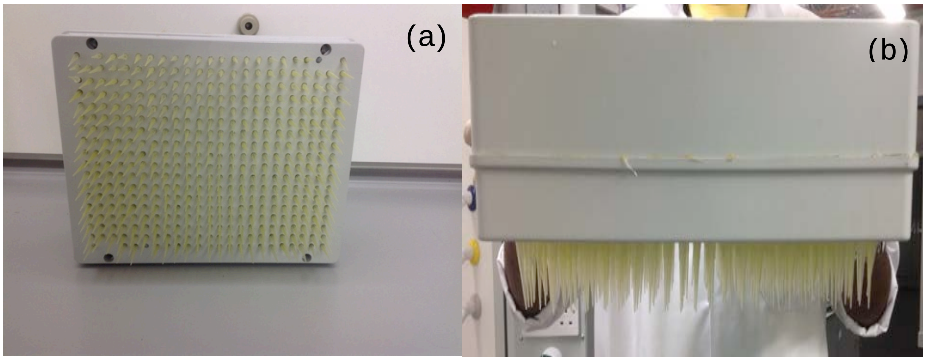

Figure 5- 2 Rainfall simulator developed for use in the soil erosion simulator (a) base view showing tips used to generate raindrops (b) side view.

5.3.2 Erosion plot

The erosion plot was based on one developed by the US Department for Agriculture (Natural Resources Conservation Service 2014) and was constructed of 8 mm thick polyvinylchloride (PVC) to allow thorough cleaning between simulations and reduce the risk of contamination. The design of the plot can be seen in figure 5-3. The plot was designed to allow the movement of sediment and tracer in both the runoff and water that travelled vertically through the plot to be monitored. At the base of the plot, a 200 µm stainless steel mesh was fixed 10 mm off the base of the plot to prevent saturation of the soil, and to allow the water which had travelled vertically through the plot to be collected. This allowed the vertical movement of the tracer to be analysed. The area under the mesh was split into three sections using PVC baffles, and the water from each section collected through 6 mm holes drilled next to each baffle as indicated in figure 5-3 (a). By splitting the plot into three sections, it allowed the effect of horizontal and vertical movement by the tracer through the soil to be analysed. Overland flow was collected via a collector plate positioned at the bottom of the plot, which directed the water into the sampling vessel. In order to ensure uniform packing of the plot, a piece of PVC was cut to the same internal dimensions of the plot, and used to pack to soil to its original density.

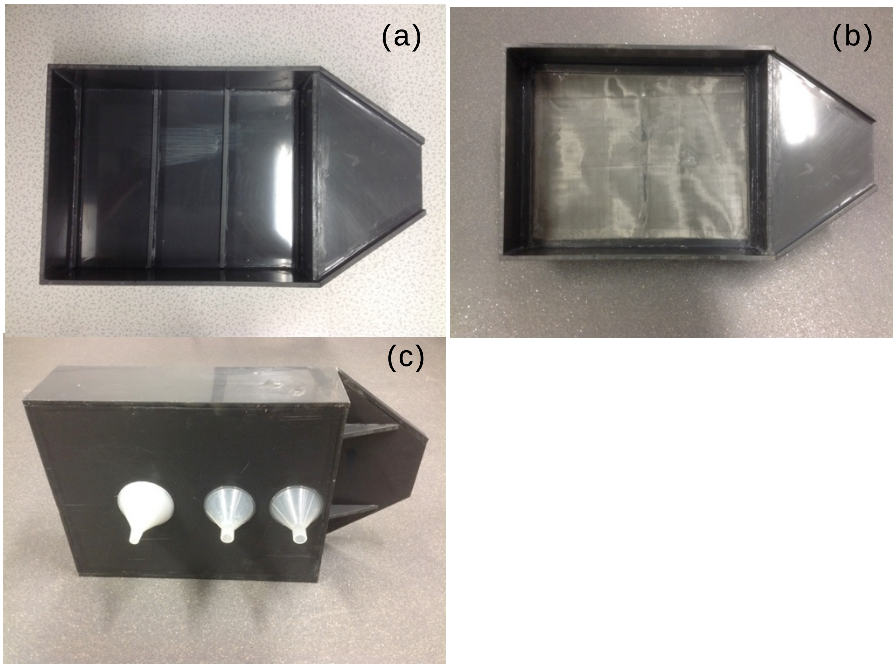

Figure 5-3 Erosion plot developed for use in the soil erosion simulator (a) top view showing division of base plot into three sections (b) top view with soil retaining mesh in place and (c) side view showing overland flow collection plate and collection points for vertical flow. Simulator dimensions 300 x 250 x 100 mm (length x width x height).

The dimensions of the erosion simulator were chosen to allow use within a laboratory, with a quantity of soil that could be obtained with minimal impact to the collection site, easily transported and stored, but which would still provide informative data about tracer behaviour. The frame to support the rainfall simulator and erosion plot was formed from Dexion units and designed to hold the rainfall simulator level, whilst providing a 5° slope angle for the erosion plot. This allowed the erosion plot to simulate a moderate slope, without affecting the performance of the rainfall simulator (Lilly et al. 2009).

5.4 Simulation conditions

All soil erosion simulations were performed using soil one, a brown forest soil collected from the Glensaugh research station (as detailed in 4.2.2.*a*). Soil was obtained from a depth less than 7 cm, and stored in sealed bags in the dark at 4

°C until required. The soil was sieved through a 8 mm sieve to remove the larger stones but allowing much of the soil structure to be maintained. Soil was then packed to a depth of 8 cm within the erosion plot, similar to that of the top soil depth at the collection site. Erosion simulations were run at two different rainfall intensities, similar to that of a high intensity rainstorm, and a more moderate intensity rainstorm in Scotland, 90 and 30 $mm.h^{-1}$ respectively for one hour to allow the behaviour of the tracer to be analysed under different conditions (Kirkbride & Reeves 1993). For each simulations, a weighed amount of soil, to give the equivalent soil density to that of the field (1.08 g/cm^3), was added to the erosion plot and evenly compressed until level with the surface of the erosion plot. The soil was then removed to a depth of 2 cm, from a 1 cm strip, 2 cm from the top of the plot (as shown in figure 5-4). This soil was then mixed with 1 g of both the fine silt and clay tracers, (to give an initial tracer concentration of 1 $g.kg^{-1}$) and then repacked to original density. The reservoir for the rainfall simulator was filled with deionised water. The rainfall simulator was then allowed to flow for one hour, with a final applied volume of 3 or 9 L, and approximately 500 mL samples taken of the overland flow and water that travelled through the plot every 10 minutes. For each simulation, the actual rainfall intensity was also measured. Once collected, the samples were filtered through weighed filter paper (Whatman number 1) to collect the suspended sediments, then dried to constant mass at 45 °C. Samples were also taken from the soil plot, at five different points down the slope, to follow the movement of any tracer which had been redeposited down the plot.

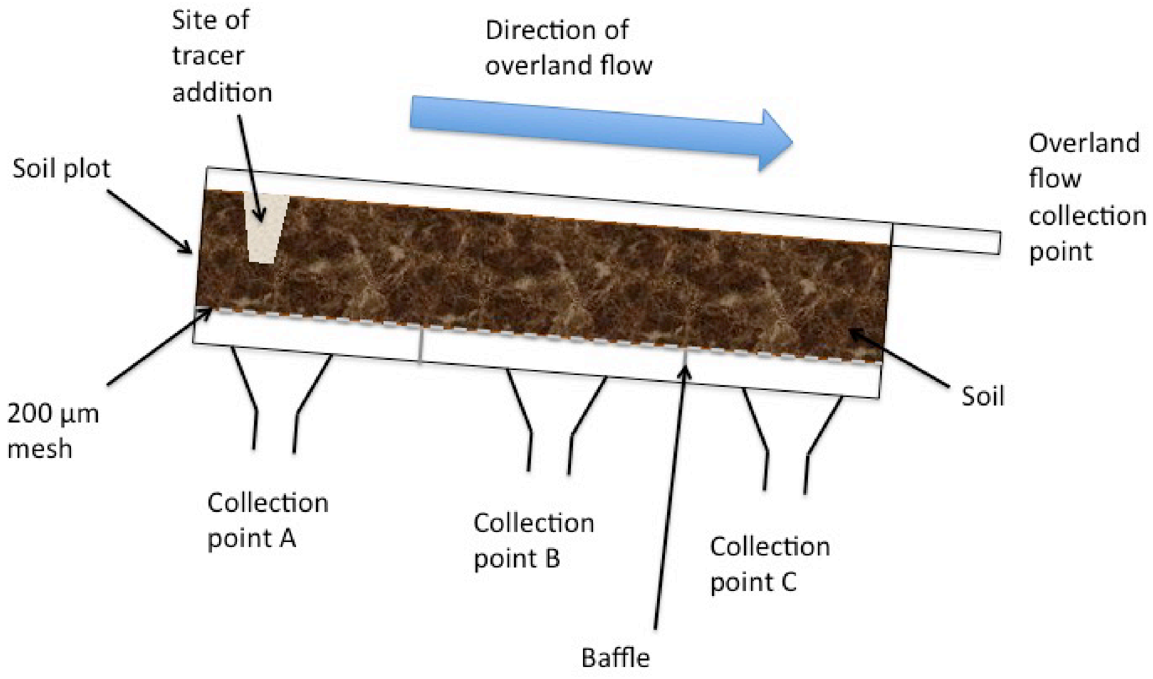

Figure 5-4 Sampling points for soil erosion experiments.

5.5 Results and discussion

The presence of the tracers within the sediments collected was determined using a fluorescence spectrometer for both tracers during each experiment (as detailed in sections 4.4.2 and 4.4.5). This allowed the behaviour of the tracers during the erosion event to be determined. Additionally, the fluorescence intensity at the emission maxima for each tracer was also analysed, to allow an estimation of tracer concentration within the sediments. This provided a measure of tracer movement during the erosion event, allowing the behaviour of the tracer to be compared to that of the soil sediment mass patterns.

The actual rainfall intensity for each simulation was determined using a 50 mL measuring cylinder and can be found in table 5-1. Based on these values it appeared that the simulator was capable of producing reproducible rainfall intensities.

Table 5-1 Measured Rainfall intensities for rainfall simulations.

Simulation	High intensity rainfall (mm.h^{-1})	Low intensity rainfall (mm.h^{-1})
1	86	32
2	89	34
3	93	31

5.5.1 Sediment loss during simulations

The mass of sediment collected during the course of the erosion simulations was analysed to monitor the rate of soil loss.

5.5.1.a High intensity rainfall

The mass of sediment collected within the overland flow increased throughout the course of the simulation (see figure 5-5 and appendix I table A-7). The maximum mass of sediment was obtained between 40 and 60 minutes (60 and 90 mm applied rainfall), varying between the three replicates. This was consistent with the mechanisms involved in soil erosion, which initially involve the detachment of the soil particles via the kinetic energy supplied by the impact of the rain drop (Grismer 2012; Kinnell 2005). This was followed by the movement of the soil away from the plot within the overland flow. Overland flow is formed when the soil becomes saturated or the intensity of the rainfall is too high to allow the infiltration of water through the soil structure (Brady & Weil 2002). The saturation levels of the soil will increase over time, and this will cause the amount of overland flow to increase, carrying more sediment with it off the plot. In addition, the amount of soil particles detached will increase over time, thus increasing the amount of sediment contained within the overland flow. This pattern of increased sediment mass over time has been widely reported elsewhere within the literature (Legout et al. 2013; Tauro et al. 2012; Ventura et al. 2001). This variation in sediment mass could be due to natural variation within the sediment overland flow, or the reduction of soil particle detachment and transport by the formation of a sheet of water covering the top of the soil which reduced the amount of sediment transported. Whilst the soil was repacked to the original field bulk density, the soil structure would have changed, with many of the pathways and spaces within the soil lost, which would affect the way in which water infiltrates through the plot. This will also alter the amount of overland flow, and thus the amount of sediment and potentially tracer which is carried through the plot.

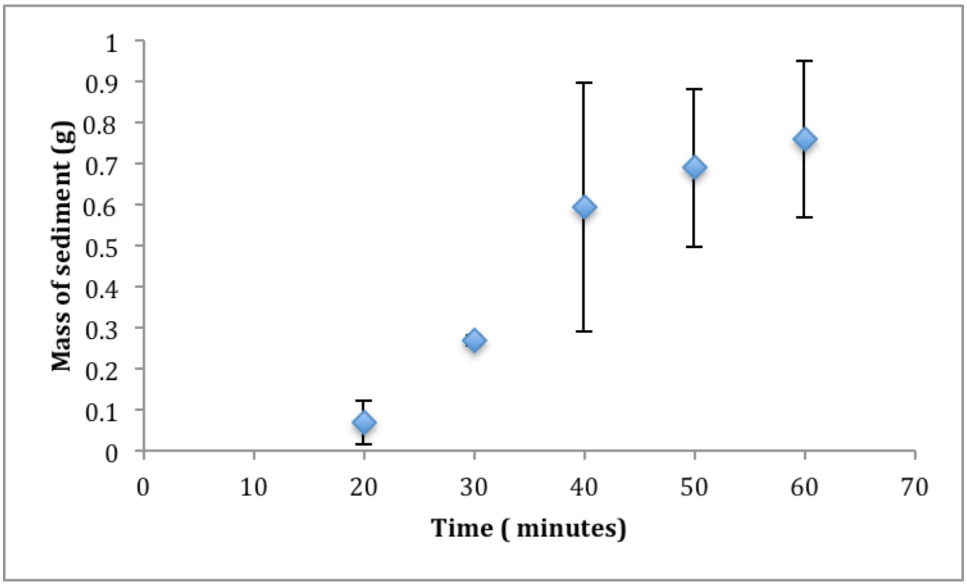

Figure 5-5 Mass of sediment in overland flow collected during high intensity rainfall soil erosion simulations (error bars represent standard deviation of mass between the three simulations performed.).

The mass of sediment collected at collection points A, B and C was also monitored to see if the movement of sediment through the plot followed a similar pattern to that within the overland flow (see appendix I table 7). Analysis of the sediment mass at each point showed that the mass travelling through the plot also increased over time, although the mass collected at each point was lower than that of the overland flow. This was likely due to the slower movement of water through the plot than over it, in conjunction with less detached particles carried down through the plot. The mass of sediment collected was highest at collection point C, which was located at the base of the plot, and lowest at the centre of the plot (collection point B). The flow at collection point C contains soil particles carried diagonally from all points in the plot, in addition to that carried vertically through the end section of the plot, and thus has the greatest time to collect sediment within it. In addition, it is possible that some of the overland flow was deflected downwards when it reached the end of the plot, instead of being carried along the collection plate. As the overland flow contained more sediment than the flow passing through the plot, this could again increase the mass of sediment collected at this point. Similarly, at the top of the plot (collection point A), excess rainwater could travel vertically down the top wall of the plot, carrying sediment with it. At the centre of the plot (collection point B), neither of these effects would occur, and this could explain the lower sediment mass collected at this point.

5.5.1.b Low intensity simulations

As with the high intensity rainfall simulations, the mass of sediment collected during the course of the erosion simulations was used to monitor the rate of soil loss (as shown in figure 5.6).

Less sediment was collected in rainwater that travelled vertically down through the plot than that carried within the overland flow (see appendix I table 8). However, the mass of sediment collected at these points showed a gradual increase, similar to that found within the overland flow. As with the overland flow, the highest mass of sediment was collected after 60 minutes (30 mm applied rainfall) for all experiments at all collection points. This sediment will consist of detached soil particles carried down from the surface of the plot, or detached within the soil structure. Water movement through the plot will also be of less energy, and lacking the initial kinetic energy of the raindrops (Pimentel & Kounang 1998; Bronick & Lal 2005). As with the high intensity simulations, the greater mass of sediment was collected at collection point C.

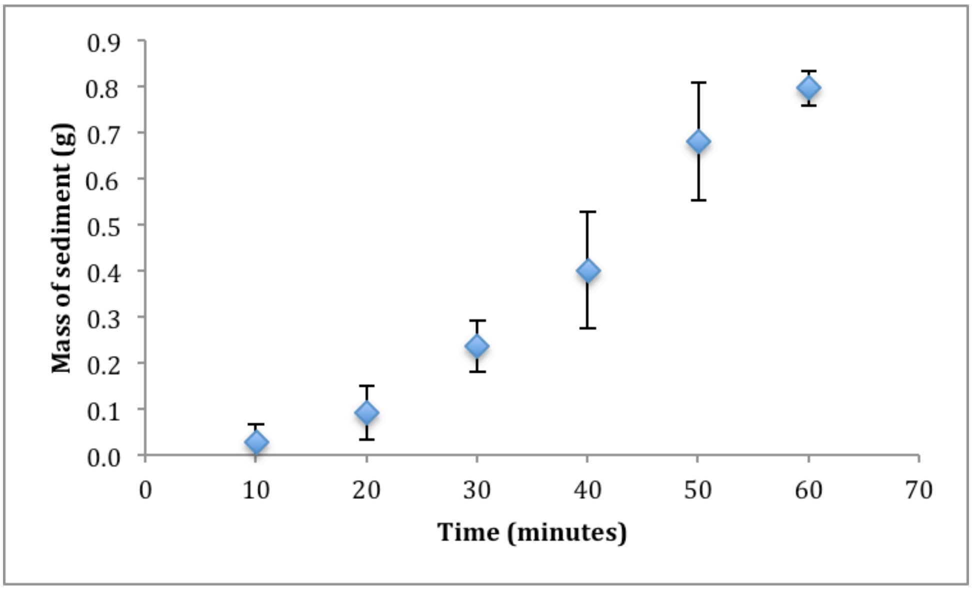

Figure 5-6 Mass of sediment in overland flow collected during low intensity rainfall soil erosion simulations (error bars represent standard deviation of mass between the three simulations performed.).

Figure 5-7 shows the cumulative mass of sediment collected in relation to total rainfall. The total mass of sediment collected during low intensity simulations compared was lower than the high intensity simulations and indicated that the amount of soil erosion which occurs during these low intensity simulations was less than during the high intensity simulations. As can be seen in figures 5-5 and 5-6, a greater movement of sediment occurred earlier in the course of the simulation, for example, between 30-40 minutes 0.4 g of sediment was collected in the overland flow during low intensity simulations whilst 0.6 g was collected in the high intensity simulations. This was as expected, as both the amount of soil particles detected due to the impact of the rain drops, and the amount of overland flow generated to carry the soil from the plot will be less than that of the high intensity simulations (Bryan & Poesen 1989). This has also been shown in other erosion simulations performed (Ventura et al. 2001; Lal 1994; Kinnell 2005).

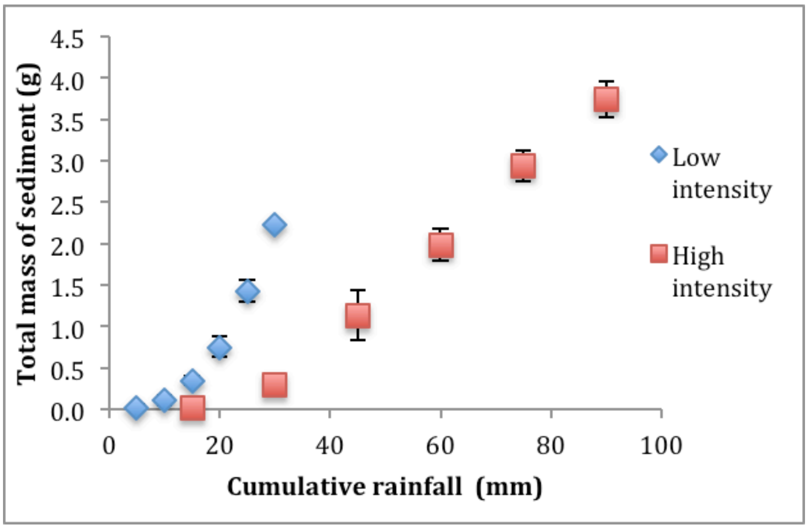

Figure 5-7 Cumulative mass of sediment collected in relation to total overall rainfall during high and low intensity rainfall soil erosion experiments.

5.5.2 Tracer movement during simulations

The fluorescence spectrum for each sample was analysed to determine the presence of the clay and fine silt tracers, using the parameters set out in 4.2.3. Before application of the soil and tracer mixture of soil on to the erosion plot, fluorescence analysis was performed to ensure that the tracers were at detectable levels (see appendix I figure A-6).

5.5.2.a High intensity simulations

It was expected that the tracers would move horizontally along the soil surface in association with soil particles contained in the overland flow, and as such a similar pattern of fluorescence intensity would be seen as for the sediment mass. To determine this, all samples were initially analysed on a Perkin Elmer LS50B bench top spectrometer, however within these simulations, it was only possible to detect the fine silt tracer within one of the replicates (as shown in figures 5-8 and 5-9). The clay tracer was not detected within any of the samples using this spectrometer. Within the second high intensity simulation performed, a clear increase in fluorescence intensity at a wavelength of 618 nm, diagnostic of the fine silt tracer, was seen after approximately 30 minutes (45 mm applied rainfall). The presence of the fine silt tracer was confirmed by the europium specific fluorescence spectra obtained for each sample. The fluorescence intensity, and therefore concentration of the tracer, peaked after 50 minutes

(75 mm applied rainfall), prior to dropping slightly (see figure 5-9). This could be natural variation in the fluorescence intensity of the samples at this point, or could be due to a reduction in tracer and sediment transport at this point. In other simulations a reduction in erosion rates over time have been reported (Kinnell 2005; Ventura et al. 2001). This is hypothesised to be due to the formation of a compact layer of detached soil particles (often termed silt capping) which are not transported with the overland flow, or by the excess water, sitting on the top of the plot, which cannot infiltrate, reducing the effect of the raindrop's kinetic energy on the surface of the plot. (Kinnell 2005; Ventura et al. 2001; Zhang et al. 2008). This process normally results in an increase in overland flow, and therefore an increase in the rate of surface erosion due to the associated increase in surface flow velocity. In order to determine if this was the case during these simulations it would be necessary to run the simulation for longer, and potentially increase the length of the erosion plot.

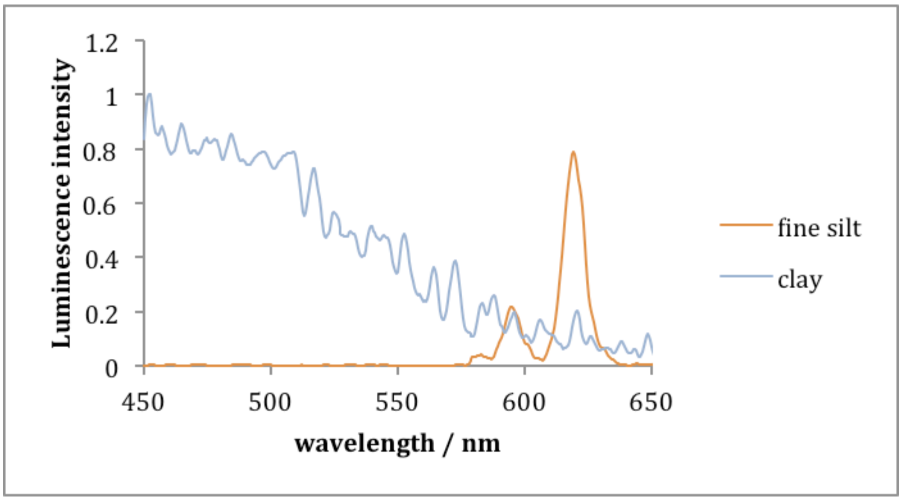

Figure 5-8 Luminescence spectra obtained from sediment collected in overland flow for fine silt and clay tracers (obtained on a Perkin Elmer LS50B in phosphorescence scan mode, excitation at 320 nm (clay tracer) or 350 nm (fine silt tracer), excitation and emission slit width: 10 nm, 395 nm emission filter, 0.03 ms delay (clay tracer) 0.1 ms delay (fine silt tracer)).

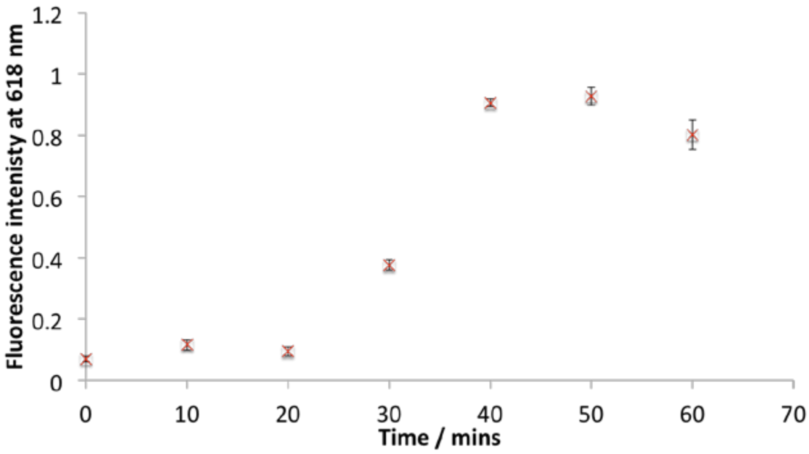

Figure 5-9 Luminescence intensity of fine silt tracer within dried sediment collected from overland flow during high intensity rainfall soil erosion simulation two (obtained on a Perkin Elmer LS50B in single read phosphorescence mode, excitation at 350 nm, excitation and emission slit width: 10 nm, 395 nm emission filter, 0.1 ms delay; error bars represent standard deviation of fluorescence intensity between the three simulations performed).

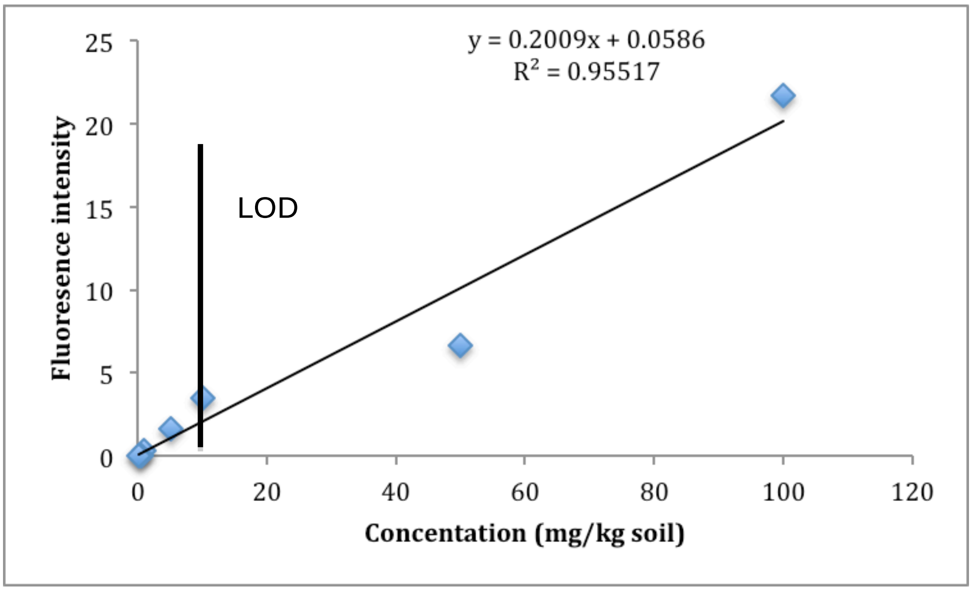

Figure 5-10 Calibration curve for fine silt tracer in soil one (obtained on a Perkin Elmer LS50B in single read phosphorescence mode, excitation at 350 nm, excitation and emission slit width: 10 nm, 395 nm emission filter, 0.1 ms delay).

The concentration of the fine silt tracer within the samples was determined from the calibration curve in figure 5-10, and the results detailed in table 5-2. The limit of detection for the fine silt was calculated to be 0.01 g tracer.kg^{-1} soil for the Perkin Elmer benchtop spectrometer. Limits of detection were calculated as three times the standard deviation of the luminescence intensity measurements divided by the slope of the calibration curve (Thomsen et al. 2003). Standard deviation was taken to be the y-intercept, and calculated using equation 5.1. This gave the lowest luminescence intensity value at which the response could be distinguished from the background, which was then converted to concentration using the equation of the line to give the limit of detection.

$$Limit\ of\ detection\ (LOD) = \frac{3\sigma}{S} \qquad \text{Equation 5.1}$$

Where σ = standard deviation (y residual) and S = slope of the calibration curve.

This was higher than many of the elemental tracers used (typically detectable at ppb concentrations) (Allaire et al. 2009), however the simplicity and low comparable cost of detection for the reported tracer makes it a favourable alternative even with a higher detection limit. The calculated concentrations of tracer within the sediment at different time points showed a maximum concentration of 0.013 g tracer/kg soil after 50 minutes. It is possible that under these conditions it was not possible to detect the tracer at lower concentrations, or that the tracer was not present in concentrations above the limit of detection before 30 minutes. In order to determine which of these is the case, it would be necessary to perform more simulations, with more samples taken (for example every 5 minutes), possibly over a larger plot size to allow for larger masses of sediment to be collected. The limit of detection for the clay tracer was calculated at 0.3 g tracer.kg^{-1} soil.

Table 5-2 Concentrations of fine silt tracer (g/kg soil) contained within sediment collected from overland flow during high intensity simulation 2 (obtained on a Perkin Elmer LS50B in single read phosphorescence mode, excitation at 350 nm, excitation and emission slit width: 10 nm, 395 nm emission filter, 0.1 ms delay) (BLD = below limit of detection).

Time (minutes)	Fluorescence intensity	Tracer concentration
0	BLD	BLD
10	BLD	BLD
20	BLD	BLD
30	0.362	0.007
40	0.475	0.008
50	0.777	0.013
60	0.423	0.008

In order to determine if the fine silt tracer moved in the other simulations, and to identify any movement of the clay tracers, the samples were reanalysed in the more sensitive Edinburgh Instruments FLS920 modular spectrometer. The limits of detection for this instrument were calculated as 0.007 and 0.006 g tracer.kg^{-1} soil for the clay and fine silt tracers respectively. Using this spectrometer, it was possible to identify both the clay and fine silt tracers in the overland flow for all three simulations, indicating that both tracers were transported along the soil plot during the high intensity rainfall (see figures 5-11, 5-12 and 5-14). This was possible as the instrument was more sensitive, and capable of obtaining spectra from luminophores with shorter lifetimes than the Perkin Elmer benchtop spectrometer. However, as can be seen from figures 5-12 to 14, there are large errors associated with the combined data from the three simulations. This is likely to be due to the natural variation in tracer movement during each of the simulations. The data obtained for each individual simulation can be seen in figures A-7 and 8, and tables A-9 and 10, which demonstrates this variation. As can also be seen from these charts the variation in response for each sample within a simulation is lower than that of the Perkin Elmer spectrometer.

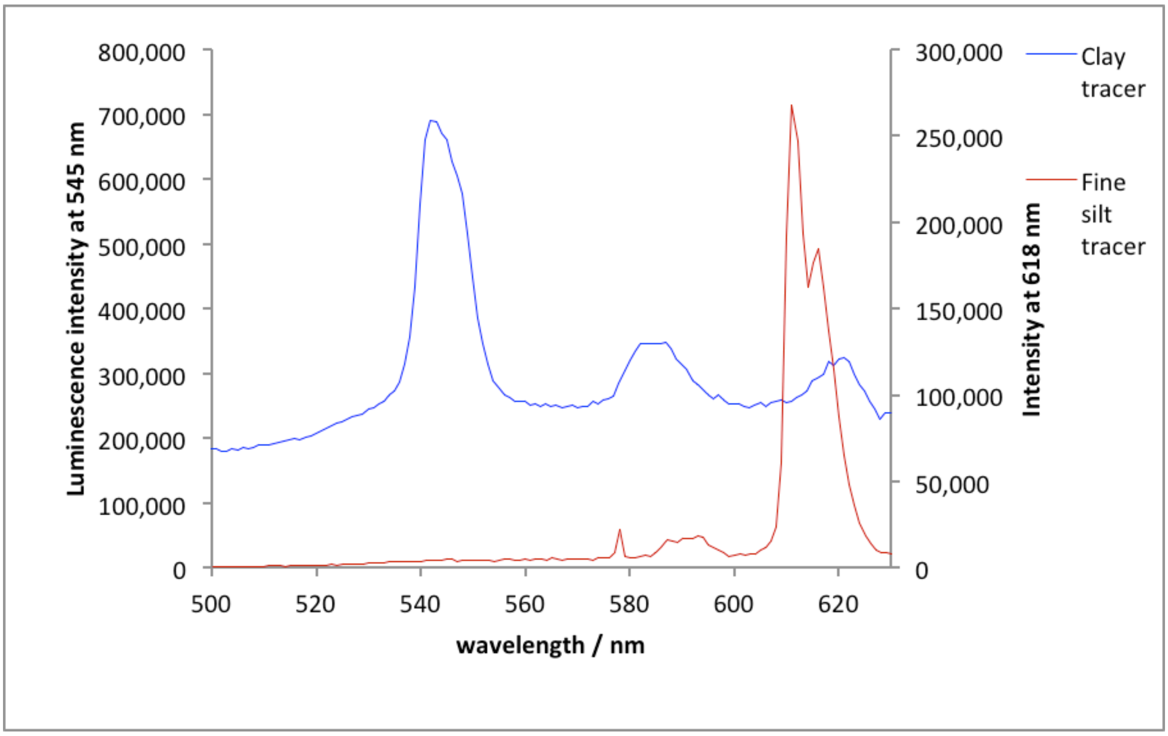

Figure 5-11 Luminescence spectra obtained from sediment collected in overland flow for fine silt and clay tracers (obtained on a Edinburgh Instruments FLS920 in time delay mode, excitation at 320 nm (clay tracer) or 350 nm (fine silt tracer), excitation and emission slit widths: 4 nm, 395 nm emission filter, 0.2 ms delay)

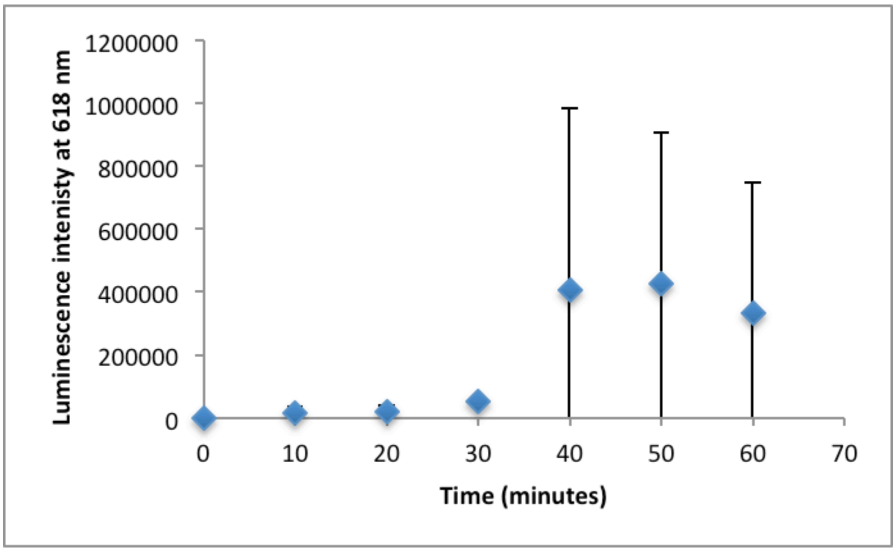

Figure 5-12 Luminescence intensity of fine silt tracer within dried sediment collected in overland flow during high intensity rainfall soil erosion simulations (obtained on a Edinburgh Instruments FLS920 in time delay mode, excitation at 350 nm, excitation and emission slit widths: 4 nm, 395 nm emission filter, 0.2 ms delay). Error bars represent standard deviation of fluorescence intensity between the three simulations performed.

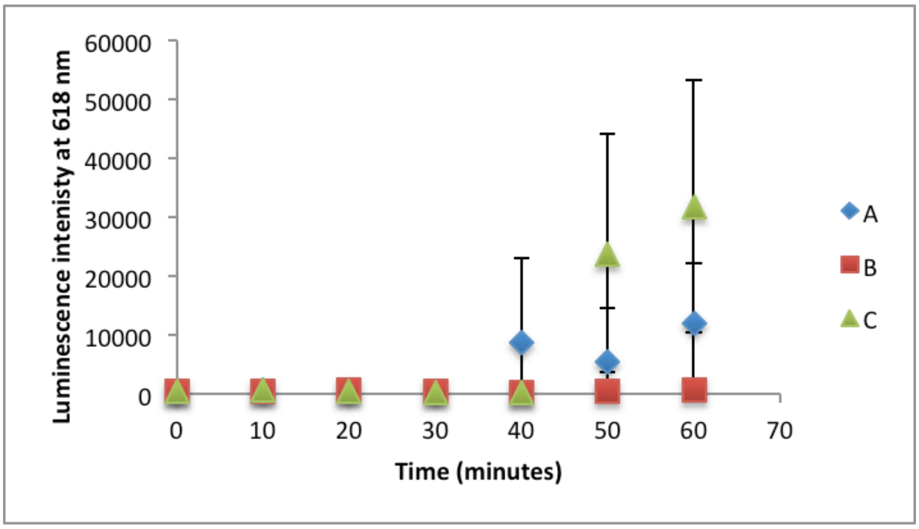

Figure 5-13 Luminescence intensity of fine silt tracer within dried sediment collected during high intensity rainfall soil erosion simulation two at collection points A, B and C (obtained on a Edinburgh Instruments FLS920 in time delay mode, excitation at 350 nm, excitation and emission slit widths: 4 nm, 395 nm emission filter, 0.2 ms delay). Error bars represent standard deviation of fluorescence intensity between the three simulations performed.

The fine silt tracer could be detected at collection points A and C, but not at collection point B. At collection points A and C it was likely that the tracers were present at the highest concentrations (see figure 5-13 and appendix I tables 9 and 10). Point A was beneath the site of tracer deployment, so any water flowing vertically through the plot at this point would potentially contain a higher concentration of the tracer. It was also possible that water could flow down the top of the plot, between the soil and wall of the erosion plot itself. As this flow would not be restricted by movement through the soil itself, with potential redeposition of the tracer within the soil structure, this could again increase the concentration at this point.

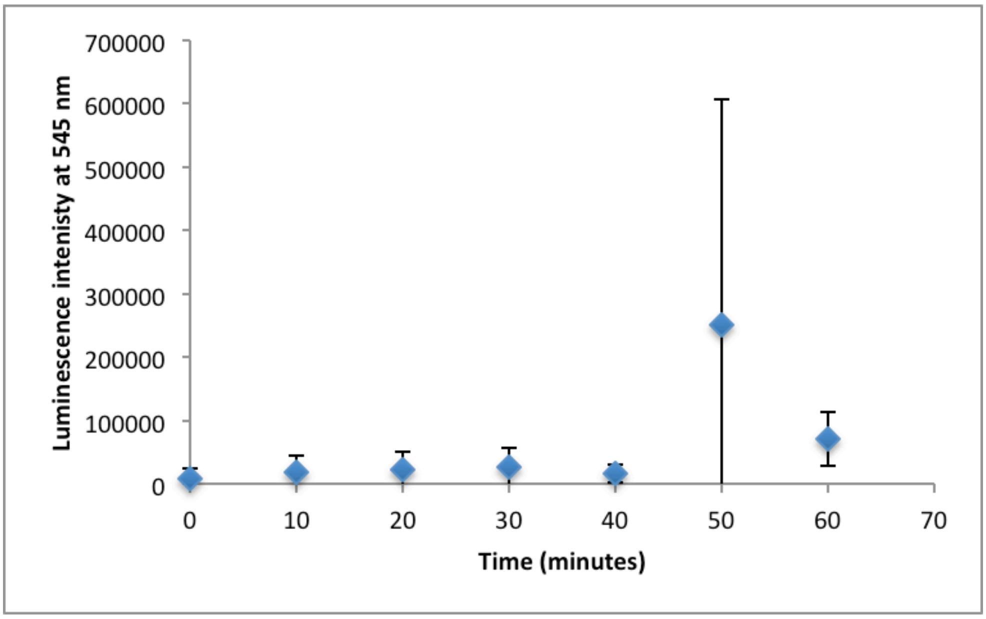

Figure 5-14 Luminescence intensity of clay tracer within dried sediment collected in overland flow during high intensity rainfall soil erosion simulations (obtained on a Edinburgh Instruments FLS920 in time delay mode, excitation at 320 nm, excitation and emission slit widths: 4 nm, 395 nm emission filter, 0.2 ms delay) (error bars represent standard deviation of fluorescence intensity between the three simulations performed.).

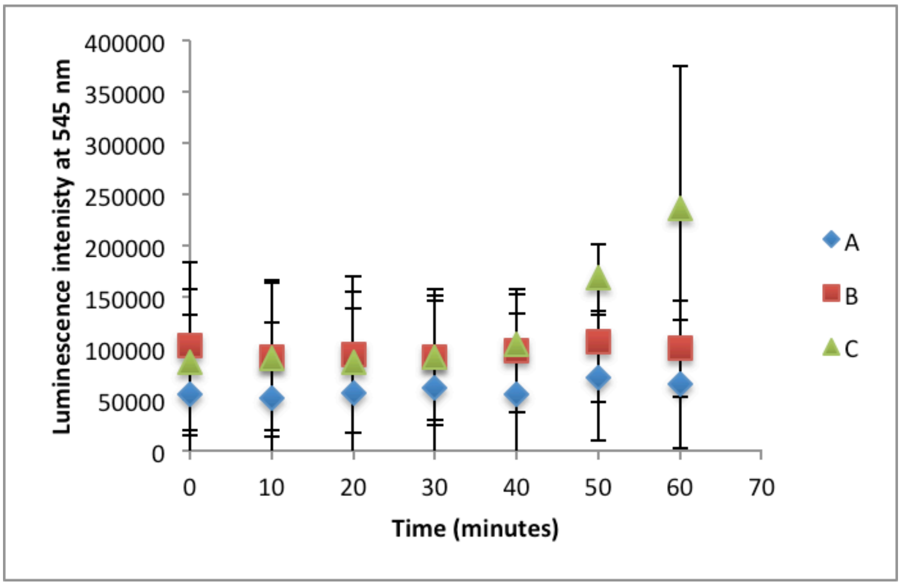

Figure 5-15 Luminescence intensity of clay tracer within dried sediment collected during high intensity rainfall soil erosion simulations at collection points A, B and C (obtained on a Edinburgh Instruments FLS920 in time delay mode, excitation at 320 nm, excitation and emission slit widths: 4 nm, 395 nm emission filter, 0.2 ms delay) (error bars represent standard deviation of fluorescence intensity between the three simulations performed.).

The clay tracer could be detected within the sediment collected at collection point C, but not in the sediments collected at points A and B (see figure 5-15 and appendix I table 11). As at collection point C, tracer which moved both vertically through the plot in the section, along with tracer which travelled diagonally down from the other two sections in the plot would be collected, therefore the concentration of the tracer would be expected to be highest at this point. As with the fine silt tracer, it was possible that some of the overland flow was diverted downwards when it reached the end of the plot, instead of all being carried across the collection plate. This would also increase the concentration of tracer present at this point.

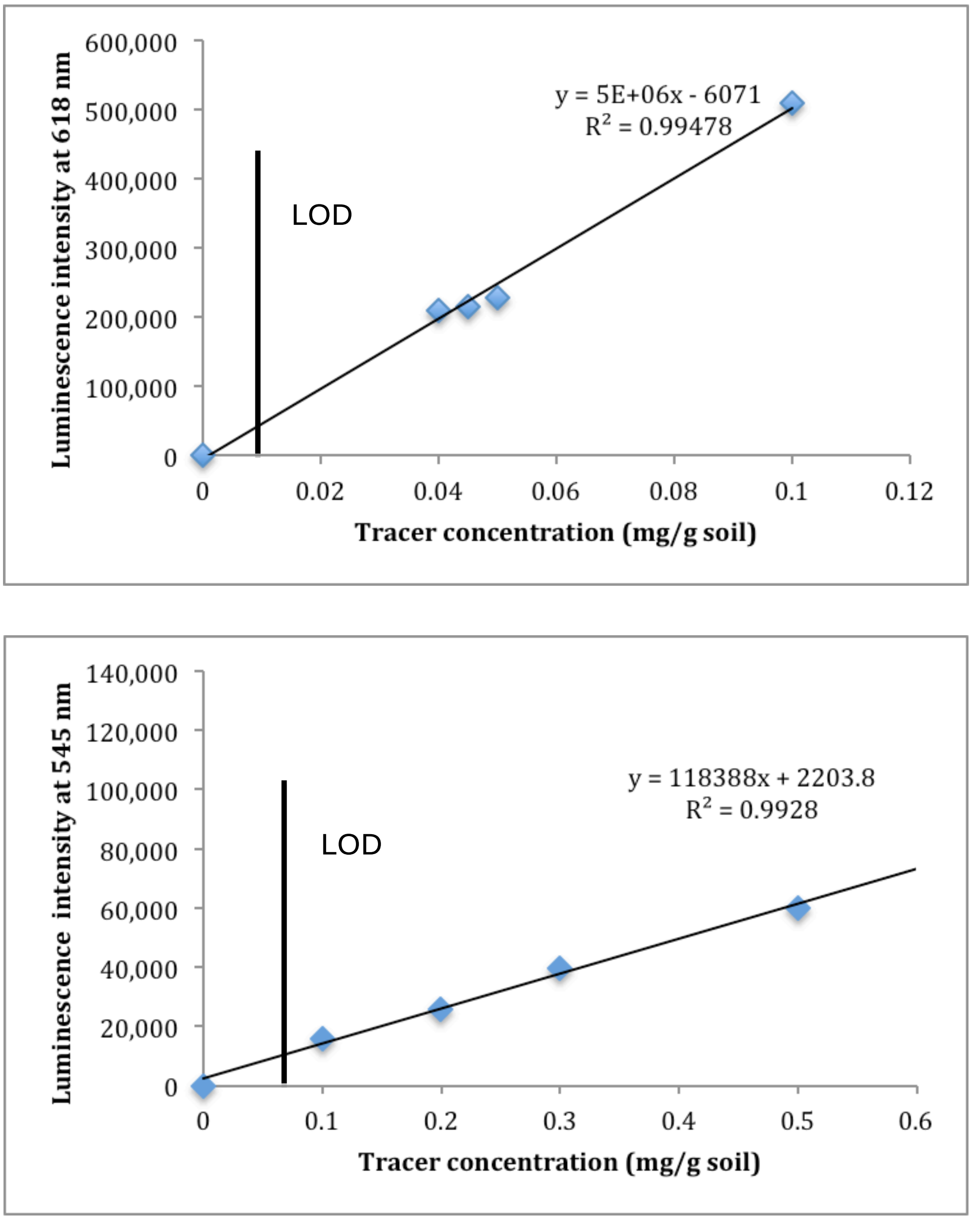

Figure 5-16 Calibration curve for (a) fine silt and (b) clay tracers in soil one (obtained on a Edinburgh Instruments FLS920 in time delay mode, excitation at 350 nm (a) and 320 nm (b) excitation and emission slit widths: 4 nm, 395 nm emission filter, 0.2 ms delay).

In order to quantify the amount of tracer movement, the concentration of each tracer within the samples was calculated using calibration curves (see figure 5-16 and tables 5-3 and 5-4) created from the tracers mixed with soil in known quantities. The data obtained from these calculations indicated that the clay tracer was carried down the plot in greater amounts at 40 and 50 minutes than the fine silt tracer, but was detected in the overland flow and at collection point C at the same time (see tables 5-3 and 5-4). Over all, the total amount of tracer detected in the overland flow was similar for both tracers, 0.24 and 0.27 g for the clay and fine silt tracers respectively. As more clay tracer was found within the sediment collected below the plot (collection points A and C), it is possible that the clay tracer could move more easily with the water travelling through the plot, or bound more strongly to the sediment fractions moved in this manner. Because of the larger size of the fine silt tracer, and the loss of natural soil structure with associated water channels in the repacked soil, it is possible that the majority of movement of this tracer was restricted to the overland flow route. Tracer size could also account for the steady increase in fine silt tracer concentration, as these sediment fractions would move more slowly with the overland flow, than the smaller clay fraction. At collection point A the clay tracer was detected later than the fine silt tracer (50 minutes for the clay tracer, 40 minutes for the fine silt). The concentration of the clay tracer in the collected sediments was 10 to 100 times greater than that of the fine silt tracer, indicating that a greater amount of the originally applied clay tracer is moved than the fine silt tracer. This was in agreement with previously observed patterns of natural soil movement during erosion events, where the clay fraction is preferentially eroded (Legout et al. 2013; Tauro et al. 2012; Ventura et al. 2001). However, the concentration of fine silt tracer remained below the previously calculated detection limits of 10 mg.kg^{-1} at both collection points A and C for the full 60 minutes of the simulation. Whilst it was not possible to distinguish the luminescence intensity of the tracer at 618 nm from that of the background, it was possible to detect the europium specific luminescence of the tracer in spectra of samples taken at this point. Therefore it can be concluded that the tracer was carried through the plot, but below limits at which it could be consistently detected. As soil is a complex chemical and biological matrix, it is likely that the interference caused by background radiation resulting from the soil will vary between samples. This could result in the presence of low concentrations of the tracer being detected in certain samples, whilst being below the limit of detection in others, due to natural variation.

Table 5-3 Concentrations of clay tracer (g/kg soil) collected during high intensity rainfall simulations at collection points A and C (BLD = below level of detection, obtained on a Edinburgh Instruments FLS920 in time delay mode, excitation at 350 nm, excitation and emission slit widths: 4 nm, 395 nm emission filter, 0.2 ms delay).

Time (minutes)	Applied rainfall (mm)	Concentration tracer in sediment		
		A	C	Overland flow
0	0	BLD	BLD	BLD
10	15	BLD	BLD	BLD
20	30	BLD	BLD	BLD
30	45	BLD	BLD	BLD
40	60	0.02	BLD	0.08
50	75	0.01	BLD	0.09
60	90	0.02	0.01	0.07

Table 5-4 Concentrations of fine silt tracer (g/kg soil) collected during high intensity rainfall simulations at collection points A and C (BLD = below level of detection, obtained on a Edinburgh Instruments FLS920 in time delay mode, excitation at 350 nm, excitation and emission slit widths: 4 nm, 395 nm emission filter, 0.2 ms delay).

Time (minutes)	Applied rainfall (mm)	Concentration tracer in sediment		
		A	C	Overland flow
0	0	BLD	BLD	BLD
10	15	BLD	BLD	BLD
20	30	BLD	BLD	BLD
30	45	BLD	BLD	0.02
40	60	BLD	0.01	0.04
50	75	0.01	0.01	0.08
60	90	0.01	0.02	0.13

5.5.2.b low intensity simulations

The fluorescence spectra of all samples were analysed to determine the presence of the clay and fine silt tracers. When the samples obtained during low intensity rainfall were analysed using the standard bench top spectrometer, it was not possible to identify either tracer (see figure 5-18). This was most likely due to lower movement of the tracer during the low intensity, in comparison with the high intensity rainfall simulator events, as the fine silt tracer was detected during the latter. As less sediment was collected, this would again indicate that the tracer moved in a similar manner to the natural soil particles, with less tracer being carried down the plot.

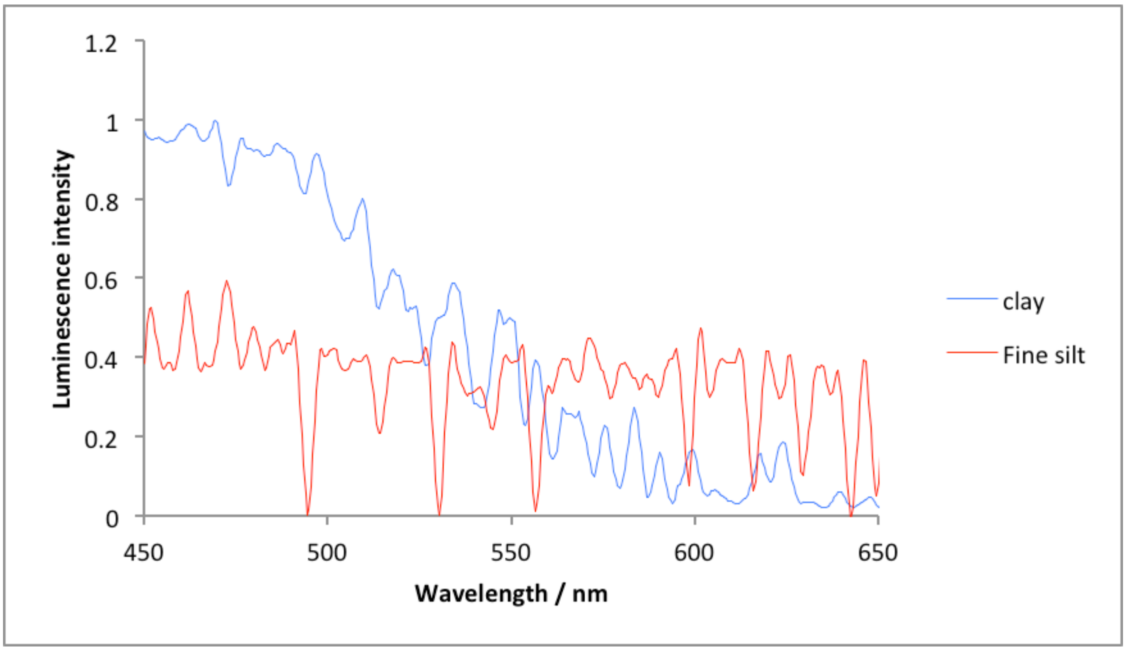

Figure 5-17 Luminescence spectra obtained from sediment collected in overland flow for fine silt and clay tracers (obtained on a Perkin Elmer LS50B in phosphorescence scan mode, excitation at 320 nm (clay tracer) or 350 nm (fine silt tracer), excitation and emission slit width: 10 nm, 395 nm emission filter, 0.03 ms delay (clay tracer) 0.1 ms delay (fine silt tracer)).

In order to determine if the tracer had moved with the sediment during the low intensity events, the samples were then reanalysed using a the Edinburgh Instruments spectrometer. Within certain overland samples, it was possible to detect both the fine silt and clay tracers, demonstrating that the tracers moved with the soil particles during low intensity rainfall (see figure 5-18).

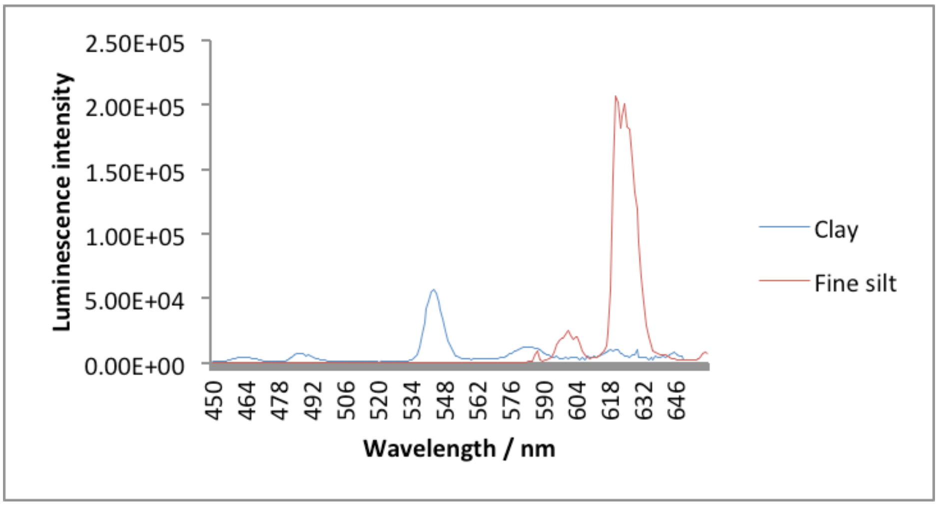

Figure 5-18 Luminescence spectra obtained from sediment collected in overland flow for fine silt and clay tracers (obtained on a Edinburgh Instruments FLS920 in time delay mode, excitation at 320 nm (clay tracer) or 350 nm (fine silt tracer), excitation and emission slit widths: 4 nm, 395 nm emission filter, 0.2 ms delay).

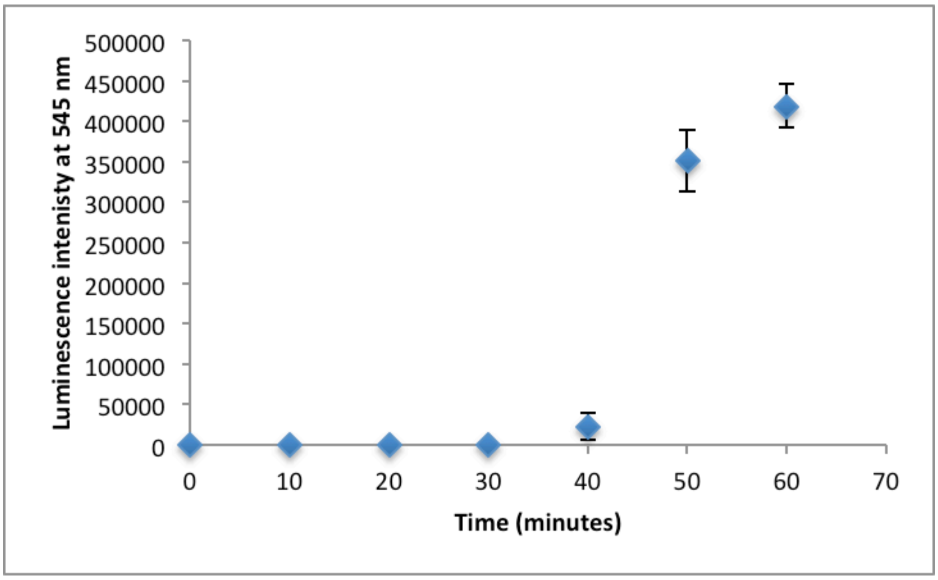

Figure 5-19 Luminescence intensity of fine silt tracer within dried sediment collected in overland flow during low intensity rainfall soil erosion simulations (obtained on a Edinburgh Instruments FLS920 in time delay mode, excitation at 350 nm, excitation and emission slit widths: 4 nm, 395 nm emission filter, 0.2 ms delay). Error bars represent standard deviation of fluorescence intensity between the three simulations performed.

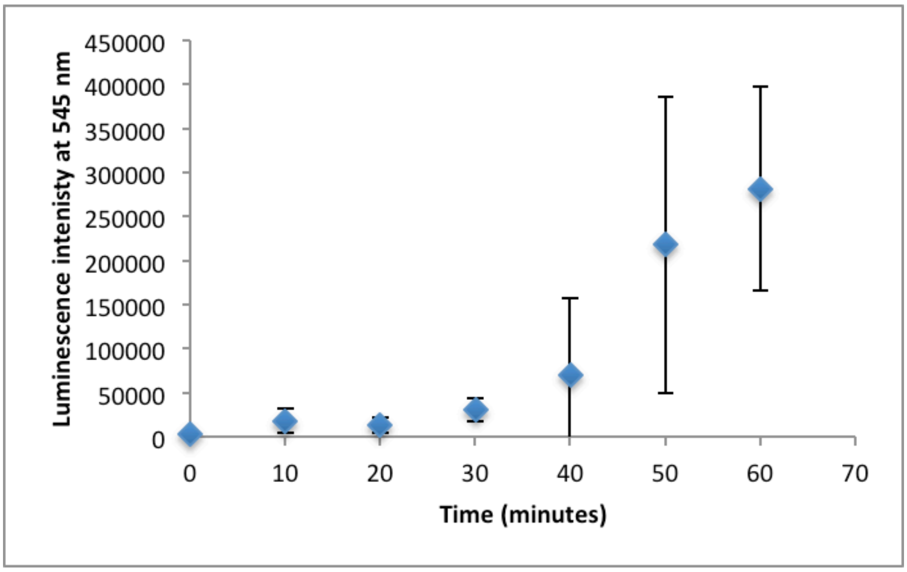

Figure 5-20 Luminescence intensity of clay tracer within dried sediment collected in overland flow during low intensity rainfall soil erosion simulations (obtained on a Edinburgh Instruments FLS920 in time delay mode, excitation at 320 nm, excitation and emission slit widths: 4 nm, 395 nm emission filter, 0.2 ms delay). Error bars represent standard deviation of fluorescence intensity between the three simulations performed.

Both the fine silt and clay tracers were detected within the overland flow after 40 minutes, with the concentrations increasing until the simulation was ended at 60 minutes (see figures 5-19 and 5-20 and appendix I tables 11 and 12). This was later than was seen during high intensity rainfall simulations, and indicates that the tracer was carried less quickly down the plot during the low intensity simulations. This was in agreement with the soil sediment masses, which were also lower in the low intensity simulations. It was not possible to determine whether the two tracers were carried at the same rate down the plot, or whether the clay tracer travels more quickly down the plot, as the detection limit of the clay tracer is higher than the silt tracer. As a result, the clay tracer could be detected at the same time as the fine silt tracer because it was either carried at the same rate down the plot, or could be carried more quickly, but not reach the detection limit until the same time as the silt tracer. As with the high intensity flows, there was a high degree of variation between the three simulations, as shown in figures A9 and 10.

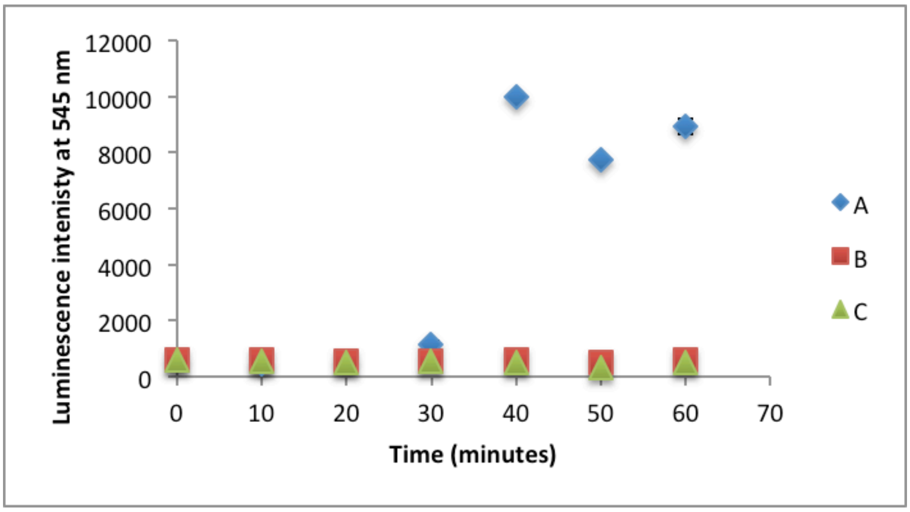

Figure 5-21 Luminescence intensity of fine silt tracer within dried sediment transported vertically through the plot, collected at three collection points (A, B and C) during low intensity rainfall soil erosion simulations (obtained on a Edinburgh Instruments FLS920 in time delay mode, excitation at 350 nm, excitation and emission slit widths: 4 nm, 395 nm emission filter, 0.2 ms delay) (error bars represent standard deviation of fluorescence intensity between the three simulations performed.).

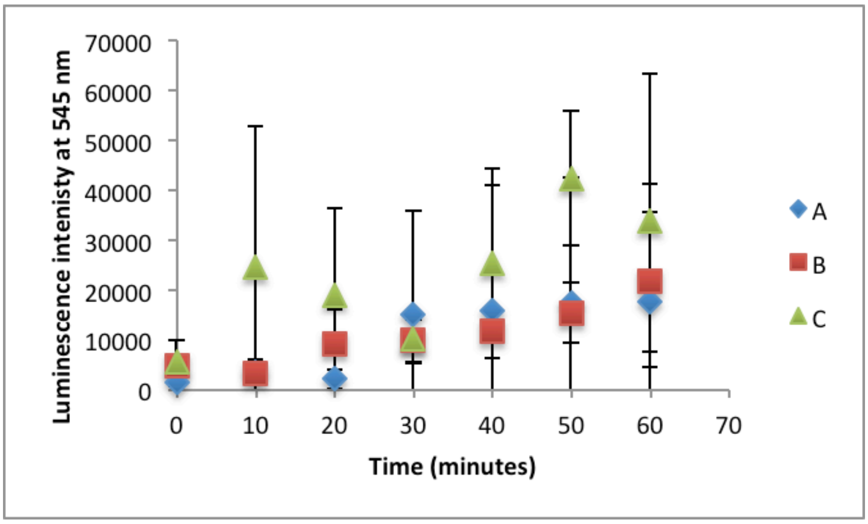

Figure 5-22 Luminescence intensity of clay tracer within dried sediment transported vertically through the plot, collected at three collection points (A, B and C) during low intensity rainfall soil erosion simulations (obtained on a Edinburgh Instruments FLS920 in time delay mode, excitation at 350 nm, excitation and emission slit widths: 4 nm, 395 nm emission filter, 0.2 ms delay) (error bars represent standard deviation of fluorescence intensity between the three simulations performed.

As the tracers were only detected within the overland flow at quantifiable levels during the low intensity rainfall simulations, it was only possible to calculate tracer concentrations for these sediments (see table 5-5). Whilst the tracer was detected within sediments collected at collection point A, the luminescence intensity was too low to reliably detect in all three replicates and therefore quantify.

Table 5-5 Concentrations of tracer collected in overland flow during low intensity rainfall events

Time (minutes)	Applied rainfall (mm)	Concentration tracer in sediment (g tracer / Kg soil)	
		Clay	Fine silt
0	0	BLD	BLD
10	5	BLD	BLD
20	10	BLD	BLD
30	15	BLD	BLD
40	20	0.03	0.00
50	25	0.11	0.07
60	30	0.14	0.08

The relative concentrations of clay and fine silt tracer showed that, as with the high intensity rainfall simulations, more of the clay tracer was carried along the plot than the fine silt tracer. In addition, this concentration of tracer showed a marked increase between 40 and 50 minutes. Within the fine silt tracer, the concentration at 40 minutes was below the quantification limit of the tracer, although the presence of the europium specific luminescence emission within the fluorescence spectrum obtained indicated that the tracer had moved with the soil at this time point. It was not possible to detect the tracers in the sediments that passed vertically through the plot (see figures 3-21 and 3-22 and appendix I tables A-11 and A-12). Again, this could have been due to lack of movement of the tracer, or the tracer being present at levels below the limit of detection, with further study required to determine which.

5.6 Conclusions

A prototype laboratory based soil erosion simulator has been developed, which allowed erosion simulations at constant rainfall intensities to be performed. The simulator was designed to allow samples of overland flow to be taken at different time points during the simulation, which allowed analysis of tracer movement over time. In addition, samples of water and sediment that passed through the plot were also collected at three discrete sample points. This allowed both vertical and horizontal movement of the tracers through the soil to be determined. The rainfall simulator integrated into the erosion simulator provided rainfall of constant intensity between 30 ±1.5 and 90 ± 3.5 $mm.hr^{-1}$. The rainfall produced was formed of discrete droplets, similar to that which would occur during a rainstorm, and as such should possess similar kinetic energy. This should allow the erosion mechanisms that occur within the plot to closely approximate those seen during natural rainstorms.

In order to monitor the rate of soil loss during the simulations, the mass of sediment contained within the overland flow and at the three other collection points was monitored at set time points assessed against cumulative volumes of applied rainfall. This demonstrated movement of soil away from the plot, predominately within the overland flow, but also within the water which travelled vertically though the erosion plot. In general, between 10 and 100 times the amount of sediment was collected from the overland flow, than the flow travelling vertically though the plot under both simulation conditions. The mass of sediment collected within the high intensity rainfall simulations was greater at all collection points than for the low intensity simulations, indicating that the rate of soil erosion was greater at higher rainfall intensities, as expected. This has also been reported in other erosion simulations (Ventura et al. 2001), and within natural soil erosion events (Grismer 2012; Kinnell 2005).

The movement of the tracer was monitored through the emission spectra obtained from the sediments collected. The presence of the tracer was initially positively identified through the lanthanide specific luminescence emission for each tracer. Following on from this, the fluorescence intensity at the emission maxima for the two tracers (545 and 618 nm for the clay and fine silt tracers respectively) was determined to allow the concentration of the tracer present within the samples to be estimated from calibration curves generated prior to the erosion experiments.

It was only possible to detect the fine silt tracer in the overland flow of one replicate of the high intensity flow simulations with the bench top spectrometer, as the concentration of tracer within these samples were below the limit of detection for this instrument. None of the samples analysed in this manner identified the presence of the clay tracer. However, when samples were reanalysed using a more sensitive modular spectrometer, it was possible to detect both tracers in the sediment collected from overland flow over time in all experiments. Analysis of these sediments showed that the tracer moved down the plot over time, appearing at approximately the same time in the overland flow. This indicated that the tracers move in a manner approximating the movement of natural soil particles under these conditions. Analysis of the concentrations of the tracers within the sediments strengthened this conclusion, with the clay tracer transported at higher concentrations than the fine silt tracer.

Movement of the tracer vertically through the plot was also analysed. This demonstrated that the tracer moved through the plot at the top and bottom sections (sections A and C), and in lower amounts than in the overland flow. The presence of the tracer within the sediments collected at these points indicates that the tracer can be used to monitor vertical movement of soil particles through a site of interest, as well as in any run off from the site. Analysis of the concentrations of the two tracers in the samples also demonstrated that increased rainfall intensity resulted in earlier and greater movement of the tracer. The pattern of observed changes in tracer concentrations also varied between the two intensities, with the high intensity rainfall simulations showing an earlier peak in concentration, followed by a decrease, whilst a constant increase was seen in the low intensity concentration. This could be due to the length of time the simulations were run for, and the same pattern might be observed later in the low intensity simulations if the time was extended. These simulations have demonstrated the effectiveness of the tracers during simulated erosion events at two different rainfall intensities, and show that the tracers are suitable for further testing and deployment as soil erosion tracers in larger scale experiments.

Chapter 6 – Overall summary and future work

6.1 Introduction

The importance of appropriately managing the soil resource has been well documented. An estimated 80 % of the worlds soil resource is predicted to have been affected by soil degradation, with soil erosion the single greatest contributor to this degradation (Ashman & Puri 2002). In order to accurately assess the effect of soil erosion and monitor remediation attempts, an effective method of tracing eroded soils and sediments from source to fate is vital.

The aim of this thesis was therefore to develop stable luminescent tracers that bound preferentially and behaved as natural soil particles, and could be quickly and easily detected within soil and sediment samples, in line with the characteristics set out by Zhang *et al* (2001). This was achieved through a series of specific objectives, detailed in section 1.7.

The soil erosion particle tracers were developed in three stages, firstly through the synthesis of suitable luminescent lanthanide complexes in line with the following objective and detailed in chapter 2:

- The development of a lanthanide chelate complex suitable for use within the environment.

The second stage was the formation of suitable sized silica sol-gel particles, as described in the following objective:

- Preparation of suitable sized silica sol-gel particles, of similar size to commonly eroded soil fractions.

The third stage involved the incorporation of the lanthanide complexes within the particles, as detailed in the following objective.

- Synthesis of lanthanide doped silica particles f a narrow size range for use as a soil particle tracer.

The second and third stages of tracer development can be found in chapter 3.

Having obtained two luminescent tracers, the next stage was to determine their behaviour within characterised soil samples, in line with the following objective:

- Analysis of soil tracer interactions.

Both the characterisation of the soils, and the analysis of the tracer behaviour can be found in chapter 4.

Finally, having obtained and characterised suitable tracers, initial soil simulations within a prototype erosion simulator were performed inline with the following objective.

- Behaviour of the tracers during simulated erosion events.

These simulations are detailed in chapter 5.

6.1.1 Development of a lanthanide chelate complex suitable for use within the environment

Two lanthanide chelate complexes were synthesised during the course of this study. Both were based on 2-pyridinol-1-oxide, a chelator used in the environment for the remediation of heavy metal contaminated watercourses, and also within MRI contrast agents and bioassay detection systems. As such, the environmental effects of the ligand should be minimal. It was found that complexes of this ligand with Tb^{3+} and Eu^{3+} were luminescent, but with low quantum yields. This was believed to be due to the incompletely filled coordination sphere, allowing deactivation of the complex by substances present within the atmosphere, such as molecular oxygen and water. Additionally, for the Eu^{3+} ion, the energy levels of the ion and ligand were similar, allowing back transfer of energy, and non radiative deactivation of the excited state. In order to increase the quantum yield of the complexes, a well-characterised ligand was added to the complex, thenoyltrifluoroacetone (TTA). In the presence of the TTA and 2PO ligands, the quantum yields of the Eu^{3+} and Tb^{3+} complexes increased to 9.9 and 8.8 % respectively. The luminescent lifetimes of these complexes also increased to 482.84 and 58.29 μs for Eu^{3+} and Tb^{3+} respectively, providing fluorophores with a longer window in which they could be read, reducing the effect of any interference from potential biological background fluorescence.

LC-MS analysis of the complexes showed that the molecular mass was consistent with a structure of Ln(2PO)$_3$ and Ln(TTA)$_3$.2PO for the complexes formed. Changes in the proton NMR, FTIR and Raman spectra indicated that the ligands coordinated with the lanthanide ions via the nitrogen and oxygen of the 2PO ligand, and the acetone group oxygens of TTA. TG/DSC analysis did not show the presence of water within the complexes, indicating that the ligands filled the coordination sphere, and that the complexes were anhydrous. Emission and excitation spectra for both these lanthanide complexes showed excitation spectra characteristic of the ligands, and emission spectra characteristic of the lanthanides, indicating that the luminescence seen was lanthanide mediated via the ligands.

The long luminescent lifetime and relatively high quantum yield, coupled with the non-toxic nature of the 2PO ligand and low concentrations of the TTA ligand provided a luminescent complex suitable for use in the environment within a particle tracer.

6.1.2 Preparation of suitable sized silica sol-gel particles, of similar size to commonly eroded soil fractions.

In order to develop particles of suitable size for soil erosion tracing, it was necessary to identify the soil fractions most commonly eroded and then target synthesis of particles within these ranges. Review of the literature highlighted the clay (< 1.2 µm) and fine silt (63-250 µm) fractions as two of the fractions most commonly eroded. Having identified these fractions, two different methods were used to produce silica sol-gel particles of appropriate size. An ammonium hydroxide catalysed sol-gel method was used to develop the clay tracer. A factorial design of experiments was incorporated into the experimental design to allow the effects of length of synthesis, temperature and volume of ammonium hydroxide to be analysed. This identified volume of ammonium hydroxide as the most important factor, with temperature also having a significant effect upon particle size. The length of synthesis did not affect particle size within this study, with final particle sizes obtained after 30 minutes. The particle sizes obtained ranged from 285 – 950 nm, with low size variation and a spherical morphology.

This method yielded particles of 950 nm, within the clay range, and close to the desired 1 µm target, and were therefore suitable for use within the development of a tracer for this size fraction.

An acid catalysed sol-gel method was adopted to produce particles within the fine silt range. This method yielded particles between 91.31 and 168.44 µm, which also possessed low size variation and spherical morphologies. These synthesis reactions were performed at a variety of different stirring speeds, and analysis identified that as the stirring speed increased, the resulting particle size decreased. A final average particle size of 115 µm, for which all particles produced during the synthesis were within the fine silt range, was chosen for use in the development of a fine silt soil erosion tracer. These particles were then doped with the lanthanide complexes synthesised in chapter 2 to provide luminescent tracers.

6.1.3 Synthesis of lanthanide doped silica particles of a narrow size range for use as a soil particle tracer

In order to create a particle tracer whose movement could be easily modelled, and in which all particles were within the size range of the targeted soil fraction a silica sol-gel method was used. The initial incorporation of both the terbium and europium complexes into the particles during synthesis resulted in the formation of particles with a large variation in size and morphology, the majority of which formed amorphous masses. From the literature, it was likely this loss of the characteristic spherical morphology of the sol-gel particles was due to the coordination of the trivalent lanthanide ions with the silica matrix, or the disruption of the silica matrix by insoluble lanthanide hydroxides. To allow the incorporation of the lanthanide complexes into the particles, whilst maintaining the desirable morphology, a core-shell approach was adopted. This allowed the lanthanide complexes to be incorporated into a silica shell formed around a blank ‘core’ particle of suitable size. These core-shell particles retained the spherical shape of the initial particles, and displayed lanthanide specific luminescence when excited at the excitation maxima for the complex. An investigation into the effect of concentration on the morphology of the particles showed that particles doped with the europium complex maintained morphology up to molar ratios of

3 % Eu:Si, whilst the terbium complex retained spherical morphology at ratios of 2 % Tb:Si. Above these ratios, the shell formed an irregular morphology around the core. Analysis of the luminescent intensity of the particles at the different concentrations showed an increase in luminescence with increased lanthanide concentrations. These followed a general upward trend, although for the europium complex there was a sharp, off trend increase at 1.5 %, there was also a similar increase in the amount of lanthanide incorporated into the particles. Analysis of the formation of insoluble lanthanide hydroxides also followed this pattern, indicating that the increased concentration of available lanthanide at this point allowed an above trend incorporation of the complex. As this allowed luminescent particles with similar lanthanide luminesce intensities to that of higher concentrations to be synthesised, with the use of lower amounts of lanthanide complex, this ratio was chosen to allow synthesis of tracers using less precursors, therefore reducing the cost of the tracer synthesis. A similar, but less marked trend was also observed for the terbium tracer. Having obtained suitable luminescent tracers, their behaviour within soils was then investigated.

6.1.4 Analysis of soil-tracer interactions

Soils from three different sites within the Glensaugh research station were collected (chapter 4). Two of these sites were from improved pasture and one was from an unimproved moorland. They represented three different soil types, brown forest soil, cultivated forest soil and a peaty podzol. The bulk soil densities of these soils, C:N ratios and loss on ignition values were typical for these soil types within this region. Analysis of particle size distribution for these soils indicated that the two tracer sizes synthesised were appropriate for tracing application involving these soils. FTIR analysis of these three soil types indicated the presence of organic groups on the surface of the soil particles that have the potential to interact with both the silica and organic groups of the lanthanide complexes present on the surface of the tracer particles. Within the cultivated soils functional groups such as waxes, carbohydrates, carboxylate, aromatic and hydroxyl groups were present at greater concentration within the clay fraction of the soils. The peaty podzol possessed a more complex IR absorbance pattern, as expected for a more organic soil, with variation between all soil fractions analysed. Whilst the presence of organic groups on the surface of the soil particles should facilitate the binding of the tracer, complex organic molecules often exhibit fluorescence, with the potential to create high levels of background fluorescence that would increase the limit of detection for the tracers.

SEM imaging of the tracers mixed with the characterised soils showed the presence of the tracers within the natural soil particles. Imaging of the fine silt tracers with soil at field moisture under ambient humidity showed the presence of smaller natural soil particles associated with the fine silt tracer demonstrating the ability of the tracer to incorporate into soil aggregates. As this was only apparent within the wet samples, it was likely that both soil moisture and the cations, which form an exchangeable layer on the soil particle surface, are required for this binding to occur. Fluorescence microscopy imaging of the fine silt tracer determined that the tracer emitted europium specific luminescence whilst mixed with soil at field moisture, demonstrating that the tracer remained stable within the soil environment. This was confirmed by benchtop and modular fluorescence spectrometers. It was possible to detect both tracers within all three soil types using time delayed spectroscopy techniques to limit interference from soil background fluorescence. The limit of detection for both tracers was highest in the organic peaty podzol soil three, and lowest in soil one. Also, due to the shorter luminescent lifetime of the clay tracer, the limit of detection for this tracer was far higher than that of the fine silt tracer. This meant that, whilst the clay tracer could be detected using the benchtop spectrometer, the modular spectrometer was required to detect it at concentrations close to those likely to be present during deployment. The fine silt tracer could be reproducibly detected at concentrations of 0.01 $g.kg^{-1}$ of soil using a benchtop spectrometer, similar to that of other applied tracers (Allaire et al. 2009) and therefore meets this criteria for an applied particle tracer (Zhang et al. 2004). Using the Edinburgh Instruments spectrometer, the limit of detection for the fine silt tracer was found to be 0.006 $g.kg^{-1}$, and for the clay tracer could be detected at concentrations above 0.007 $g.kg^{-1}$. In order to determine the detection lifetime of the fine silt tracer, a stability study, replicating natural soil conditions, was performed using soil one. This study demonstrated a steady loss of luminescence over time, resulting in the intensity dropping below the detection limit after 105 days. This means the tracer has a detection lifetime of approximately three months, or one season, allowing the same site to be used for tracing studies each year, without risk of interference from previously deployed tracers.

In order to identify any potential toxicity to the soil microbial environment analysis of the soil microbial respiration rate in the presence of the tracers, lanthanide complexes and core particles used during tracer synthesis were performed. In addition, a previously deployed particle environmental tracer was also analysed (Pollard et al. 2007) to allow comparison with other particle tracers. Whilst the lanthanide complex itself decreased the respiration rate, once incorporated into the tracer particles, there was no change in respiration rate to that of the blank soil, or the other environmental tracer. This indicates that the tracer should be non-toxic to the soil bacteria, another property desirable for applied particle tracers (Zhang et al. 2004). Another necessary property of a soil erosion particle tracer is that it is transported in a similar manner to natural soil particles (Zhang et al. 2004). In order to analyse the behaviour of the synthesised tracers, a series of soil sedimentation experiments were performed. These experiments showed that the two tracers settled out with their targeted soil fractions, and should therefore behave in a similar manner to natural soil particles. Given the interactions and behaviour of the soil tracers within the characterised soils, and the lower cost of synthesis, the fine silt tracer with the commercial core was used within soil erosion simulations. Whilst the clay tracer could not be detected at appropriate levels using a benchtop spectrometer, it could be detected using the modular spectrometer, and so was also used within the soil erosion experiments to provide information on any differences in behaviour between the fine silt and clay fractions during erosion events. However, it would be necessary to modify this tracer to improve the detection limits prior to deployment during field trials.

6.1.5 Behaviour of the tracers during simulated erosion events.

Analysis of the tracers during simulated erosion events demonstrated that the tracers were transported over the course of the study, with the tracers detected in both the overland flow from the plot, and the water that travelled vertically through the plot itself. Soil erosion simulations were performed at two different rainfall intensities. It was possible to detect the fine silt tracer within the high intensity rainfall experiments using a benchtop spectrometer. However, the concentration of the clay tracer was not above the limit of detection (300 mg.kg^{-1}) for this instrument in either simulation. Initial work was carried out with a benchtop spectrometer, as this type of instrument is commonly found within many laboratories. Therefore, detection of the tracer using a system such as this would allow analysis of the tracers with the minimum of equipment outlay and staff training. However, as it was not possible to detect the clay tracer within the sediment samples using this instrument and, in order to allow the presence of the tracer to be determined under all conditions a more sensitive modular research level spectrometer was also used. This identified an increase in concentration of the tracer within the collected sediment over time. The clay and fine silt tracers could be detected within the sediment after 30 minutes (45 mm applied rainfall) in the high intensity rainfall, and 40 minutes (20 mm applied rainfall) in the low intensity rainfall simulations. Whilst both tracers could be detected at the same point in the simulation, the concentrations of the clay tracer were far greater than the fine silt tracer, indicating that the clay tracer was transported more readily than the fine silt tracer. However, as the limit of detection was far higher for the clay tracer, it was likely that although the tracer was present within the sediment collected prior to this point, it was not at a detectable amount. The concentration of tracer was estimated using a calibration plot of premixed soil and tracer at known concentrations. To further improve this calibration, it would be necessary to repeat these concentrations curves against the matrix of the eroded soil fractions, to determine whether they match that of the bulk soil. When compared to the mass of sediment collected at each point, as an indication of rate of soil erosion, there was a good correlation between the concentration of tracer and amount of soil lost. This indicated that the movement of the tracer approximated the movement of eroded soil particles.

6.2 Overall conclusion

This study has successfully synthesised and characterised two luminescent soil erosion particle tracers. This was achieved via the incorporation of novel lanthanide complexes within a silica matrix. The luminescence emission of these particles could be detected against the natural soil background, and remained stable within the soil environment. During initial soil erosion simulations, the tracers exhibited similar transport behaviours to the natural soil particles. Therefore, these tracers appear to be suitable candidates for continued investigation as soil erosion tracers capable of tracing the movement of soil particles from source to fate.

6.3 Future work

Whilst the work detailed within this study has identified two potential candidates for use as soil erosion tracers, further work is necessary to determine the effectiveness of these tracers within field systems. This includes the development of an alternative terbium based complex, with a longer luminescent lifetime, and higher quantum efficiency for use within the clay tracer. This would allow detection of the clay tracer using standard benchtop fluorescence spectrometers at lower concentrations, closer to those likely to be present within environmental samples during erosion monitoring studies. Having developed a clay tracer which can be detected at lower concentrations, analysis of the detection limit and lifetime within the soil should be once again analysed to determine appropriate concentrations to apply, and the stability of the tracer within the soil and thus the length of time the tracer could be used to monitor soil movement within a site.

As it was not possible to reliably detect the tracers within the low intensity rainfall simulator experiments, it would be of benefit to design a larger erosion plot, with a longer length for the tracers to travel. This would allow analysis of the tracer along the plot, and over a greater length of time. It would also allow for the vertical movement of the tracer to be re-examined. In addition to designing a larger plot, varying the intensity of the rainfall during the simulation would allow movement of the tracers under more natural storm conditions to be analysed. The development of a portable, hand held fluorescence detector for use within soil and aquatic environments would allow the detection of tracers *in situ*, and provide a simple method of monitoring. Such a detector could be developed alongside laboratory based simulations, before being trialled in field scale studies of tracer movement.

Given the wide variety of soils present within Scotland (Dobbie et al. 2011), and in order for the tracer to be widely applied, it would be necessary to repeat the erosion simulations in a variety of different characterised soils, including peats. This would ensure that any tracers developed could be used in all sites within a catchment, as the ability of the tracer to bind with the soil, and be transported with it will vary with the individual soil. Also, the fluorescence background of each soil, and any potential interference in detecting the tracer could also vary with the individual soil type. Analysis of the tracers within each soil type will allow detection methods to be optimised for use across different soils.

Analysis of the tracer toxicity to the soil microbial population indicated that the tracers did not adversely affect soil respiration rates. However, it would be prudent to perform additional experiments looking at any potential toxicity to invertebrate, plant or aquatic life. This could include analysis of the growth of crops and grasses on soil containing the tracer, or analysis of growth or variety of aquatic microorganisms contained within river water samples.

Prior to any larger scale deployment within a field system, it would be necessary to upscale the tracer production to generate the necessary amounts of tracer. Initial upscale experiments performed within this study have shown that it is possible to upscale the tracer production from 0.1 to 1 g by increasing the reactants by the same factor. It was also possible to reuse the reaction mixture as the ethanol, ammonium hydroxide and water are not used up during the synthesis. As only a portion of the lanthanide complex is incorporated, additional complex could be added to ensure the starting concentrations remained constant. Reusing the reactants where possible would reduce the cost of producing the tracers in larger amounts. In order to allow multiple sites within a catchment to be monitored, a method to develop a series of tracers doped with multiple lanthanide complexes with discrete luminescence profiles would need to be developed. This would allow a larger number of tracers to be synthesised from a small number of well characterised lanthanide complexes. Prior to any testing of these tracers, it would be necessary to ensure all conditions necessary to obtain permission from Scottish Environmental Protection Agency (SEPA) for use within a catchment were met.

References

Al Dwayyan, A.S. et al., 2012. Structural and spectral investigations of Rhodamine (Rh6G) dye-silica core–shell nanoparticles. *Optical Materials*, 34(5), pp.761–768.

Allaire, S.E., Roulier, S. & Cessna, A.J., 2009. Quantifying preferential flow in soils: A review of different techniques. *Journal of Hydrology*, 378(1–2), pp.179–204.

Anthoni, F., 2000. Soil geology. Available at: http://www.seafriends.org.nz/enviro/soil/geosoil.htm [Accessed April 2, 2011].

Armelao, L. et al., 2010. Design of luminescent lanthanide complexes: From molecules to highly efficient photo-emitting materials. *Coordination Chemistry Reviews A Tribute to Fausto Calderazzo on the Occasion of his 80th Birthday*, 254(5-6), pp.487–505.

Artz, R.R.E. et al., 2008. FTIR spectroscopy can be used as a screening tool for organic matter quality in regenerating cutover peatlands. *Soil Biology and Biochemistry*, 40(2), pp.515–527.

Ashman, M.R. & Puri, G., 2002. *Essential Soil Science*, Oxford: Blackwell Publishing.

Aspinall, H.C., 2001. *Chemistry of the f-Block Elements*, CRC Press.

Atkins, P. & de Paula, J., 2005. *Elements of Physical Chemistry* 4th edition., Oxford University Press.

Attia, M.S. et al., 2012. A highly luminescent complexes of Eu(III) and Tb(III) with norfloxacin and gatifloxacin doped in sol–gel matrix: A comparable approach of using silica doped Tb(III) and Eu(III) as optical sensor. *Journal of Luminescence*, 132(10), pp.2741–2746.

Bae, S.W., Tan, W. & Hong, J.-I., 2012. Fluorescent dye-doped silica nanoparticles: new tools for bioapplications. *Chemical Communications*, 48(17), pp.2270–2282.

Bakhmutov, V.I., 2011. *Solid-State NMR in Materials Science: Principles and Applications*, CRC Press.

Belyaev, V.R. et al., 2009. Quantitative assessment of effectiveness of soil conservation measures using a combination of 137Cs radioactive tracer and conventional technique. *Catena*, 79, pp.214–227.

Binnemans, K. et al., 2004. A luminescent tris(2-thenoyltrifluoroacetonato)europium(iii) complex covalently linked to a 1,10-phenanthroline-functionalised sol-gel glass. *Journal of Materials Chemistry J. Mater. Chem.*, 14(2), pp.191–195.

Binnemans, K., 2005. *Handbook on the Physics and Chemistry of Rare Earths, Vol. 35, edited by KA, Gschneidner, JCG Bünzli & VK Pecharsky*, Amsterdam: Elsevier.

Binnemans, K., 2009. Lanthanide-Based Luminescent Hybrid Materials. *Chemical Reviews*, 109, pp.4283–4374.

Blake, W.H., Walling, D.E. & He, Q., 1999. Fallout beryllium-7 as a tracer in soil erosion investigations. *Applied radiation and Isotopes*, 51(5), pp.599–605.

Blanco, H. & Lal, R., 2010. *Principles of soil conservation and management* 1. softcover print., Dordrecht: Springer.

Boens, N. et al., 2007. Fluorescence Lifetime Standards for Time and Frequency Domain Fluorescence Spectroscopy. *Analytical Chemistry*, 79(5), pp.2137–2149.

Boix-Fayos, C. et al., 2006. Measuring soil erosion by field plots: Understanding the sources of variation. *Earth-Science Reviews.*, 78, pp.267–285.

Bonte, P.H. et al., 2000. Buffering of suspended sediment transport in lowland river during low water stages: quantifiation in river Seine using environmental radionuclides. *Acta Geologica Hispanica*, 35, pp.339–355.

Brady, N.C. & Weil, R.R., 2002. *The Nature and Properties of Soils* Thirteenth., New Jersey: Prentice Hall.

Braimoh, A.K. & Velk, P.L.G., 2008. *Land Use and Soil Resources*, Springer Science.

Brinker, C.J. & Scherer, G.W., 1990. *Sol–gel science, the physics and chemistry of sol–gel processing*, Boston: Academic Press.

Bronick, C.J. & Lal, R., 2005. Soil structure and management: a review. *Geoderma*, 124(1–2), pp.3–22.

Bryan, R. & Poesen, J., 1989. Laboratory experiments on the influence of slope length on runoff, percolation and rill development. *Earth Surface Processes and Landforms*, 14(3), pp.211–231.

Buchter, B., Hinz, C. & Leuenberger, J., 1997. Tracer transport in a stony hillslope soil under forest. *Journal of hydrology*, 192(1), pp.314–320.

Bünzli, J.-C.G. & Piguet, C., 2005. Taking advantage of luminescent lanthanide ions. *Chemical Society Reviews*, 34(12), pp.1048–1077.

Campbell, C.D. et al., 2003. A Rapid Microtiter Plate Method To Measure Carbon Dioxide Evolved from Carbon Substrate Amendments so as To Determine the Physiological Profiles of Soil Microbial Communities by Using Whole Soil. *Applied and Environmental Microbiology*, 69(6), pp.3593–3599.

de Carlo, E.H., Beltran, V.L. & Tomlinson, M.S., 2004. Composition of water and suspended sediment in streams of urbanized subtropical watersheds in Hawaii. *Applied Geochemistry*, 19, pp.1011–1037.

Carter, J. et al., 2003. Fingerprinting suspended sediment sources in a large urban river system. *Science of the total environment*, 314, pp.513–534.

Carter, M.R., 1993. *Soil sampling and methods of analysis*, CRC Press.

Chapman, A.S. et al., 2001. Particulate phosphorus transport by sub-surface drainage from agricultural land in the UK. Environmental significance at the catchment and national scale. *The Science of the Total Environment*, 266, pp.95–102.

Cingarapu, S. et al., 2014. Nanofluids with encapsulated tin nanoparticles for advanced heat transfer and thermal energy storage. *International Journal of Energy Research*, 38(1), pp.51–59.

Clark, E.H., 1985. The off-site costs of soil erosion. *Journal of Soil and Water Conservation*, 40(1), pp.19–22.

Collins, A.L. & Walling, D.E., 2002. Selecting fingerprint properties for discriminating potential suspended sediment sources in river basins. *Journal of Hydrology*, 261, pp.218–244.

Cooper, J.T., Peterson, E.M. & Harris, J.M., 2013. Fluorescence Imaging of Single-Molecule Retention Trajectories in Reversed-Phase Chromatographic Particles. *Analytical Chemistry*, 85(19), pp.9363–9370.

Costa, C.A.R., Leite, C.A.P. & Galembeck, F., 2003. Size Dependence of Stober Silica Nanoparticle Microchemistry. *Journal of Physical Chemistry B*, 107, pp.4747–4755.

Coynel, A. et al., 2004. Sampling frequency and accuracy of SPM flux estimates in two contrasted drainage basins. *Science of the Total Environment*, 330, pp.233–247.

Cresswell, H.P. & Hamilton, G.J., 2002. Bulk density and pore space relations. In *Soil Physical Measurement and Interpretation for Land Evaluation*. Csiro publishing.

Crosby, G.A. & Demas, J.N., 1971. Measurement of photoluminescence quantum yields. Review. *The Journal of Physical Chemistry J. Phys. Chem.*, 75(8), pp.991–1024.

Cundy, C.S. & Cox, P.A., 2003. The hydrothermal synthesis of zeolites: history and development from the earliest days to the present time. *Chemical Reviews*, 103(3), pp.663–702.

Dieke, G.H., 1968. *Spectra and energy levels of rare earth ions in crystals*, Interscience Publishers New York.

Dobbie, K.E., Bruneau, P.M. & Towers, W., 2011. The State of Scotland's Soil. *Natural Scotland Available at: www. sepa. org. uk/land/land_publications. aspx [accessed on 20 April, 2011]*.

Dorenbos, P., 2002. Crystal field splitting of lanthanide 4f n− 1 5d-levels in inorganic compounds. *Journal of alloys and compounds*, 341(1), pp.156–159.

Dotterweich, M., 2013. The history of human-induced soil erosion: Geomorphic legacies, early descriptions and research, and the development of soil conservation—A global synopsis. *Geomorphology*, 201(0), pp.1–34.

Dowding, P.J. & Vincent, B., 2000. Suspension polymerisation to form polymer beads. *Colloids and Surfaces a-Physicochemical and Engineering Aspects*, 161(2), pp.259–269.

Enrichi, F., 2008. Luminescent Amino-functionalized or Erbium-doped Silica Spheres for Biological Applications. *Annals of the New York Academy of Sciences*, 1130(1), pp.262–266.

Enrichi, F. et al., 2008. Synthesis and characterization of monodisperse Eu-doped luminescent silica nanospheres for biological applications. In *Photonics Europe*. International Society for Optics and Photonics, p. 69912E–69912E–8. Available at: http://dx.doi.org/10.1117/12.781504.

Everett, S.E. et al., 2008. Comparison of Pu and 137Cs as tracers of soil and sediment transport in a terrestrial environment. *Journal of Environmental Radioactivity*, 99, pp.383–393.

Feng, J. & Zhang, H., 2013. Hybrid materials based on lanthanide organic complexes: a review. *Chemical Society Reviews*, 42(1), pp.387–410.

Gai, S. et al., 2010. Fabrication of luminescent and mesoporous core–shell structured nanocomposites and their application as drug carrier. *Microporous and Mesoporous Materials*, 131(1–3), pp.128–135.

García-Ruiz, J.M., 2010. The effects of land uses on soil erosion in Spain: A review. *CATENA*, 81(1), pp.1–11.

Georges, J., 1993. Lanthanide-sensitized luminescence and applications to the determination of organic analytes. A review. *Analyst*, 118, pp.1481–1486.

Glentworth, R. & Hart, R., 1943. The Soils of Glensaugh.

Görller-Walrand, C. & Binnemans, K., 1998. Spectral intensities of ff transitions. *Handbook on the physics and chemistry of rare earths*, 25, pp.101–264.

Green, D.., Jayasundara, S., et al., 2003. Chemical reaction kinetics leading to the first Stober silica nanoparticles – NMR and SAXS investigation. *Journal of Non-Crystalline Solids*, 315(1–2), pp.166–179.

Green, D.., Lin, J.., et al., 2003. Size, volume fraction, and nucleation of Stober silica nanoparticles. *Journal of Colloid and Interface Science*, 266(2), pp.346–358.

Grismer, M.E., 2012. Standards vary in studies using rainfall simulators to evaluate erosion. *California Agriculture*, 66(3), pp.102–107.

Guo-Qing, H.U. et al., 2011. Laboratory testing of magnetic tracers for soil erosion measurement. *Pedosphere*, 21(3), pp.328–338.

Gutierrez, F. et al., 2004. Quantum chemistry-based interpretations on the lowest triplet state of luminescent lanthanides complexes. Part 1. Relation between the triplet state energy of hydroxamate complexes and their luminescence properties. *Dalton Transactions Dalton Trans.*, (9), pp.1334–1347.

Gutsche, A. et al., 2015. Synthesis and small angle X-ray scattering (SAXS) characterization of silica spheres covered with gel-like particles formed by means of solvent evaporation. *Powder Technology*, 278(0), pp.257–265.

Gyssels, G. et al., 2002. The impact of sowing density of small grains on rill and ephemeral gully erosion in concentrated flow zones. *Soil & Tillage Research*, 64, pp.189–201.

Hemmila, I. & Laitala, V., 2005. Progress in Lanthanides as Luminescent Probes. *Journal of Fluorescence*, 15, pp.529–542.

Hench, L.L. & West, J.K., 1990. The sol-gel process. *Chemical Reviews*, 90(1), pp.33–72.

Henderson, W. & McIndoe, J.S., 2005. *Mass Spectrometry of Inorganic and Organometallic Compounds: Tools-Techniques-Tips*, John Wiley & Sons.

Ingledew, W.J. & Ohnishi, T., 1977. The probable site of action of thenolytrifluoracetone on the respiratory chain. *Biochemical Journal*, 164, pp.617–620.

Insin, N. et al., 2008. Incorporation of Iron Oxide Nanoparticles and Quantum Dots into Silica Microspheres. *ACS Nano*, 2(2), pp.197–202.

Jenkins, A.L. & Murray, G.M., 1998. Enhanced Luminescence of Lanthanides: Determination of Europium by Enhanced Luminescence. *Journal of Chemical Education*, 75(2), p.227.

Jin, J. et al., 2012. Silica nanoparticle-embedded sol–gel organic/inorganic hybrid nanocomposite for transparent OLED encapsulation. *Organic Electronics*, 13(1), pp.53–57.

Jin, T. et al., 1997. Preparation and luminescence characteristics of the europium and terbium complexes incorporated into a silica matrix using a sol–gel method. *Journal of Alloys and Compounds*, 252(1–2), pp.59–66.

Jobin Yvon Horiba, 2012. A guide to recording Fluorescence Quantum Yields. *Jobin Yvon Horiba Ltd., Stanmore, Middlesex, UK*.

Jocher, C.J. et al., 2008. Aqueous Ln(III) Luminescence Agents Derived from a Tasty Precursor. *Inorganic Chemistry*, 47, pp.7951–7953.

Kaltsoyannis, N. & Scott, P., 1999. *The f elements*, Oxford: Oxford University Press.

Kang, J.-G. et al., 2005. Thermal and luminescent properties of polymeric acidic organophosphorus complexes of Eu(III) and Tb(III) undoped and doped with 1,10-phenanthroline. *Materials Chemistry and Physics*, 91(1), pp.172–179.

Karmakar, B., De, G. & Ganguli, D., 2000. Dense silica microspheres from organic and inorganic acid hydrolysis of TEOS. *JOURNAL OF NON-CRYSTALLINE SOLIDS*, 272(2-3), pp.119–126.

Kinnell, P.I.A., 2005. Raindrop-impact-induced erosion processes and prediction: a review. *Hydrological Processes*, 19(14), pp.2815–2844.

Kirby, M.J. et al., 2004. *Pan-European Soil Erosion Risk Assessment: The PESERA Map*, European Soil Bureau.

Kirkbride, M.P. & Reeves, A.D., 1993. Soil erosion caused by low-intensity rainfall in Angus, Scotland. *Applied Geography*, 13(4), pp.299–311.

Koiter, A.J. et al., 2013. The behavioural characteristics of sediment properties and their implications for sediment fingerprinting as an approach for identifying sediment sources in river basins. *Earth-Science Reviews*, 125, pp.24–42.

Koptsik, S., Strand, L. & Clarke, N., 2003. On the calculation of the surface area of different soil size fractions. *Applied Geochemistry*, 18, pp.629–651.

Kumpiene, J., Lagerkvist, A. & Maurice, C., 2007. Stabilization of Pb- and Cu-contaminated soil using coal fly ash and peat. *Environmental Pollution*, 145(1), pp.365–373.

Lal, R., 1994. *Soil erosion research methods*, CRC Press.

Lechevallier, S. et al., 2013. Luminescence Properties of Mesoporous Silica Nanoparticles Encapsulating Different Europium Complexes: Application for Biolabelling. *Journal of Nanomaterials*, 2013, p.11.

Legout, C. et al., 2013. Quantifying suspended sediment sources during runoff events in headwater catchments using spectrocolorimetry. *Journal of Soils and Sediments*, 13(8), pp.1478–1492.

Lev, O. et al., 1995. Organically Modified Sol-Gel Sensors. *Analytical Chemistry*, 67(1), p.22A–30A.

Lilly, A. et al., 2009. Climate change, land management and erosion in the organic and organo-mineral soils in Scotland and Northern Ireland. *Climate change, land management and erosion in the organic and* *organo-mineral soils in Scotland and Northern Ireland*.

Li, M. et al., 2006. Using rare earth element tracers and neutron activation analysis to study rill erosion process. *Applied radiation and isotopes*, 64(3), pp.402–408.

Lindberg, R. et al., 1997. Multivariate analysis of the size dependence of monodisperse silica particles prepared according to the sol-gel technique. *Frontiers in Colloid Chemistry an International Festschrift to Professor Stig E. Friberg*, 123–124(0), pp.549–560.

Li, Q., Li, T. & Wu, J., 2001. Luminescence of europium (III) and terbium (III) complexes incorporated in poly (vinyl pyrrolidone) matrix. *The Journal of Physical Chemistry B*, 105(49), pp.12293–12296.

Liu, P.-L. et al., 2004. Stable rare earth element tracers to evaluate soil erosion. *Soil and Tillage Research*, 76(2), pp.147–155.

Lobb, D.A., Kachanoski, R.G. & Miller, M.H., 1999. Tillage translocation and tillage erosion in the complex upland landscapes of southwestern Ontario, Canada. *Soil and Tillage Research*, 51(3), pp.189–209.

Lobb, D.A., Kachanoski, R.G. & Miller, M.H., 1995. Tillage translocation and tillage erosion on shoulder slope landscape positions measured using 137Cs as a tracer. *Canadian Journal of Soil Science*, 75(2), pp.211–218.

Lu, H.-F. & Yan, B., 2008. Lanthanide-centered luminescent hybrid microsphere-particles obtained by sol–gel method. *Journal of Photochemistry and Photobiology A: Chemistry*, 194(2–3), pp.136–142.

Lunstroot, K., 2008. *Spectroscopy of Lanthanides in Ionic Liquids*. Katholieke Universiteit Leuven.

Lu, Q. et al., 2010. Structure and Luminescence Properties of Eu(3+)-Doped Cubic Mesoporous Silica Thin Films. *Nanoscale Research Letters*, 5(4), pp.761–768.

Lv, Y. et al., 2007. Synthesis and characteristics of a novel rare earth complex of Eu(TTA)2(N-HPA)Phen. *Journal of Photochemistry and Photobiology A: Chemistry*, 188(2–3), pp.155–160.

McGuire, K.J., Weiler, M. & McDonnell, J.J., 2007. Integrating tracer experiments with modeling to assess runoff processes and water transit times. *Advances in Water Resources*, 30(4), pp.824–837.

Menges, F., 2013. *Spekwin32–optical spectroscopy software, Version 1.71. 6.1*,

Michéli, E. et al., 2006. *World reference base for soil resources: 2006: a framework for international classification, correlation and communication*, FAO.

Moore, E.G. et al., 2007. An Octadentate Luminescent Eu(III) 1,2-HOPO Chelate with Potent Aqueous Solubility. *Inorganic Chemistry*, 46, pp.5468–5470.

Moore, E.G. et al., 2010. Eu(III) Complexes of Functionalized Octadentate 1-Hydroxypyridin-2-ones: Stability, Bioconjugation, and Luminescence Resonance Energy Transfer Studies. *Inorganic Chemistry*, 49(21), pp.9928–9939.

Moore, E.G. et al., 2008. Highly Luminescent Lanthanide Complexes of 1-Hydroxy-2-pyridinones. *Inorganic Chemistry*, 47, pp.3105–3118.

Moore, E.G., Samuel, A.P.S. & Raymond, K.N., 2009. From Antenna to Assay: Lessons Learned in Lanthanide Luminescence. *Accounts Of Chemical Research*, 42, pp.542–552.

Moran, C.E., Hale, G.D. & Halas, N.J., 2001. Synthesis and Characterization of Lanthanide-Doped Silica Microspheres. *Langmuir*, 17(26), pp.8376–8379.

Morgan, R.P.C., 2009. *Soil erosion and conservation*, John Wiley & Sons.

Nakahara, Y. et al., 2015. Fluorescent silica nanoparticles modified chemically with terbium complexes as potential bioimaging probes: their fluorescence and colloidal properties in water. *New Journal of Chemistry*, 39(2), pp.1452–1458.

Natural Resources Conservation Service, U.D. of A., 2014. Soil Health. Available at: http://www.nrcs.usda.gov/wps/portal/nrcs/detail/ny/soils/health/?cid=stelprdb1186190 [Accessed July 2, 2014].

Nearing, M.A., 2012. Soil Erosion and Conservation. In *Environmental Modelling: Finding Simplicity in Complexity*. Wiley, pp. 365–378.

Nearing, M.A. et al., 1999. Soil erosion by surface water flow on a stony, semiarid hillslope. *Earth Surface Processes and Landforms*, 24(8), pp.677–686.

Newman, B.D., Campbell, A.R. & Wilcox, B.P., 1997. Tracer-based studies of soil water movement in semi-arid forests of New Mexico. *Journal of Hydrology*, 196(1–4), pp.251–270.

Norton, L.. et al., 2009. *Countryside Survey: Scotland Results from 2007.*, NERC/Centre for Ecology and Hydrology.

Osman, K.T., 2014. *Soil Degradation, Conservation and Remediation*, Dordrecht: Springer Netherlands. Available at: http://link.springer.com/10.1007/978-94-007-7590-9 [Accessed May 25, 2015].

Parker, D. & Williams, J.A.G., 1996. Getting excited about lanthanide complexation chemistry. *Journal of the Chemical Society, Dalton Transactions J. Chem. Soc., Dalton Trans.*, (18), pp.3613–3628.

Parsons, A.J. & Foster, I.D., 2011. What can we learn about soil erosion from the use of 137 Cs? *Earth-Science Reviews*, 108(1), pp.101–113.

Patra, A. et al., 1999. Sonochemical Preparation and Characterization of Eu2O3 and Tb2O3 Doped in and Coated on Silica and Alumina Nanoparticles. *The Journal of Physical Chemistry B*, 103(17), pp.3361–3365.

Peacock, R.D., 1975. The intensities of lanthanide f↔ f transitions. In *Rare Earths*. Springer, pp. 83–122.

Perrin, J., Carrier, F. & Guillot, L., 2006. Determination of the vertical distribution of radioelements (K, U, Th, Cs) in soils from portable HP-Ge spectrometer measurements: A tool for soil erosion studies. *Applied radiation and isotopes*, 64(7), pp.830–843.

Pimentel, D. & Kounang, N., 1998. Ecology of Soil Erosion in Ecosystems. *Ecosystems*, 1(5), pp.416–426.

Poleto, C., Merten, G.H. & Minella, J.P., 2009. The identification of sediment sources in a small urban watershed in southern Brazil: an application of sediment fingerprinting. *Environmental technology*, 30(11), pp.1145–1153.

Pollard, P. et al., 2007. Sensitive novel fluorescent tracers for environmental monitoring. In *Marine Challenges: Coastline to Deep sea*. IEEE Oceans 07.

Poreba, G.J., 2006. Caesium-137 as a Soil Erosion Tracer: A review. *Geochronometria*, 25(37-46).

Quine, T.A. et al., 1999. Fine-earth translocation by tillage in stony soils in the Guadalentin, south-east Spain: an investigation using caesium-134. *Soil & Tillage Research*, 51, pp.279–301.

Rendell, D. & Mowthorpe, D.J., 1987. *Fluorescence and phosphorescence spectroscopy*, Published on behalf of ACOL, London by Wiley.

Rossi, L.M. et al., 2006. Fluorescent silica nanospheres for digital counting bioassay of the breast cancer marker HER2/nue. *Biosensors and Bioelectronics*, 21, pp.1900–1906.

Rossi, L.M. et al., 2005. Stöber Synthesis of Monodispersed Luminescent Silica Nanoparticles for Bioanalytical Assays. *Langmuir*, 21, pp.4277–4280.

Russell, M.A. et al., 1998. The composition of nutrient fluxes from contrasting UK river basins. *Hydrological Processes*, 12, pp.1461–1482.

Sac, M.M. et al., 2008. Estimates of soil erosion using cesium-137 tracer models. *Environmental Monitoring and Assessment*, 136, pp.461–467.

Santra, S. et al., 2001. Conjugation of Biomolecules with Luminophore-Doped Silica Nanoparticles for Photostable Biomarkers. *Analytical Chemistry*, 73(20), pp.4988–4993.

Scherr, S.J., 1999. *Soil degradation: A threat to developing-country food security by 2020?*, Intl Food Policy Res Inst.

Selvan, S.T. et al., 2010. Functional and multifunctional nanoparticles for bioimaging and biosensing. *Langmuir*, 26(14).

Shen, J., Zhao, L. & Han, G., 2013. Lanthanide-doped upconverting luminescent nanoparticle platforms for optical imaging-guided drug delivery and therapy. *Inorganic nanoparticle platforms*, 65(5), pp.744–755.

Shimura, N. & Ogawa, M., 2007. Preparation of surfactant templated nanoporous silica spherical particles by the Stöber method. Effect of solvent composition on the particle size. *Journal of Materials Science*, 42, pp.5299–5306.

Skoog, D.A., Holler, F.J. & Crouch, S.R., 2007. *Principles of Instrumental Analysis* 6th edition., Thomson Brooks/Cole.

Smith, H.G. & Blake, W.H., 2014. Sediment fingerprinting in agricultural catchments: A critical re-examination of source discrimination and data corrections. *Geomorphology*, 204, pp.177–191.

Stevens, C.J. & Quinton, J.N., 2008. Investigating source areas of eroded sediments transported in concentrated overland flow using rare earth element tracers. *Catena*, 74, pp.31–36.

Stöber, W., Fink, A. & Bohn, E., 1968. Controlled growth of monodisperse silica spheres in the micron size range. *Journal of Colloid Interface Science*, 26, pp.62–69.

Stutter, M.I. et al., 2009. Multi-element signatures of stream sediments and sources under moderate to low flow conditions. *Applied Geochemistry*, 24(5), pp.800–809.

Stutter, M.I., Langan, S.J. & Cooper, R.., 2008. Spatial and temporal dynamics of stream water particulate and dissolved N,P and C forms along a catchment transect, NE Scotland. *Journal of Hydrology*, 350, pp.187–202.

Stutter, M.I., Langan, S.J. & Demars, B.O.L., 2007. River sediments provide a link between catchment pressures and ecological status in a mixed land use Scottish River system. *Water Research*, 41, pp.2803–2815.

Stutter, M.I. & Lumsden, D.., 2008. Interactions of land use and dynamic river conditions on sorption equilibria between benthic sediments and river soluble reactive phosphorus concentrations. *Water Research*, 42, pp.4249–4260.

Stutter, M.I., Lumsdon, D.G. & Cooper, R.J., 2007. Temperature and soil moisture effects on dissolved organic matter release from a moorland Podzol O horizon under field and controlled laboratory conditions. *European journal of soil science*, 58(5), pp.1007–1016.

Tao, Y. et al., 2006. Mesopore-modified zeolites: preparation, characterization, and applications. *Chemical reviews*, 106(3), pp.896–910.

Tauro, F. et al., 2012. Fluorescent particle tracers in surface hydrology: a proof of concept in a semi-natural hillslope. *Hydrology and Earth System Sciences*, 16(8), pp.2973–2983.

Taylor, A. et al., 2012. Sorption behaviour of beryllium-7 and implications for its use as a sediment tracer. *Geoderma*, 187, pp.16–23.

Tedeschi, C. et al., 2003. A solid-state study of eight-coordinate lanthanide(iii) complexes (Ln = Eu, Gd, Tb, Dy) with 1-hydroxy-2-pyridinone. *Dalton Transactions Dalton Trans.*, (9), pp.1738–1745.

Thapa, B.B., Cassel, D.K. & Garrity, D.P., 1999. Assessment of tillage erosion rates on steepland Oxisols in the humid tropics using granite rocks. *Soil & Tillage Research*, 51, pp.233–243.

The James Hutton Institute, 2013. Glensaugh Research Station. Available at: http://www.hutton.ac.uk/about/facilities/glensaugh [Accessed July 6, 2013].

Thomas, R. & Meybeck, M., 1992. The use of particulate material. In D. Chapman, ed. *Water Quality Assessments - A Guide to use of biota, sediments and water in environmental monitoring*. UNESCO/WHO/UNEP.

Thomsen, V., Schatzlein, D. & Mercuro, D., 2003. Limits of detection in spectroscopy. *Spectroscopy*, 18(12), pp.112–114.

Tiessen, K.H.D. et al., 2007. Tillage erosion within potato production systems in Atlantic Canada: I. Measurement of tillage translocation by implements used in seedbed preparation. *Soil and Tillage Research*, 95(1), pp.308–319.

Towers, W. et al., 2006. *Scotland’s Soil Resource - Current State and Threats*, The Scottish Government. Available at: http://www.gov.scot/Publications/2006/09/21115639/0 [Accessed April 29, 2015].

USDA-NRCS, 1998. Vulnerability to Water Erosion Map.

Van Reeuwijk, L.P., 2002. *Technical Paper 7: Procedures for soil analysis* Sixth., International soil reference and information centre.

Ventura, E., Nearing, M.A. & Norton, L.D., 2001. Developing a magnetic tracer to study soil erosion. *Catena*, 43, pp.277–291.

Verheijen, F.G. et al., 2009. Tolerable versus actual soil erosion rates in Europe. *Earth-Science Reviews*, 94(1), pp.23–38.

Virto, I. et al., 2014. Soil Degradation and Soil Quality in Western Europe: Current Situation and Future Perspectives. *Sustainability*, 7(1), pp.313–365.

Walling, D.E., 2005. Tracing suspended sediment sources in catchments and river systems. *Science of the Total Environment*, 344, pp.159–184.

Walling, D.E., Woodward, J.C. & Nicholas, A.P., 1993. A multi-parameter approach to fingerprinting suspended-sediment sources. *IAHS PUBLICATION*, pp.329–329.

Wang, J., Pamidi, P.V.A. & Zanette, D.R., 1998. Self-Assembled Silica Gel Networks. *Journal of the American Chemical Society*, 120(23), pp.5852–5853.

Wang, X.-D. et al., 2010. Preparation of spherical silica particles by Stöber process with high concentration of tetra-ethyl-orthosilicate. *Journal of Colloid and Interface Science*, 341(1), pp.23–29.

Werts, M.H., 2005. Making sense of lanthanide luminescence. *Science progress*, 88(2), pp.101–131.

White, J.C. et al., 1999. Correlation between biological and physical availabilities of phenanthrene in soils and soil humin in aging experiments. *Environmental Toxicology and Chemistry*, 18(8), pp.1720–1727.

Willenbring, J.K. & Blanckenburg, F., 2010. Meteoric cosmogenic Beryllium-10 adsorbed to river sediment and soil: Applications for Earth-surface dynamics. *Earth Science Reviews*, 98, pp.105–122.

Wright, J.D. & Sommerdijk, N.A., 2000. *Sol-gel materials: chemistry and applications*, CRC press.

Xu, J. et al., 2004. Gadolinium(III) 1,2-Hydroxypyridonate-Based Complexes: Towards MRI Contrast Agents of High Relaxivity. *Inorganic Chemistry*, 43, pp.5492–5494.

Xu, Y. et al., 2013. Plutonium in Soils from Northeast China and Its Potential Application for Evaluation of Soil Erosion. *Sci. Rep.*, 3. Available at: http://dx.doi.org/10.1038/srep03506.

Yang, W. et al., 2008. Quantitative determination of red-soil erosion by an Eu tracer method. *Soil and Tillage Research*, 101, pp.52–56.

Yantasee, W. et al., 2009. Selective removal of lanthanides from natural waters, acidic streams and dialysate. *Journal of Hazardous Materials*, 168(2-3), pp.1233–1238.

Yan, Y.-L. & Cohen, S.M., 2007. Efficient Synthesis of 5-Amido-3-hydroxy-4-pyrones as Inhibitors of Matrix Metalloproteinases. *Organic Letters*, 9(13), pp.2517–2520.

Yin, Y.-M. et al., 2012. Dummy molecularly imprinted polymers on silica particles for selective solid-phase extraction of tetrabromobisphenol A from water samples. *Journal of Chromatography A*, 1220(0), pp.7–13.

Yuan, J. & Wang, G., 2006. Lanthanide-based luminescence probes and time-resolved luminescence bioassays. *Trends in Analytical Chemistry*, 25, pp.490–500.

Yu, J. et al., 2005. Efficient Electroluminescence from New Lanthanide (Eu3+, Sm3+) Complexes. *Inorganic Chemistry*, 44(5), pp.1611–1618.

Zaitoun, M.A. et al., 2008. Luminescence properties of europium (III) cryptates trapped in sol-gel glass. *Journal of Luminescence*, 128(2), pp.227–231.

Zaitoun, M.A. et al., 2013. Synthesis and luminescence properties of encapsulated sol–gel glass samarium complexes. *Spectrochimica Acta Part A: Molecular and Biomolecular Spectroscopy*, 115(0), pp.810–814.

Zapata, F., 2003. The use of environmental radionuclides as tracers in soil erosion and sedimentation investigations: recent advances and future developments. *Soil and Tillage Research*, 69(1), pp.3–13.

Zhang, G. et al., 2010. Correction factor to dye-measured flow velocity under varying water and sediment discharges. *Journal of hydrology*, 389(1), pp.205–213.

Zhang, H.J. et al., 1999. Luminescence characteristics of europium and terbium complexes with 1,10-phenanthroline in-situ synthesized in a silica matrix by a two-step sol-gel process. *Materials Letters*, 38(4), pp.260–264.

Zhang, J.H. et al., 2004. Assessment of tillage translocation and tillage erosion by hoeing on the steep land in hilly areas of Sichuan, China. *Soil & Tillage Research*, 75, pp.99–107.

Zhang, Q., Lei, T. & Zhao, J., 2008. Estimation of the detachment rate in eroding rills in flume experiments using an REE tracing method. *Geoderma*, 147, pp.8–15.

Zhang, X.C. et al., 2001. Potential use of Rare Earth Oxides as Tracers for Soil Erosion and Aggregation Studies. *Soil Sci. Soc. Am. J.*, 65(5), pp.1508–1515.

Zhao, X. et al., 2004. A rapid bioassay for single bacterial cell quantitation using bioconjugated nanoparticles. *PNAS*, 101, pp.15027–15032.

Zhu, M.-Y. et al., 2010. A review of REE tracer method used in soil erosion studies. *Agricultural Sciences in China*, 9(8), pp.1167–1174.

Appendix I – supplementary data

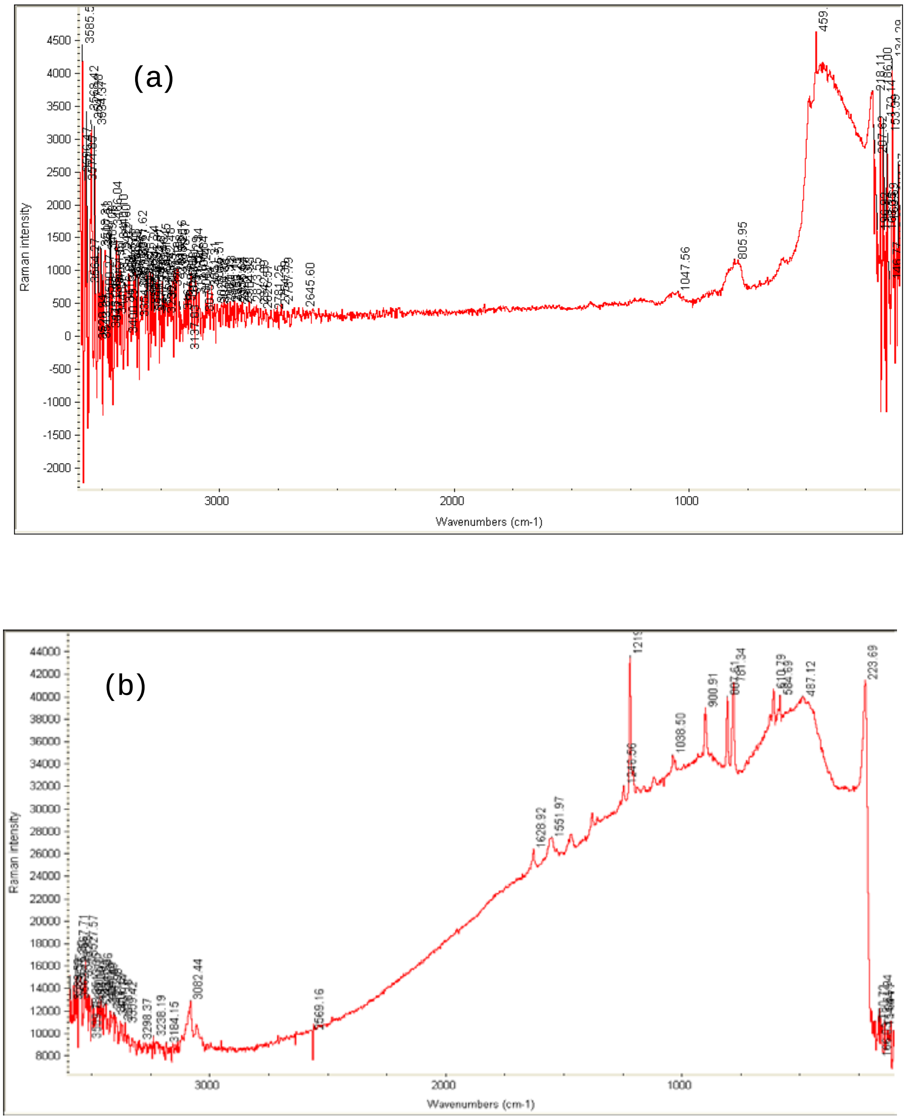

Figure A-1 Raman spectra for (a) Tb^{3+} $2PO_3$ and (b) Tb^{3+} $TTA_3.2PO$

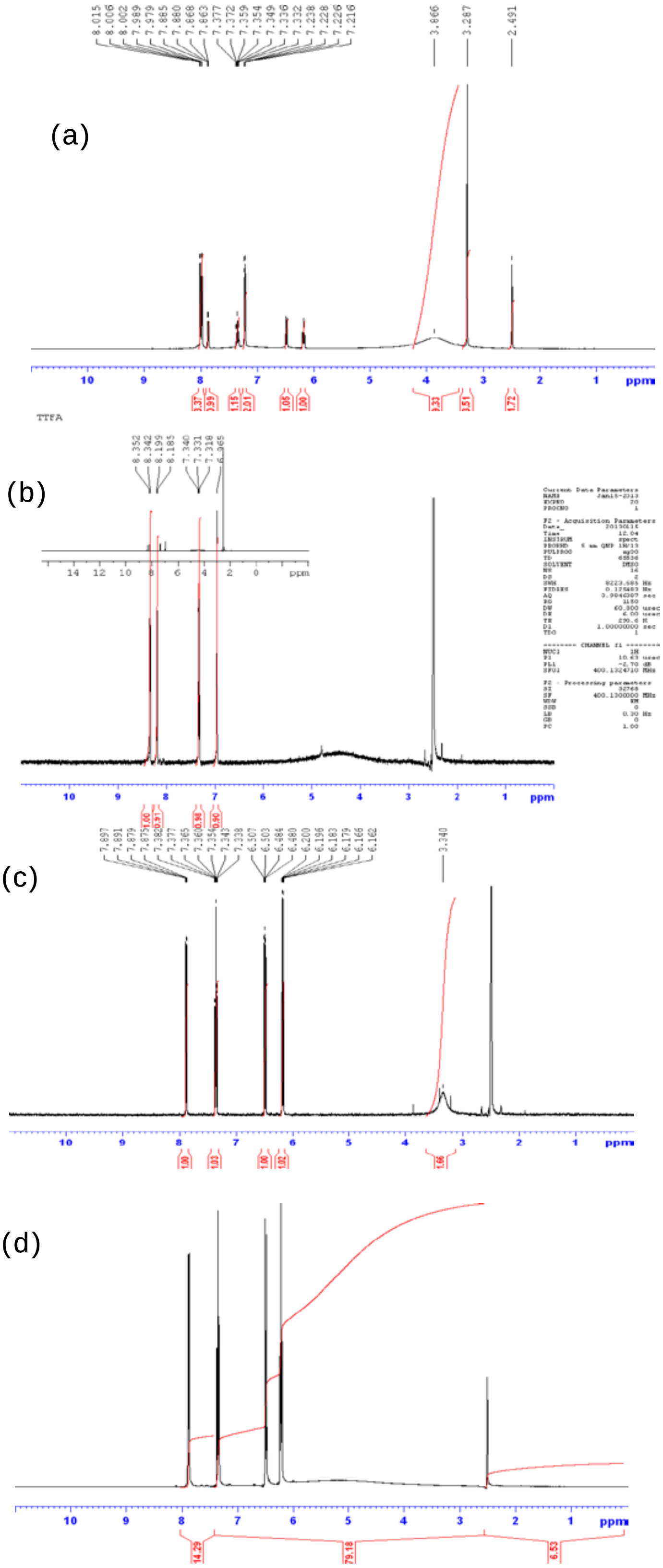

Figure A-2 NMR spectra obtained in d6DMSO for (a) 2PO, (b) mix 3:1 TTA:2PO (c) La(2PO)$_3$ and (d) La(TTA)$_3$2PO

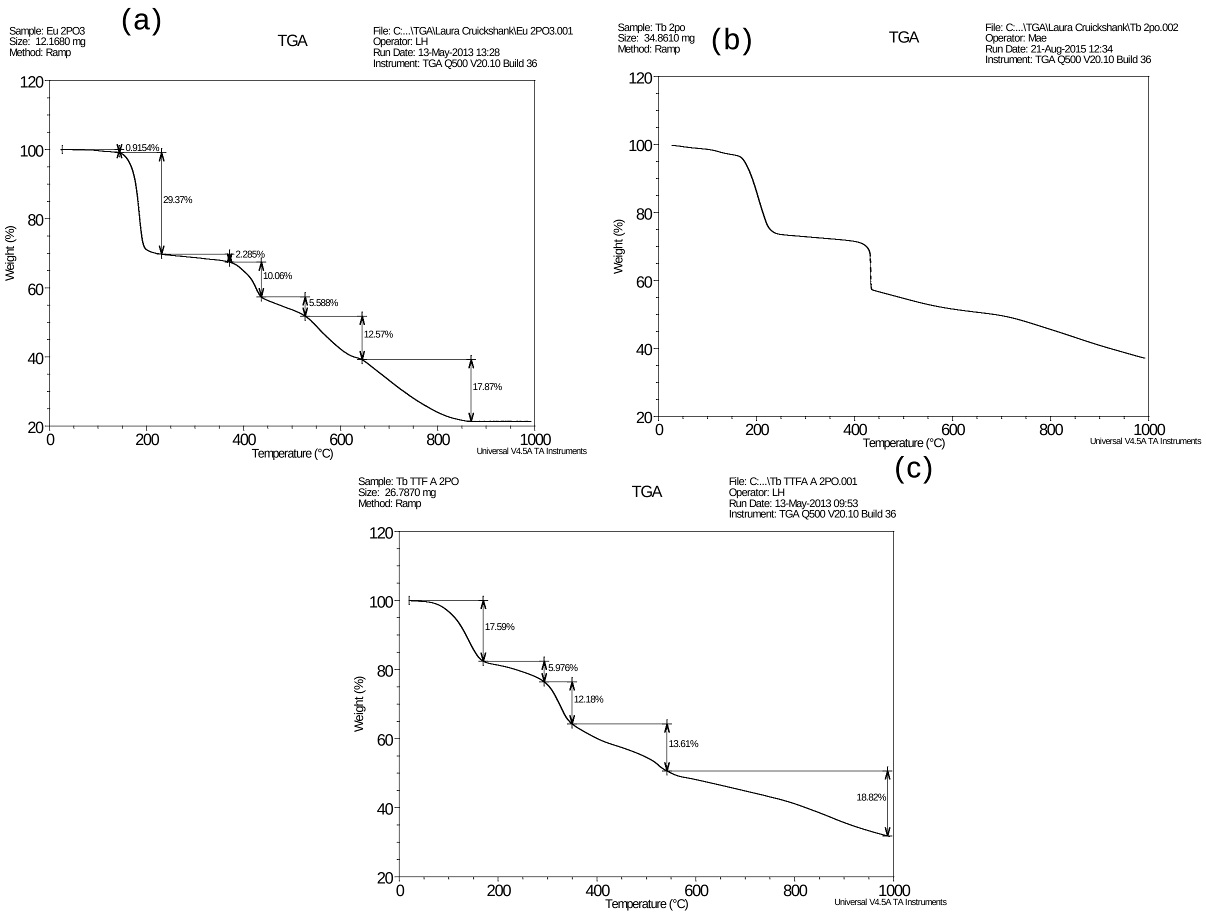

Figure A-3 TGA curves (a) $Eu(2PO)_3$, (b) $Tb(2PO)_3$ and (c) $Tb(TTA)_3 2PO$

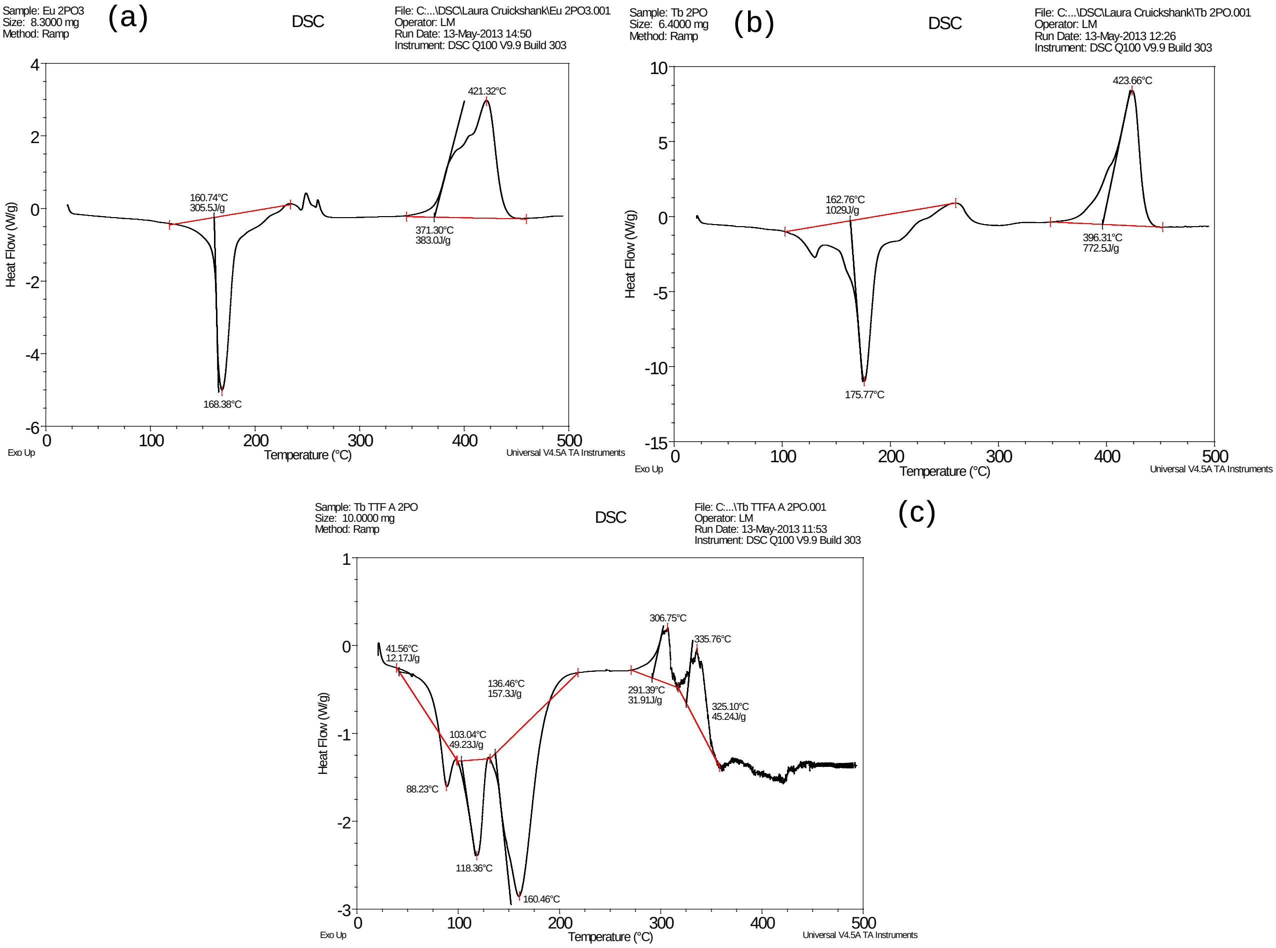

Figure A-4 Differential Scanning Colorimetry curves (a) Eu(2PO)$_3$, (b) Tb(2PO)$_3$ and (c) Tb(TTA)$_3$2PO

Table A-1 Details for Karl Fischer titrations for $2PO_3$ and $TTA_3.2PO$ complexes.

Complex	Eu^{3+} $2PO_3$		Tb^{3+} $2PO_3$		Eu^{3+} $TTA_3.2PO$		Tb^{3+} $TTA_3.2PO$	
	End point (mL)	Water (%)	End point (mL)	Water (%)	End point (mL)	Water (%)	End point (mL)	Water (%)
Titration 1	0.0000	0.00	0.0000	0.00	0.0000	0.00	0.0000	0.00
Titration 2	0.0000	0.00	0.0000	0.00	0.0000	0.00	0.0000	0.00
Titration 3	0.0000	0.00	0.0020	0.01	0.0000	0.00	0.0000	0.00
Average	0.0000	0.00	0.0006	0.00	0.0000	0.00	0.0000	0.00

Table A-2 Average particle diameters determined for particles synthesised as part of initial experiments into factors affecting ammonium hydroxide catalysed silica sol-gel particle synthesis.

Experimental set	Ammonium hydroxide / mL	Temperature / °C	Time / h	Average particle diameter/ nm	SD / nm
A	3	20	1	281	29
B	7	20	1	Not measured	N/A
C	10	20	1	674	35
D	7	5	1	837	78

Table A-3 Average particle diameters obtained for particles synthesies during Taguchi design of experiments

Experimental set	Ammonium hydroxide / ml	Temperature / C	Time / h	Average particle diameter/nm	SD / nm
1	12	20	1	606	29
2	10	20	2	747	39
3	8	20	1	698	30
4	4	20	2	358	33
5	12	15	1	528	36
6	10	15	2	485	56
7	8	15	1	857	42
8	4	15	2	602	57
9	12	5	1	659	79
10	10	5	2	757	93
11	8	5	1	784	60
12	4	5	2	608	41

Table A-4 Average diameters of ammonium hydroxide particles obtained during test of Taguchi design

Experimental set	Ammonium hydroxide / ml	Temperature / C	Time / h	Average particle diameter / nm	SD / nm
DOE 1	8	5	0.5	767	72
DOE 2	7	5	1	950	65
DOE 3	9	5	1	791	31
DOE 4	8	10	1	589	46

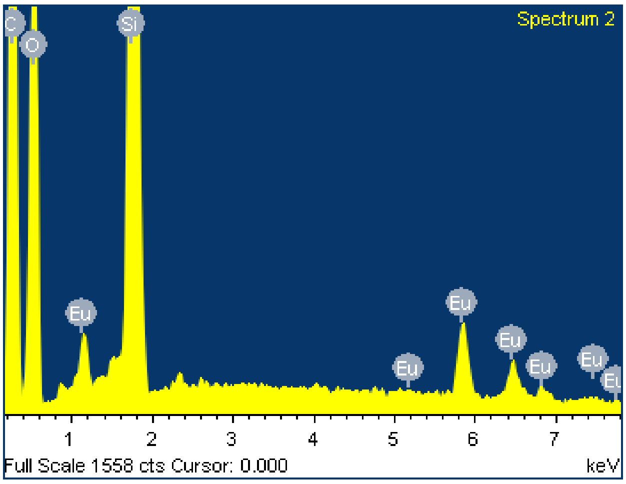

Figure A-5 EDXA spectrum of core shell particles synthesised using the commercially available silica bead as a core, and the shell doped with Eu^{3+} TTA$_3$.2PO

Table A-5 C:N data for whole soil, fine silt and clay fractions of the three soils collected from the Glensaugh research station

Soil	Wt (mg)	N (%/w)	C (%/w)	C:N ratio
Soil 1 fine silt	15.711	0.41	4.64	11.32
Soil 2 fine silt	15.685	0.25	2.64	10.56
Soil 3 fine silt	15.532	0.82	12.05	15.24
Soil 1 colloidal clay	15.795	0.78	7.71	9.8
Soil 2 colloidal clay	15.66	0.48	4.49	9.35
Soil 3 colloidal clay	15.109	1.1	16.26	15.16
Soil 1 2mm	15.743	0.38	4.08	10.74
Soil 2 2mm	15.361	0.25	2.59	10.36
Soil 3 2mm	14.996	0.79	11.79	14.92

Table A-6 Concentrations of oxalate extractable ions present within whole soil, fine silt and clay fractions of the three soils collected from the Glensaugh research station.

	ppm/kg soil				
	Al	Fe	Mn	P	Si
Soil1 fine silt	2.855661	6.868494	0.413918	1.285657	0.186132
Soil 2 fine silt	1.650685	3.262976	0.250285	0.713837	0.086489
Soil 3 fine silt	2.017651	5.099461	0.059397	0.384277	None detected
Soil1 colloidal clay	6.108597	14.61363	0.455553	3.044775	0.194183
Soil 2 colloidal clay	3.822282	6.510494	0.326083	1.507406	0.453155
Soil3 colloidal clay	3.391272	6.931206	0.071946	0.582977	0.175654
Soil 1 2mm	3.116741	11.7813	0.446633	1.423083	0.237006
Soil 2 2mm	1.93307	5.40756	0.258467	0.833018	0.09326
Soil 3 2mm	1.926768	4.973006	0.066995	0.353192	None detected

Table A-7 Mass of sediment collected during high intensity rainfall soil erosion simulations. Mass at each collection point shows average and standard deviation for the three replicates performed. (SD = standard deviation for triplicate samples in g).

	Sediment at collection point (g)							
Time (minutes)	A	SD ±	B	SD ±	C	SD ±	Overland flow	SD ±
10	0.0004	0.0002	0.0008	0.0006	0.0011	0.0006	0.0687	0.0528
20	0.0010	0.0001	0.0007	0.0006	0.0016	0.0010	0.2679	0.0128
30	0.0018	0.0006	0.0021	0.0008	0.0034	0.0008	0.5930	0.3037
40	0.0042	0.0028	0.0027	0.0002	0.0036	0.0015	0.6900	0.1930
50	0.0039	0.0009	0.0027	0.0006	0.0063	0.0020	0.7586	0.1902
60	0.0053	0.0011	0.0040	0.0009	0.0083	0.0023	0.7862	0.2172

Table A-8 Mass of sediment collected during low intensity rainfall soil erosion simulations. Mass at each collection point shows average and standard deviation for the three replicates performed. SD = standard deviation for triplicate samples in g.

	Sediment at collection point (g)							
Time (minutes)	A	SD ±	B	SD ±	C	SD ±	Overland flow	SD ±
10	0.0003	0.0000	0.0005	0.0003	0.0006	0.0003	0.0270	0.0400
20	0.0007	0.0003	0.0008	0.0003	0.0012	0.0002	0.0916	0.0582
30	0.0012	0.0005	0.0013	0.0004	0.0026	0.0013	0.2360	0.0564
40	0.0018	0.0009	0.0018	0.0007	0.0045	0.0014	0.4001	0.1269
50	0.0030	0.0012	0.0027	0.0014	0.0058	0.0007	0.6796	0.1285
60	0.0044	0.0010	0.0044	0.0007	0.0080	0.0004	0.7963	0.0386

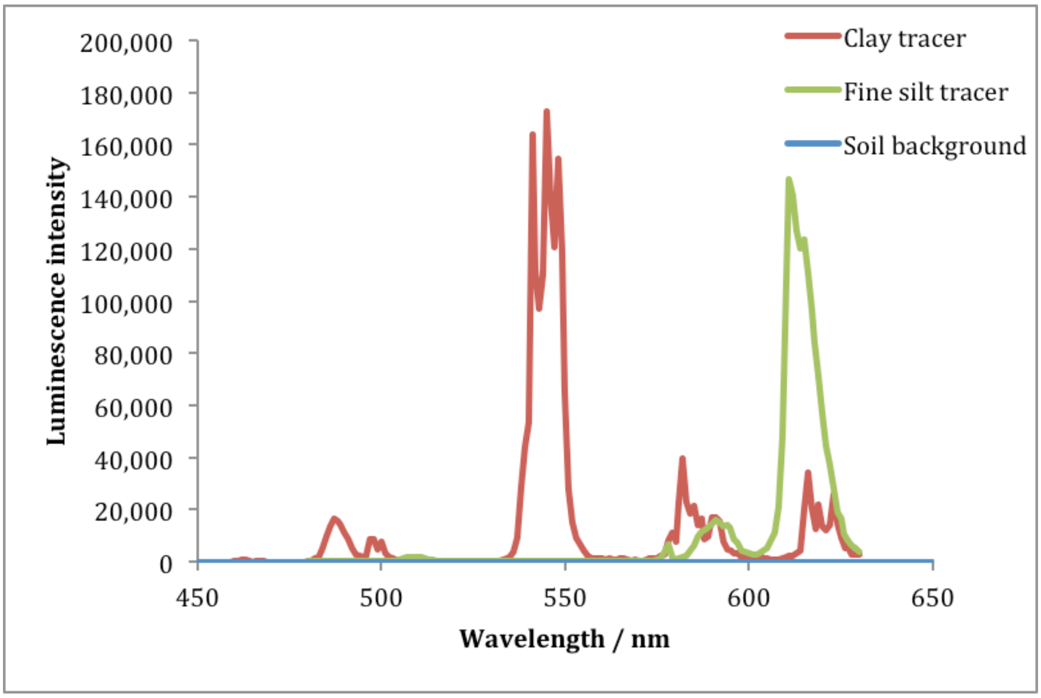

Figure A-6 Fluorescence spectra showing initial luminescence of applied soil and tracers mix prior to soil erosion simulations (obtained on a Edinburgh Instruments FLS920 in time delay mode, excitation at 320 (clay tracer) or 350 nm (fine silt tracer), excitation and emission slit width: 4 nm, 395 nm emission filter, 0.1 ms delay).

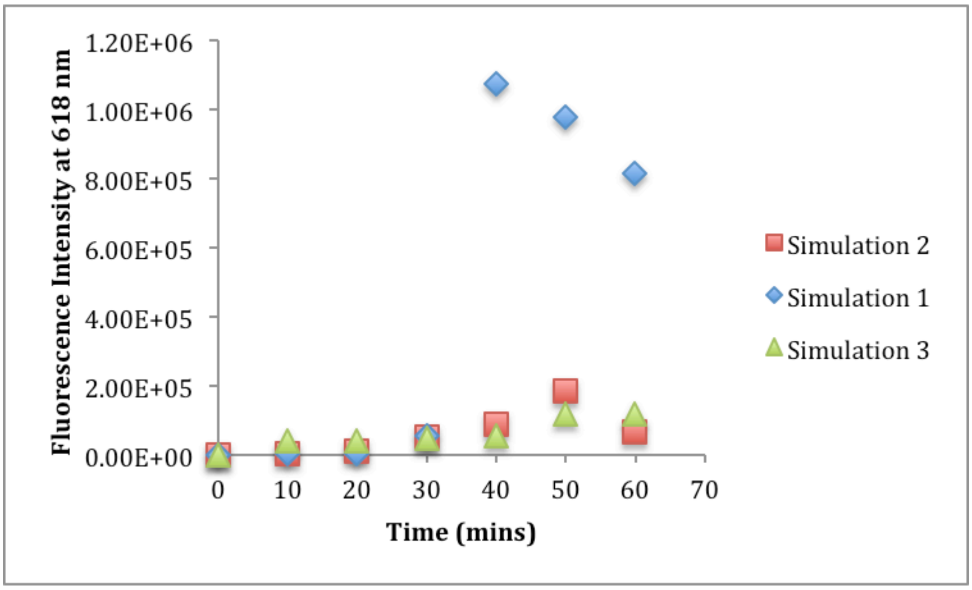

Figure A - 7 Fluorescence intensity of fine silt tracer within dried sediment collected in overland flow during high intensity rainfall soil erosion simulations (obtained on a Edinburgh Instruments FLS920 in time delay mode, excitation at 350 nm, excitation and emission slit width: 4 nm, 395 nm emission filter, 0.2 ms delay). Error bars represent standard deviation of fluorescence intensity between the three replicate measurements.

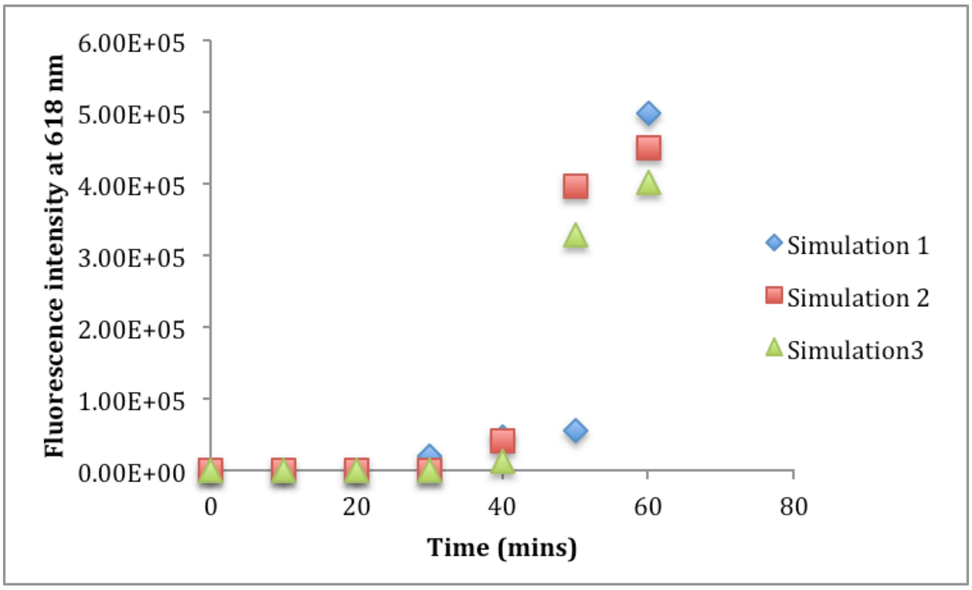

Figure A - 8 Fluorescence intensity of fine silt tracer within dried sediment collected in overland flow during low intensity rainfall soil erosion simulations (obtained on a Edinburgh Instruments FLS920 in time delay mode, excitation at 350 nm, excitation and emission slit width: 4 nm, 395 nm emission filter, 0.2 ms delay). Error bars represent standard deviation of fluorescence intensity between the three replicate measurements.

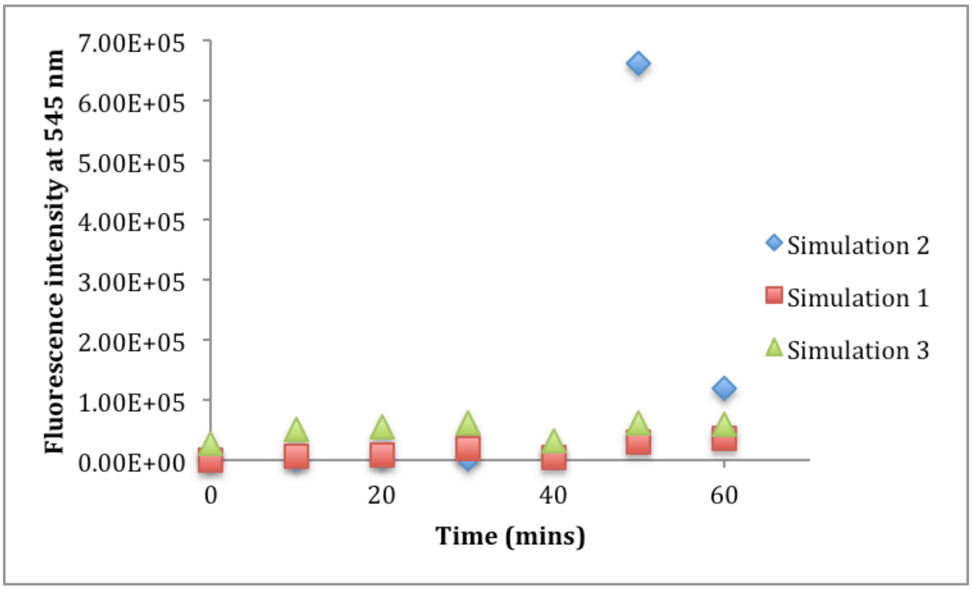

Figure A - 9 Fluorescence intensity of clay tracer within dried sediment collected in overland flow during high intensity rainfall soil erosion simulations (obtained on a Edinburgh Instruments FLS920 in time delay mode, excitation at 320 nm, excitation and emission slit width: 4 nm, 395 nm emission filter, 0.2 ms delay). Error bars represent standard deviation of fluorescence intensity between the three replicate measurements.

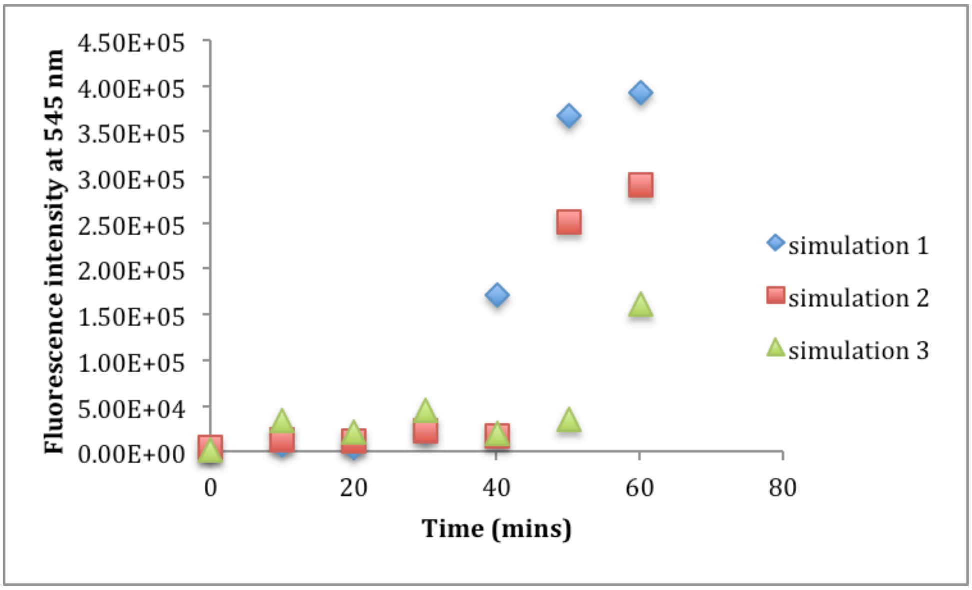

Figure A - 10 Fluorescence intensity of clay tracer within dried sediment collected in overland flow during low intensity rainfall soil erosion simulations (obtained on a Edinburgh Instruments FLS920 in time delay mode, excitation at 320 nm, excitation and emission slit width: 4 nm, 395 nm emission filter, 0.2 ms delay). Error bars represent standard deviation of fluorescence intensity between the three replicate measurements.

Table A-9 Luminescence intensity at 545 nm for clay tracer in sediment collected during high intensity rainfall soil erosion simulations. Intensity at each collection point shows average and standard deviation for the three replicates performed (obtained on a Edinburgh Instruments FLS920 in time delay mode, excitation at 320 nm, excitation and emission slit width: 4 nm, 395 nm emission filter, 0.1 ms delay).

Time (minutes)	Fluorescence intensity at 545 nm							
	A	SD ±	B	SD ±	C	SD ±	Overland flow	SD ±
0	5.51E+04	7.76E+04	1.02E+05	8.17E+04	8.68E+04	7.13E+04	9.38E+03	1.54E+04
10	5.19E+04	7.33E+04	9.17E+04	7.20E+04	9.00E+04	7.61E+04	1.88E+04	2.70E+04
20	5.68E+04	8.17E+04	9.40E+04	7.61E+04	8.62E+04	6.85E+04	2.27E+04	2.78E+04
30	6.12E+04	8.56E+04	9.16E+04	6.67E+04	9.09E+04	6.10E+04	2.66E+04	3.07E+04
40	5.51E+04	7.82E+04	9.79E+04	6.02E+04	1.04E+05	4.93E+04	1.70E+04	1.47E+04
50	7.19E+04	6.14E+04	1.07E+05	5.95E+04	1.69E+05	3.26E+04	2.51E+05	3.57E+05
60	6.53E+04	6.23E+04	9.98E+04	4.66E+04	2.36E+05	1.39E+05	7.16E+04	4.31E+04

Table A-10 Luminescence intensity at 618 nm for fine silt tracer in sediment collected during high intensity rainfall soil erosion simulations. Intensity at each collection point shows average and standard deviation for the three replicates performed (obtained on a Edinburgh Instruments FLS920 in time delay mode, excitation at 350 nm, excitation and emission slit width: 4 nm, 395 nm emission filter, 0.1 ms delay).

Time (minutes)	Fluorescence intensity at 618 nm							
	A	SD ±	B	SD ±	C	SD ±	Overland flow	SD ±
0	4.86E+02	1.85E+02	6.15E+02	3.02E+01	5.92E+02	2.08E+00	4.78E+02	1.53E+02
10	6.27E+02	3.00E+00	6.10E+02	2.11E+01	6.27E+02	4.73E+00	1.52E+04	2.09E+04
20	4.25E+02	1.77E+02	6.30E+02	5.69E+00	5.29E+02	2.96E+02	1.80E+04	2.03E+04
30	5.56E+02	5.26E+02	5.96E+02	9.87E+01	3.54E+02	2.52E+02	5.16E+04	4.71E+03
40	8.66E+03	1.43E+04	3.84E+02	1.32E+02	2.61E+02	2.70E+02	4.07E+05	5.78E+05
50	5.57E+03	9.08E+03	4.34E+02	7.60E+01	2.39E+04	2.02E+04	4.28E+05	4.78E+05
60	1.21E+04	1.02E+04	6.28E+02	1.04E+02	3.19E+04	2.13E+04	3.33E+05	4.17E+05

Table A-11 Luminescence intensity at 545 nm for clay tracer in sediment collected during low intensity rainfall soil erosion simulations. Intensity at each collection point shows average and standard deviation for the three replicates performed. SD = standard deviation for triplicate samples (obtained on a Edinburgh Instruments FLS920 in time delay mode, excitation at 320 nm, excitation and emission slit width: 4 nm, 395 nm emission filter, 0.1 ms delay).

Time (minutes)	Fluorescence intensity at 545 nm							
	A	SD ±	B	SD ±	C	SD ±	Overland flow	SD ±
0	1.34E+03	7.48E+02	4.78E+03	5.21E+03	5.63E+03	4.40E+03	2.58E+03	1.47E+03
10	3.57E+03	2.55E+03	3.11E+03	1.56E+03	2.46E+04	2.81E+04	1.81E+04	1.40E+04
20	2.09E+03	2.01E+03	9.14E+03	6.94E+03	1.89E+04	1.74E+04	1.26E+04	8.76E+03
30	1.50E+04	2.08E+04	9.83E+03	4.27E+03	1.02E+04	4.93E+03	3.00E+04	1.34E+04
40	1.59E+04	2.50E+04	1.18E+04	1.41E+03	2.54E+04	1.90E+04	6.97E+04	8.79E+04
50	1.74E+04	2.52E+04	1.53E+04	6.07E+03	4.24E+04	1.35E+04	2.18E+05	1.68E+05
60	1.76E+04	2.38E+04	2.17E+04	1.40E+04	3.39E+04	2.94E+04	2.82E+05	1.16E+05

Table A-12 Luminescence intensity at 618 nm for fine silt tracer in sediment collected during low intensity rainfall soil erosion simulations. Intensity at each collection point shows average and standard deviation for the three replicates performed. SD = standard deviation for triplicate samples (obtained on a Edinburgh Instruments FLS920 in time delay mode, excitation at 350 nm, excitation and emission slit width: 4 nm, 395 nm emission filter, 0.1 ms delay).

Time (minutes)	Fluorescence intensity at 618 nm							
	A	SD ±	B	SD ±	C	SD ±	Overland flow	SD ±
0	6.16E+02	3.46E+00	6.17E+02	1.73E+00	6.14E+02	2.31E+00	6.25E+02	9.90E+00
10	4.79E+02	2.28E+02	6.01E+02	1.89E+01	5.47E+02	1.00E+02	4.83E+02	2.20E+02
20	5.49E+02	3.70E+01	5.55E+02	1.04E+02	5.09E+02	1.10E+02	4.93E+02	5.77E-01
30	1.17E+03	8.99E+02	5.32E+02	1.28E+02	5.64E+02	1.30E+02	5.06E+02	1.15E+00
40	9.97E+03	1.64E+04	6.14E+02	8.43E+00	5.06E+02	6.10E+01	2.26E+04	1.68E+04
50	7.76E+03	1.25E+04	4.90E+02	8.94E+01	3.08E+02	1.15E+01	3.51E+05	3.86E+04
60	8.94E+03	6.31E+03	6.18E+02	2.87E+02	4.98E+02	3.41E+00	4.19E+05	2.73E+04